UNIVERSITAT DE BARCELONA

Transport and assembly of colloids in liquid crystals

Josep M. Pagès Casas

DOCTORAT EN NANOCIÈNCIES

Transport and assembly of colloids in liquid crystals

Josep M. Pagès Casas

Advisors: Profs. J. Ignés Mullol[1,2] and F. Sagués Mestre[1,2]

Tutor: Prof. J. Ignés Mullol

[1]Departament de Ciència dels Materials i Química Física, Universitat de Barcelona.

[2]Institut de Nanociència i Nanotecnologia de la Universitat de Barcelona (IN[2]UB).

The research described in this thesis has been performed at the group “Self-Organized Complexity and Self-Assembled Materials” from the Department of Materials Science and Physical Chemistry of the University of Barcelona.

Agraïments

Ja fa quatre anys que per primer cop vaig passar pel despatx del Francesc i em va dir: " Bueno, ara anirem a veure el lab, però esperem que hi hagi algú, ja que jo no tinc claus...". Des del moment d'aquesta primera anècdota fins avui, són moltes les experiències viscudes amb el grup, només donar-los gràcies a tots per tots els moments.

En primer lloc, vull agrair als meus directors de tesis, Jordi Ignés i Francesc Sagués per donar-me l'oportunitat de cursar un doctorat sota la seva direcció, i també per endinsar-me dins al món de la "Soft Matter". També cal fer una menció molt especial al Jordi Ignés pel seu temps i la seva gran dedicació. Més concretament, gràcies Francesc per sempre estar al teu despatx disposat a explicar teoria, amb la llum tènue i a qualsevol hora del dia. A tú Jordi, pel teu bon rollo i per sempre tenir algo en ment amb el que continuar o amb el que arreglar l'experiment en qüestió. Sense vosaltres aquesta tesis no hagués estat possible!

També vull donar les gràcies a tots els membres més joves del grup, primerament als que han set companys de feina, alegries, penes i doctorat durant aquest llarg recorregut, Pau, Berta, Jérome i Mohammad. Al Pau per sempre tenir un, dos, tres...moments per mi; per ensenyar-me i guiar-me dins del lab i per ser un "col·lega dels bons". A la Berta, com diria el Pau, per revolucionar el galliner, però simplement, per ser allà els quatre anys que hem compartit de ciència, i de vida, sense deixar-nos algun que altre càlcul. Al Jérome per la seva gran formalitat i simpatia, típica d'un filòsof europeu. Finalment, al Mohammad per les seves xarrades sobre Irán i la seva constant pregunta sobre els papers i la tesis. Més enllà, també vull mencionar els doctorands orgànics, Omar, Tomeu, Anna, Albert... amb els quals hem passat mil estones, sobretot els divendres de cervesseta, i els "teòrics" del departament pels "últims" dinars. I finalment, a tots els estudiants que han passat pel lab, els més recents, en Raimon (sempre està alegre i, a més, és el successor dels col·loïds forètics) i l'Ignasi (l'home dels restaurants, i el bon beure i menjar).

Crec que també cal una menció pels Drs. Pietro Tierno i Arthur Straube, amb els quals hem estat col·laborant durant la realització d'aquesta tesis. Especialment, gràcies per les simulacions i el treball en la part teòrica. També vull agrair al Dr. Antonio Ortiz per la seva gran amabilitat i disposició tant per deixar-nos material (objectius, partícules...) com per l'ajuda en la mesura de la viscositat del cristall líquid.

Una altra persona a la que m'agradaria agrair les seves discussions és en John Toner, com ell diu, "just call me plain, old John", amb el qual vam interaccionar en la seva estada a Barcelona.

Abans dels agraïments personals, m'agradaria donar gràcies a la comissió de seguiment, R. Albalat, P. Tierno i J.A. Farrera, per la facilitat en tota la burocràcia, però també als que seran membres del tribunal, H.Löwen, A. Fernández-Nieves i L. Casanellas-Vilageliu per formar part d'aquesta tesi.

Finalment, vull agrair a la meva família, papa i mama, per estar sempre allà. Mama: "Tranquil, no et preocupis. No et posis nerviós. Bueno home, de vegades s'ha d'apexugar....". Al final, sort de tanta paciència junta. Papa: " Ja cobres prou per lo que fas home. Treballar, tú? Vols dir? Jo crec que no massa, només fer bombes....". Només, gràcies. També cal fer una menció molt especial a la meva xicota, la Clàudia, per estar al meu costat durant tot aquest temps, i especialment, per aguantar-me, i a la seva família, a en Salvi "noi, això ho publicarem al Planeta?", i també a la Rosa Mª pels tuppers de cada cap de setmana. A la gent del poble, a la troupe de sempre, Konya, Martí, Ulong... i els 20...30...40 que falten. A la gran família gironina, que ens trobem poc, però de qualitat, i a qui cal una menció especial, Gerard, que crec que sense tú, aquest doctorat tampoc hagués estat possible. I ara si, per acabar, a les bèsties, a la Tuca, per la seva companyia canina des de l'inici fins al final del doctorat, i també a l'Obi i en Kai.

Contents

Resum

Abstract

Particles dispersed in nematic liquid crystals, also called nematic colloids, are nowadays typical experimental systems studied in the field of Soft Matter. In this scenario, the interactions and forces between colloidal particles are in equilibrium, and thus, elasticity governs inter-particle interactions. Furthermore, the application of an external field leads to a totally different scenario where the system is out-of-equilibrium, and thus, new physical phenomena can emerge. Nematic colloidal particles can be propelled under the application of an electric field, which allows for driven particles scenarios. Although particles dynamics of these systems are being studied in detail, there is still absence of true control capabilities, which could bring new possibilities in the use or application of driven nematic colloids. To this end, this work has essentially focused on studying the transport and assembly of micron-sized particles dispersed in nematic liquid crystals.

In this thesis, first, we report the transport of a single particle featuring either dipolar or quadrupolar configurations of the surrounding environment of the liquid crystal. From these observations we study the transport modes of driven colloidal particles. While motion is ballistic in the driving direction, namely along the nematic far-field director, our experiments show that transversal fluctuations become superdiffusive for the topological defects featuring dipolar configuration around the inclusions. In contrast, results barely differ from normal diffusion for particles displaying quadrupolar configurations. Additionally, we have observed that the phenomenon can be reproduced with different driving methods and propulsion speeds, while it is strongly dependent on particle size and temperature. We have proposed a mechanism based on the geometry of the liquid crystal backflow around the inclusions to justify the persistence of thermal fluctuations affecting on the point defect-hedgehog (dipolar configuration) orientation, but also to explain the observed temperature and particle size dependence of the superdiffusive behavior based on material and geometrical parameters.

The second part of this thesis is based on colloidal assembly. Here, we combine experiments, theory and simulations to investigate the collective dynamics of an ensemble of anisometric colloids assembled above a single topological defect, which acts as attractor point, in a nematic liquid crystal. The nematic liquid crystal elasticity allows to define two different patterns by manipulating the anchoring conditions at the bounding plates by means of a photosensitive surface, namely aster (pure splay texture) and rotating-mill like (bend-splay texture). For pure radial configurations (aster), we observe the formation of stationary clusters that display a radially extended density gradient with three different states of aggregation. The innermost part of the cluster corresponds to a solidified core, which is followed by a liquid-like corona and finally, ending in a diluted gas-like phase. Moreover, we describe our system with a non-equilibrium equation of state and directly determine the effective pressure and temperature in the system. In contrast, for the bend-splay texture we obtain a spatially extended spiral pattern of the liquid crystal orientation that induces the dynamic assembly of a rotating mill. To understand either the different assemblies obtained or the phases observed in the asters case, we develop a theoretical model that combines different interactions resulting from phoretic propulsion, dipolar forces and hydrodynamics,

allowing to capture the basic physics of the process. Further, Dr. Arthur Straube perform simulations based on this model which reproduces qualitatively but also quantitatively the obtained experimental results.

The third and last part of this thesis is based on steering and guiding the collective colloidal transport by means of both photo-patterning and confining devices. The first set of experiments is based on understanding the dynamics of an ensemble of flocking particles dispersed in a nematic liquid crystal. This procedure is achieved by means of the above mentioned photosensitive surface. Taking advantage of the latter, an array of topological defects can also be patterned onto the liquid crystal which allows for the study of both topology and collective colloidal transport. Furthermore, we show the implementation of obstacles for the flock to pass through by using microfluidic devices.

To conclude, this work not only increases our fundamental knowledge of micron-sized particles dispersed in anisotropic materials, such as nematic liquid crystals, but it serves as a starting platform to explore the motion of driven colloids inside them. Special emphasis will be put on the implementation of new techniques for guiding and steering the colloidal trajectories by means of both photo-patterning and microfluidic devices, as it has been demonstrated to be key towards the control of colloidal trajectories.

List of figures

Below, find a list of the figures present in this thesis.

List of videos

Below, find a list of videos that complement some of the figures and explanations of this thesis.

- **Video 1. Colloidal particle automatically tracked.** Bright-field micrograph sequence showing a sedimenting 5 µm silica spherical particle displaying a point defect-hedgehog distortion. Typical configuration for experiments shown in Chapter 3. The black zone consists of pixels that are used to calculate the particle's centre coordinates. After particle detection, the red line is the trajectory defined by particle motion.

- **Video 2. Colloidal particle driven in an isotropic fluid.** Bright-field micrograph sequence of a 5 µm colloidal particle dispersed in a water/glycerol mixture sedimenting by means of the in-plane component of gravity after tilting the sample an angle, $\alpha=8.5^0$.

- **Video 3. Sedimentation of a colloidal particle featuring dipolar liquid crystal configuration.** Micrograph sequence obtained between crossed polarizers showing the trajectory of a 5 µm colloidal particle. The particle is driven by means of the in-plane component of gravity. The temperature in this experiment is 27.5^{o}C.

- **Video 4. Electrokinetically-driven particle featuring dipolar liquid crystal configuration.** Bright-field micrograph sequence of a 10 µm particle with dipolar configuration dispersed in the nematic liquid Crystal CCN-37 driven by means of the liquid crystal-enabled electrokinetics (LCEEK) mechanism. The temperature in this experiment is 40^{o}C.

- **Video 5. Sedimentation of a colloidal particle featuring quadrupolar liquid crystal configuration.** Bright-field micrograph sequence of a 5 µm colloidal particle dispersed in a liquid crystal featuring quadrupolar liquid crystal distortion and sedimenting by means of the in-plane component of gravity.

- **Video 6(a,b). Saturn-Rings oscillating periodically.** Micrograph sequence obtained between crossed polarizers of a 10 µm colloidal particle featuring quadrupolar configuration of the surrounding nematic director in form of a Saturn-Ring. The two oscillating modes of the dynamics defects (**a**, **b**) correspond to a frequency, f = 50 Hz (**a**) and f = 60 Hz (**b**).

- **Video 7. Saturn-Rings oscillation induces motion.** Micrograph sequence obtained between crossed polarizers of a 10 µm colloidal particle featuring Saturn-Ring quadrupolar configuration of the surrounding nematic director. Under energetic supply, the particle transports along the far-field director.

- **Video 8(a,b). Transport of inclusions featuring distorted quadrupolar nematic configurations.** Micrograph sequence of a 10 µm colloidal particle observed between

crossed polarizers featuring distorted Saturn-ring configurations. The particles moves along the far-field director in both, **a** and **b**, but in opposite senses.

- **Video 9. Saturn-ring transit to a butterfly-like structure.** Micrograph sequence of a 10 µm colloidal particle observed between crossed polarizers featuring Saturn-ring configurations that spontaneously transit to butterfly-like structures under energetic supply.

- **Video 10. Backflow-mediated particle propulsion in colloidal assemblies.** A carrier sinusoidal wave (1 KHz) is modulated with a lower frequency allowing for peanut-shaped particles to propel due to the nematic bulk reorientation. The images are bright-field obtained.

- **Video 11. Self-assembling nematic colloidal asters.** Bright-field images sequence of a growing colloidal aster assembling towards an attractive topological defect while an AC of amplitude $0.76\,V\cdot\mu m^{-1}$ and f = 20 Hz is being applied. The particles display radial trajectories, as are driven along the radial UV-imprinted pattern.

- **Video 12. Formation of a rotating mill colloidal assembly.** Bright-field micrograph sequence of a rotating mill assembly growing while an AC of amplitude $0.76\,V\cdot\mu m^{-1}$ and f = 20 Hz is being applied.

- **Video 13. Simulation for asters.** Simulated cluster assembly obtained at a f = 10 Hz while keeping constant the amplitude of the electric field $0.76\,V\cdot\mu m^{-1}$. The clusters are simulated with 700 particles with the model described in the thesis.

- **Video 14. Simulation for rotating mills.** Simulated dynamic assembly obtained at a f = 10 Hz while keeping constant the amplitude of the electric field $0.76\,V\cdot\mu m^{-1}$. The clusters are simulated with 700 particles with the model described in the thesis.

- **Video 15. Formation of the distorted conformal crystal lattice in a planar geometry.** Bright-field images of the cluster assembling towards a plane wall while an AC of amplitude $0.76\,V\cdot\mu m^{-1}$ and f = 15 Hz is being applied.

- **Video 16. Colloidal swarm translocation.** Bright-field micrograph sequence of the swarm translocation. The cluster is transported by *in situ* reconfiguration of the nematic liquid crystal elastic matrix. In this experiment the applied AC electric field is of amplitude $0.76\,V\cdot\mu m^{-1}$ and f = 10 Hz.

- **Video 17. Simulations of the colloidal swarm translocation.** Simulation showing the translocation process for 1000 particles with the model described in the thesis. This process is achieved while an AC of amplitude $0.76\,V\cdot\mu m^{-1}$ and f = 10 Hz is being applied.

- **Video 18. Colloidal transport between rotating mills.** Bright-field micrograph sequence showing two consecutive rotating mills which mediate particle transport by means of topological defects specifically located. The particles are propelled under an AC of amplitude $0.76\ V \cdot \mu m^{-1}$ and f = 10 Hz.

- **Video 19. Two-dimensional array of photo-induced objects.** Mixed polarized-light and bright-field micrograph sequence of an array of an imprinted pattern of 3x3 photo-induced topological defects while an AC of amplitude $0.76\ V \cdot \mu m^{-1}$ and f = 10 Hz is being applied.

- **Video 20. Colloidal clogging effect in nematic liquid crystals.** Bright-field micrograph sequence of a flock of peanut-shaped particles driven along the far-field director and passing through a narrow constriction. The particles are propelled under an AC electric field of amplitude $0.76\ V \cdot \mu m^{-1}$ and f = 10 Hz.

- **Video 21. Switching the chirality of a rotating mill by means of UV-light.** Polarized-light micrographs sequence showing the handedness switch in the bend-splay configuration by *in situ* reconfiguration of the nematic liquid crystal elasticity. Here, the applied electric field is of amplitude $0.1\ V \cdot \mu m^{-1}$ and f = 1 KHz to keep particles immotile.

-

List of abbreviations and symbols

Below, find a list of abbreviations and symbols for important terms and concepts used in this thesis.

- LC(s) – Liquid Crystal(s)
- LLC(s) – Lyotropic Liquid Crystal(s) / Living Liquid Crystal(s)
- TLC(s) – Thermotropic Liquid Crystal(s)
- NLC(s) – Nematic Liquid Crystal(s)
- T_m – Melting point
- T_c – Clearing point
- k_B – Boltzmann constant
- PAA – 4'4'-azoaxyanisole
- CB – Cianobyphenil
- **n** , $\vec{n}$ – Director vector
- **n(r)**, $\vec{n}(r)$ – Director vector field
- SmA – SmecticA liquid crystal phase
- SmC – SmecticC liquid crystal phase
- θ – Polar angle
- ϕ – Azimuthal angle
- *S* – Nematic Order Parameter
- $n_{\parallel}$ – Material refractive index parallel to the director field
- $n_{\perp}$– Material refractive index perpendicular to the director field
- POM – Polarizing Optical Microscope/y
- E – Electric field
- ε – Electric permittivity
- ε_a – Dielectric anisotropy
- $\varepsilon_{\parallel}$ – Electric permittivity parallel to the director field
- $\varepsilon_{\perp}$ – Electric permittivity perpendicular to the director field
- H – Magnetic field
- χ – Diamagnetic susceptibility
- $\Delta\chi$ – Diamagnetic anisotropy
- R – Particle radius
- K_i – Elastic liquid crystal constants, where $i = 1$, 2 and 3 for splay, twist and bend distortions, respectively
- AC – Alternating current
- DC – Direct current
- $D_{\parallel}$ – Diffusion coefficient parallel to the director field
- $D_{\perp}$ – Diffusion coefficient perpendicular to the director field
- η – Viscosity coefficient
- $\eta_{\parallel}$ – Viscosity parallel to the director field
- $\eta_{\perp}$ – Viscosity perpendicular to the director field
- W_{anch} – Anchoring parameter
- λ_{dGK} – Characteristic de Gennes-Klemann length

- FPCM – Fluorescence Confocal Polarizing Microscope/y
- MSD – Means square displacement (Second moment)
- MD – Mean displacement (First moment)
- R_e – Reynolds number
- D_T – Translational diffusion coefficient
- D_R – Rotational diffusion coefficient
- ICEO – Induced-Charged Electrosmosis
- ICEP – Induced-Charged Electrophoresis
- LCLCs – Lyotropic Chromonic Liquid Crystal(s)
- T_{NI} – Temperature of the nematic – isotropic transition
- LCEEK – Liquid Crystal-Enabled Electrokinetiks
- LCEEP – Liquid Crystal-Enabled Electrophoresis
- LCEEO – Liquid Crystal-Enabled Electrosmosis
- v – Particle velocity
- ITO – Indium-Tin-Oxide
- $\Delta\sigma$ – Conductivity Anisotropy
- λ_D – Debye screening length
- τ_c – Characteristic particle charging time
- τ_e – Characteristic electrode charging time
- UV – UltraViolet
- SAM – Self-Assembled Monolayer
- PS – Polystyrene
- fps – Frames per second
- $\nu -$ Exponent of the diffusive scaling
- SR(s) – Saturn-Ring(s)

Preface

This PhD dissertation has been written taking as a basis the experiments performed in the group "Self-Organized Complexity and Self-Assembled Materials" in the Department of Materials Science and Physical Chemistry and in the Institute of Nanoscience and Nanotechnology (IN2UB) of the University of Barcelona, in the period between November 2015 and February 2019. The research described herein has been conducted under the supervision of professors J. Ignés and F. Sagués.

The text has been structured in six main chapters. **Chapter 1** is an introduction to the fields of Liquid Crystals and Active particles dispersed either, in isotropic fluids or in liquid crystals. The next **Chapter 2** contains the Materials and Methods used during this thesis realization. Here, I show the protocols for the preparation and characterization of the experimental realizations. Following, **Chapter 3**, **4 and 5** consist on a summary of our contributions to the field of "Driven Nematic Colloids". They all include an introductory section, an experimental section detailing the systems, a summary of the obtained results and the discussion, followed by some open questions, and finally the conclusions. In **Chapter 6**, I expose closing remarks including general conclusions and open questions and future perspectives for all the overall work.

Chapter 1

Introduction

1. Liquid Crystals

Liquid crystals (LCs) are anisotropic fluids that present states of matter intermediate between isotropic liquids, such as water, and crystalline solids (**Fig. 1**) ([1]–[4]). Even though LCs are typically viscous fluids, at the molecular scale they also present some degree of internal order (**Fig. 1b**). For this reason, LCs are also called mesomorphic phases or mesophases. These materials are formed by anisometric units, which interact each other conferring particular properties to LCs. Actually, this interaction enhances the orientational order of the LCs constituents, meaning that, on average, they will locally point in the same direction.

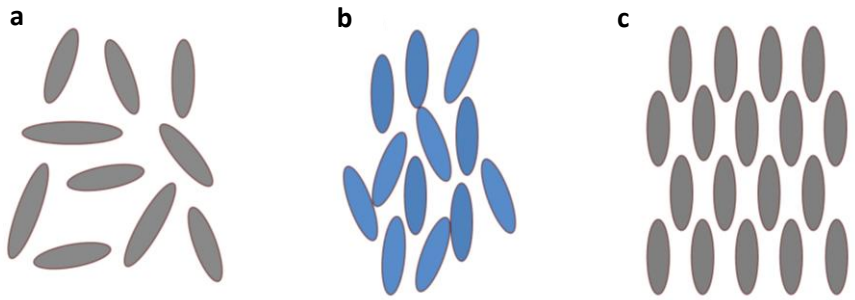

Fig. 1. The liquid crystal phase. Schematic representation of **(a)** an isotropic fluid, which presents neither orientational nor positional order, **(b)** a liquid crystal with orientational order and **(c)** a crystal, exhibiting both orientational and positional order.

Due to their internal order, LCs exhibit anisotropy in most of the physical properties, i.e. the values for a given magnitude along and perpendicular to the preferred axis are not equivalent. The manifestations of this anisotropy effect will be detailed in forthcoming sections.

1.1. Main classification

There are different classifications for LCs; perhaps the most generic one is based on the nature of their constituents. So, LCs can be classified in two main categories: lyotropic and thermotropic.

Lyotropic LCs (LLCs) are based on concentrated aqueous solutions of amphiphiles ([5],[6]), aromatic compounds such as dyes (usually chromonic LCs) ([7]), polymers ([8]), or dense dispersions of anisometric particles ([9],[10]). The different structures formed by unitary building-blocks in LLCs depend on both the concentration and the temperature, hence the prefix *lyo-* indicating the dispersion.

On the other hand, thermotropic LCs (TLCs) are obtained by melting a crystalline solid, hence the prefix *thermo-*. They are oily substances composed of organic molecules that self-assemble into liquid-like ordered phases under a temperature range: before the melting, T_m, and the clearing temperatures, T_c.

The constituents forming TLCs usually present structural features that enhance molecular ordering: they display a rod-like shape that will define the long axis of the molecule (**Fig. 2a**).

Moreover, an important feature that will affect how these materials will interact with external fields, either electric or magnetic, are the functional polarizable groups.

Common examples of TLCs are 4,4'-azoxyanisole (PAA) or cyanobiphenyl (CB) derivatives, such as 4-pentyl-4'-cyanobiphenyl (5CB) (**Fig. 2b**).

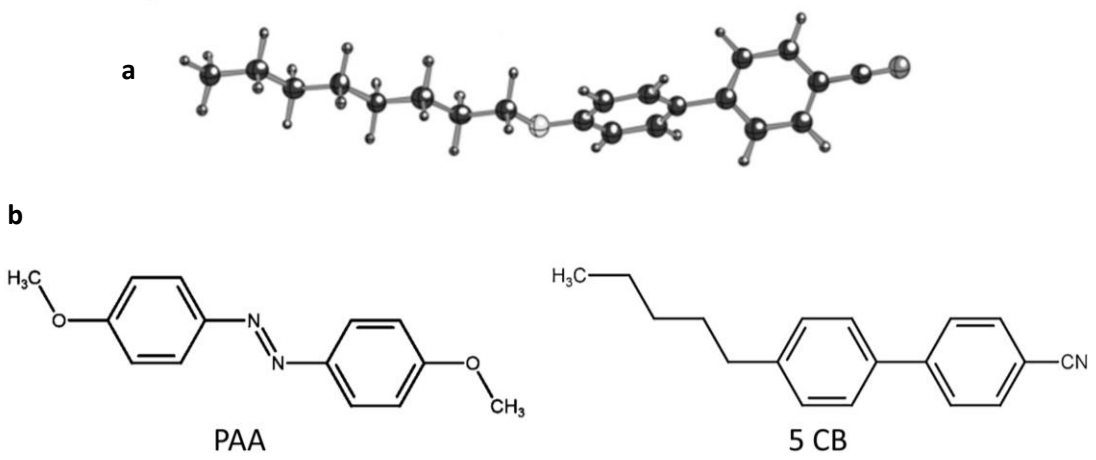

Fig. 2. Molecular structure of the thermotropic liquid crystal constituents. a) Schematic representation of the basic molecular structure constituting TLC molecules. **b)** Chemical structure of two well-known TLC molecules. Cyanobyphenil derivatives, like 5CB, are really stable at room temperature. Thus, they are widely used nowadays. Adaptation from ref.[2].

1.2. Liquid crystal phases

The molecular constituents of LCs self-assemble into different organizations giving rise to the so-called LC phases ([2], [11]). The most common LC phases are the nematic, the cholesteric, the smectic and the columnar.

- The nematic is the less ordered LC phase; its components feature orientational order, which results from the interaction of its building-blocks to align with each other in a preferred direction (**Fig. 3a**). Since nematic constituents are free to slide past one another, there is no long-range order in the positions of their centres of mass.

In the nematic phase, the long-range mean molecular orientation is described by the unit vector, $\vec{n}$ (also denoted as **n**), called the director field (**Fig. 3a**). Although the nematic constituents are polar, there is a centrosymmetric re-arrangement in the bulk of the material, so the directors $\vec{n}$ and $-\vec{n}$ are equivalent.

- The cholesteric phase, also called chiral nematic phase, shares many of the nematics properties. That is, long-range orientational order and its influence on the physicochemical properties. As its name indicates, the cholesteric phase is formed by chiral molecules which spontaneously self-assemble into a helical structure. The presence of these molecules causes the director profile to assume a twisted configuration throughout the medium, meaning that, the different molecules rotate a certain angle perpendicularly to their long axis. The spacing within molecules separated by a full rotation of orientation with respect to the twist axis is called the pitch (*p*). Nevertheless, as half rotation is indistinguishable from a full rotation, since $\vec{n} = -\vec{n}$,the spatial period is one half of *p* (**Fig. 3b**).

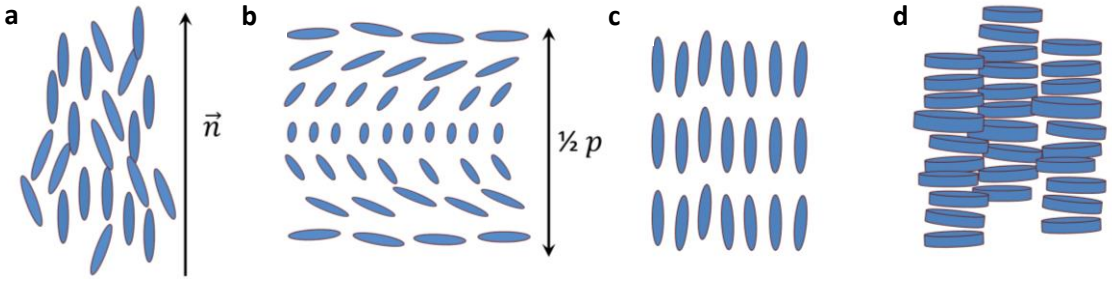

Fig. 3. Liquid crystal phases. Schematic representation of the LCs phases constituted by ellipsoid and disk-like shape building blocks. a) The nematic phase whose constituents tend to align along a preferred direction defined by the director field, **n**. The molecular positions are not correlated. **b)** In the cholesteric phase molecules organize in layers with no positional ordering and vary regularly along a direction perpendicular to the molecular main axes, with a periodicity distance 1/2 p. As in the nematic phase, the molecular positions are not correlated. **c)** The Smectic-A phase. The building-blocks dispose in planes perpendicular to the average molecular axis. **d)** The columnar phase is usually constituted of disk-like objects that self-assemble to form cylindrical structures.

The nematic and cholesteric phases present orientational order and are different from those smectic and columnar phases that also present a certain degree of long-range positional order.

- Smectic phases combine orientational and a partial positional order. In these phases the density of the constitutive entities is not uniform as there is some correlation between the molecules centres of mass. This results in a layered structure where the constitutive molecules are organized in planes with well-defined inter-layer spacing (**Fig. 3c**). Thus, it can be seen as one dimensional order in a three dimension system.

There are different smectic phases ([12]); these phases are characterized by the molecular packing formation and the tilt angle with respect to the normal layer. For example, in SmA phases the constitutive units are disposed perpendicular to the smectic plane while in the SmC the molecules are tilted with respect to this plane.

- Finally, the columnar phase can be regarded as an array of flat-shaped disks which self-assemble into columns that self-organize in periodic structures (**Fig. 3d**). These structures lead to a two-dimensional order in a three dimension system.

In contrast to nematic and cholesteric phases where the constitutive units are elongated, also called calamitic LCs, columnar phases are often found in LCs made of disk-like entities (discotic LCs).

Although most of the considerations below apply to both LLCs and TLCs, we will be generally considering TLCs and in particular nematics, as they present the simplest phase for introducing the most characteristic features of LCs. Moreover, nematic liquid crystals (NLCs) have been the main dispersing medium during the realization of this thesis.

1.3. Order in liquid crystals

LCs constituents present some degree of alignment although these substances are not as ordered as a solid crystal. This is in contrast to materials in the isotropic phase, which have no intrinsic order. Thus, LCs feature lower symmetry than isotropic fluids as their constituents tend to be parallel to some common axis. Most of the interesting phenomena

arising from LCs involve the geometry and dynamics of this preferred axis, so it is useful to use the above defined vector field **n**(r) to define the local orientation of the LCs.

Rigid cylinders can be assumed as the simplest type of constitutive elements that allow describing nematic behaviour, or in other words, the orientational order of the LC phase. The axis of these cylinders is labelled by a unit vector **a**. Then, we can define **a** using the angles θ and ϕ (**Fig. 4**).

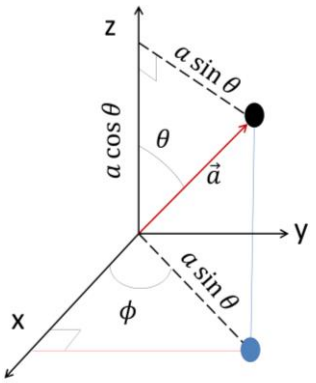

Fig. 4. Relationship between Spherical and Cartesian coordinates. Adapted from ref.[2].

The profile for the alignment state of the cylinders can be described by a distribution function $f(\theta,\phi)d\Omega$, which gives the probability of finding cylinders in a small solid angle $d\Omega = sin\theta d\theta d\phi$ around the direction (θ,ϕ) (**Fig. 5a**). In other words, it gives the probability of finding a molecule at a certain angle with respect to the director field.

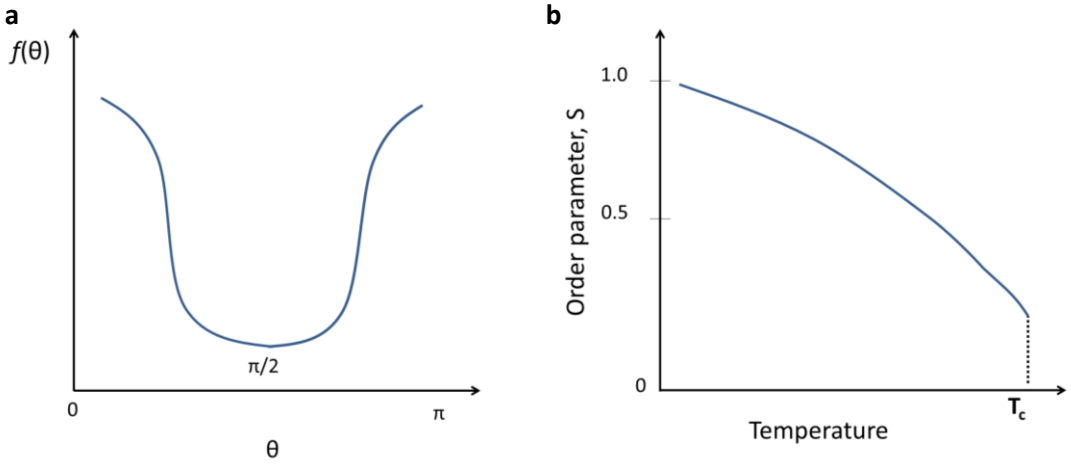

Fig. 5. The distribution function f(θ) vs θ and the scalar order parameter vs temperature for a system of cylinders in the nematic phase. a) Here, we assume that the average orientation is along the z axis. f(θ) is large around θ=0 or π, i.e. for constituents parallel to **n**, and it is small for $\theta = \pi/2$. **b**) The scalar order parameter decreases with temperature. Tc is the clearing temperature where the material becomes isotropic. Adaptation from ref.([2]).

To specify quantitatively the amount of orientational order in the nematic LC phase, or in other words, to compare the orientation of every single constituent of the LC with the average preferred direction defined by **n**, the first moment of the distribution function, S, can be written as [2],

$$S = \int_0^{\pi} f(\theta) \frac{1}{2} (3cos^2\theta - 1) \sin\theta \, d\theta,$$

Thus, the obtained order parameter for a LC is,

$$S = \frac{1}{2} \langle 3cos^2\theta - 1 \rangle$$

Where θ is the angle between the molecular long axis of a molecule and **n**, and the brackets indicate a temporal and spatial average value over all the possible orientations.

In the isotropic case, S tends to 0 for symmetry reasons. On the other cases, when using anisotropic materials, S show different values depending on the molecular orientation with respect to the director field. When the molecular alignment is perfectly parallel to the director, $cos^2\theta = 1$ and S = 1. Moreover, the nematic order decreases by increasing the system temperature as shown in (**Fig. 5b**).

1.4. Anisotropy in liquid crystals

Liquid crystals present internal order, where the direction of the preferred orientation of the LC molecules is given by the director. Thus, they exhibit different values for a given magnitude when measured along axes in different directions, namely, the parallel and perpendicular directions with respect to the main molecular orientation (**Fig. 6**). This feature is called anisotropy and is one of the main properties of these materials. This anisotropic behaviour is present in practically all their physicochemical properties.

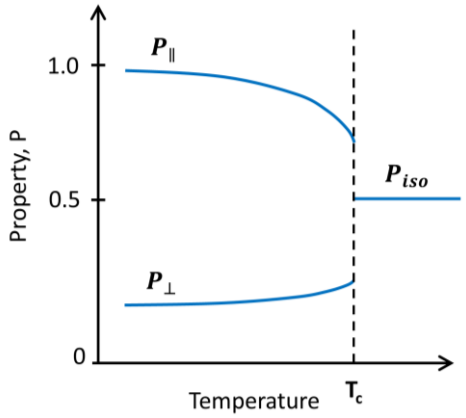

Fig. 6. Graphical representation of the anisotropic behaviour for a given physical property P in temperature-dependent liquid crystals. A given physical property present different values when measured parallel ($P_{\parallel}$) or perpendicular ($P_{\perp}$) to **n**. The fluid loses the anisotropic properties above a clearing temperature (T_c) reaching a common value in the isotropic phase, P_{iso}. Adapted from ref.([13]).

In this section, the most relevant manifestations of this material property are briefly introduced, namely, optical, dielectric and diamagnetic anisotropy.

1.4.1. Optical anisotropy: birefringence

Typically, transparent solids are optically isotropic. In this case, the index of refraction is equal along all the possible directions throughout the internal structure as all their axes are

equivalent. Light interacting with an isotropic crystal is refracted at a constant angle and passes through the material at a certain velocity without being polarized by the crystal molecular structure.

Materials presenting a preferred molecular orientation interact with light differently than isotropic crystals, meaning that light travels at different speeds depending on the "crystallographic" direction it is propagating through. This is a typical phenomenon experienced by many anisotropic crystalline solids, but also for LCs.

In LCs, light travels at different speed depending on whether it is polarized, parallel or perpendicular to **n**. Consequently, LCs present two different refractive indexes corresponding to the light rays polarized along and perpendicular to **n** ($n_{\parallel}$ and $n_{\perp}$, respectively). The difference between the two refractive indexes, which can be quantified, is called birefringence.

Birefringent materials can be characterized by the polarized-light optical microscopy (POM) (see Materials and Methods, Chapter2, Section 6.1). Briefly, this technique consists on initially exciting the sample, followed by recombining the light components that are out of phase along the same optical path. The phase shift or retardation between the two rays gives information about the LC director configuration throughout a sample (**Fig. 7**).

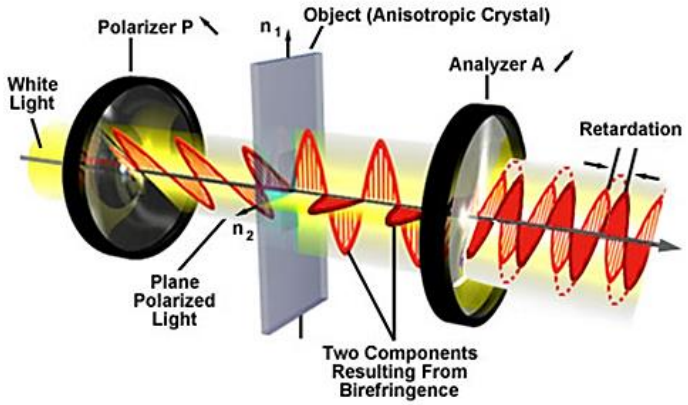

Fig. 7. Anisotropic crystals between crossed polarizers. Source ref.([14]

1.4.2. Dielectric anisotropy

Molecules constituting LCs can be polar or non-polar. Both types of molecules display the same behaviour under the application of an external electric field (E) even though polar molecules present a permanent dipole.

The electric permittivity (ε) describes the ability of a material to polarize in response to the application of E, but also how an electric field affects and is affected by the medium. In LCs, this quantity is different when measured along ($\varepsilon_{\parallel}$) and perpendicular ($\varepsilon_{\perp}$) to the director field. The difference between the two constants defines the dielectric anisotropy of the material ($\varepsilon_a = \varepsilon_{\parallel} - \varepsilon_{\perp}$).

For LCs presenting positive values of the dielectric anisotropy ($\varepsilon_a > 0,\ \varepsilon_{\parallel} > \varepsilon_{\perp}$), molecules tend to align parallel to the applied external field. Thus, the preferred dipole moment

alignment of each molecule matches within the main molecular orientation (**Fig. 8a**). In contrast, a material where the dipole moment is normal to the director field aligns perpendicularly to the external applied field ($\varepsilon_a < 0,\ \varepsilon_{\parallel} < \varepsilon_{\perp}$) (**Fig. 8b**) ([2]).

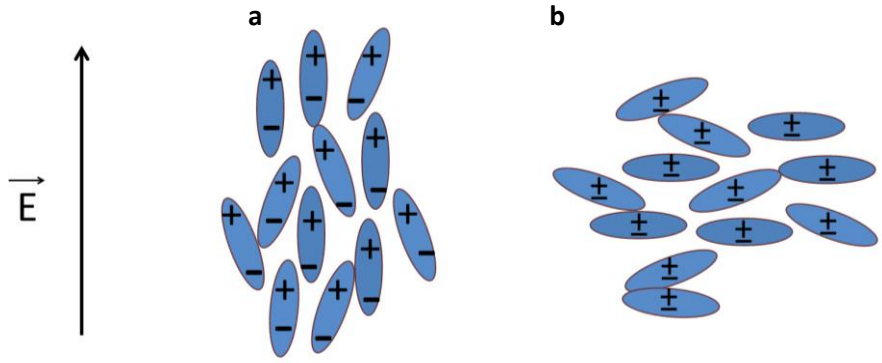

Fig. 8. Interaction between the liquid crystal molecules and the external applied electric field. a) Molecules align along the electric field direction ($\varepsilon_a > 0$) while in **b)** molecules align perpendicular to the external field direction ($\varepsilon_a < 0$).

1.4.3. Diamagnetic anisotropy

Analogously to the previous section, when an external magnetic (H) field is applied over LCs a reorientation phenomenon also occurs.

Most organic molecules are diamagnetic; the diamagnetism of LCs can be attributed to the aromatic rings present in the molecular structure. This property is enhanced as the molecules tend to align such as H is parallel to the plane of the rings.

Diamagnetic susceptibility (χ) in LCs is also anisotropic thus having two components for each molecular axis ($\chi_{\parallel}, \chi_{\perp}$). The difference between the parallel and perpendicular magnetic susceptibilities defines the reorientation behaviour of the LC, and so the diamagnetic anisotropy of the material, which for nematics is usually positive, $\Delta\chi > 0$ ([15]).

Typical values for the alignment of liquid crystals by the application of an external magnetic field are on the order of hundreds of milliTesla.

1.5. Distortions in nematic liquid crystals

NLCs in equilibrium, and in absence of external forcing, are locally aligned along one direction, **n**. However, the presence of thermal fluctuations, bounding walls or external fields can induce inhomogeneities or deformations to the material, thus varying the director field throughout the sample.

1.5.1. Long-range distortions: Frank-Oseen free energy

In out-of-equilibrium scenarios or by imposing external forces, the LC director can be distorted. In this case, the length scale of the deformation is much larger than the constituent building-blocks size and can be described and modelled by the Frank-Oseen elastic free energy functional, which can be written as ([16], [17]),

$$f = \frac{1}{2}K_1(\text{div}\,\mathbf{n})^2 + \frac{1}{2}K_2(\mathbf{n}\cdot\text{curl}\,\mathbf{n})^2 + \frac{1}{2}K_3(\mathbf{n}\,\text{x}\,\text{curl}\,\mathbf{n})^2$$

where K_1 , K_2 and K_3 are the distortion constants related with the different splay, twist and bend deformations of a NLC (**Fig. 9**). In contrast to the twist distortion which is 3D (**Fig. 9b**) ([3], [4]), the splay and bend distortions are 2D in-plane deformations of the nematic director and are represented in (**Fig. 9a**) and (**Fig. 9c**) respectively. Typical values for elastic constants in NLCs are in the order of 10^{-12} N ([18]).

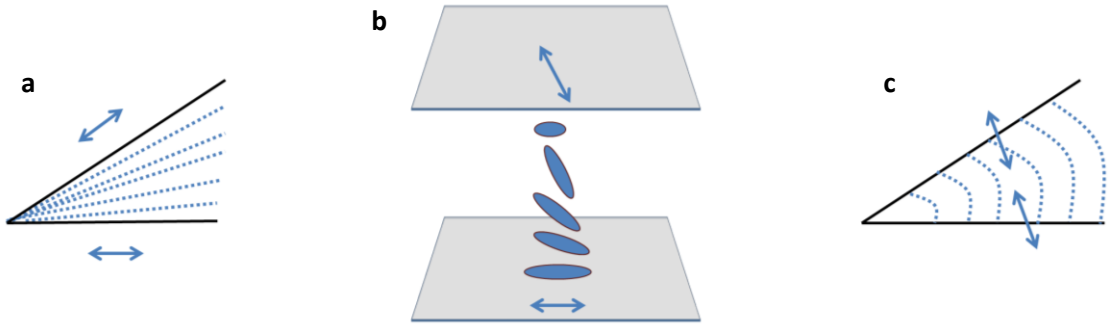

Fig. 9. Long-range distortions in nematic liquid crystals. Schematic representation of **a)** Splay **b)** Twist and **c)** Bend deformations. Double arrows indicate the orientation imposed by the confining walls. Discontinuous blue lines depict the nematic director.

1.5.2. Liquid crystals at interfaces: Anchoring conditions

In practice, LCs are usually confined between surfaces that induce, after treatment, a well-defined LC far-field disposition due to the interaction surface-LC. This interaction is known as LC anchoring ([19]–[21]).

The confining materials are usually solid plates coated or functionalized specifically to achieve a pre-defined orientation of **n** at the interface. In display devices, this interaction becomes crucial to initially determine the equilibrium configuration of **n** at the interface.

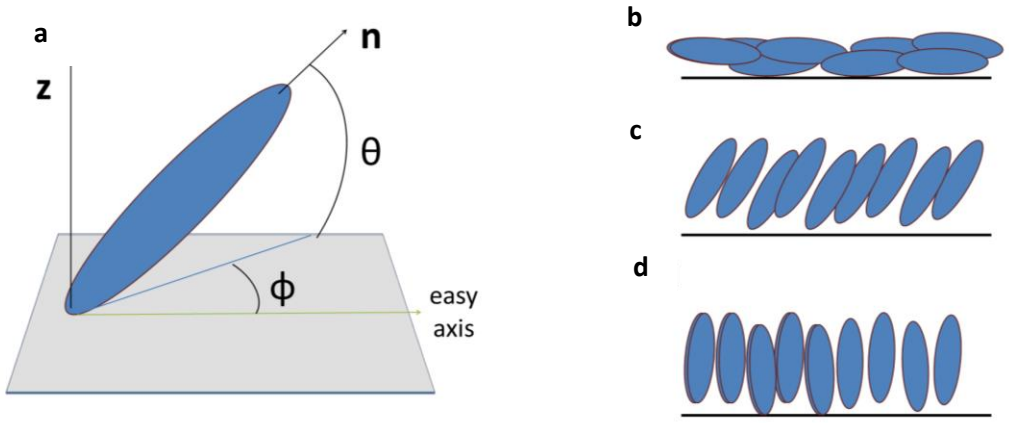

Fig. 10. Schematic representation of nematic director orientations near a solid surface. a) Director field orientation defined by the polar (θ) and azimuthal (ϕ) angles. **b)** Planar, **c)** Tilted and **d)** Homeotropic anchoring conditions of the LC molecules to a solid surface.

The nematic director can basically be oriented in three different ways with respect to the plane of the interface. This interaction is defined by the polar angle θ (**Fig. 10a**). When the LC

molecules are disposed parallel to the surface, the anchoring is planar and $\theta \sim 0^{o}$ (**Fig. 10b**). In contrast, when the main molecular orientation is perpendicular to the surface, thus $\theta \sim 90^{o}$ and the anchoring is called homeotropic (**Fig. 10d**). The tilted anchoring corresponds to the existing intermediate states between the previous configurations (**Fig. 10c**). The LC anchoring at a surface depends basically on two effects, the anchoring energy and the preferred angle of the LC for the surface. The surface coating induces forces that are strong enough to impose a well-defined direction of **n** at the surface although there is a competition with the elastic properties of the material. Moreover, chemical or physical surface treatments are usually used to achieve a specific orientation of the material at the interface (see Chapter 2, section 3).

In the case of NLCs both hydrophilic and hydrophobic surfaces can be used ([22]). Hydrophilic surfaces usually provide planar anchoring and examples are clean glass or some polymeric coatings. On the other hand, to achieve a homeotropic anchoring of the mesogens hydrophobic conditions can be used, such as silanes or polymers. In most cases this "rule" is satisfied, even though it must be experimentally tested for each system.

1.5.3. Fréedericksz transition

As mentioned in Section 1.4, LCs align under the application of external fields, either electric or magnetic. The induced-distortion due to the competition between elastic and anchoring forces under electric or magnetic forcing is known as Fréedericksz transition ([23]).

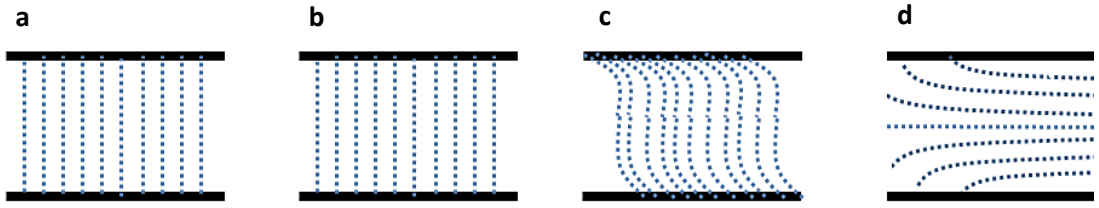

Fig. 11. Schematic representation of the nematic director under the application of an electric AC field perpendicular to the bounding plates. a) Initial homeotropic state with no AC applied. Boundary conditions maintain the director orientation perpendicular to the plates. **b)** LC with positive ε_a aligns within the field. **c)** Above a threshold value, LCs featuring negative ε_a start to deform from its initial equilbrium state, reaching a **d)** planar degenerate anchoring for larger values of the field. Discontinuous blue lines depict the nematic director.

A common example of Fréedericksz transition present in this thesis has been induced by electric AC fields. Consider one possible scenario where the initial situation consists on homeotropic anchoring conditions of the mesogens to the bounding plates and the applied AC field is perpendicular to the plane of the surfaces (**Fig. 11a**). At this point, the dielectric properties of the NLC molecules will determine the far-field director alignment. If the dielectric anisotropy is positive, the material will align within the external field and no effect will be seen under POM (the NLC will dispose perpendicular to the plates) (**Fig. 11b**). In contrast, if ε_a is negative, the material will tend to align perpendicular to the external applied field, so parallel to the plates (**Fig. 11d**). Above a certain threshold value of the electric field, E_c, the molecular reorientation will occur, that is well-known as the Fréedericksz transition, and Schlieren textures (discussed in Section 1.5.4) will appear ([2]).

For a given NLC, the threshold field for the Fréedericksz transition is given under the approximation of equal elastic constants by,

$$E_c = \frac{\pi}{d}\sqrt{\frac{K}{|\varepsilon_a| \cdot \varepsilon_0}}$$

where ε_0 is the vacuum dielectric permitivitty, ε_a is the dielectric anisotropy of the NLC, d is the cell thickness and K is an averaged value of the three Frank elastic constants. The threshold voltage does not depend on cell thickness, $E_c = \frac{V_c}{d}$.

One of the typical NLCs used in this thesis is the commercial mixture MLC-7029. For this NLC the dielectric anisotropy is $\Delta\varepsilon = -3.6$ and the averaged elastic constants can be approximated to $K = 15.6\ pN$. Thus, the resulting threshold voltage is about 2.2V.

1.5.4. Short-range distortions: Topological defects

In the sections 1.4.2 and 1.4.3, the nematic director field deformations occurred at the far-field scale. Despite this, inhomogeneous dispositions of the NLC mesogens can also locally be present in the form of point defects or singularities, also called topological defects and disclination lines, respectively. Briefly, topological defects are regions where the nematic director orientations are incompatible, and can be found at the bulk or at the boundaries ([24]), while disclination lines can be analogously described as in crystalline solids ([17]).

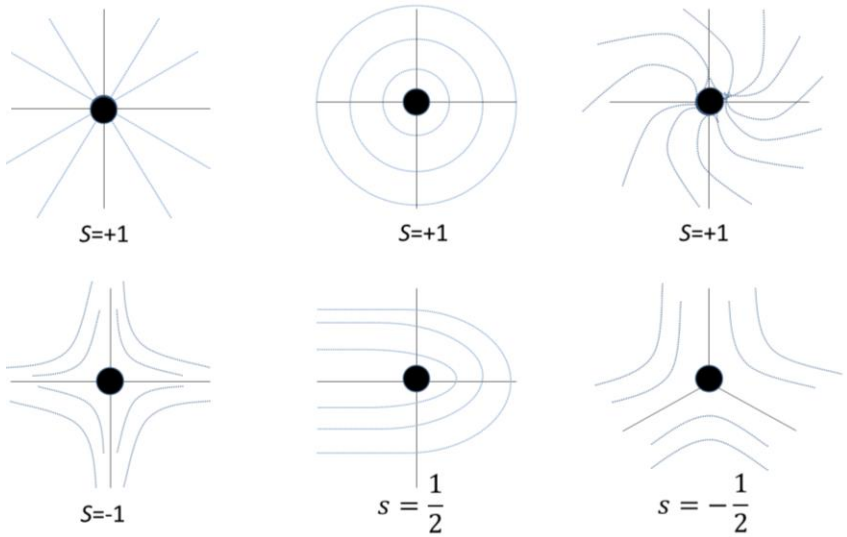

Fig. 12. Topological defects in two-dimensional nematic liquid crystals. Schematics of director field configurations around defect cores with integer and semi-integer topological strengths, both positive and negative.

In a typical confined LC cell the most common elastic distortions found are 2D deformations, involving bend and splay, which are directly related to the topological incompatibilities at the boundaries. These defects are characterized by a topological strength *s*, also called the topological charge, which quantifies the director field rotation around the defect core. The topological charge can be determined by defining a closed loop which encircles the defect core, the *Burgers* circuit, and a sense of rotation for it. A polar object following the director field in the *Burgers* circuit will display positive integer (1) or half-integer ($\frac{1}{2}$) values for full or half rotations, respectively. If the rotation around the defect has the same sense as the

Burgers circuit, e.g. clockwise, the topological charge is positive (+) and, in contrast, negative values are found for rotations counter-clockwise (-) to it (**Fig. 12**) ([25]).

There are different strategies to induce the formation of topological defects. One widely used strategy is the confinement of LCs between surfaces imposing different anchoring conditions ([26]–[28]). Moreover, the disposition of the topological defects can be controlled by using surface patterns, both chemically or topographically treated ([29], [30]). In this case, the nematic elastic matrix is frustrated due to degenerate boundary conditions which lead to the formation of lines and point-like defects. Under a POM (Chapter 2, section 6.1) the connection between point-like defects through disclination lines can be observed as dark branches. These dark branches correspond to the extinction orientation of the NLC, when the director adopts parallel or perpendicular orientations with respect to the polarizer or analyser axes. This are the so-called Schlieren textures (**Fig. 13**) ([31]).

Any elastic deformation has a contribution to the free elastic energy, thus, the formation of defects with lower s is energetically favoured. Consequently, defect density tends to decrease by annihilation of opposite topological charges, which are attracted each other.

Although, at a first point of view, topological defects seem to be undesired, LC defects have shown applicability in optical devices and materials ([32]) but also in colloidal self-assembly ([33]–[35]) as discussed in the next section.

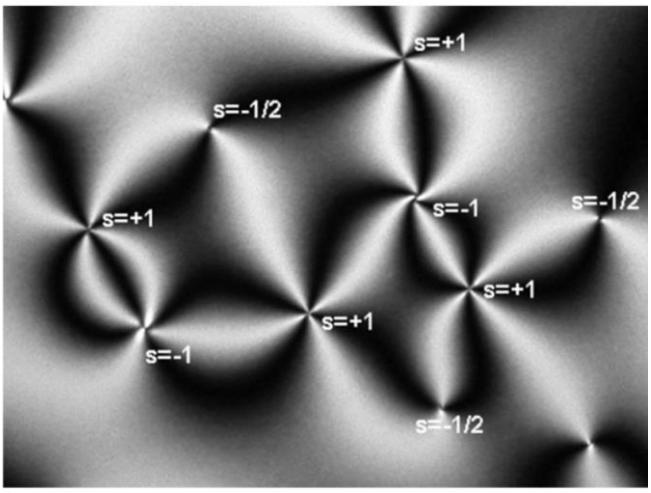

Fig. 13. The Schlieren textures. NLC featuring planar degenerate anchoring conditions and observed between crossed polarizers. Topological defects of strength s=±1/2 and s=±1 can be present in nematics, as depicted in the picture ([2]). The points where four branches (dark or white) meet correspond to $s = \pm 1$ topological defects, while points with two branches correspond to $s = \pm\frac{1}{2}$ ones. By rotating the sample one can distinguish between topological defects featuring different molecular structure. Source: ref.([13]).

2. Colloids in Nematic Liquid Crystals

Particles dispersed in complex fluids, such as LCs, feature a rich variety of interactions. Moreover, nematic colloids (i. e. colloidal particles dispersed in a NLC) behave very differently from their counterparts in isotropic fluids. Both, the elastic nature of the material orientational order and the surface anchoring of the director lead to the phenomenon of levitation due to the presence of long-range elastic interactions. Moreover, the LC environment enables colloidal self-assembly mediated by elasticity, giving rise to a wide range of possible structures.

Additionally, particles dispersed in NLCs feature Brownian motion. In the latter, the anisotropic nature of the material is evidenced with a different diffusion coefficient parallel ($D_{\parallel}$) and perpendicular ($D_{\perp}$) to the director field.

2.1. Colloidal inclusions

Particles dispersed in LCs distort the elastic matrix. The latter tends to accommodate to the new condition by inducing topological defects close to the surface of the inclusion ([36]). Far away from the inclusion, **n**(r) is uniform, so the total topological charge of the whole system is zero. The local distortion of **n** near the particle surface depends basically on three parameters: the size of the particle, the anchoring conditions at the particle surface and the elastic properties of the LC ([37]).

The work per unit area needed to distort the nematic director at the particle vicinity, depends on the anchoring parameter, W_{anch} (J·m^{-2}), and the director field orientation. The characteristic de Gennes-Klemann length, λ_{dGK}, is the ratio between the averaged elastic constants (10^{-12}N) and the anchoring coefficient, $\lambda_{dGK} = \frac{K}{W_{anch}}$ ([38]). For spherical confined inclusions, which usually provide a robust method to study topological configurations in LCs, the balance between both effects suggests that small particles ($R \ll K/W_a$) do not significantly change the surrounding director, while larger particles, ($R \gg K/W_a$) distort their neighbourhood (**Fig. 14**). The latter is enhanced when particles size is increased ([39]). Thus, the balance of the elastic and anchoring forces near the particle surface results on different configurations of the nematic director around the particle.

In practice, spherical inclusions with strong homeotropic anchoring confine the director field towards a point defect, *(s* =-1*)*, located near one of the particle poles. This defect is called hedgehog and is compensated by a "virtual" defect, *s* =+1, placed at the centre of the sphere (**Fig. 14b,f**). However, for weaker homeotropic anchoring, where the elastic free energy is favoured versus the anchoring conditions, disclination lines around the inclusion appears. This defect is called Saturn-ring and also satisfies the topological constraints by setting a disclination loop around particles equator (**Fig. 14c,g**) ([40]). Other possible scenarios are the inclusions displaying tangential (planar) anchoring conditions at the surface. Different particle shapes are possible such as spherical or peanut-like. The configuration of **n** surrounding the particle present two point surface defects called Boojums. The two defects are located at both poles, each one presenting a topological charge *s* =-1/2 (**Fig. 14d,h**) ([36],[41]).

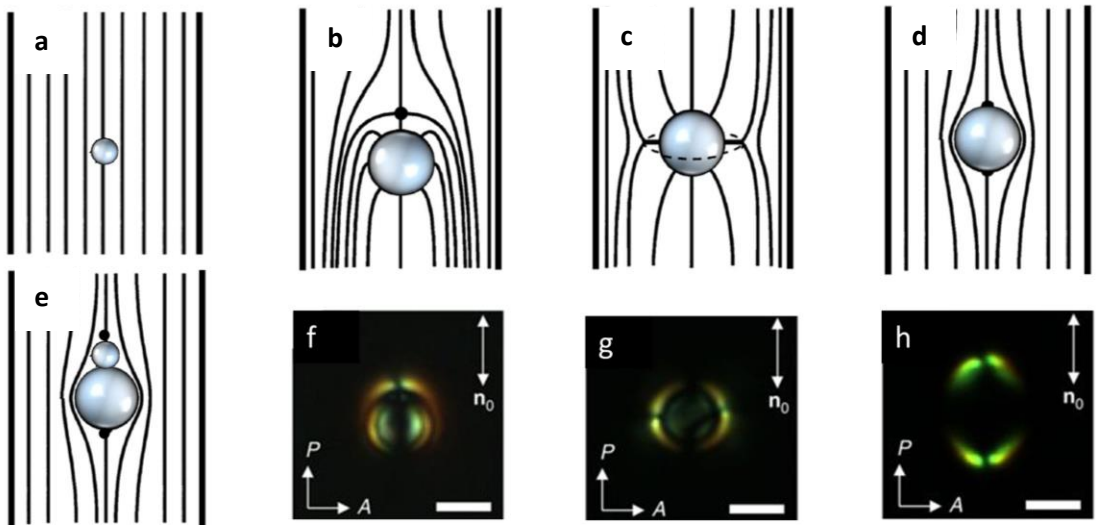

Fig. 14. Schematically depicted and experimentally obtained distortions around particles of different shape and anchoring conditions dispersed in NLCs. **a**) Small particles do not distort the director field ($R \ll K/W_a$). **b**)-**h**) Larger particles, $R \gg K/W_a$, distort **n** in order to satisfy the boundary conditions. Particles featuring a homeotropic anchoring (perpendicular alignment with respect to **n**) can exhibit a **b**) hyperbolic point defect-hedgehog (s = -1) located at one of the particles poles or **c**) an equatorial disclination loop located around the particle, the so-called Saturn Ring. Spherical **d**), and peanut-like **e**) shaped particles featuring a planar (tangential) anchoring present two surface defects located at particles poles called Boojums. **f**)-**h**) Experimental polarizing optical micrographs of dispersed particles in a NLC displaying **f**) a hyperbolic point defect-hedgehog, **g**) a Saturn-ring disclination loop and **h**) a double-boojum. In optical micrographs, **n** is perpendicular to the analyser. The scale bars are 4 µm large. Adapted from ref. ([42]).

Different possible symmetries of the nematic director around the particles are possible. Particles featuring a homeotropic anchoring can present either a point defect-hedgehog or a Saturn ring disclination loop configurations which have respectively dipolar and quadrupolar symmetries. Although particles sharing planar anchoring but with different shape display the same double-boojum defect, ideal quadrupolar symmetries can just be attributed to spherical particles. Further studies based on particle-particle or LC-particle interactions are related to elastically-mediated colloidal self-assembly ([34]) or the propulsion of particles inside LCs ([38], [43]), as will be discussed in Sections 2.4 and 4.2, respectively.

Besides the configurations shown in this section, more complex structures can be found. The variety of structures, around the colloid, depends basically on colloidal shapes and anchoring conditions ([44]) (**Fig. 15**). Here, the colloidal particles induce the elastic deformation, which is set by the minimum nematic length scale and is on the molecular scale ([45]). Another interesting feature of colloids dispersed in LCs is the presence of a conically degenerated tilted anchoring. This anchoring condition of **n** at the colloid surface allows inducing both, point and line defects at the same time. Thus, the formation of a Saturn-ring line and double-boojum defects shared for the same colloid are promoted ([42]).

There are several experimental realizations for the preparation of colloidal dispersions ([39]–[41], [46]), i.e. water-in-oil emulsions ([39], [46]) or solid particles suspended in LCs ([40], [41]). As mentioned before for bounding plates (Section 1.5.2), experimentally, controlling the LC anchoring at the particles surface is achieved by using surface treatment techniques that will be crucial on the final configuration of **n** around the inclusion (Chapter 2, Section 3).

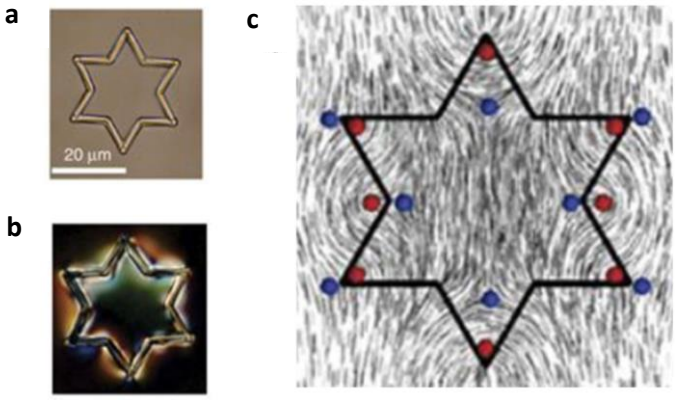

Fig. 15. Experimentally obtained nematic director distortions. a),**b**) Koch-star particles dispersed in a **a**) LC in its isotropic phase or in **b**) a LC in its nematic phase observed under crossed polarizers. **c**) Pairs of $s = \pm\frac{1}{2}$ and the surrounding director induced by Koch particles. Extracted from ref. ([45]).

2.2. Elastic levitation

A particle dispersed in an isotropic medium, such as water, will experience sedimentation when featuring different density with respect to the dispersing medium, $\Delta\rho = \rho_p - \rho_m$ being ρ_p and ρ_m the particle and the medium densities, respectively. This effect is counteracted by thermal noise. The balance between thermal noise and sedimentation allows particle to reach a certain height of the cell, which is called the sedimentation length, z_s.

In LCs not only thermal noise is opposed to sedimentation but also elastic forces mediate particle levitation (**Fig. 16**) ([47]). In this case, the particle height is much larger than in isotropic fluids.

In NLC colloids, the elastic forces compete with gravity, while thermal noise is negligible. Consider a sphere with homeotropic anchoring featuring a point defect-hedgehog and dispersed in a NLC cell with a uniform planar far-field (see **Fig. 14b**). Anchoring conditions, on the colloid and on the plates surface, are thus different and incompatible (**Fig. 16a**). Taking into account the balance between the elastic repulsion and gravity, the equilibrium height of the levitating particle, $z_{elastic}$, increases compared to the case in the isotropic medium z_s. Thus, elastic interactions govern particle levitation and set a value of $z_{elastic}$, that is one order of magnitude larger than in isotropic fluids z_s, being about 10 µm and 1 µm, respectively for typical systems ([38]).

The levitating particles in LCs are placed approximately at the centre of the cell for thickness < 20 µm (The particle diameter in these experiments is 4 µm). Above this value, particles present a shift (δ) with respect to the height of the centre cell (**Fig. 16b**). Even though this is a "reference" value, the height at which particles levitate is dependent on the radius of the particle, increasing with particle size.

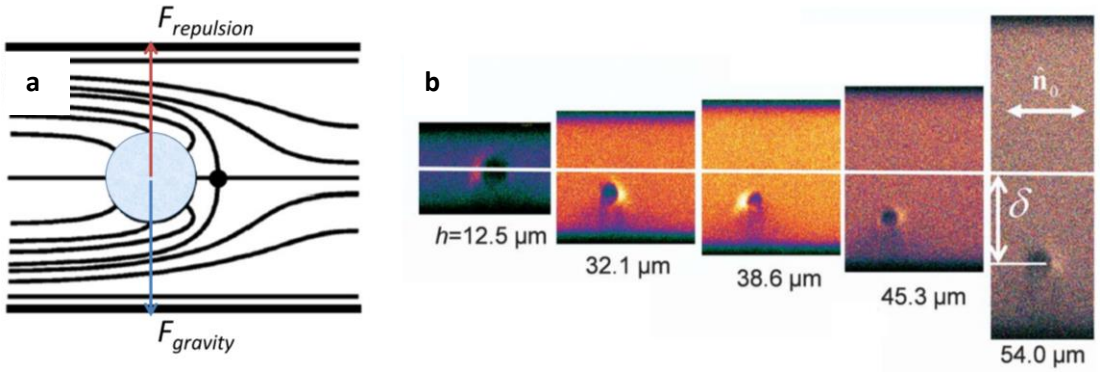

Fig. 16. Colloidal levitation in NLCs. a) Schematically depicted balance between elastic and gravity forces. The particle is kept levitating in the nematic bulk. **b**) Fluorescence Confocal Polarizing Microscopy (FCPM) cross section images of levitating silica spheres displaying a hyperbolic point defect-hedgehog placed in planar aligned cells of different thickness, *h*. As cell thickness is increased, the levitating height also increases although the shift from the centre is larger. Adapted from ref. ([38]).

2.3. Elastically-mediated colloidal self-assembly

In liquid suspensions, particle self-assembly is a balance between attractive and repulsive forces. In isotropic solvents, this balance is usually obtained from Van der Waals forces mediating particle aggregation and countervailed by repulsive forces, such as Coulomb or steric ones. Van der Waals forces are directly related to the dipolar moment adopted by the molecular constituents, which can be permanent or not. Under the application of an AC external field, these interactions can be tuned to control and manipulate the different colloidal self-assembled states ([48]–[50]).

Colloidal self-assembly in NLCs is in addition mediated by its elasticity. The elastic interaction can occur spontaneously, if particles are near each other, or externally forced, i.e. by light action. There are some antecedents reported, of colloidal self-assembly in NLCs, for different inclusions, i.e. liquid droplets ([39], [46]) or solid particles ([34], [47]). These soft matter systems show a rich variety of colloidal self-assembled structures, such as linear chains ([39],[51]) , hexagonal lattices ([52] or anisotropic clusters ([46]). In this section of the thesis we will just focus on solid particles.

The experimental realizations based on nematic colloidal self-assembly can be promoted using optical tweezers. Briefly, this technique is used to trap the particles and transport them along the LC cell. The optical trapping method is based on the difference of the medium and the particle refractive indexes. When a laser beam irradiates the particle, photons interact with the dielectric material and some of the momentum is transferred to the particle which results in particle translation. Another useful feature derived from this technique allows to locally heating the liquid crystal around the selected particle into the isotropic phase and quenching it back to the nematic phase by switching-off the laser beam. This allows the *in situ* modification of the topological defects present surrounding the particle ([53]–[56]).

Particles displaying dipolar configurations of the nematic director (**Fig. 17a**) interact via dipole forming chain-like structures (**Fig. 17d**). As explained in section 2.1, the point defect-hedgehog corresponds to a dipolar configuration similar to that of the electric dipoles. Thus,

colloids spontaneously assemble into chains with all the dipoles aligned in the same direction, namely forming a ferroelectric chaining. Even though chaining can be achieved spontaneously by the system, other more complex 2D structures can also be obtained in form of 2D crystals by optical tweezers colloidal manipulation (**Fig. 18**) ([57]).

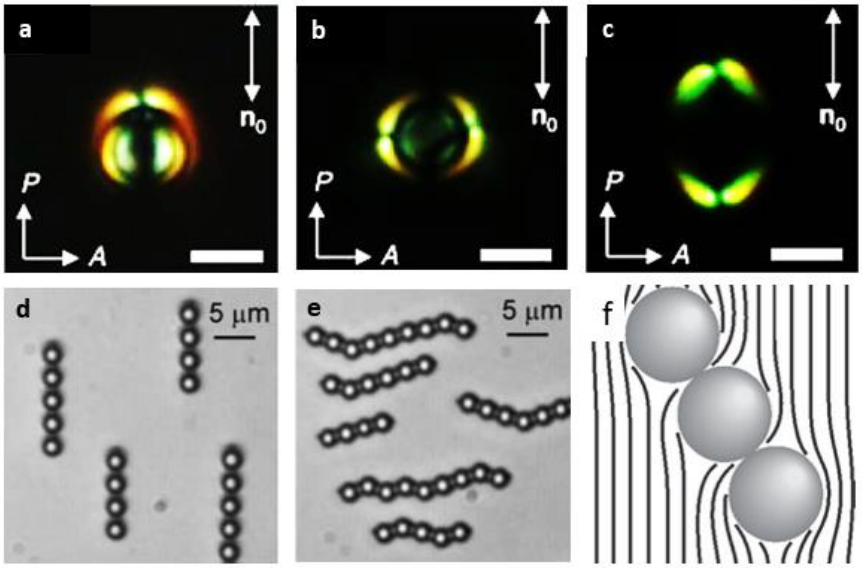

Fig. 17. Elastically-mediated colloidal self-assembly in NLCs. a)-**c**) Experimentally obtained configurations of **n** around particles with **a**), **b**) homeotropic and **c**) tangential anchoring displaying **a**) dipolar and **b**),**c**) quadrupolar symmetries respectively. Images obtained under POM. **d**), **e**) Experimentally bright-field micrographs of self-assembled particles with **a)** dipolar and **b)** quadrupolar configurations. **d)** The elastic dipoles (point defect-hedgehog) form ferroelectric chains in the direction parallel to the director, while in **e**) the chains are perpendicular to **n** and distorted due to the relative orientation of the Saturn-Ring induced-defect from one particle to the adjacent one. **f**) Schematically depicted self-assembly for colloids with tangential anchoring featuring double-boojums defects. Adapted from refs. ([42], [57], [58],[59]).

Quadrupolar defect configurations can be seen under a POM as two point surface defects, boojums, located at both poles (**Fig. 17c**) of the particle or as a Saturn-ring disclination loop around the particle equator (**Fig. 17b**). In the former case, when particles are close enough they attract each other and form chains at a certain angle with respect to the director field to satisfy the symmetric condition imposed by the elastic constraint. About 30^{o} has been observed to be the optimal angle for the self-assembly (**Fig. 17e,f**) ([58], [59]). As for the dipolar configurations, by increasing particle density and thus, enhancing the probability for particles to interact, more complex structures with different particle rearrangement are possible (**Fig. 18b**).

So, in conclusion, the elastic properties at the particle surface will determine the colloidal self-assembly structure.

Other self-assembled structures for nematic colloids consist on mixing both interactions, dipolar and quadrupolar ones, acting at the same time. In this case, the elastically mediated self-assembly between colloids can be performed parallel or perpendicular to the nematic bulk obtaining different structures. The hyperbolic dipolar hedgehog is always parallel to **n** at the bulk, while the Saturn ring loop can be perpendicular or with some tilt angle with respect to the far-field director ([60]).

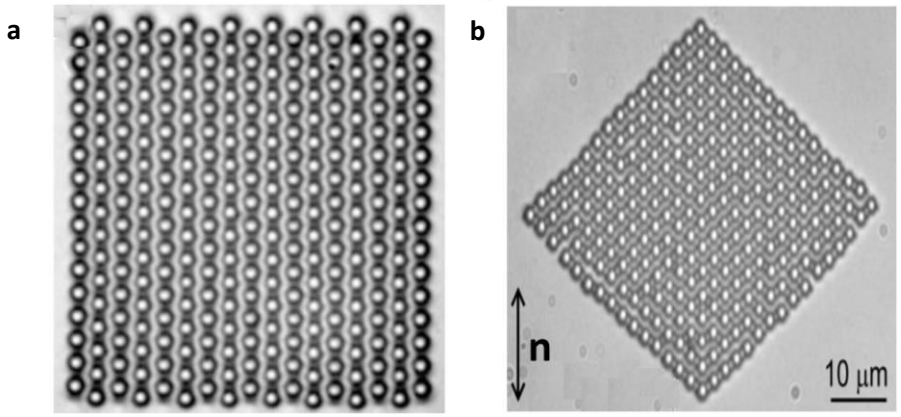

Fig. 18. Typical examples of self-assembled objects in NLCs obtained experimentally. a),**b**) Bright-field micrographs showing examples of 2D self-assembled structures constituted by particles featuring homeotropic anchoring. The 2D structures form crystals depending on their interaction, **a**) dipolar or **b**) quadrupolar. Extracted from refs. ([61], [62]).

2.4. Brownian motion

Brownian motion is the random displacement of particles dispersed in a fluid controlled by thermal fluctuations. The random motion is characterized by a null mean displacement and a mean square displacement (MSD) that grows linearly with time, $< \Delta r^2(\tau) >= 6D\tau$ (see Chapter 2, Section 8.1). Moreover, particle displacement is characterized by a diffusion coefficient, D, which satisfies the Stokes-Einstein relation, $D = K_B T / 6\pi\eta R$ ([63]).

This Brownian behaviour is not universal, and often breaks down when addressing complex fluids. In the latter, the scaling of the MSD may follow a power-law $< \Delta r^2(\tau) >= \tau^\alpha$, allowing to identify anomalous diffusive behaviours. Superdiffusion occurs for $\alpha > 1$ and is typically observed in systems of swimming bacteria ([64]) or polymer-like micelles ([65]). In contrast, subdiffusive behaviours are characterized by $\alpha < 1$ and are found in F-actin networks ([66]) or surfactant dispersions ([67]) (see **Fig. 19a**).

NLCs are ordered fluids with a preferred direction. Besides, when an inclusion is added to the NLC, the particle distorts the NLC surroundings, as commented in the previous section 2.1. Thus, Brownian particles dispersed in NLCs can present both, anisotropy on the diffusion coefficient ([44], [68]) and anomalous diffusive behaviour ([69], [70]). On the one hand, at relatively large time scales, the anisotropic nature of the LC attribute a diffusion coefficient for the displacements parallel to **n**, $D_\parallel$, and a different one for the displacements perpendicular to it, $D_\perp$. This is a consequence of the viscous anisotropy, which depends on the molecular orientation of the NLC and the relation Stokes-Einstein becomes $D_{\parallel,\perp} = K_B T / 6\pi\eta_{\parallel,\perp} R$ (**Fig. 19b**) ([68]). On the other hand, at time scales on the order of seconds, not just the typical diffusive modes are present but also the molecular reorientation of the nematic director around the colloid plays a role ([69]).

The Brownian motion of a particle is directly related to the surrounding fluid configuration. As seen in section 2.1, different anchoring conditions lead to different configurations of the nematic director. Thus, different anomalous diffusive behaviour may be found in particles depending on the anchoring conditions. Particles displaying a planar anchoring feature a

subdiffusive behaviour while particles with homeotropic anchoring feature a superdiffusive one. This can be explained as the interplay between the "fore-aft" elastic forces acting on particle displacements. At time scales in the order of seconds just molecular fluctuations near the particle will be important. In other words, the fluctuating modes of **n** around the sphere trigger the anomalous diffusion of Brownian colloids dispersed in NLCs. In the subdiffusive regime, fluctuating displacements of the particle increases the elastic energy in that direction. Thus, an elastic difference is generated and induces a restoring elastic force that slows down the diffusive motion (**Fig. 19c**). The contrary effect is observed for a normally anchored particle which experiences an elastic force towards the distortion leading to a superdiffusive motion (**Fig. 19d**) ([69]).

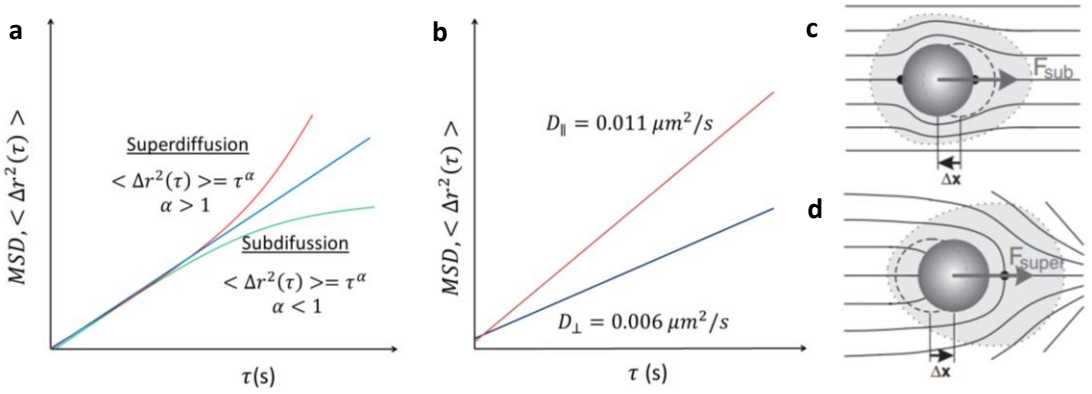

Fig. 19. Colloidal Brownian motion in NLCs. a) Plot of the MSD vs time allows identifying diffusive behaviours. The MSD grows linearly with time for a generic diffusive (α=1) regime, while anomalous diffusive behaviours (α≠1) deviate from linearity, either with a super- or sub- linear growth. **b**) MSD vs time for the two components of displacement, $D_\parallel$ and $D_\perp$, for particles dispersed in NLCs. **c**) Restoring force due to fluctuating director gradients contrary to particle motion leads to a subdiffusive behaviour, while in **d**) the elastic force moves the sphere towards the splay acquiring a superdiffusive behaviour. Adapted from refs. ([38], [69]).

3. Active and driven particles in isotropic fluids

The term “active particles” refer to self-propelled units which are capable to extract energy from the surrounding environment and convert it into directed or persistent motion. In natural systems, such as flocks of birds ([71]), shoals of fish ([72]) or people crowds ([73]), swimming affects not only on the individual but at the collective scale (**Fig. 20**). Thus, particles are interacting with their neighbourhood and as a consequence complex collective phenomena emerge. Many systems present common characteristics, e.g. nearly constant averaged velocity, the existence of pair-pair interactions or the characteristic size and shape of the constituents. So, the different observed collective dynamic states can feature similar behaviours even though being the length scales very different ([74]).

The incoming flow of energy sets the system persistently out of equilibrium and thus promotes novel physical behaviours not present in thermal equilibrium such as collective motion ([75]), large-scale patterns ([76]), swarming ([77], topological defects ([78]) or active turbulence ([79]).

Fig. 20. Natural and biologically-based systems, which display disparately different length scales, showing emergent collective phenomena due to particle-particle interactions. **a**) Flock of sheep where the interaction between individual units induces a spiral large-scale motion pattern. Photography by Tim Whitaker®. **b**) Defect dynamics of active nematic swirls confined at soft interfaces. Extracted from ref. ([80]).

Although a large variety of systems are constituted by active particles, in this thesis the term active particles refer to particles on the micron scale dispersed in a fluid medium. We briefly mention first biological microswimmers followed by artificial ones, which are more prominent in this thesis (except in Section 4.1).

When referring to swimming at the microscale the ratio between inertial and viscous forces, the well-known Reynolds number (R_e), becomes very important. This relation can be written as $R_e = \rho u L/\mu$, where ρ is the density, u is the swimming velocity, L is a characteristic linear dimension and μ is the dynamic viscosity of the fluid. When R_e is small, viscous forces dominate and inertia does not play any role ([81], [82]). The way to induce a constant motion to swimming particles is by applying some kind of cyclic deformation to their body. Despite this, a reciprocal motion (as it is named in [83]), where the initial and final states are symmetrically equivalent, will induce no net displacement in the regime of small R_e. To

break this symmetric motion from the fluid around the particle, microswimmers must perform nonreciprocal modes of deformation, thus enabling, the propulsion in a preferred direction. In conclusion, the main consideration to take into account behind any designed particle is that its symmetry and that one of the surrounding fluid must be globally broken under motion as described by Purcell's "scallop theorem" ([83]).

Flagellated bacteria are typical examples of biological microswimmers, such as E. Coli, where the single flagellum unit is rotated as a motor protein complex. The motion of this bacterium is based on a 'run-and-tumble' mechanism which consists of two stages, the run and the repeating randomized tumble. During the run phase, flagella rotate collectively counter-clockwise inducing ballistic motion along the bacterium long axis. When the tumble step occurs, the rotation is clockwise leading to a random reorientation of the bacterium ([84]). Another interesting system from the point of view of biological swimming is cilia. Cilia are organelles directly attached to cells that collectively induce non-synchronized beating patterns, known as "metachronal waves", used to transport cells ([85]).

Laboratory-built microswimmers have been developed during the last two decades to achieve efficient propulsion mechanisms at the microscale. In spite of that, perspectives for potential utilities focus on nanoscale swimmers which are optimally sized from a biological and medical point of view ([86]).

The variety of designed active particles systems is very wide, and all of them satisfy Purcell's scallop theorem. Different examples of microswimmers can be distinguished by their propulsion mechanism. The first example is the use of interfacial reactions to support the propulsion of particles chemically heterogeneous, which are activated by the addition of hydrogen peroxide ([87]). On the other hand, a microswimmer based on a red blood cell with a DNA-linked magnetic chain was forced externally with an oscillating magnetic field ([88]). These two examples allow the classification between internally active mechanisms, i.e., phoretic based, which are discussed in section 3.1, and externally driven mechanisms, such as magnetic or electric fields, which mediate particles propulsion, as commented in section 3.2 ([89]–[92]).

3.1. Internally, phoretic-based, active propulsion

Propulsion based on chemical, electric or temperature gradients is attributed to the interaction between the particle and a driving field, a chemical concentration gradient, an electrostatic potential or a temperature imbalance, respectively. The application of field gradients allows tuning inter-particle interactions but also to set the system out-of-equilibrium with a defined driving. This phoretic-based propulsion is known as self-phoresis and is based on a symmetry-breaking flow field generated around the particles ([93]–[95]).

The first experimental realizations, involving particle motion based on the self-phoresis mechanism, consisted on microrods featuring a mixed chemical composition on its surface (Au-Pt) or (Au-Ni). Due to surface inhomogeneity, and after immersing into a hydrogen peroxide solution, particles acquire motion (**Fig. 21a**) ([96]). Here, the formation of bubbles is not only indicative of a redox process during the hydrogen peroxide decomposition but can also help particle propulsion by inducing internal electrokinetic effects ([97]).

A clear example of self-diffusiophoresis corresponds to particles made of silica or polystyrene with one side coated with Pd or Pt, which acts as catalyst. These particles, presenting one half made of a material and the other half of another, are also called Janus particles. The metallic catalyst promotes the hydrogen peroxide decomposition into water and oxygen, $H_2O_2 \rightarrow H_2O + {}^{1}/_{2}\, O_2$, thus propelling the particle (**Fig. 21b**). Perhaps nowadays these experimental realizations are the most popular in active colloids due to their simplicity and robustness.

Self-propelled particles do not show a typical "passive" Brownian motion where particle behavior is purely diffusive, as explained in Section 2.4 for particles dispersed in isotropic fluids. This means that, in these types of fluids, the translational and rotational modes for passive particles are independent while this is not the case for active ones. Thus, in active colloids rotation and translation are coupled. The direction of motion of active particles is subjected to rotational diffusion, as particles present a defined velocity in a preferred direction. The translational diffusion coefficient takes the form, $D_T = {}^{K_B T}/_{6\eta\pi R}$, where K_B is the Boltzmann constant, T is the temperature, η is the viscosity of the medium and R the particle radius.

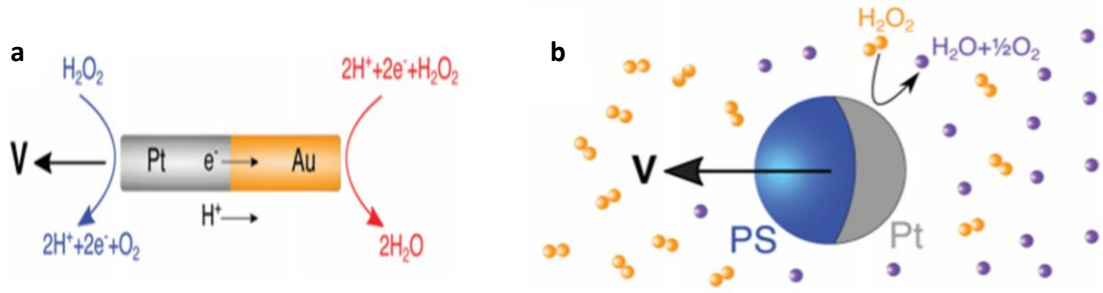

Fig. 21. Self-phoresis and diffusiophoresis processes. a) Bimetallic rod driven by a self-phoretic mechanism under a hydrogen peroxide solution. **b**) Janus particle driven by a self-diffusiophoretic mechanism by decomposing hydrogen peroxide. Orange molecules represent H_2O_2 molecules**.** Adapted from source: ([95]).

On the other hand, rotation takes into account the volume of the particle in the diffusion coefficient, $D_r = \tau_r^{-1} = {}^{K_B T}/_{8\eta\pi R^3}$. For instance, for particles dispersed in water and with a hydrodynamic radius of $R = 1\mu m$, diffusion coefficients can be estimated as, $D_T \approx 0.2\ \mu m^2 \cdot s^{-1}$ and $D_r \approx 0.17\ rad^2 \cdot s^{-1}$. When particle size is decreased, both D_T and D_r increase, dramatically in the latter ([92]). In this case, the mean square displacement for active self-propelled particles can be written as ([94]),

$$\mathrm{MSD} = 4D\Delta t + \frac{v^2\tau_r^2}{2}\left[\frac{2\Delta t}{\tau_r} + e^{-2\Delta t/\tau_r} - 1\right]$$

This expression takes into account the translation and rotation contributions with their characteristic times. At short times, $\Delta t \ll \tau_r$, the motion along a random preferred direction is linear in time, and is coupled to the typical translational Brownian motion. In contrast, at larger times, $\Delta t \gg \tau_r$, rotational diffusion randomizes the directions of propulsion and particle displays an enhanced random walk. As a consequence, the typical effective diffusion coefficient is obtained as $D_{eff} = D + \frac{1}{4}v^2\tau_r$.

3.1.1. Collective phenomena emerging from active colloids

Going further on phoretic-based mechanisms, one can explore the use of light as a catalytic precursor ([98]–[101]). In this case, the actuation mechanism cannot just play a role on the fuel source but can also be involved in the pair-pair interaction between particles as described in ([98]). Additionally, all these ingredients together take the system out of equilibrium, for a dense colloidal suspension, mediating self-organization in 2D "living" crystals, which are reversible in nature, meaning that, switching off the light melts the cluster (**Fig. 22**). A particular realization of this scenario is achieved by replacing the metallic coating by a hematite cube which responds to blue light.

Active artificial colloids ([99], [100]) but also active biological swimmers ([101]) can be used as power sources for micromachines although presenting different forcing mechanisms, either catalytic under a hydrogen peroxide solution or photo-induced. The fabrication of micro-engineered gears with sharp corners allows self-propelled particles to stick and power the micromachine. Particles align to the gear wall, used as a predefined path to slide along, until reaching the corner after few seconds of the hydrogen peroxide addition. Here, the gear starts to rotate as more particles reach the cluster. The angular speed for a gear can be measured, being function of the particles attached but also of their activity. Even though the efficiencies reached so far are low, this is a nice example of how to get novel strategies to design micromachines at the micro scale ([100]).

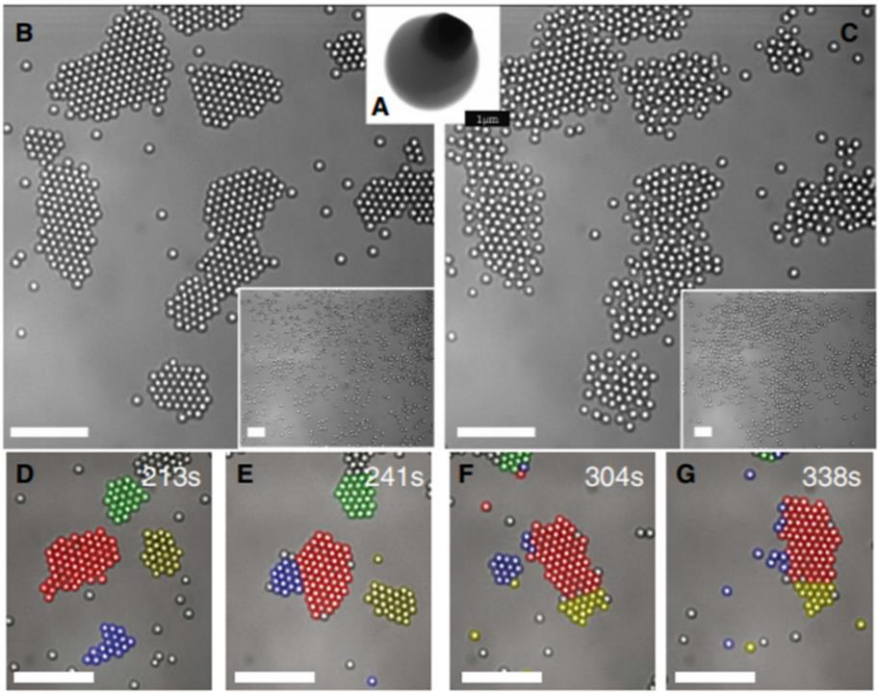

Fig. 22. Self-organization of photo-activated colloidal propellers. a) Scanning electron microscopy (SEM) of one particle: a polymer colloidal sphere with a hematite cube (black dot). **b**) Particle self-organization due to the application of blue light. Inset shows the initial dispersed state. **c**) Turning off blue light 10s melts the cluster by thermal diffusion. Inset shows the cluster melt after 100s. **d-g**) Different colours show particles belonging to the same cluster. As time evolves, particle assemblies rearrange, break or even "explode". Scale bar is 10 μm. Source: Adapted from ref. ([98]).

Taking advantage of these systems allows building experimental setups capable to study non-equilibrium statistical physics. Nowadays, one of the aims of the research based on self-propelled colloids has focused on understanding whether there is the possibility to establish a non-equilibrium equation of state for active colloidal systems ([102], [103]).

An initial work consisted on estimating the effective temperature of an active suspension based on catalytic self-propelled Janus particles dispersed in a custom-build experimental setup. Initially, the self-propelled particle MSD was calculated from the equation shown in section 3.1, and extracted D_{eff} as a function of the colloidal activity. Moreover, at thermal equilibrium, the Boltzmann distribution function of a colloidal suspension takes the form, $\rho(z) = \rho_0 \exp(-\frac{z}{\delta_{eff}})$, being z the colloidal height experimentally obtained and δ_{eff} the sedimentation length, which balances the gravitational and thermal energy and seems to strongly depend on colloidal activity. The sedimentation length for a self-propelled particle system is given by the Smoluchowski equation and is predicted to be, $\delta_{eff} = \delta_0 \frac{D_{eff}}{D}$, with $\delta_0 = \frac{K_B \cdot T}{m \cdot g}$. Moreover, the sedimentation length also depends on activity, and thus, an effective temperature of the system can be interpreted as, $T_{eff} = T \cdot \frac{D_{eff}}{D}$. From these observations a physical relevant parameter appears, which is the "active" Péclet number, Pe, and is directly related to particle activity. The active Péclet number compares two time scales. On the one hand, the ballistic time $t_0 = \frac{2R}{v_o}$, which the microswimmer (an sphere of radius R) needs to swim its own diameter with a prescribed velocity, v_o , and, on the other hand, the typical diffusive time scale $t_d = \frac{R^2}{D}$ ([104]).

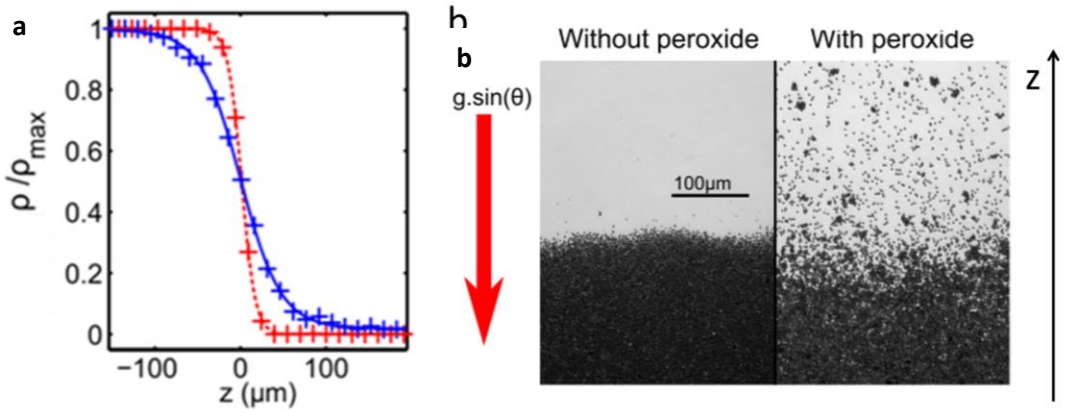

Fig. 23. Phoretic self-propelled particles. **a**) Normalized density profiles versus the position z along the cell, without hydrogen peroxide (red line) and with hydrogen peroxide (blue line). **b**) Sedimentation-diffusion experiment for both, passive colloids, left, and active colloids, right, dispersed in water. The effective gravity is indicated by the red arrow. Source: ref. ([105]).

Following this work and by using similar self-propelled entities, phoretic gold-platinum Janus particles, sedimentation experiments performed tilting the experimental setup allowed the characterization of a non-equilibrium equation of state for colloidal self-propelled particles (**Fig. 23**)([102]).

3.2. Externally driven propulsion

As commented before, externally driven microswimmers are structurally very different. One of the best microswimmers (biologically-inspired) consists on a flagellated tail containing magnetic actuators ([88]). Going further, and by using designed silicon dioxide chiral particles under the application of an oscillatory magnetic field, inclusions can be propelled following a predefined path (**Fig. 24a**) ([106]). Synthetic paramagnetic doublet particles, displaying different size, have also been prepared by adding streptavidin in a solution containing biotin. The biotin links both entities, DNA and streptavidin, ensuring strong and stiffness, thus the doublet can rotate, close to a bounding plate, as a solid body under the application of an external magnetic field (**Fig. 24b**) ([107], [108]).

Changing the propulsion forcing to electric fields, metallodielectric Janus particles dispersed in isotropic fluids, such as water, can be propelled as well ([109]–[111]). Under the application of an AC electric field each half of the particle polarizes differently from the other and induces an inhomogeneous double layer surrounding it. The electric potential decay from the particle to the fluid can be associated as an "effective thickness", the so-called Debye screening length ([112]). Close to this double layer, mobile ions create a gradient in the charge concentration around particles. In the present case of a Janus particle, this induces a symmetry breaking of the flow patterns around inclusions, caused by the double layer inhomogeneity, and allows the propulsion under AC electric fields. The two phenomena related to particle propulsion are known as Induced-Charged Electrosmosis (ICEO) and Induced-Charge Electrophoresis (ICEP), which are related to the induced flows around the particle and to particle motion, respectively (see section 4.2.2) (**Fig. 24c**) ([111]).

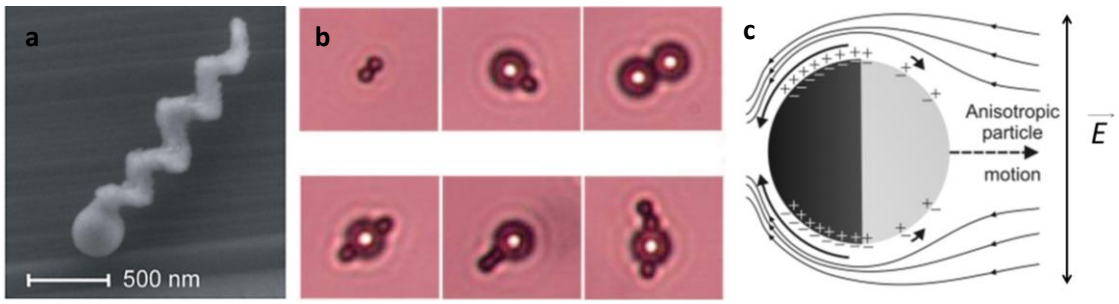

Fig. 24. Externally actuated microswimmers. a) Experimentally obtained SEM image of an individual silicon dioxide screw with nanostructured helicity. Source: ref. ([106]). **b**) Different possible structures obtained by linking paramagnetic colloids. Source: ref. [108]. **c**) Schematics of a metallodielectric Janus particle under an AC electric field perpendicular to particle motion. The different material polarizability at both sides of the particle induces charge gradients at the particle surface. Thus, breaking the flow symmetry patterns around the particle allows particle propulsion. Source: ref. ([111]).

Particles electrically driven in this thesis take as a basis of their driven motion the fundamental concepts of ICEO and ICEP, not using isotropic fluids as dispersing media but NLCs (discussed in section 4.2.2).

3.2.1. Collective phenomena emerging from externally driven colloids

For driven particles, colloidal collective motion arises from the dynamical assembly under the application of an external field either electric or magnetic.

Following the work in ([107], [108]), spinning magnetic micro-particles deposited close to a substrate were self-assembled under the application of an elliptically polarized magnetic field. When particles are energized, and close to the bottom surface, flows induced into the fluid act cooperatively allowing the propulsion. This is evidenced by faster velocities obtained for larger chains until reaching a saturation speed ([113]).

More complex structures have been obtained, propelled and self-assembled using AC magnetic fields perpendicular to the plane of the particles ([114]–[117]). Under the application of the AC magnetic field, particles self-assemble at an air-water interface forming snake-like entities. Tuning the magnetic field conditions permits the self-propulsion by breaking the symmetry of surface flows around the entities. The flow field control around the snake-like chain was not only achieved by the modification of the magnetic field but also by placing a bead in one of the entity endings (**Fig. 25a**) ([114]). Following these experiments, other forms of self-assembly were reached by placing the magnetic colloidal particles in a liquid-liquid interface ([115]). A variety of aster-like structures, which are dynamic in nature, meaning that under no energy supply they disassemble, arise from tuning the AC magnetic field. This collective phenomenon is attributed to the particle collective response to the application of the field and its interaction with the interface (**Fig. 25b**). Moreover, by placing the magnetic particles in a concave surface and by inducing rolling motion, different states or transitions can be appreciated, such as flocking ([116]).

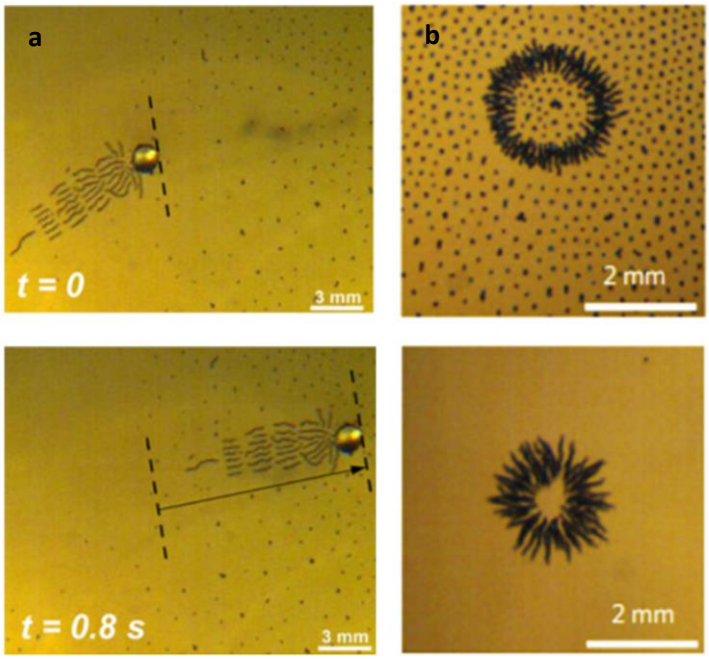

Fig. 25. Collective emerging phenomena in magnetically driven microswimmers. a) Self-driven snake-like hybrid particle system under the application of an AC magnetic field**.** Source: ref. ([114]). **b**) Magnetic particles dynamically self-assemble into aster-like shapes under the application of an AC external magnetic field. Source: ref. ([115]).

Changing to electrically driven colloids, Quincke rotation has become a smart mechanism to induce colloidal motion. Briefly, Quincke rotators can be considered as dielectric polarizable particles which under the application of a DC electric field experience a charge separation. Above a critical field amplitude, E_0, the charge distribution around the sphere becomes unstable and fluctuations spontaneously break the symmetry due to the difference between particle and fluid charging characteristic times. This symmetry breaking results in a net torque and the particle starts to rotate at a certain constant speed with a random displacement perpendicular to the applied electric field ([118]).

This mechanism has been exploited to study the collective emerging phenomena in confined environments ([118]–[120]). In these realizations, polymeric-based micron sized particles were dispersed in an isotropic fluid confined in both curvy-linear and circular racetracks. Low densities regimes do not present special collective interest as particle-particle interaction and confinement do not play a role. However, particles driven in high density regimes feature velocity-alignment, thus collective unidirectional motion emerges. In the curvy-linear experimental setup, the electric rollers spontaneously form a band propagating along the racetrack with almost constant velocity and with a strongly asymmetric density profile. Thus, the system can be seen as colloidal flocks travelling in an isotropic fluid (**Fig. 26a**) ([118]). On the other hand, circular confinements do not present steady flocking states but transient ones. In this geometry, the colloidal swarms self-organize into a single vortex pattern with a random constant orientation. The particles span along the walls of the confining disk avoiding the centre, with a non-uniform velocity profile. Thus, a colloidal phase-separation expanding from the annulus centre to its periphery spontaneously appears (**Fig. 26b**) ([119]).

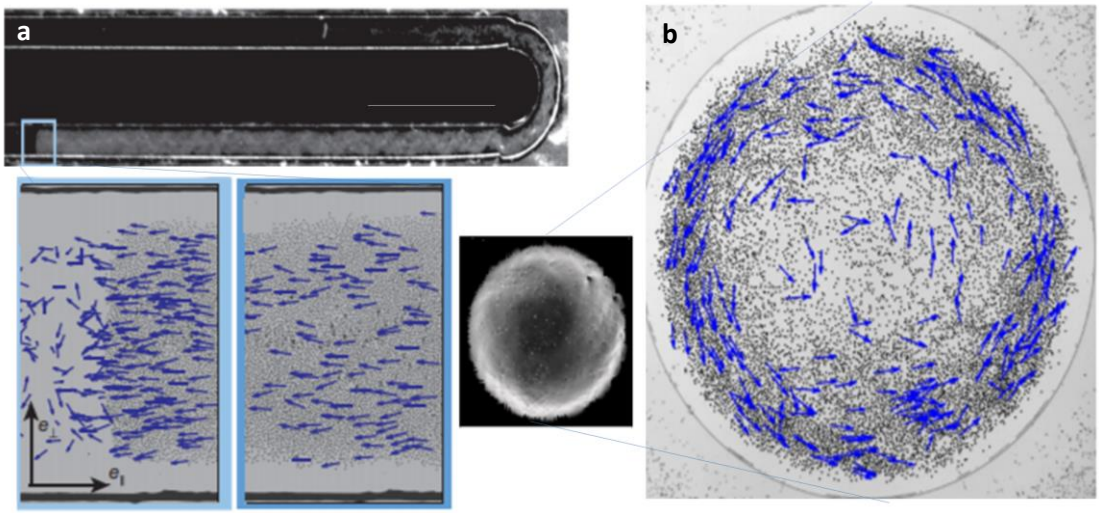

Fig. 26. Collective emerging phenomena in electrically actuated microswimmers. a) Dark-field images of a curvy-linear racetrack where colloidal particles spontaneously form a propagating band under the application of a DC electric field. Source: ref. ([118]). Inset shows the propagating band (left) and a homogenous polar phase (right). The scale bar is 5mm. e refers to polar vector alignment parallel ($e_{\parallel}$) or perpendicular ($e_{\perp}$) to the racetrack represented by blue vectors. **b**) Micrograph of a vortex performed by the rollers where the blue vectors represent their instantaneous speed**.** Inset shows the superposition of the local packing fraction averaged over time. Source: ref. ([119]).

4. Active and driven particles in liquid crystals

Motion of colloids in LCs can be classified in two different classes depending on the propulsion mechanism. The first class corresponds to swimmers that are self-propelled, such as bacteria, and are included in the "internally driven active colloids in liquid crystals" group ("internally driven" ACLCs). On the other hand, particles whose motion is powered by an external electric field are known as "externally driven ACLCs". In the first case, the compatibility between bacteria and conventional thermotropic nematic liquid crystals seemed to be inexistent, as evidenced by bacterial death, thus, experimental realizations must be performed in biocompatible LCs ([38]).

4.1. Active colloids in chromonic liquid crystals

The dispersion of active particles in liquid crystals has introduced a new class of active matter called "living liquid crystals" (LLCs)([121]–[123]), which is different from similar experiments based on either, dense suspensions of self-propelled units in isotropic fluids, also known as "active fluids" ([124], [125]), or bacteria dispersed in complex fluids at low density regimes ([126], [127]). Living liquid crystals consist on dispersing common swimming bacteria, i.e. Bacillus Subtilis, in a biocompatible lyotropic chromonic LC, disodium cromoglycate (DSCG). This lyotropic chromonic LC (LCLC) in equilibrium, for a given concentration and temperature, displays characteristics of a nematic phase allowing the material alignment in one preferred direction, **n**. On the other hand, a typical bacterium consists of a central body of about 5 – 7 µm in length and 0.7 µm in width. The central body has attached to it helicoidal long flagella filaments which allow its propulsion performing a unidirectional "head-forward" motion.

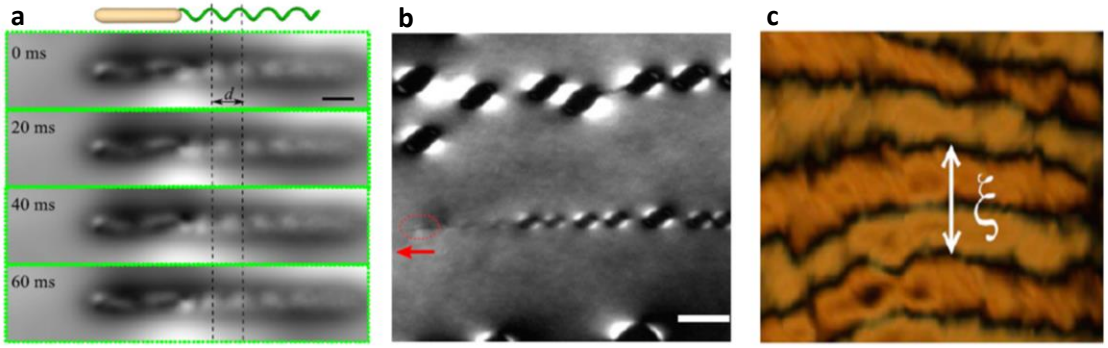

Fig. 27. Distortions of the nematic director induced by flagellated bacteria and observed under POM. a) Time evolution of the director waves generated by the bacteria flagella rotation. **b**) Trace of isotropic tactoids induced by rotating flagella at a temperature about 0.5 ^{o}C below the nematic-isotropic coexistence transition point. **c**) Active bacteria produce stripped periodically distortions of the nematic director with a characteristic length scale (ξ). Scale bars are: (**a**) 10 µm, (**b**) 20 µm and (**c**) 100 µm. Adapted from ref. ([121]).

When a bacterium is dispersed in a LCLC, it perturbs its local director field (see Section 2.1). In samples where bacteria are not active (without oxygen), the LC is in an aligned steady state and also the immotile bacteria are aligned in the same direction. After the addition of oxygen, which controls bacteria activity, self-propelled units tend to swim parallel to **n** (this is a consequence of both anisotropies, the one related to the LC and the other to the bacterium shape). The motion is induced by the rotating flagella, which perturbs **n** at the

micron scale, even though flagella lengths are on the nanometre scale (**Fig. 27a**) ([121]). Perturbations originated by the moving flagella can be observed under POM revealing two different spots. This means that the local director is tilted with respect to **n**. From these observations, the frequency ratio between flagella and body rotation could be extracted (~6:1), showing a frequencies ratio similar to that obtained under normal conditions (7:1) ([128]).

Individual behaviour becomes especially interesting when the system temperature is increased and the LLC approaches the nematic – isotropic phase coexistence. In phase coexistence, isotropic zones appear as elongated "dark tactoids" along the surrounding far-field director. The dark tactoids distort **n** and modifies bacteria trajectories, which follow the local distorted director. Another peculiar effect observed nearly T_{NI} is the creation of isotropic tactoids due to the rotation of the bacteria flagella, which can be attributed to a reduction of the molecular orientational order (**Fig. 27b**).

Collective effects arising from LLCs are usually attributed to high density suspensions of bacteria. In this case, the long-range orientational order of the liquid crystal is affected by the flow induced by the motive bacteria. Thus, the coupling between orientational order (LC) and hydrodynamic flow field (bacteria motion affecting LC) gives rise to dynamic patterns. In this study ([121]) the authors find an instability, featuring a characteristic length scale (ξ), which develops in stripe patterns featuring bend-like periodic deviations of **n** from $\mathbf{n_o}$ (**Fig. 27c**). The characteristic length scale (ξ) increases inversely proportional to bacterial activity (oxygen input) and to bacterial concentration, and increases with cell thickness. Thus, the balance between bacterial activity and viscoelastic LC forces is fundamental on the creation of the striped-based self-organized structures.

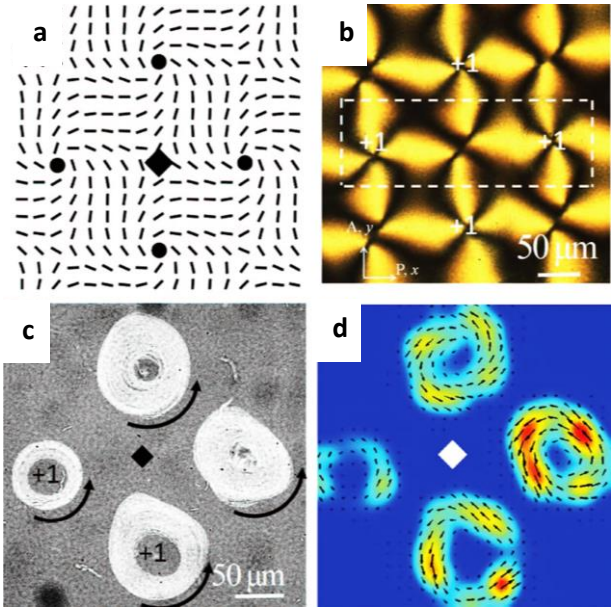

Fig. 28. Polar-defined bacterial circular flows in a periodic defect pattern. a) Underlying director field pattern displaying +1 (cores marked with a circle) and -1 (core marked with a diamond) topological defects. **b**) Polarizing optical microscopy texture of the pattern. A (y) refers to analyser and P (x) to polarizer. **c**) Bacterial trajectories follow the bend-splay underlying pattern inducing counter-clockwise spiralling vortices. **d)** Velocity map for the vortices observed in **c**). Extracted from ref. ([122]).

Remarkably, the absence of an aligned nematic phase induces persistent rearrangement of **n**, thus topological defects with charges s=±1/2 appears. Similarly to experiments based on microtubules, the s=±1/2 discontinuities continuously annihilate and nucleate in pairs ([129]).

To envisage the use of self-propelled particles as entities to power dynamic materials, chaotic motion must be controlled. Following the above mentioned work ([121]), swimming bacteria placed in an anisotropic environment with a well-defined underlying pattern seems to be one of the strategies to command active matter (**Fig. 28**). Other interesting features to control such as geometry or polarity of bacteria trajectories could be potentially considered in relation to other active systems ([130], [131]).

Bacteria can distinguish director field discontinuities even though these deformations occur at larger length scales. Thus, topological charges will affect bacterial dynamics: they preferentially get attracted to underlying positive topological defects while they tend to avoid negative ones.

4.2. Driven colloids in nematic liquid crystals

Different driving mechanisms for the transport of colloids in NLCs involve the application of an external AC electric field. In this section we will explain two different mechanisms which are present direct or indirectly, in this thesis. The main driving mechanism is the Liquid Crystal-Enabled Electrokinetiks (LCEEK), which will be developed in section 4.2.2. A secondary mechanism that can be present in our samples, depending on the initial LC cell configuration, is colloidal transport mediated by backflow effects. We will start the description with this last one.

4.2.1. Backflow – mediated colloidal transport

Transport of particles mediated by backflow effects result from the reorientation of the nematic director at the boundaries induced by an external AC field. This phenomenon can be observed in complex fluids (not isotropic) for both, dielectric and charged particles. To better understand this phenomenon, let us suppose a NLC cell displaying a planar homogeneous NLC far field in one direction (x direction). This cell is filled with a colloidal dispersion of silica-coated particles featuring a point defect-hedgehog dispersed in the LC E7 ($\varepsilon_a > 0$). At the initial equilibrium state, particles "levitate" (see Section 2.3) at a certain height, which is about the middle of the cell, as the gravity is balanced by the wall-dipole elastic interactions (**Fig. 29a**) ([47]). Under the application of an AC electric field perpendicular to the plane of the particles (x,y), **n** reorients along the z axis due to the positive anisotropy of the material, and lifts the particles towards one of the plates depending on the sense of the dipolar defect (**Fig. 29b**).

When the AC polarity is reversed, the LC returns to its equilibrium state inducing a hydrodynamic flow to the fluid resulting from director field reorientation (backflow effect), which allows for particle propulsion. Here, the colloidal motion can take place in both senses with respect to **n**, and can mediate colloidal self-assembly by particle aggregation ([38]). The applied AC electric field consists on a high frequency carrier sinusoidal wave, which avoids

ionic currents, and is enveloped with a low frequency wave allowing backflow mediated colloidal transport (see Chapter 2, Section 5.2).

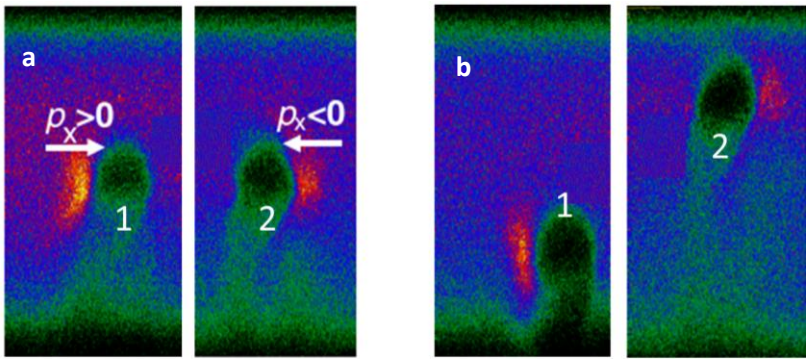

Fig. 29. Elastic point defect-hedgehog dipoles and their FCPM textures. a) In the initial equilibrium state, particles levitate due to elastic repulsion. The dipole of both particles points in different senses with respect to particles centre. This is defined by p_x. The red point near the particles defines the point defect-hedgehog in these micrographs. **b**) Under the application of an AC field perpendicular to the electrodes, **n** gets reoriented and pushes particle 1 to the bottom and 2 to the top depending on its dipole sense. Adapted from ref. ([47]).

4.2.2. Liquid crystal – enabled elektrokinetics (LCEEK)

LINEAR ELECTROPHORESIS – ISOTROPIC FLUIDS

One of the most studied colloidal transport techniques based on the application of an electric field is the well-known linear electrophoresis ([132]). This process takes place for surface charged particles dispersed in an isotropic fluid under the application of a DC electric field (**Fig. 30a**). In the initial equilibrium state, without any applied external field, the system remains neutral, meaning that particle charges are counterbalanced by the medium ones.

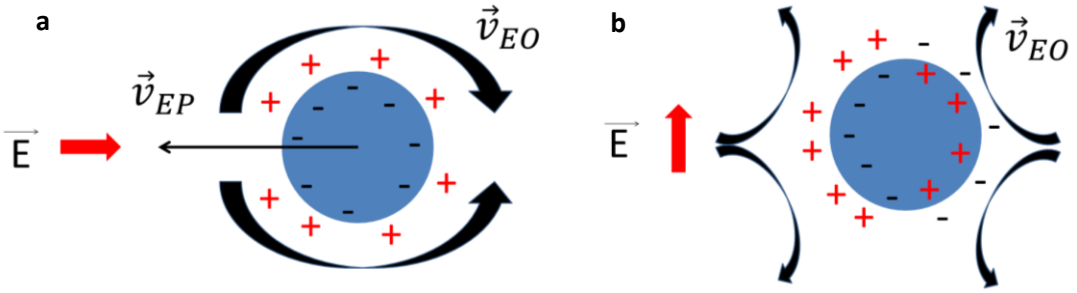

Fig. 30. Schematic mechanisms of colloidal electrophoresis in isotropic electrolytes. a) Linear electrophoresis of a charged particle with surface charges screened by counter ions. Black curved arrows show the electroosmotic flow around the sphere whose velocity is proportional to the applied electric field, v∝E. **b**) An AC electric field induces double layers around a polarizable particle and triggers fluid vortices around the particle surface (ICEO). The resulting pattern is symmetric, thus the sphere does not move.

In contrast, when an external electric DC is applied, particle electric charges are separated in space, within an "effective" characteristic length, the well-known Debye screening length ([112]). Here, the electrophoretic velocity is determined by the Smoluchowski formula, $v = \mu \cdot E$, which is proportional to the electrophoretic mobility and to the applied field (**Fig. 30a**). The electrophoretic mobility takes the expression, $\mu = {}^{\varepsilon_r \varepsilon_0 \zeta}/_{\eta}$, where ε_r is the dielectric constant, ε_0 is the vacuum permittivity, η is the dynamic viscosity of the medium and ζ is the particle zeta-potential (which is the electrokinetic potential in colloidal

suspensions, in other words, the potential that develops in between a solid surface and its liquid medium). Thus, velocity scales proportional to the zeta-potential (related to charge separation) and inversely proportional to the medium viscosity ([132]).

LINEAR ELECTROPHORESIS – LIQUID CRYSTALS

LCs has some ionic content resulting for instance, from chemical synthesis. Thus, the application of the electrophoretic technique can also be extended to LCs. To illustrate the situation, imagine a nematic planar cell consisting of two ITO glass plates glued together and facing inwards (The xy plane is the one corresponding to the electrodes) and filled with a dispersion of particles in a NLC of negative dielectric anisotropy ($\varepsilon_a < 0$). The material director is aligned parallel to the electrodes plane, while the applied DC field is perpendicular to the electrodes plane, so in the z direction. At that point, charged particles will move along the z axis while uncharged particles will remain quiet ([133]).

When particle driving is based on DC fields, steady flows are not persistent for a large period of time, they stop at the saturation time of the electrodes. This is the time needed for the ions contained in the electrolyte to move towards the corresponding electrode and screen the applied field. Also, other non-desirable features that can be present are: the appearance of secondary reactions at the surface, low velocities or poor control on particle surface charges ([134], [135]).

Most of the above mentioned handicaps can be overcomed by using AC instead of DC electric fields. In this case, it is much easier to produce steady flows and avoid electrochemical reactions although the propulsion mechanism becomes non-linear, as commented in section 3.2.

NON-LINEAR ELECTROPHORESIS – ISOTROPIC FLUIDS

Non-linear elektrokinetic effects, such as ICEO and ICEP, can be present in both isotropic and anisotropic fluids. For isotropic fluids, the main difference with respect to linear effects refers to the initial equilibrium dispersion state, where in absence of electric field, particles displaying no net charge do not show charge separation. Remarkably, colloids presenting no charge can also be propelled. The basic expression for electrophoretic velocities takes the form, $v = \mu \cdot E$, where the mobility is taken as before, $\mu = \varepsilon_r \varepsilon_0 \zeta(E)/\eta$. Here, one power of E induces the charge separation $\zeta(\mathrm{E})$ creating charge densities ρ at particle surface proportional to the applied electric field , while the second one acts on this charge to drive the resultant ICEO flow, explaining the quadratic dependence, $v \propto E^2$ (**Fig. 30b**).

Experimental realizations based on studying the ICEO flows generated around dispersing colloids involve the use of highly polarizable particles, such as metal spheres ([136]) or metallic cylinders ([134]). As seen in **Fig. 31a**, the flows induced around the particle display quadrupolar symmetry which results in no net pumping of the fluid. Thus, particle motion will not take place unless the symmetry of the induced flows around the particle becomes unbalanced. Janus particles seemed to be a good choice in order to break the symmetry of the flow field around the colloid, thus allowing a net pumping (see also section 3.2) (**Fig. 31b**) ([111]).

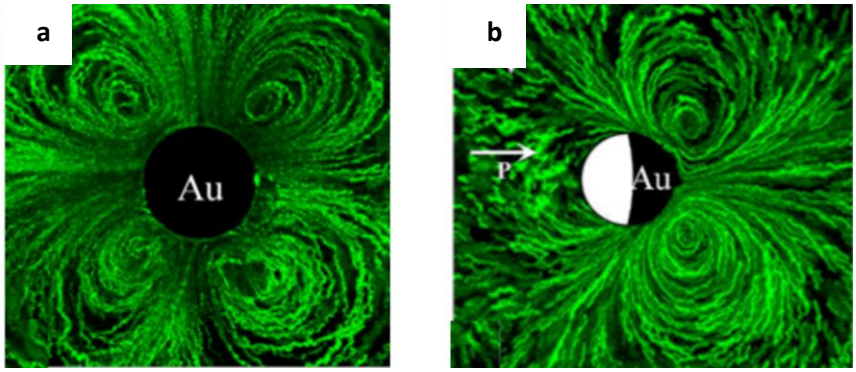

Fig. 31. Experimentally obtained ICEO flow trajectories. FCPM micrographs of particles featuring different composition dispersed in water. a) Quadrupolar ICEO flows induced around a metal polarizable sphere. **b**) ICEO flows around Janus particles are unbalanced, thus allowing particle propulsion. The applied electric field is perpendicular to particle motion. The fluid flows are visualized using fluorescent nano-particles as tracers. Adapted from ref. ([137]).

NON-LINEAR ELECTROPHORESIS – LIQUID CRYSTALS

The ICEO and ICEP mechanisms do not just work for isotropic fluids but also for LCs. However, in the latter, the material anisotropy implies a different mechanism, the so-called Liquid Crystal-Enabled Electrokinetics (LCEEK), which involves electrophoresis (LCEEP) and electro-osmotic flows (LCEEO) ([38], [43], [133], [138]–[140]). Usually, electrophoresis is related to the motion of the particle inside a fluid under the application of an electric external field, and electrosmosis to the motion of the fluid with respect to a solid (particle) surface. Particles are propelled by the action of unbalanced vortices generated around them which provide a constant electrophoretic velocity.

As commented in Section 2.1 particles dispersed in LCs distort the elastic matrix inducing a topological constraint on its surroundings. Depending on the anchoring conditions, different configurations of **n** around the colloids are possible, dipolar or quadrupolar. Under the application of an AC electric field, the induced charge separation is sensitive to the nematic configuration. Thus, the nematic configuration will set the pattern of the LCEEO flows: quadrupolar (dipolar) director patterns induce quadrupolar (dipolar) flows. The induced LCEEO flows for both configurations are defined as “puller”-like for homeotropic anchoring (**Fig. 32a-b,e-f**) and “pusher”-like for tangential (**Fig. 32c,d**) one ([139]). For puller-like swimmers fluid moves towards the particle while pusher-like swimmers eject the fluid to the bulk. To obtain a net pumping of the electroosmotic flows, fore-aft symmetry must be broken, which is only observed for dipolar nematic configurations. As a consequence, only dipolar configurations of the nematic director will allow particle propulsion as seen in (**Fig. 32e-f**).

In LCEEK, charge separation induced by the application of an electric field is coupled to the nematic director, thus, material anisotropy must be taken into account. Here, as before, charge separation is proportional to the applied electric field. Additionally also the LC anisotropy plays a role, namely director gradients (distortions) and dielectric and conductivity anisotropies ($\rho \propto \Delta\sigma\, \Delta\varepsilon$). This is in contrast to ICEO in isotropic fluids where the particle properties, alone, determine the charge separation, although flow velocities are proportional to the square of the electric applied field, $v \propto E^2$, for both mechanisms.

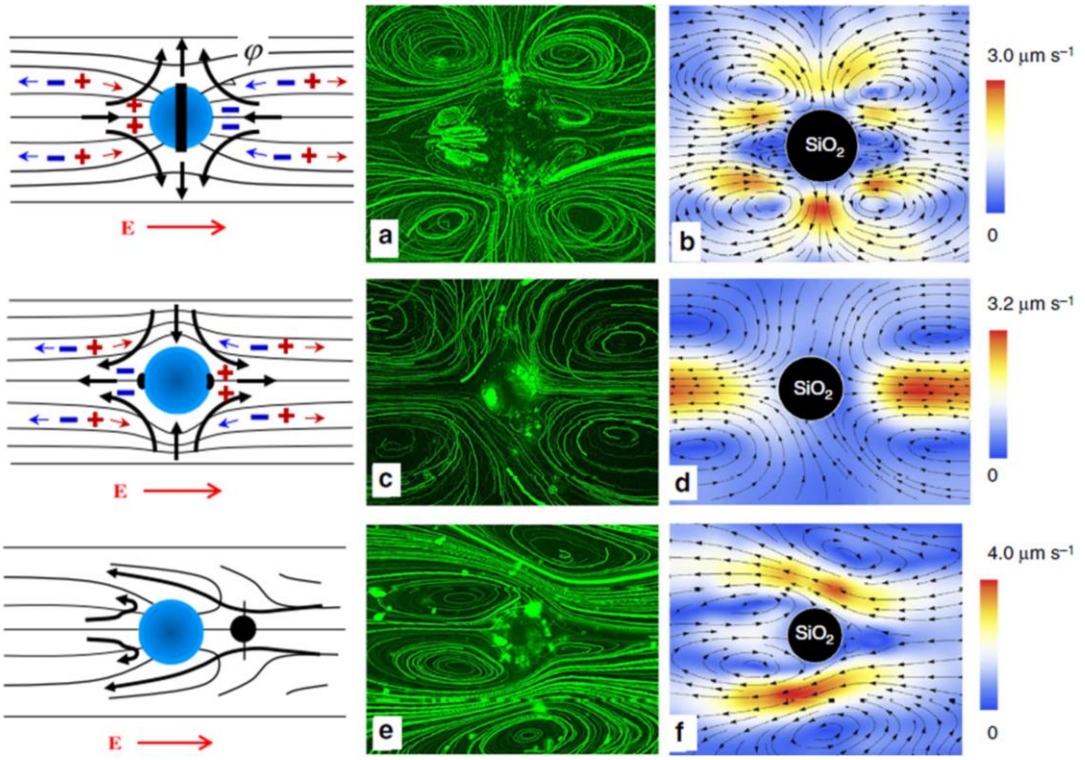

Fig. 32. Experimentally obtained LCEEO flow trajectories of particles featuring different anchoring conditions. a,c,e) Experimentally obtained FCPM micrographs of the fluid flows using fluorescent tracer particles. **b, d, f**) Computer simulations of the flows obtained for different anchoring conditions. **a, b**) Particle with perpendicular anchoring featuring a disclination Saturn-Ring display quadrupolar director patterns. **c, d**) Bipolar (double-boojums) sphere with tangential anchoring featuring quadrupolar symmetry. Velocities in (**b**) and (**d**) are of opposite polarity, inducing patterns of a puller (**b**) and a pusher (**d**) type. **e, f**) Particle featuring a point defect-hedgehog, homeotropic anchoring, induces a dipolar director pattern; thus, particle is propelled. Note pumping from right to left in (**f**). Adapted from refs. ([43], [139]).

The amplitude of the electroosmotic flows around particles endows an electrophoretic velocity for colloids displaying a dipolar configuration of **n**. This velocity is proportional to the square of the applied electric field, $v \propto E^2$, as previously commented. The electrophoretic velocity of the dipolar particle follows from the balance of the driving Coulomb force, $f = \rho E_x$ (related to charge separation) where E_x is the applied electric field in the x direction, and a viscous drag force $\eta \cdot v$, where η is an averaged viscosity and v is the particle velocity. This balance, for weak director distortions and small dielectric anisotropies, can be written as

$$|v| = \frac{\alpha \varepsilon_o \bar{\varepsilon} R}{\eta} \left| \frac{\Delta\sigma}{\bar{\sigma}} - \frac{\Delta\varepsilon}{\bar{\varepsilon}} \right| E^2$$

where α is a dimensionless coefficient which takes into account gradients of director distortions (director strength and direction), ε_o is the vacuum permittivity, $\bar{\varepsilon}$ is an averaged dielectric constant of the medium, R is the particle radius, η is an averaged viscosity, $\Delta\sigma$ is the conductivity anisotropy, $\bar{\sigma}$ is an averaged conductivity ($\bar{\sigma} = (\sigma_{\parallel} + \sigma_{\perp})/2$), $\Delta\varepsilon$ is the dielectric anisotropy, $\bar{\varepsilon}$ is an averaged electric permitivitty of the medium and E is the applied electric field. The velocity dependece on E^2 has been verified experimentally ([138], [141]). Another control parameter of the electric field is frequency, which importantly plays a role on the charging times of both, the particle and the electrodes. The characteristic time

scale for the particle charging is $\tau_c = \frac{\varepsilon_m \lambda_D^2}{\varepsilon_d D}$, where ε_m is the medium dielectric constant, $\lambda_D$is the Debye screening length, ε_d is the dielectric constant of the particle and *D* is the diffusion coefficient. On the other hand, the characteristic time for electrode charging goes as: $\tau_e = \frac{\lambda_D L}{2D}$ being L the distance between electrodes. Taking typical values for particles dispersed in liquid crystals (taking into account the material anisotropy), these two time scales are on the order of: τ_c ~ 10^{-2} s and τ_e ~ 10^{-2} to 10^2 s, depending on the distance between electrodes. Finally, the resulting velocity dependence on frequency is given by a non-monotonic function (see Chapter 4, Section 2),

$$v(f) = \frac{f^2 {\tau_e}^2}{(1 + f^2 {\tau_c}^2)(1 + f^2 {\tau_e}^2)}.$$

Where the velocity increases as f^2 for low frequencies, but after reaching a maximum decreases for high f because in the fast polarization regime, ions cannot follow the AC. Experimentally, the maximum achieved velocities are on the order of 10-20 μm/s and are achieved in the range of frequencies 5 to 50 Hz even though particle motion can be found until about 500 Hz.

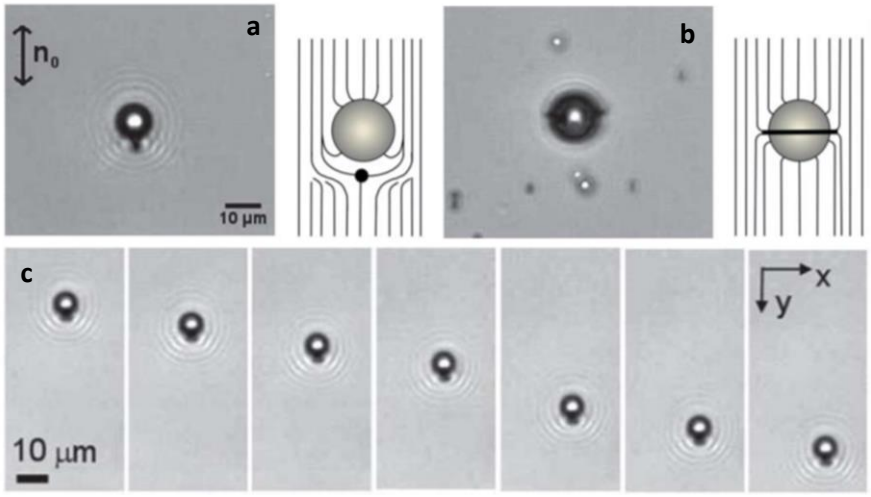

Fig. 33. Colloidal transport in NLCs under LCEEK mechanism. Optical microscope images showing water micro-droplets characterized by a hyperbolic point defect-hedgehog (**a**) and a disclination loop Saturn-Ring (**b**) defect. The double arrow indicates the direction of **n**. Inset shows a schematic configuration of **n** around the water droplets. **c**) Optical micrographs sequence of a water droplet featuring a dipolar configuration of **n** which is propelled under the application of an AC field perpendicular to the electrodes plane. Adapted from ref. ([141]).

Using LCEEK enables the application of AC fields to propel particles endowing lots of different geometrical possibilities when designing the experimental setups ([138]). This has some important applicability on the transport and assembly of colloids, namely to transport particles following pre-defined trajectories (**Fig. 33**) ([141]), which is directly related to the design of micro-reactors, or even to control colloidal collective behaviour such as swarming ([142]).

5. Main goals and objectives

This work aims at the development of strategies to study from single particle transport to colloidal collective dynamics in complex fluids, such as LCs. In order to achieve the different goals, an initial research plan contemplated, among others, the following objectives:

- SINGLE PARTICLE TRANSPORT

- To design an experimental system to study the propulsion of a single particle inside a LC matrix.
- To study the transport modes parallel and perpendicular to both, the aligned nematic director and the driving force, at different temperatures. In other words, how thermal fluctuations affect a particle moving in a LC environment.

- COLLOIDAL ASSEMBLIES

- To study the effect of varying the frequency of an AC electric field on the formation of colloidal assemblies for different underlying NLC configurations.
- To make an exhaustive quantification of the performed colloidal assembly experiments, in terms of driving force, inter-particle interactions and NLC elasticity.

- COLLECTIVE COLLOIDAL TRANSPORT

- To study the collective motion of flocks of particles traveling along a pre-defined path.
- To implement new strategies to better control colloidal collective dynamics, either by using photo-patterned substrates or microfluidic devices.

Chapter 2

Materials and methods

In this section, firstly, I will describe in detail the procedures involved in the preparation of the NLC cells employed in the experiments further presented. From these cells, I will detail the most relevant parameters to take into account and the procedures involved, such as cell thickness and surface treatments. After, I will explain the colloidal dispersions giving details of the NLCs used and how particles are treated to achieve specific anchoring conditions at convenience. Next, I describe the instrumentation and the typical parameters used during the application of external fields and temperature control. Finally, I explain how the samples have been irradiated and characterized using optical techniques, which involves the polarizing optical microscope, and the basics of the tracking routines used for image processing and data analysis.

1. Experimental NLC cells

The experimental cells used in this thesis for the transport and assembly of colloids dispersed in NLCs consist on two glass plates, functionalized to achieve a specific configuration of **n**, with the functionalized face facing inwards and glued together. For colloids propelled under the LCEEK mechanism, these plates feature a thin transparent indium-tin-oxide (ITO) coating, which acts as electrode. The separation between plates is achieved by using Mylar (commercial name for PolyEthyleneTerephthalate in USA) spacers.

To be more precise, we use 0.7mm thick microscope slides with an area of 15x25 mm^2, typically, coated with a thin layer of indium tin oxide (ITO) with a sheet resistance of 100 $\Omega \cdot sq^{-1}$ (VisionTek Systems). The plates are assembled, with the ITO facing inwards, using either two-component epoxy glue (3450 LOCTITE) or UV-curing glue (Norland, NOA81). Typically, separations between plates range between 15 µm and 25 µm (Mylar spacers), although extra tests are performed using larger spacers (50 µm and 100 µm). Conducting wires are attached to the ITO faces using the same glues mentioned above, and a colloidal silver dispersion (RS silver conductive paint, 5g, 186-3593) is used to make the electric contacts between the wires (Alphawire 5851 BK005 - 30AWG) and the ITO layers. The cell is schematically depicted in **Fig. 34**.

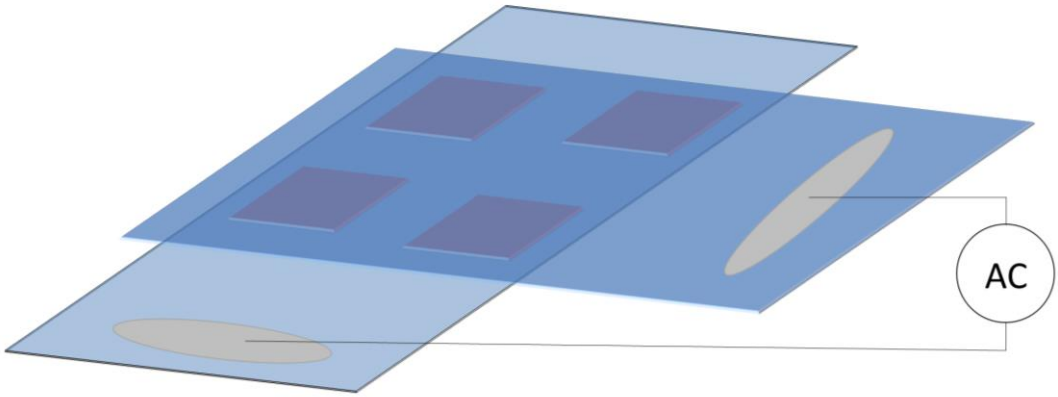

Fig. 34. Schematically depicted NLC cell. ITO plates are glued facing inwards within a defined cell thickness, typically, both 15 µm and 25 µm. The electric contact is achieved by a silver colloidal dispersion placed between the wire and the ITO surface.

2. **Cell spacing**

The accurate cell gap thickness of a NLC cell has been measured using a UV-Vis spectrophotometer (Ocean Optics USB4000-UV-VIS) coupled to OceanView's software. This technique can be applied to any designed cell featuring transparent glass substrates. The technique measures the constructive and destructive interferences between multiple reflections of light inside the cell gap, as seen in **Fig. 35**. The separation between two plates can be extracted from the interference spectrum using the equation,

$$d = \frac{M}{2n} \cdot \frac{\lambda_2 \cdot \lambda_1}{|\lambda_2 - \lambda_1|}$$

Where d is the cell thickness, n is the index of refraction of the medium between plates (the experiment is performed with an empty cell and the index of refraction is the one corresponding to air, $n \approx 1$), and M is the number of maxima present in the interference pattern between the wavelengths λ_1 and λ_2.

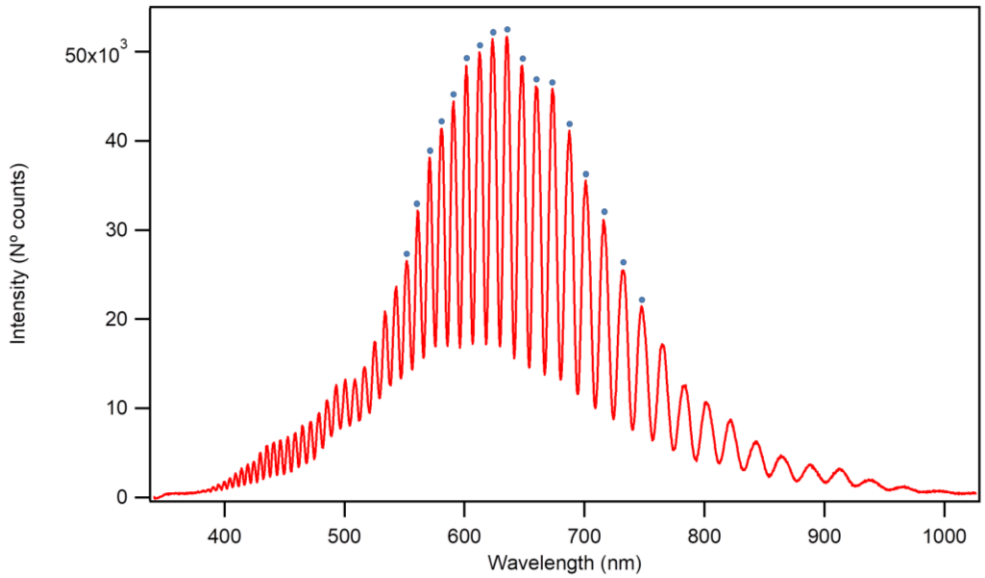

Fig. 35. Example of an interference pattern spectrum. The resolved interferences (M=17) between two well-defined wavelengths (λ_1=550 nm and λ_2=750 nm) in a typically used empty cell result on a thickness ~ 15 µm.

3. Surface treatments

During the preparation of the different experimental setups used in this thesis, substrates are always cleaned before use. Afterwards, they are chemically treated to impose both well-defined anchoring conditions to the confined material and patterned tracks defining colloidal trajectories. To achieve specific anchoring conditions two experimental techniques can be used: spin-coating or self-assembled monolayers.

3.1. Cleaning procedures

Glass (Thermo Scientific-Menzel Glässer) or ITO-coated glass were received as standard microscope slides. First, the substrates are degreased to ensure a correct functionalization. In a first step, both substrates are manually cleaned with a diluted solution of dishwasher soap (Procter&Gamble) in Milli-Q water (18.2 MΩ·cm, Millipore Gradient A-10), followed by a second cleaning under a Micro-90 (Sigma-Aldrich) surfactant diluted solution (~ 1%). In both cases, plates are rinsed with Milli-Q water after cleaning. These procedures are performed under sonication action, where plates are placed in a Coplin staining jar. In case of using a glass plate, the substrate is cleaned and activated at the same time by immersing it in a piranha solution, 1:3 H_2O_2 (33% wt., Sigma 216763) / H_2SO_4 (96% v/v, lab. grade Scharlau). Note the heat generated due to the exothermic reaction. On the other hand, the cleaning procedure of an ITO-coated glass must be carried out with a less aggressive procedure to avoid ITO detachment, usually in a mixture 5:1:1 in volume, H_2O / H_2O_2 (33% wt., Sigma 216763) / NH_4OH (28-30% v/v, Sigma V000637). Alternatively, ITO-coated glass slides can be cleaned and activated with O_2 plasma surface treatment equipment (ZEPTO, Diener Electronics).

3.2. Self – assembled monolayers (SAMs)

One easy and widely used way to functionalize the substrates is to adsorb a self-assembled monolayer (SAM) on its surface. Self-assembled monolayers, as its name indicate, are molecular films formed by the interacting molecules on a surface ([143]). This procedure basically involves dipping the substrate onto a solution containing the adsorbated molecule. The SAM characteristics are controlled by temperature, dipping time (from minutes to hours) and the kinetics of the specific substrates.

In this thesis, functionalization with SAMs, have been performed for different target molecules. On the one hand, alkyl silane compounds are used to achieve strong homeotropic anchoring of the mesogen to the substrates. On the other hand, an azo-based compound was used to form a photosensitive self-assembled monolayer allowing the *cis-trans* isomerization under light irradiation.

- HOMEOTROPIC ANCHORING

DMOAP

The molecule Dimethyl octadecyl [3-(trimethoxysilyl)propyl] ammonium (42 % wt. in MeOH, Aldrich Chemistry), also known as DMOAP (**Fig. 36**), is a typically used compound to achieve

perpendicular anchoring conditions at the surface of the bounding plates. The clean substrates are immersed in a Milli-Q water solution containing 1% v/v of DMOAP for about 30 minutes at room temperature. Afterwards, the plates are rinsed with running Milli-Q water and dried with a N_2 stream. Finally, the plates are baked at about 130^{o}C during 1.5 hours to chemically enhance the binding of the silane group onto the glass or ITO-glass substrate ([144]).

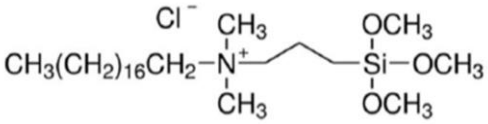

Fig. 36. Formula of DMOAP.

AQUAPEL®

Aquapel® (PPG Industries) is a commercial solution of different chemicals including a fluoroalkyl silane (**Fig. 37**). A droplet of the mixture is deposited above the substrate and a fast functionalization (1-2 minutes) occurs. The procedure is performed at room temperature without any curing step. Finally, plates are rinsed with plenty of water to avoid precipitates.

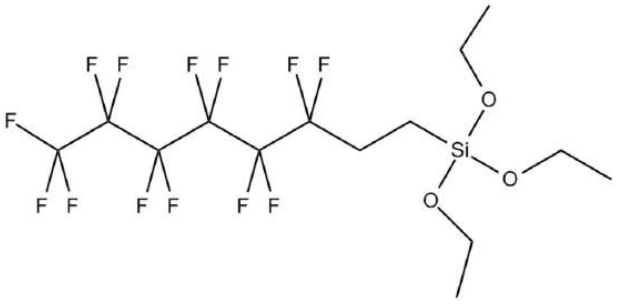

Fig. 37. Formula of fluorooctylsilane, the main component of Aquapel®.

- PHOTOSENSITIVE ANCHORING

Photosensitive SAMs substrates are prepared with a mixture of both photosensitive and non-photosensitive silanes (**Fig. 38**). The reaction using only photosensitive silanes results on a compact molecular distribution not allowing the photosensitive molecules to switch conformations. Thus, addition of short-chain non-photosensitive silanes allows the optimal molecular re-arrangement when triggering the *trans* to *cis* isomerization under light irradiation.

In contrast to other earlier protocols ([142]), where the SAM was obtained in a 2 step reaction between a precursor aminosilane and a carboxylic-acid azobenzene derivative, here, the photosensitive substrate is obtained in a single step following well-known procedures ([145]). The photosensitive compound is, (E)-4-(4-((4-octylphenyl)diazenyl)phenoxy)-N-(3-(triethoxysilyl)propyl)butanamide (Galchimia, Spain) (**Fig. 38a**) – henceforth called AZO, while the non-photosensitive compound is (3-aminopropyl) triethoxysilane (APTES, Sigma-Aldrich). Both compounds are combined at a

ratio 5:1 (AZO:APTES) to improve systems photo-response ([146]). The deposition solution is prepared by dissolving the silanes and butylamine (Sigma-Aldrich; used as catalyser) in toluene (peptide synthesis grade, Scharlau) at a ratio 1:7:173. The cleaned plates are dipped in the resulting solution and the self-assembled monolayer is allowed to form for about 120 minutes at 80°C. Upon removal, the slides are quickly rinsed with toluene to avoid precipitation of the solute, followed by a 10 minutes wash with toluene under ultrasounds, and they are either readily used or stored in the dark under vacuum or Argon atmosphere until used, typically within a week.

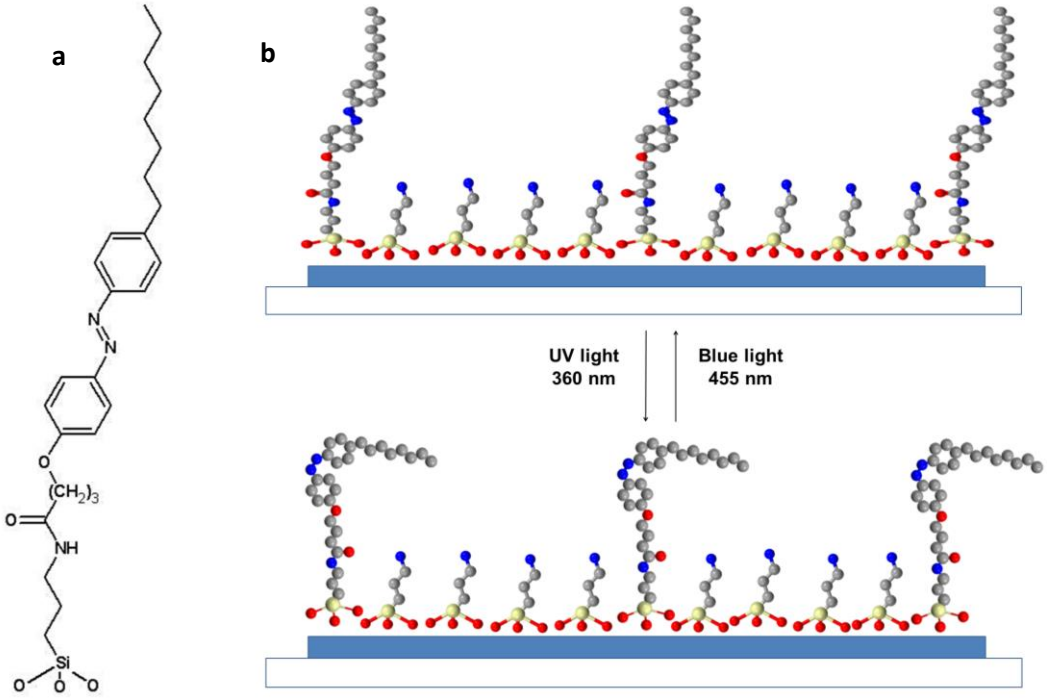

Fig. 38. One-step functionalization method to prepare photosensitive substrates using a mixture of silanes (AZO/APTES). a) Chemical formula of the AZO compound. **b**) Resulting photosensitive SAM from the reaction of both silanes, photo- and non-photosensitive. Application of UV light triggers the *trans* to *cis* isomerization. The reverse modulation is achieved by blue light.

Different tests have been performed to characterize the photosensitive SAM. A UV-Visible spectrophotometer (Shimadzu UV-1603) is used to verify the photo-sensitivities of both, the AZO-based monolayer deposited on the ITO-glass substrate (**Fig. 39a**) and a solution of the same AZO compound dissolved in EtOH (96% v/v for analysis, Panreac) featuring a $0.5 \cdot 10^{-4}$ M concentration (**Fig. 39b**).

The AZO compound dissolved in EtOH display a peak located at λ ~ 365 nm, corresponding to the transition from the *trans* to the *cis* isomer. On the other hand, the small peak located at λ ~ 430 nm matches within the reverse transition from the less abundant *cis* to *trans* isomer. The spectra of the AZO monolayer also exhibits a peak at λ ~ 365 nm, corresponding to the main transition, although the small peak relative to the *cis* to *trans* transition is hidden under the tail of the largest peak. Thus, the AZO compound is present on the substrates.

The isomerization of the AZO compound triggers the modulation of the NLC anchoring conditions at the bounding plates. Briefly, the AZO stable form is the *trans* isomer, which

induces homeotropic anchoring of the NLC. When the photosensitive surface is irradiated with UV light, *trans* to *cis* isomerization occurs and NLC molecules adopt a planar configuration which can be observed under POM (see Chapter 4, Section 2).

The relaxation time of the isomerization can be monitored by acquiring the transmittance under crossed polarizers. Here, maximum transmittance is expected in the *trans* form, relaxing to a minimum of transmittance in the *cis* form. This experiment is performed under red light (red longpass filter, Lambda, 645 nm) to avoid perturbing the photosensitive substrate. Immediately after irradiation, the amount of transmitted light is maximum, and gradually decreases until extinction, being about 15 minutes the estimated half-life time (**Fig. 39c**). That is, when all the *cis* AZO molecules have turned to the stable *trans* configuration, thus, the NLC molecules are disposed perpendicular to the plates (homeotropic) and the light polarization is not modified when going through the sample.

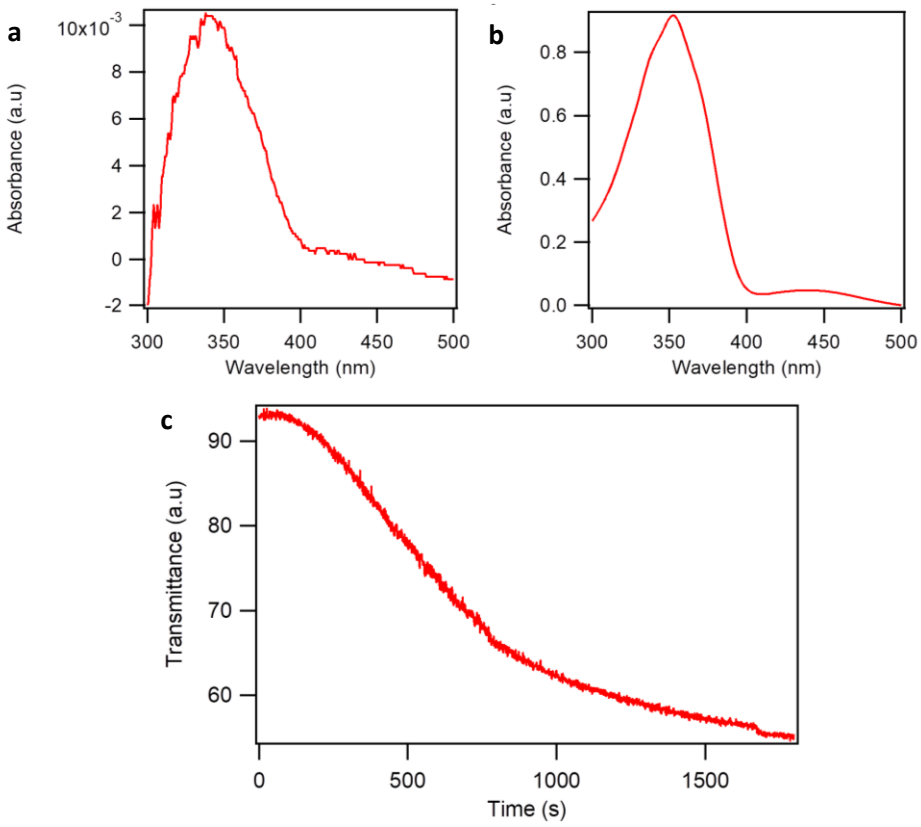

Fig. 39. Characterization of the photosensitive surface. UV-Visible spectrum of the **a**) azosilane-coated glass plate and **b**) an ethanolic solution of the same compound. **c**) Relaxation of an irradiated light spot. The measurement has been performed during the transition from the *cis* (planar) configuration of the AZO (NLC) molecules to the *trans* (homeotropic) state at 25°C in presence of natural light.

3.3. Spin – coating

Spin-coating is a process used to coat (ITO)-glass slides with thin uniform films which usually employ resin or polymer solutions. The basic operation consists on first depositing a droplet of the target solution above the substrate, and then rotates the substrate at high speed in order to deposit a homogeneous layer. Here, the centrifugal force plays a role on both, spreading homogeneously the substrate and ejecting the excess of fluid. This results in a thin

film whose thickness, typically on the order of µm, depends on the compound to attach, the spin-coating velocity and the time of spinning. Usually, the substrate is baked to evaporate the excess of solvent as well as to anneal the resin or polymer onto the surface (**Fig. 40**). In the experiments described in this thesis, the used spin-coater is a Chemat Technologies Spin-Coater KW-4A.

With this technique is possible to obtain both, planar and homeotropic anchoring of the NLC at the bounding plates, as described below.

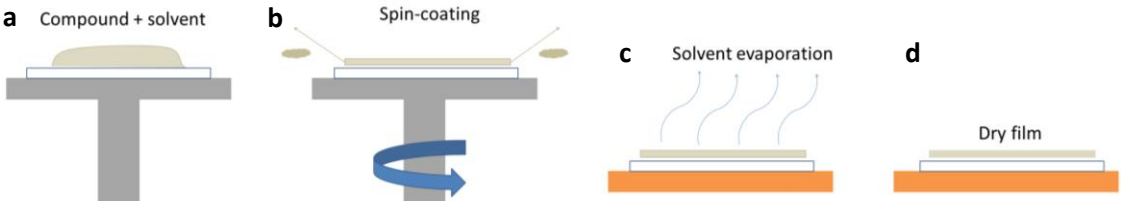

Fig. 40. Spin-coating, process deposition. a) Deposition of the resin or polymer solution onto the surface. **b**) Rotation of the surface at high velocity homogenously spread the solution and ejects the excess, creating a thin film. **c**) The surface is placed onto a hot plate to evaporate the solvent annealing the resin or polymer onto the surface **d**).

- HOMEOTROPIC ANCHORING

The compound used is NISSAN 0626. This resin is dissolved in solvent 26 (both from Nissan Chemical Industries) at a concentration 5% (w/w). The spin-coating protocol for this resin involves depositing about 10 µL · cm^{-2} of the solution to the substrate, which is attached to the spin-coater by means of vacuum. The initial rotation step consists of spinning the sample at 750 rpm for 3 seconds followed by a spontaneously velocity increase up to 2500 rpm, which is kept for 90 seconds. Afterwards, the substrate with the thin film is pre-baked onto a hot plate at 80°C during 1 minute and left for 1.5 hours at 180°C.

- PLANAR ANCHORING

Two different compounds have been used in this thesis to achieve a parallel orientation of **n**, a solution of polyvinyl alcohol (PVA, 88% hydrolysed, MW 88000, Across Organics) or a solution of resin 0825 in solvent 25 (both from Nissan Chemical Industries) featuring a 3% concentration (w/w). For the polyimide compound the protocol is basically the same as described for the homeotropic anchoring. On the other hand, the PVA coated-substrates are achieved via spin-coating at 750 rpm for 3 seconds, and then at 2000 rpm for 30 seconds. The coated film is then enhanced by placing the substrate onto a hot plate at about 130°C for 1 hour.

Usually, after treatment, the planar coated-substrates are rubbed with a velvet cloth, 10-20 times along the same direction and in the same sense, to induce “micro-pipelines” which define a preferred in-plane direction for LC alignment.

Most of the experiments shown in this thesis have been performed using Nissan resins.

4. Colloidal dispersions

Nematic liquid crystals, CCN-37 (Nematel) and MLC-7029 (Merck), have been used as dispersing medium during this thesis. As inclusions, micron-sized particles featuring differences on both material (silicon and polystyrene) and shape (spherical or peanut-like) have been dispersed.

One technique to disperse the clean microparticles in the NLC is by evaporating about 0.2 µL of the initial suspending solution featuring a ~1% w/v concentration, containing typically a water/EtOH mixture (1:1), in the desiccator by vacuum effect. Afterwards, an amount of ~ 10 µL NLC is added in the Eppendorf (Thermo Scientific) container and the mixture is stirred in the vortex and finally sonicated for about 5-10 minutes before adding in the NLC cell. Another alternative method consists on the evaporation of the suspending solution above a clean glass substrate which is thermalized at about 60°C. Then, the NLC is deposited onto the particles with a micropipette, and the mixture is gently stirred with the tip. The latter is the preferred process used in this thesis where particles should appear disaggregated under the microscope. The typical particle density in the NLC dispersion is ≤ 1% w/v to avoid particle aggregation.

Once the colloidal nematic dispersions are prepared in a 100 µL Eppendorf, they are subsequently confined between the functionalized surfaces to impose a well-defined far-field orientation of the LC.

4.1. Liquid Crystals

The liquid crystals CCN-37 and MLC-7029 can be classified in the thermotropic group, and here, in all experiments they feature the nematic phase. The main characteristics of these NLCs are the negative dielectric anisotropy, the large range of temperatures exhibiting the nematic phase and also the commercial availability (**Table 1**).

Property	CCN-37 (Nematel)	MLC-7029 (Merck)
Dielectric anisotropy	-5.4	-3.6
Nematic-isotropic T (°C)	~ 55	~ 95
Birefringence	0.03	0.13
K1 (pN)	4.9	16.1
K2 (pN)	4.4	-
K3 (pN)	10.2	15
Viscosity ‖ to n (10^3 Pa·s)		1.4
Viscosity ⊥ to n (10^3 Pa·s)		3.4

Table 1. Main properties of CCN-37 and MLC-7029 at room temperature (25°C).

For experiments performed in Chapter 3 we use the NLC CCN-37, while in experiments shown in Chapters 4 and 5 the NLC is MLC-7029. Both LCs present negative dielectric anisotropy (ε_a < 0). Thus, application of an electric field perpendicular between surface electrodes induces the in-plane reorientation of the nematic bulk.

In contrast, some test experiments shown in Chapter 4 were performed using 5CB, which presents positive dielectric anisotropy (ε_a > 0), thus the material will align within the applied electric field and no reorientation will be induced.

Furthermore, experiments shown in Chapter 3 have been performed varying temperature. In the range of temperatures studied, the main material properties exhibited changes, for instance, the elastic constants or the rotational viscosity (**Fig. 41**), which are important when colloids are dispersed and propelled under temperature. This is in contrast to experiments shown in Chapter 4 and 5, where all experiments are performed at room temperature ~ 25°C, far from the T_{NI} transition, where material properties are not affected by thermal fluctuations.

The viscosity parallel and perpendicular to **n** for the NLC MLC-7029 has been measured, in separate experiments, by comparing the motion of paramagnetic colloidal particles, which are propelled by the action of an external magnetic field gradient both, in water and in the aligned NLC MLC-7029 (see Section 8.2).

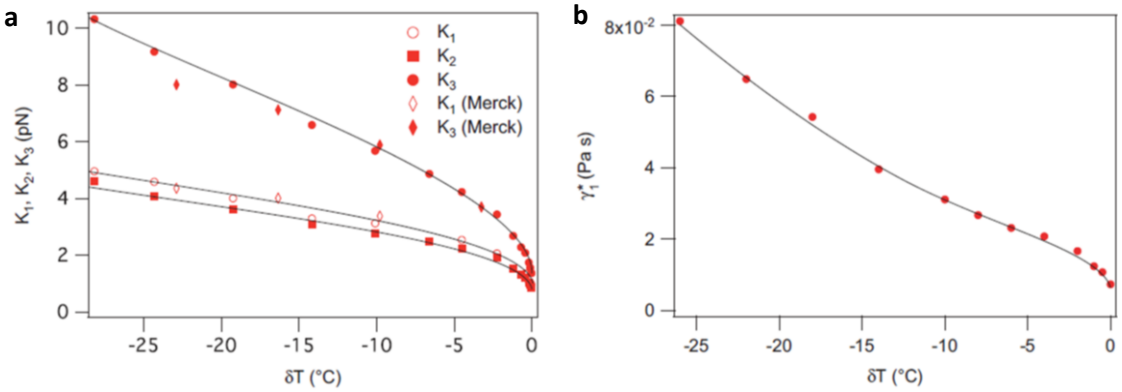

Fig. 41. Elastic constants and effective rotational viscosity for CCN-37 as a function of temperature. a) Splay (K1), Twist (K2) and Bend (K3) constants versus temperature. The experimental data agrees with the data supplied by Merck company. **b**) Effective rotational viscosity decreases as a function of temperature. The solid line is a guide to the eye. δT(ºC) = T - T_{NI} , where T stands for the current experiment temperature and T_{NI} ~ 55°C. Adapted from ref. ([147]).

4.2. Colloidal particles

Silica spherical inclusions (Kisker Biotech), used in Chapter 3, or anisometric polystyrene-based particles (Magsphere Inc.),used in Chapter 4 and 5, which allow surface modification, are chosen as inclusions.

Silica spherical particles used in thesis realization present different size, typical diameters are ϕ = 5 µm and ϕ = 10 µm. When dispersed in NLCs, bare and functionalized particles, promote different configurations of **n** around the inclusion, either dipolar or quadrupolar, as further explained. Note that LCEEK mechanism is only valid for dipolar configuration of **n**, while quadrupolar must be avoided.

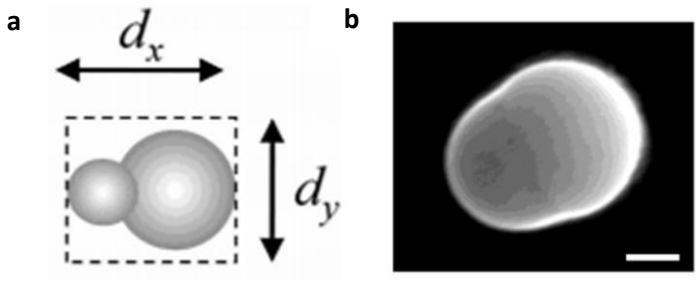

Fig. 42. Peanut-shaped polystyrene particles. a) The colloid can be characterized by two different lateral dimensions, being, typically d_x = 4μm and d_y = 3μm. **b**) SEM image of a PS peanut-like shape particle. The scale bar is 1 μm.

On the other hand, anisometric peanut-like shaped particles are characterized by different lateral dimensions (**Fig. 42**). The material is polystyrene (PS) and the dimensions are typically d_x = 4μm and d_y = 3μm, although other tests have been performed with larger particles, d_x = 10.2μm and d_y = 8.2μm. To enhance the dispersion of these particles in the NLC, silica coatings can be achieved using well-known protocols ([148]), as further described.

- CLEANING PROCEDURE

In all the experiments presented, commercial colloidal particles are cleaned before used by re-dispersion in different fluid media. This process ensures the elimination of surfactants or other chemicals present in the original stock solution, such as stabilizers.

The cleaning process consists on taking an amount of typically 100 μL from the commercial solution, centrifuge it, and re-disperse the pellet into 1 mL of Milli-Q water. Here, the centrifugation time depends on the material and size of particles, resulting on larger times for smaller and less dense particles. Once the particles are sedimented, a syringe is used to extract the supernatant liquid, and then, the 1 mL Eppendorf is re-filled with water or a mixture water/EtOH. This process is repeated three times.

When particles are cleaned and dispersed in a water/EtoH mixture, they can be either used immediately or further chemically functionalized, as explained as follows. Once particle dispersions are used, are left in the fridge in order to avoid biological proliferation.

- HOMEOTROPIC ANCHORING – SILICA PARTICLES

Perpendicular alignment of **n** onto the surface of silica particles is obtained by using long-chain alkylsilanes. The procedure is similar to that described in Section 3.2 for self-assembled monolayers. The specific anchoring conditions are achieved by different coating protocols depending on particle size.

For small particles (ϕ = 5 μm) we use, n-Octadecyltrichlorosilane (OTS, Gelest), while DMOAP is used for larger ones (ϕ = 10 μm).

For DMOAP functionalization, clean particles are suspended in a DMOAP solution, 0.5% (v/v), in Milli-Q water for 30 minutes under sonication. Afterwards, the suspension is cleaned 3 times with water by centrifugation - redispersion. The solvent is subsequently extracted and particles are redispersed in a water/EtOH mixture.

In contrast, OTS functionalization consists on dispersing the particles in a 0.5% (v/v) solution of the compound in EtOH. The mixture is left during 30 minutes under sonication. Afterwards, the clean particles redispersed in EtOH are used.

- SILICA COATING – PEANUT POLYSTYRENE PARTICLES

Peanut-shape particles have been coated with silica following well-known procedures ([148]). The protocol is based on two different steps. The first one, where clean PS peanut-shaped particles are introduced in a recipient containing a solution of polyvinylpyrrolidone (PVP, $3.6 \cdot 10^5$g/mol, Sigma) in Milli-Q water featuring a concentration ~ 0.75% (v/v). The polidispersion is stirred under vortex action for 24 hours. The PVP polymer gets adsorbed onto the polystyrene surface. The second step consists on transferring the particles into EtOH for further silica shell growth using a silane compound. Thus, particles are first centrifuged and the supernatant liquid is extracted. After, particles are re-dispersed in a solution of NH_3 (Sigma-Aldrich 30%) in EtOH, which features a concentration ~ 4.2% (v/v) and containing a 10% (v/v) of tetraethoxysilane (TES, 99%, Aldrich Chemistry,). The particles are left under vortex stirring action for about 24 hours. Finally, particles are cleaned with Milli-Q water and redispersed in a water/EtOH mixture. For polystyrene colloids, the shell thickness is estimated to be on the order of tens of nanometres ([148]).

5. Application of external fields and temperature control

LCs reorient under the application of external fields (see Chapter 1, Section 1.5.3). In this thesis, the application of electric external fields can induce both director field reorientation and particle propulsion. This is in contrast to the application of magnetic fields, which have been only used to propel paramagnetic particles, in test experiments during this thesis realization, by means of magnetic gradients.

5.1. Magnetic field gradients

The disposition of a magnet nearly a NLC cell, compatible with our microscope setups, provides a unidirectional in-plane magnetic gradient which will exert a force on paramagnetic particles that will move in a viscous fluid.

In these experiments the used paramagnetic particles are magnetic beads (Dynabeads) either of ϕ = 2.7 µm or ϕ = 4.7 µm.

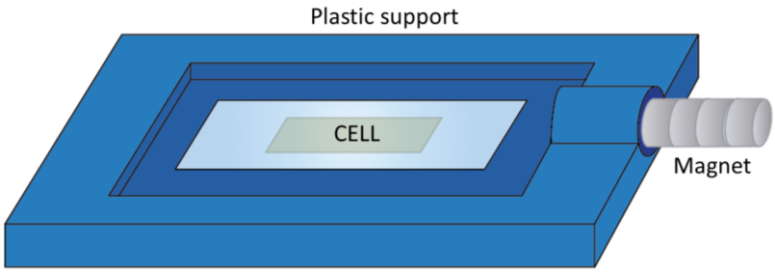

Fig. 43. Schematically depicted experimental setup for magnetic field gradients application. The NLC cell is fixed at a specific location with respect to the magnet. Thus, the magnetic force that propels paramagnetic colloids is kept constant across different experiments.

The magnet is placed at a certain distance from the sample, which is kept fixed for the different experiments, to ensure the same acting force for each system (**Fig. 43**).

The in-plane magnetic field gradient has strength of 25.0 ± 0.5 milliTesla·mm^{-1} (Teslameter, Project Elektronik GmbH, Germany), in the focused area, allowing particle propulsion but not affecting on the LC reorientation (the magnetic field intensity is about one hundred milliTesla which is weaker than the field needed to reorient LCs). These experiments allow measuring the LC viscosity at room temperature (see Section 8.2).

5.2. Electric fields

Electric fields have been applied with a function generator (Agilent Technologies, DSO-X 2002A) between the two ITO-coated glass plates constituting the NLC cell. The function generator is connected to a power amplifier (TREK PZD700) and monitored with a multimeter (Hewlett-Packard 34401A) integrated in the current generator circuit.

Typically, to lead to the LCEEK mechanism, the applied fields are sinusoidal AC fields in the range from 0 to 30 Volts peak to peak, and the range of frequencies vary from 5 to 50 Hz.

Test experiments, where ionic currents are avoided but backflow-mediated colloidal transport is wanted, must be performed with a high frequency carrier wave. In this case, the amplitude of a 1 KHz carrier sinusoidal wave is modulated with a frequency in the range f_m = 10 -100 Hz.

5.3. Temperature control

The sample temperature is controlled with a precision of 0.1^{o}C by means of a custom-built cell that is adapted to the microscope stage. Control is exerted by means of custom-made LabVIEW programs.

6. Imaging

The main optical technique for the characterization of samples involving NLCs is polarizing optical microscopy. Here, I describe the technique and give details about the microscopes used. Also the irradiation protocol of the photosensitive surface mediated by LED sources is explained (see Chapter 2 Section 3.2 and Chapter 4 Section 2).

6.1. Polarizing optical microscope

The optical property characterizing anisotropic materials is birefringence, and polarized-light microscopy allows determining the director field configurations (**Fig. 44**) (see also Chapter 1, Section 1.4.1). A polarizing optical microscope is based on two crossed polarizers (called polarized and analyser) that can be rotated independently. Usually they are rotated so that their directions of polarization are orthogonal. The NLCs cells are placed between both optical elements. Initially, light coming from the source passes through the polarizer, and it gets polarized. When polarized light interacts with the sample, it splits in two different waves with orthogonal polarization. The velocities of these two waves, which are called ordinary and extraordinary waves, are different and vary with the propagation direction throughout the sample. The light components become out of phase, but are recombined when passing through the analyser (inset **Fig. 44**) ([14]). The interactions light-LC will induce variations on light intensity that provide information about the local disposition of the NLC molecules.

In this thesis, polarized light microscopy is mainly performed with a Nikon Eclipse 50iPol upright microscope, although Nikon Eclipse E400 has also been used. Images are acquired with both an AVT Marlin 131B CMOS digital video camera, usually fitted to the Nikon Eclipse 50iPol microscope, and a Pixelink camera (PL-A741) using the software AVT_Smartview and PixeLINK CaptureOEM, respectively. Both microscopes are shown and depicted in Section 6.2.

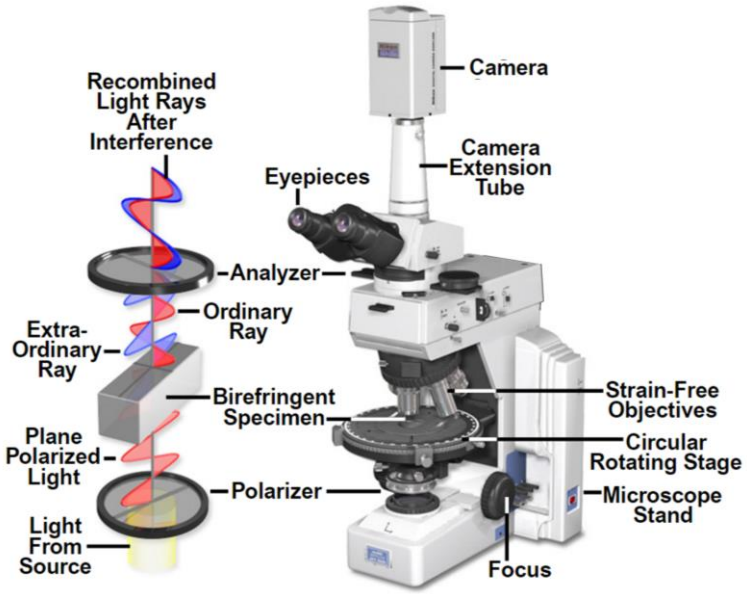

Fig. 44. Polarized light microscopy. Schematics of an optical polarization microscope. Adapted from ref. ([14]).

6.2. Experimental setup

A custom-build experimental setup mediates the isomerization from the *trans* to the *cis* form of a photosensitive substrate used in experiments shown in Chapter 4 and Chapter 5. In this thesis two different protocols of irradiation have been performed although sharing the same optic principle: the first one allows inducing single point topological defects (+1) (see Chapter 1, section 1.5.4 and Chapter 4, section 2) while the second one printing larger pre-defined patterns using designed masks 8 (see Chapter 5, section 3.2).

The sample observation must be performed under a red filter placed in front of the light source (long pass red filter, λ=645 nm, Thorlabs) in order to avoid perturbing the photosensitive surface. Optionally, the standard polarizer and analyzer of the microscope can be used to obtain images between crossed polarizers, as they do not interfere with the irradiation path.

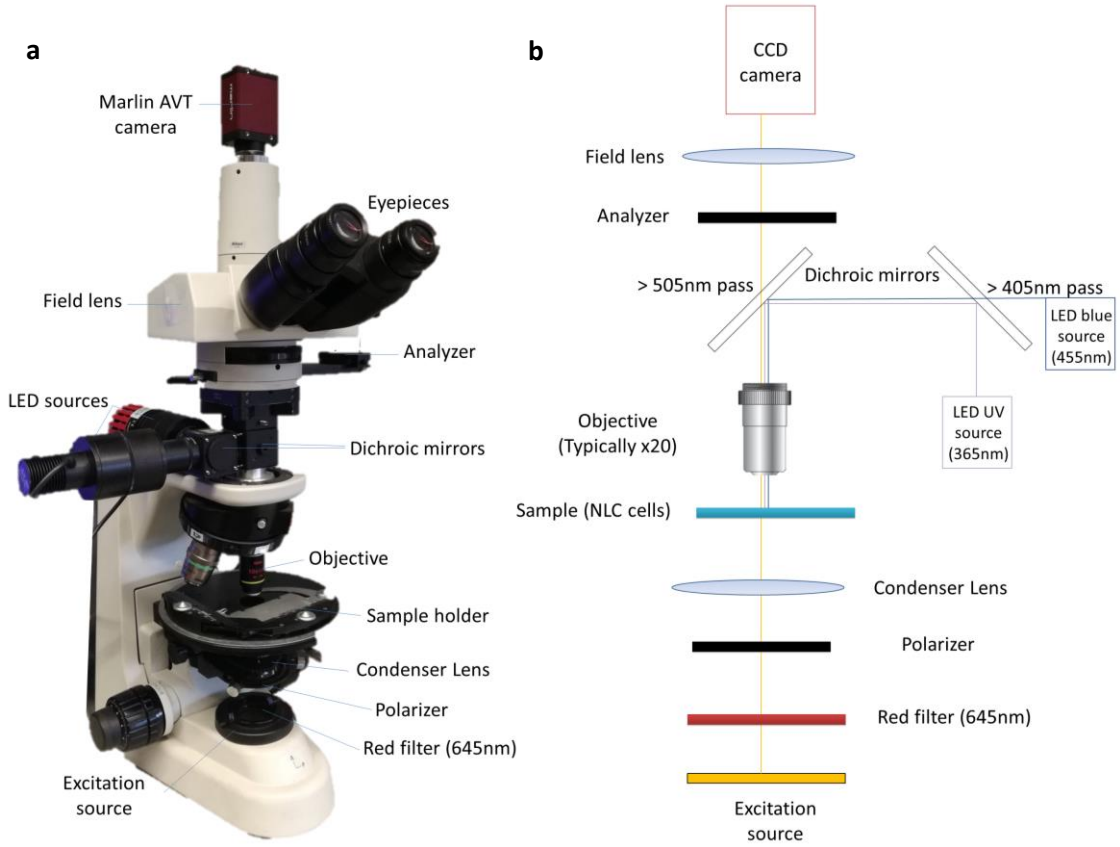

Fig. 45. Custom-built LED epi-illumination setup mounted on the optical polarization microscope. **a**) Photography of the microscope and its main components. **b**) Schematic representation of the microscope, indicating the principal components and the optical path for each wavelength. Yellow lines indicate the path for white light, while blue and purples lines indicate the path for blue and UV-light, respectively.

On the other hand, the irradiation setup consists on a custom-built LED epi-illumination setup integrated in the optical polarization microscope (**Fig. 45**). The irradiation optical path features a long-pass dichroic mirror (cut-off wavelength – λ = 405 nm) which allows blue (λ = 455 nm) light transmittance while reflects UV (λ = 365 nm) light. A second long-pass dichroic mirror (cut-off wavelength, λ = 505 nm) prevents excitation light from reaching the camera. The light beam is focused on the experimental cell by the same microscope objective, which

in turn, triggers the photo-isomerization of the azosilane derivative. This POM (**Fig. 45**) has been used in experiments shown in Chapter 4.

The light power density of the LEDs used has been measured using an optical power and energy meter (PM100USB-Thorlabs Inc.). The power light supplied by the blue light LED (M455L3, 900 mW, Thorlabs) at wavelength – λ = 455 nm, is measured at the output of the objective after following the above described optical path, thus, before reaching the experimental cell. The typical blue light power density used in experiments is ~ 1 $W \cdot cm^{-2}$. The same procedure has been performed for the UV-LED irradiation (M365L2, 190mW, Thorlabs), obtaining a power density ~ 0.2 $W \cdot cm^{-2}$.

After irradiation with UV light, the light spot zone features a sub-millimetre size and is not uniform. Here, the light intensity has rotational symmetry and decreases with the distance to the centre of the spot, thus the originated light spot performs a Gaussian profile of intensities. As a consequence, *trans* to *cis* isomerization starts at the spot centre and propagates outwards, which originates the reported radial orientation of the NLC anchoring (see Chapter 4).

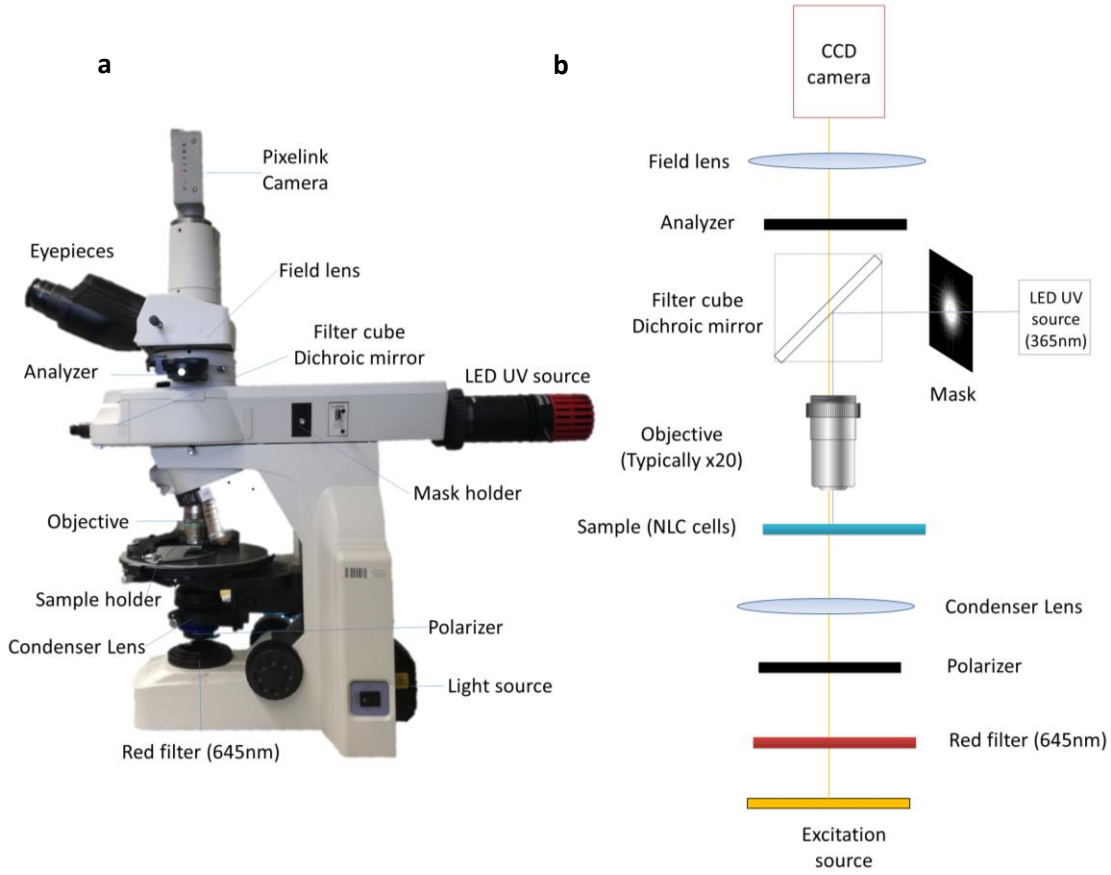

Fig. 46. Custom-built LED epi-illumination setup mounted on the optical polarization microscope (2). a) Photography of the microscope and its main components. **b**) Schematic representation of the microscope, indicating the principal components and the optical path where the mask is placed in between the LED source and the objective. Here, yellow lines indicate the path for white light, while purple lines indicate the path for UV light.

Another irradiation protocol proposed in this thesis is based on placing a physical mask between the LED UV source and the microscope objective (**Fig. 46**). The mask consists on an

acetate slide that selectively blocks light using high resolution motifs printed at 50k dpi (Micro Litography Services, Ltd). To project it in our samples, the masks are placed at the field diaphragm of an epi-illumination module in the microscope, and focused on the sample by means of the microscope objective. Different motifs have been printed and tested, as detailed in Chapter 5.

7. Image and data analysis

In this section, the methods used for image and data analysis are summarized. The software's used during the entire thesis have been ImageJ for data treatment and IgorPro or Mathematica for data analysis.

7.1. Topological distortions

The topological defects located at particles surroundings have been imaged between crossed polarizers in a POM (see section 6). From these observations, the structure of **n**(r) for different anchoring conditions can be uncovered, as schematically depicted in **Fig. 47a,b,c**. Both, Saturn-rings (homeotropic) (**Fig. 47d**) or double-boojums (planar) (**Fig. 47e**) defects display a quadrupolar configuration with four bright lobes, while point defect-hedgehog (homeotropic) (**Fig. 47f**) defects are dipolar and just two bright lobes, parallel to **n**, at the sides of the particle will appear. To better enhance the defect position determination, bright-field micrographs allow the visualization with enhanced contrast of the disclination loop formed around the equator of a particle for Saturn-ring defects (**Fig. 47g**), the two surface point defect boojums parallel to **n** (**Fig. 47h**), and the single point defect-hedgehog located at one of the particles side (**Fig. 47i**).

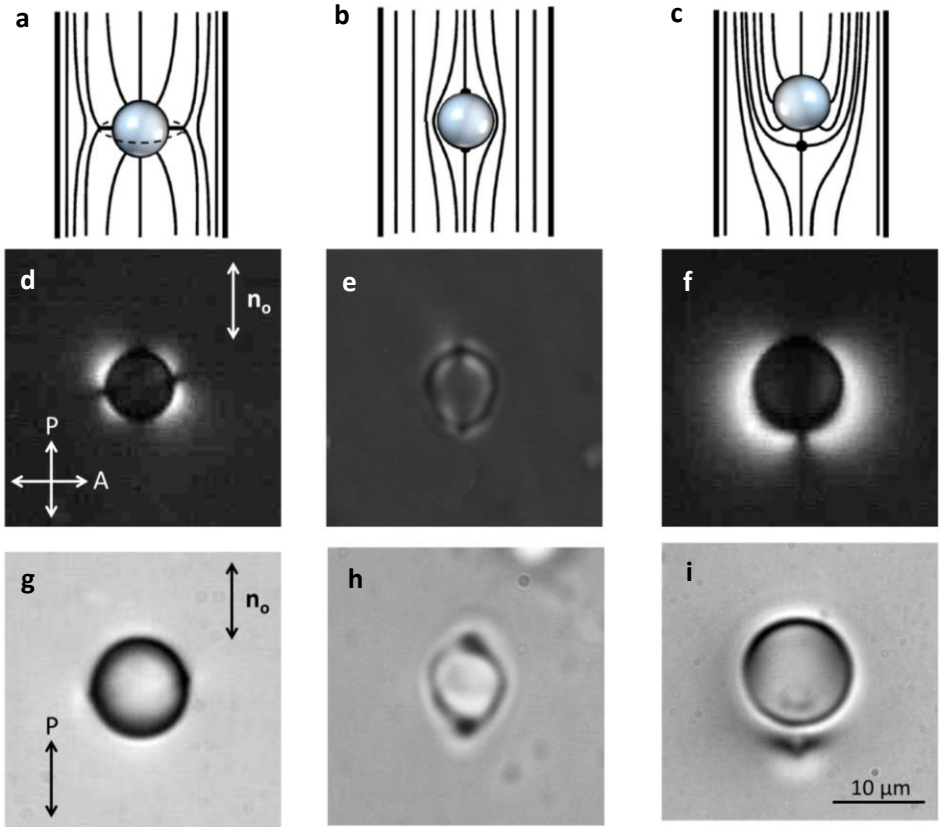

Fig. 47. Topological distortions under POM. a-c) Schematically depicted director configurations around nematic colloids featuring different anchoring conditions, homeotropic (**a,c**) and planar (**b**). **d-f)** POM micrographs for a **d)** Saturn ring, **e)** Double-boojum and **f)** Hedgehog point defects. The analyzer is perpendicular to both the polarizer and the director far-field. **g-i)** Bright-field micrographs for the same topological defects. Black points refer to the topological point defects induced around particles in **a-c**. The scale bar in **i)** apply for all micrographs.

7.2. Particle tracking

The position (x,y) of moving particles is automatically tracked from micrographs acquired, typically, at 1 frame per second (fps), although other experiments at 15 fps have also been performed (**Fig. 48**).

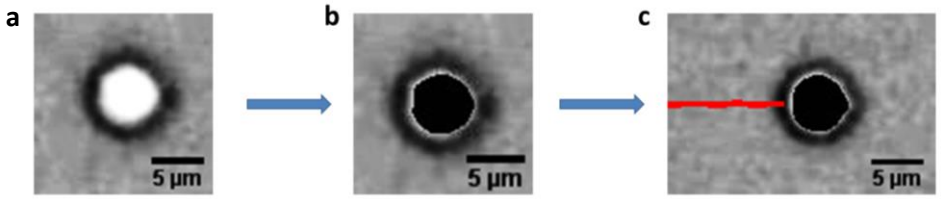

Fig. 48. Colloidal particle automatically tracked. a) 5 µm silica spherical particle displaying a point defect-hedgehog distortion. Typical configuration for experiments shown in Chapter 3. **b**) Particle detection. The black zone consists of pixels that are used to calculate the particle's centre coordinates. **c)** After particle detection, the red line is the trajectory defined by particle motion. See **Video1**.

Both Manual Tracking and Particle Detection plugins (parts of a program with a specific function) have been used, allowing particle position determination, but also velocity and direction tracking of the moving particles. To better define particle contour, POM images have been acquired under decrossed polarizers. Particle detection has been performed after thresholding the micrographs, where the black zone in **Fig. 48b** denote the area used to determine the centre coordinates of the particle.

7.3. Area fraction of particles

In experiments shown in Chapter 4, the radial distribution of area fraction of particles is directly determined from the self-assembled cluster micrographs, and it is measured as the area occupied by the particles in a certain corona of radius r with respect to the total corona area (**Fig. 49**). The coronas are initiated at the centre of the cluster and are expanded to the outer region until reaching a zone where almost no particles are present.

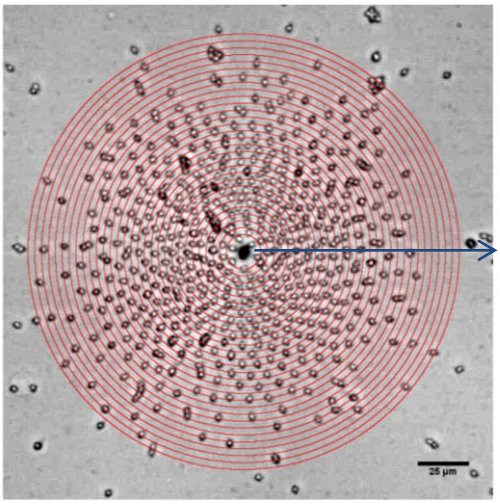

Fig. 49. Definition of the area fraction measurement. Coronas illustrate how the area fraction profiles of particles assembled in clusters shown in Chapter 4 are measured. The coronas are initiated at the centre of the cluster and expanded to the outer region.

The coronas have different width for aster and rotating mill-like assemblies, featuring a width of 3 and 6 µm respectively, to ensure a monotonic detection distribution of the area fraction of particles. This determination, combined with particle position tracking, allows quantifying cluster aggregation.

8. Benchmark experiments

In order to better illustrate the tracking routines and introduce the analysis protocols performed in this thesis, here, I will show complementary experiments and their data treatment. These experiments have been used, on one hand to test tracking routines used in Chapter 3 and on the other hand, to determine a specific LC property, such as viscosity (used in Chapter 4).

8.1. Tracking routines and diffusion modes

Benchmark experiments to test the tracking routines used in this thesis consisted on tilting the sample a certain angle $\alpha = 8.5^{o}$. Here, the colloids will sediment along the driving force (gravity) direction. The experimental cell contained a dispersion of magnetic beads ($\phi = 4.7$ µm) dispersed in a water/glycerol mixture (20% wt.), displaying a viscosity similar to that of LCs, $\eta \sim (1.5 - 2) \cdot 10^{3}$ Pa·s (**Fig. 50a**).

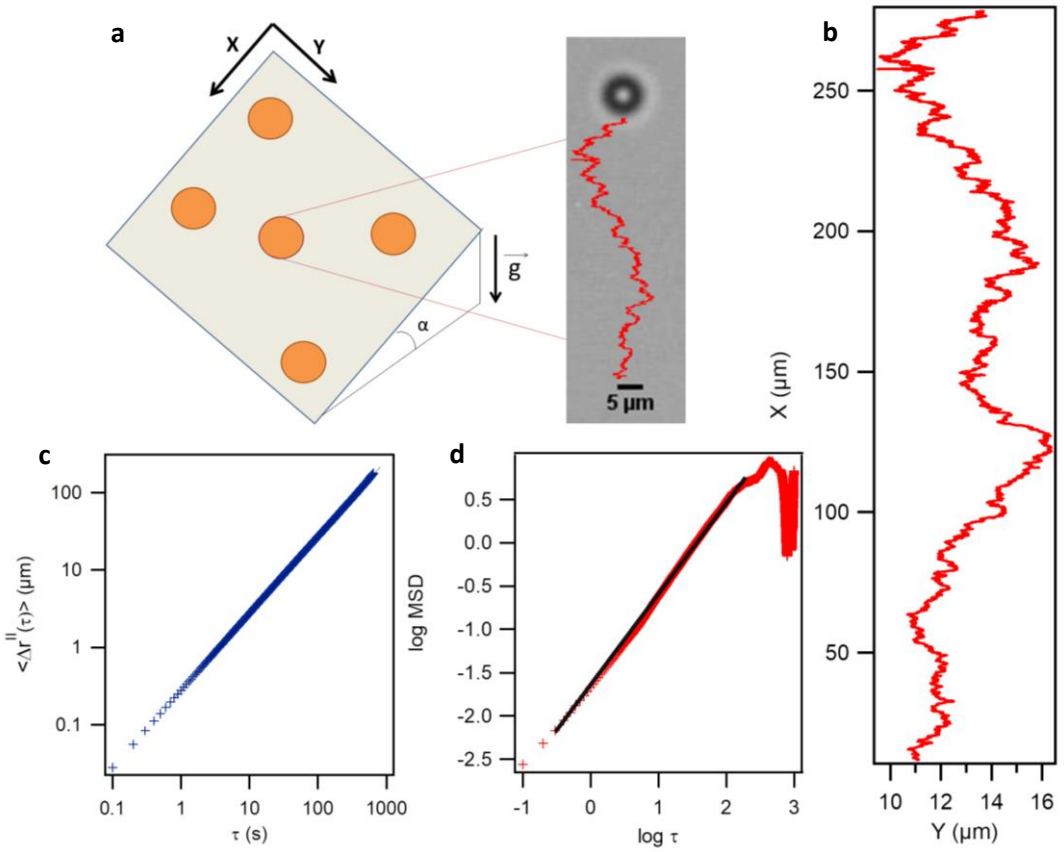

Fig. 50. Testing tracking routines of particles driven in isotropic fluids. a) Schematically depicted experimental geometry, where particles are driven by the in-plane component of gravity, showing the effect of tilting the sample a certain angle $\alpha = 8.5^{o}$. Inset shows the trajectory followed by the magnetic particle. See **Video2**. **b**) Particle trajectory at the x/y plane at room temperature. **c**) Mean displacement (MD) vs. τ displays a ballistic trend with a particle velocity $v = 0.26$ µm·s^{-1}. **d**) On the other hand, the log-log plot of the mean square displacement (MSD) vs. τ shows a diffusive behaviour with an exponent $\nu \approx 1$, as expected for particles dispersed in isotropic fluids. See **Video2**.

Initially, particle trajectory (x,y positions) is extracted from **Video2** as explained in Section 7.2 (**Fig. 50b**). After that, particle motion behaviour has been determined by the first (MD)

and the second moment (MSD) parallel and perpendicular to the driving force, respectively. The first moment parallel to the driving force is the mean displacement and is defined as the difference of particle's coordinates at two different given time windows, $\langle \Delta r^{\parallel}(\tau) \rangle = \langle r^{\parallel}(t+\tau) - r^{\parallel}(t) \rangle$, where $r^{\parallel}$ denotes the particle position and $\langle \dots \rangle$ a time window average. The MD parallel to the driving force displays a ballistic trend, as expected, with a velocity v = 0.26 µm·s^{-1} (**Fig. 50c**). On the other hand, the second moment perpendicular to the driving force is an indicative of the diffusion modes present in particle transport. The second moment is calculated as the mean square displacement, $\langle (\Delta r^{\perp}(\tau))^2 \rangle = \left\langle \left[r^{\perp}(t+\tau) - r^{\perp}(t) \right]^2 \right\rangle$. The power-law $\langle (\Delta r^{\perp}(\tau))^2 \rangle$ vs. t can be linearized by a log-log transformation, where the exponent,ν, of the power law becomes now the slope of the linear regression. Exponents from experiments reported here display nearly $\nu \approx 1$ (**Fig. 50d**), indicative of a diffusive, Brownian behaviour, while exponents $\nu \approx 2$ are indicative of ballistic trends. Different values for the exponents to that described above, $\nu \approx 1$ and $\nu \approx 2$, are the consequence of anomalous diffusive modes, either subdiffusion $\nu < 1$ or superdiffusion $1 < \nu < 2$, as further evidenced in Chapter 3 experiments for superdiffusive regimes.

For the experiment of driven colloids in isotropic fluids reported here, motion parallel (x) to the driving force features a ballistic trend, while motion perpendicular (y) to it displays a diffusive behaviour, as expected.

8.2. Viscosity estimation

Particles translating in a viscous fluid media experiment a friction force opposite to motion. The balance between drive and viscous forces leads to a constant velocity of the particle, thus, it can be written as, $F = \gamma \cdot v_0$, where γ is the friction coefficient, which is proportional to the viscosity, $\gamma(\eta)$, and v_0 is the particle velocity. Thus, by maintaining the driving force fixed at a constant value and comparing the velocities in the viscous fluid (NLC) and in a fluid with a well-known viscosity, water for instance (η ~ 1·10^3 Pa·s), the fluid viscosity can be determined.

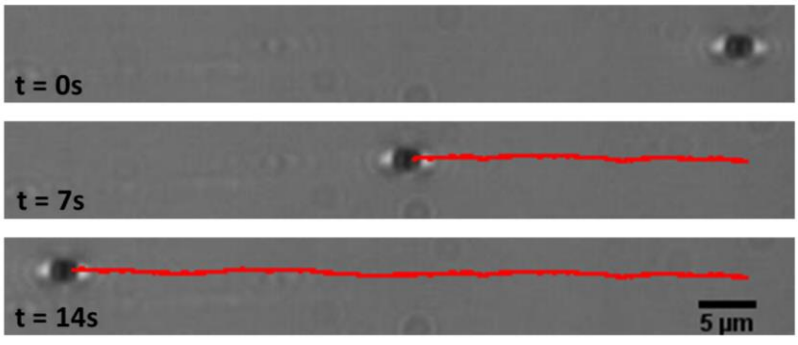

Fig. 51. Particle tracking for viscosity estimation. The viscosity parallel to **n** for the NLC MLC-7029 is estimated to be $\eta^{\parallel}_{NLC} \approx 1.4 \cdot 10^3$ Pa·s. $\eta^{\parallel}_{NLC}$ is measured by the velocities ratio in both water and the aligned NLC.

The experimental setup is performed as explained in Section 5.1 and particle velocity is automatically extracted from the micrographs trajectories (**Fig. 51**). The velocities for both directions, the parallel and the perpendicular allow determining the anisotropy viscosity for

the NLC MLC-7029, where viscosities have been estimated using the relation, $v_{H2O} \cdot \eta_{H2O} = v_{NLC} \cdot \eta_{NLC}$. The NLC viscosity relative to water parallel to the director field is estimated to be $\eta_{NLC}^{\parallel} \approx 1.4 \cdot 10^3$ Pa·s and the perpendicular one, $\eta_{NLC}^{\parallel} \approx 3.4 \cdot 10^3$ Pa·s, although this last one is not important in forthcoming sections.

Chapter 3

Single particle transport

1. Introduction

Dispersed colloids perform random motion, which arises from the thermal fluctuations of the solvent where they reside. Typically, this leads to normal diffusion, evidenced as a linear growth with time of the mean square displacement. This behaviour is not always satisfied, and it often breaks down, when involving structurally complex fluids. Anomalies deviating from normal diffusion can feature either subdiffusion (sublinear growth) when diffusion occurs in a crowded environment ([149]) or superdiffusion (superlinear growth) where the fluctuations are made more persistent by the surrounding medium ([150]) (see Chapter1, section 2.4).

When colloids are dispersed in fluids featuring some degree of orientational order, such as NLCs, Brownian motion is anisotropic ([44], [68]). Moreover, the surface properties of the dispersed colloids determine the LC configuration around the inclusions, which can also lead to anomalous diffusive behaviour at short time scales. These complex behaviours arises due to fluctuations in the near-field orientational order of the LC-inclusion interface ([69], [70]) (see Chapter 1, sections 2.1 and 2.4).

Understanding the physics of microswimming has raised recent interest, either when referring to living species or to artificially engineered particles. Earlier studies have addressed the specific characteristic of complex fluids during the motion of active or driven inclusions ([151], [152]). In particular, simulations of active point particles ([153],[154]) moving in an anisotropic liquid show that the swimmers feature a superdiffusive behaviour for the transversal fluctuations with respect to the far-field director. Note that these simulations only take into account the long-range NLC fluctuations. In experiments, however, this result cannot be separated from the intrinsic distortions caused by the inclusions on the NLC matrix, which induces topological defects at particles apexes and alter the diffusion behaviour in Brownian particles ([69]). Thus, the deformation modes of the elastic matrix around the colloid are likely to play a role in active or driven scenarios.

In this Chapter 3, two kinds of experiments based on single particle transport in NLCs are presented. In the simpler case, colloidal particles are put into motion by means of sedimentation-diffusion experiments. These experiments allow investigating the relationship between the diffusive transport and the LC structure around the driven particles. On the other hand, propulsion has also been achieved, from a disparate driving scenario, by means of LCEEK, where colloids are phoretically propelled. From both scenarios, the motion parallel and perpendicular to the director field have been studied. Superdiffusive behaviour perpendicular to **n** is observed depending on the boundary condition at the motile inclusion surface. More precisely, this behaviour has been observed for dipolar, point defect-hedgehog configurations. From these observations, a mechanism for superdiffusion related to the backflow pattern (puller) around the particles is proposed, and show that the reported behaviour does not depend on the propulsion mode for equal nematic configurations around inclusions. Going further, one can relate the change of the anomalous diffusion exponent with temperature and particle size to the amplitude and persistence of orientational fluctuations around the colloid, which can be estimated from material parameters and from the measured geometry of topological defects around the inclusions.

2. Experimental setup, materials and methods

The experimental NLC cells constructed for the two driving mechanisms show common features although sedimentation-diffusion experiments are performed in a simpler manner.

The experimental cells are prepared as explained in Chapter 2, Section 1. For sedimentation experiments the cell consists of two coated glass slides, while for phoretic experiments the glass slides feature a thin transparent electrode coating the inner size of the LC cell plates. For all experiments, regardless of the driving mechanism, the cell gap thickness is of 15±2 μm and all the substrates are coated with the polyimide compound Nissan 0825 that provide planar anchoring conditions, and after rubbing, an aligned homogenous far-field (see Chapter 2, Section 3.3).

Silica spherical particles of diameter 5 and 10 μm are used as colloidal inclusions. Homeotropic anchoring at the colloid – LC interface, giving rise to single dipolar hyperbolic hedgehog defects, are promoted using specific coating protocols depending on particle size, as explained in Chapter 2, Section 4.2. In contrast, plain, non-functionalized particles, favouring planar anchoring, induce quadrupolar distortions in the form of dual surface point defects (boojums).

The NLC used is CCN-37, which presents negative dielectric anisotropy (ε_a= –5.4 at 1 KHz), and a nematic – isotropic transition temperature $T_{NI} \approx 55^{\circ}C$ (see Chapter 2, Section 4.1).

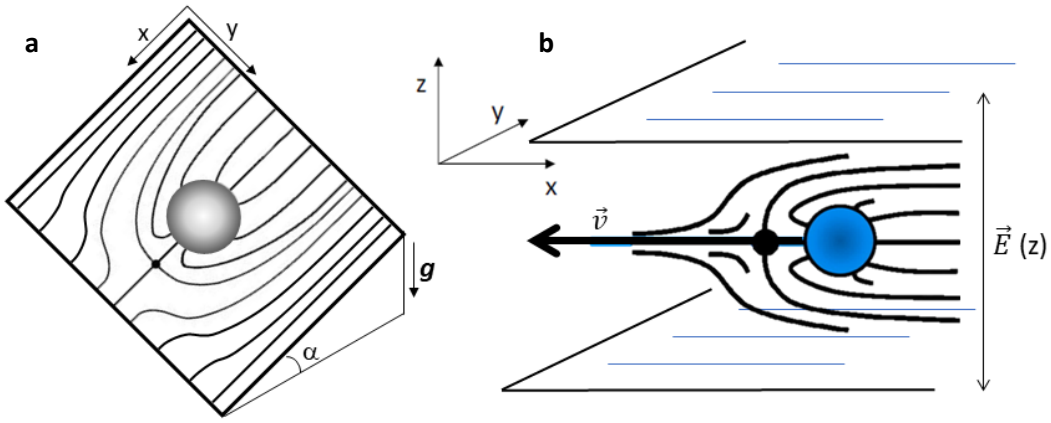

Fig. 52. Schematical diagram of the experimental systems allowing single particle transport. a) Sedimentation of a particle with dipolar LC configuration. **b)** Particle electrokinetically-driven featuring a dipolar defect. The applied electric field is perpendicular to the confining plates although particle motion is induced on the x/y plane. In both geometries, the NLC far-field is homogenous in the x direction and silica spherical particles of two different sizes (5 and 10 μm) have been used.

For sedimentation experiments, the sample is tilted an angle α = 8.5° with respect to the horizontal, so that particle velocity is parallel to the LC far-field and to the driving force. The experimental system used is depicted in **Fig. 52a**. In the alternative scenario, colloidal driving is induced through the well-known Liquid Crystal-Enabled Elektrokinetik (LCEEK) mechanism (see Chapter 1, Section 4.2.2). Notice that plain, non-functionalized silica particles are not a choice here. The quadrupolar distortions around the inclusions and, thus, the generated quadrupolar flows result on a symmetric pumping of the fluid and no propulsion is observed. In contrast, particles with dipolar distortion are propelled along the far-field director after

application of an alternating electric field perpendicular to the plates. In this case, the colloidal motion arises from uncompensated electro-osmotic flows permanently induced around the inclusions. Although particle speed depends on the amplitude and frequency of the applied field, the AC frequency has been specifically chosen for each particle size (10 Hz for 5 µm and 50 Hz for 10 µm) to achieve comparable speeds. In this experimental configuration, where the plates impose a homogenous far-field and the NLC presents a negative dielectric anisotropy, out-of-plane fluctuations of the director are largely supressed by the imposed electric field (**Fig. 52b**). In other words, NLC bulk reorientation is prevented by the experimental geometry.

Experiments in a well-defined range of temperatures have been performed for both sedimentation and LCEEK driving mechanisms. The temperature is expressed as $T - T_{NI}$ where T denotes the working temperature and T_{NI} the nematic – isotropic transition temperature. For this purpose, the cells are placed in a custom-build aluminium enclosure to ensure sample thermalization (see Chapter 2, Section 5.3).

The position of the centroid of moving particles is tracked automatically, using the open source software ImageJ, from micrographs acquired at rate of 1fps for sedimenting particles and 15 fps for particles driven under LCEEK, using a Nikon Eclipse 50 iPol POM and observed under an x40 objective (see Chapter 2, Section 6.1). From the trajectories, we compute the mean displacement along the far-field director, $\langle \Delta r^{\parallel}(\tau) \rangle = \langle r^{\parallel}(t+\tau) - r^{\parallel}(t) \rangle$, and the mean square displacement in the perpendicular direction, $\langle (\Delta r^{\perp}(\tau))^2 \rangle = \left\langle \left[r^{\perp}(t+\tau) - r^{\perp}(t) \right]^2 \right\rangle$, where $\langle \dots \rangle$ denotes an average over time windows of width τ (see Chapter 2, Section 8.1).

3. Results

To better encompass this section, the obtained results has been classified depending on the nematic configuration around the inclusions (dipolar or quadrupolar).

3.1. Dipolar configuration

The first experimental results are those related to the sedimentation-diffusion of 5 µm particles with dipolar, point defect-hedgehog, NLC distortions (**Fig. 53**) (see also complementary videos attached at the Multimedia Content). The trajectories performed by the motile colloids are at least of 100 µm long (**Fig. 53a**). The latter allows to resolve the diffusive scaling on time windows that span between the time needed for the particle to travel its own size and that needed to travel a distance equal to the cell thickness gap. As could be expected, particle motion along the far-field director is essentially ballistic, with speeds of order 0.1 $\mu m \cdot s^{-1}$ (**Fig. 53b**). On the other hand, for the analysis shown in **Fig. 53** performed at $T-T_{NI} = -27.5^{o}C$ ($T \approx 27.5^{o}C$), displacements perpendicular to the far-field director yields a superdiffusive behaviour with an exponent $\nu \approx 1.4$ for the transversal fluctuations (**Fig. 53c**).

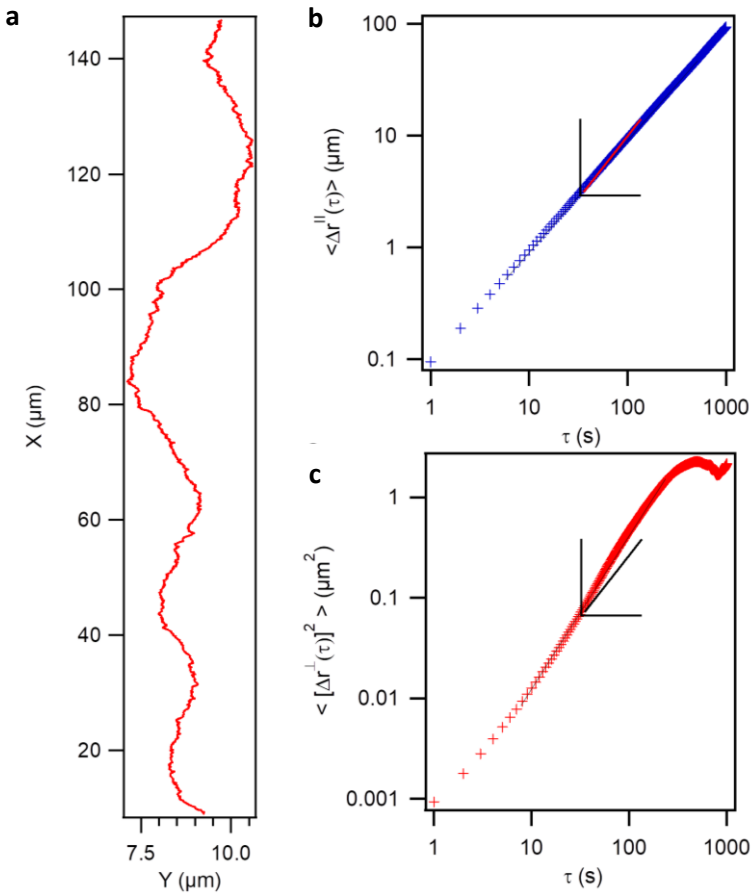

Fig. 53. Sedimentation of a 5 µm particle featuring dipolar LC configuration. a) Particle trajectory in the x/y plane at $T - T_{NI} = -27.5^{o}C$. **b)** Mean displacement parallel to the director field vs. time, showing a ballistic trend, with a velocity, $v \approx 0.10 \pm 0.01$ $\mu m \cdot s^{-1}$. The inset plot denotes a linear fit. **c)** Mean square displacement for the motion perpendicular to the director field. The solid line is a power law fit that yields an exponent $\nu = 1.41 \pm 0.04$. The inset plot denotes a pure diffusive regime with exponent $\nu = 1$. See **Video3**.

Similar superdiffusive behaviour has been found for another set of sedimentation-diffusion experiments performed with 10 µm silica particles, which also feature dipolar LC configuration. For these larger particles, the obtained values of the evaluated exponents are notoriously larger (see **Fig. 54a**), singularly at the smallest temperatures investigated. Moreover, the differences due to particle size vanish at high temperatures (still-below the NI transition), and extracted ν values approach $\nu \approx 1.8$ (see **Fig. 54a**).

Larger particles sediment at larger speed, thus, this parameter could play a role on the diffusive scaling. However, we tend to believe that this parameter has a minor influence on the transversal fluctuations, as shown below for particles driven under LCEEK mechanism (**Fig. 54b**).

Benchmark experiments (see Chapter 2, section 8.1), using the same sedimenting particles, have been performed to test the tracking routines. The experiments consisted on replacing the LC with a mixture of water and glycerol to match the viscosity of the LC at room temperature. As expected motion along the driving force is ballistic, while for the perpendicular direction, the MSD analysis yields to the normal diffusive behaviour $\nu \approx 1.0$ (see Chapter 2, section 8.1, **Fig. 50**).

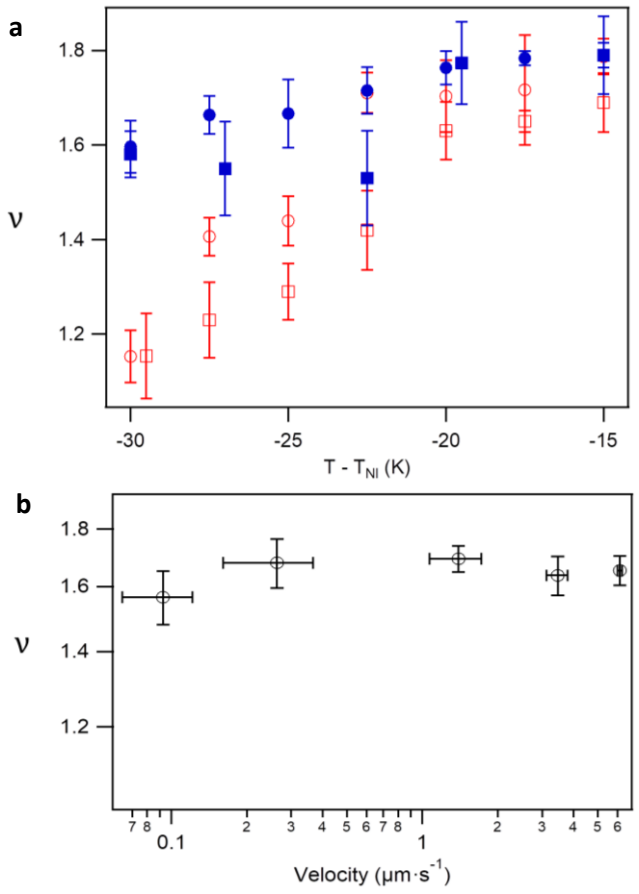

Fig. 54. (a) Temperature dependence of the superdiffusive exponent in the transversal fluctuations of nematic colloids featuring a dipolar configuration for the two different driving mechanisms. Particles diameters are 5 µm (red, empty symbols) and 10 µm (blue, solid symbols), and driving mechanisms are sedimentation (○) and LCEEK (□). **(b)** Exponents (ν) versus speed at $T-T_{NI}= -20^{o}C$ for 5 µm electrokinetically-driven particles featuring a dipolar defect. Different speeds are achieved by tuning the electric field amplitude with a constant frequency of 10 Hz. Error bars indicate the standard deviation over different experimental realizations. See **Video4**.

From another disparate driving scenario, LCEEK-driven particles have also been investigated in a similar way, varying both particle size and temperature. In these experiments, results for perpendicular displacements show analogous superdiffusion trends for both particle size and temperature (**Fig. 54a**). As expected, motion along the far-field is essentially ballistic although with more than one order of magnitude larger ballistic speeds, when compared to sedimenting experiments. For instance, for experiments performed with the smaller particles, the applied electric field has been tuned for each investigated temperature in such a way that the speed of colloidal motion is kept constant, $v \sim 1\ \mu m \cdot s^{-1}$, although we verified that the ballistic speed does not influence the superdiffusive behaviour in the range of speeds in our experiments (**Fig. 54b**).

Another interesting experimental measurement consists on rotating the cell so that the far-field nematic director is perpendicular to the driving force (**Fig. 55**). This scenario cannot be achieved under LCEEK forcing since particle propulsion is only achieved along the local nematic director. The particle motion along the driving force shows a ballistic trend although velocities are lower compared to the experiments where the forcing and the far-field director are parallel aligned. Here, the transversal viscosity is larger than the parallel one.

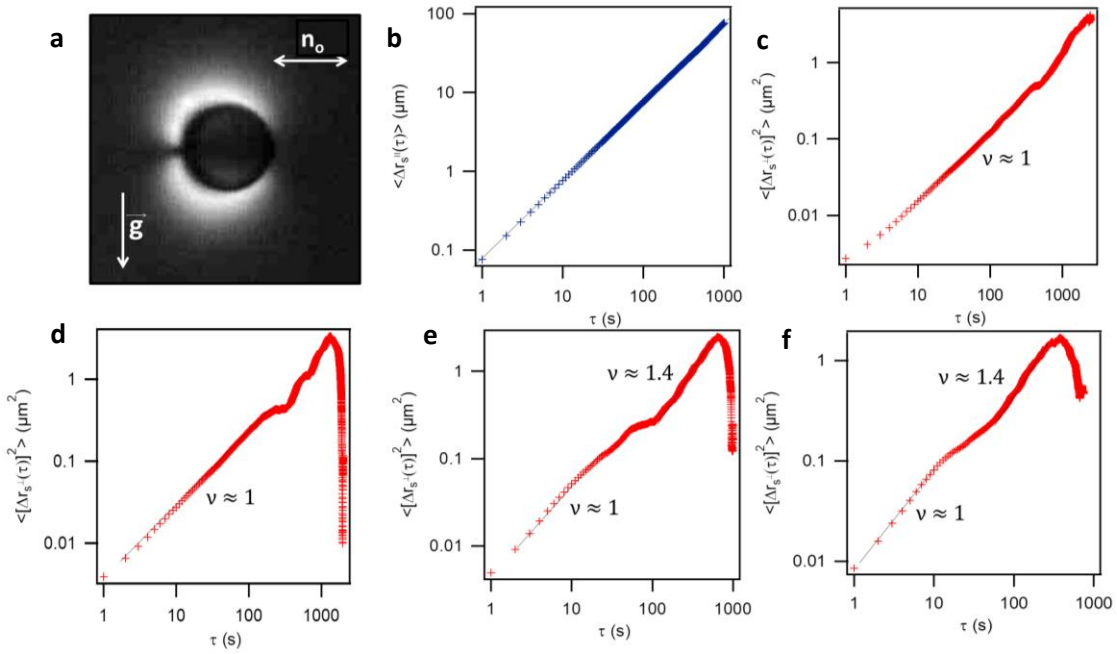

Fig. 55. Dipolar colloid motion perpendicular to the nematic director field. a) Representation of the experimental geometry where the driving force, g, is perpendicular to the nematic far-field director. **b)** Mean displacement parallel to the driving force (thus, perpendicular to the nematic director) vs. time, showing a ballistic trend, with a velocity, $v \approx 0.08 \pm 0.01\ \mu m \cdot s^{-1}$ for an experiment performed at $T - T_{NI} = -25^{o}C$. **c) – f)** Mean square displacement for the motion perpendicular to the director field vs. time for experiments performed at different temperatures, **c)** $T - T_{NI} = -30^{o}C$ **d)** $T - T_{NI} = -25^{o}C$, **e)** $T - T_{NI} = -15^{o}C$ and **f)** $T - T_{NI} = -5^{o}C$. The solid line is a power law fit that yields an exponent $\nu \approx 1.0$ for **c)** and **d)**. In contrast, **e)** and **f)** feature a transition between a diffusive $\nu \approx 1.0$ and a superdiffusive $\nu \approx 1.4$ behavior for the larger temperatures studied.

Interestingly, a transition between a diffusive and a superdiffusive behaviour is observed for the transversal displacements when increasing the system temperature. This roughly coincides with the time needed for the particle to travel its own size and that needed to

travel a distance equal to the cell thickness gap, which actually are two time scales that can define the dynamics of the system ([155]) (**Fig. 55c-f**).

3.2. Quadrupolar configuration

The particle surface allows addressing the influence of the LC distortions around the particles. Another set of sedimentation experiments has been performed, but now replacing the functionalized colloids by bare, non-functionalized particles. The non-coated particles induce planar anchoring, and thus, a quadrupolar configuration of **n** around the inclusion in form of two surface point defects (boojums) (**Fig. 56a**). As commented above, LCEEK is not a choice here due to the absence of symmetry breaking, which impedes this type of driven motion. The results obtained for this nematic configuration are shown in **Fig. 56**. As expected, the motion along the far-field follows a ballistic trend, as observed for dipolar configurations (**Fig. 56c**). In contrast, and compared to the case of dipolar configurations, exponents are now markedly smaller for the diffusive modes perpendicular to **n**, and they barely differ from normal diffusion (**Fig. 56e**). This conclusion applies to the whole range of temperatures investigated.

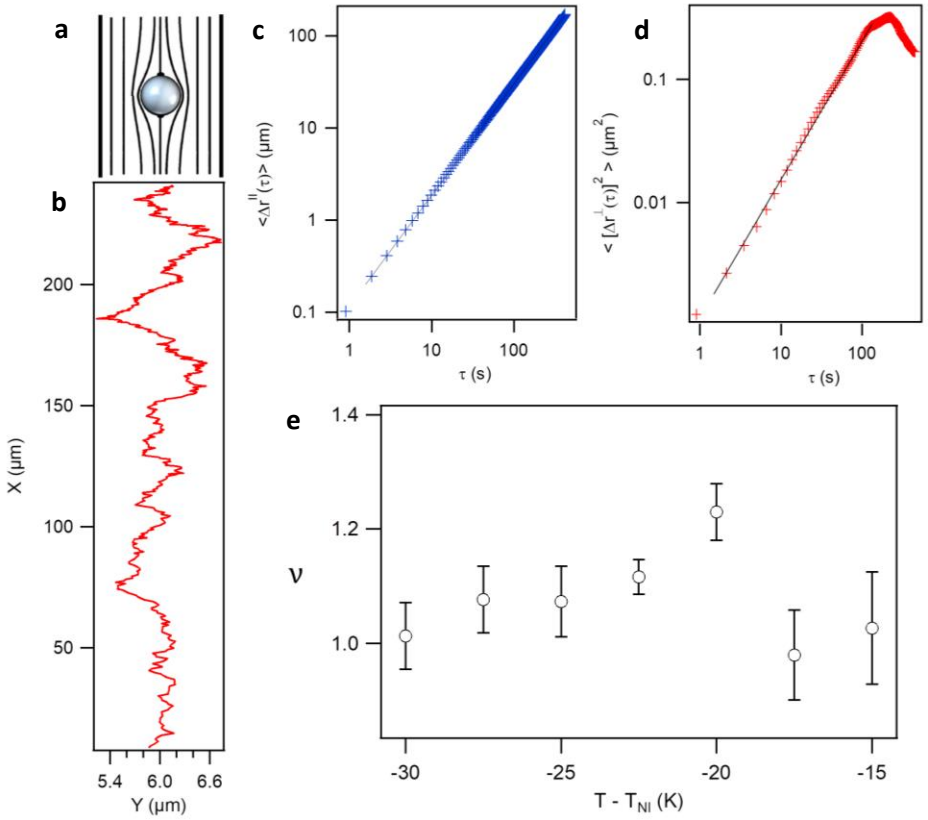

Fig. 56. Sedimentation of a 5 µm particle featuring quadrupolar LC configuration. a) Sketch of the LC configuration around the inclusion. **b)** Particle trajectory in the x/y plane at $T-T_{NI}= -17.5^{o}C$. **c)** Mean displacement vs. time, for the motion parallel to **n**, showing a ballistic trend with $\nu \approx 0.40 \pm 0.02\ \mu m \cdot s^{-1}$. **d)** Mean square displacement for the transversal direction with respect to **n** vs. time. The solid line is a power law fit that yields an exponent $\nu = 1.0 \pm 0.1$. **e)** Temperature dependence of the nearly diffusive exponent in the transversal fluctuations. Error bars indicate the standard deviation over different experimental realizations. See **Video5**.

4. Discussion

In order to analyse the single particle diffusive transport, we will separate the two main results of the reported experiments based on, I) The relationship between the diffusive particle transport and the LC configuration around the driven nematic colloid, and, II) the origin and temperature dependence of the superdiffusive behaviour for particles featuring dipolar configurations.

This discussion is better framed by first comparing the different transport mechanisms that are involved in particle motion. Thermal fluctuations drive both anisotropic Brownian motion, with an intrinsic length scale $\tau_{diff} \sim \frac{R^2}{D}$, and random orientational fluctuations at the particle – LC interface, evolving at a time scale $\tau_{reor} \sim \frac{\gamma R^2}{K}$. Here R is the radius of the spherical particles, γ is the LC rotational viscosity and, D and K, are respectively, the average diffusion coefficient and the LC elastic constant, neglecting anisotropic effects. Typically, for micron-sized particles and commonly employed NLCs, $\tau_{diff} \gg \tau_{reor}$. Thus at large times, anisotropic Brownian motion predominates, while at time scales on the order of seconds, molecular reorientations of the nematic director around the inclusion leads to anomalous diffusive behaviours depending on the anchoring conditions of the NLC at the colloid surface ([69]). Another important time scale is provided by the advection time on both Brownian and driven colloids. In Brownian colloids, the advection time can be estimated as the time needed for the fluid to fill the void left by the small particle displacements, $\tau_a \sim \frac{\rho d^2}{\eta} \sim 10^{-6}$ s. Here, ρ is the density and η the viscosity of the fluid, and d, which is of the order of R, is the distance travelled for the fluid to fill the void left for the displaced particle. These estimations results in a situation where particle "advection" occurs really fast, meaning that hydrodynamics does not play a role, while director fluctuations are the mechanism promoting anomalous diffusive behaviours in nematic Brownian colloids.

Transport mechanism	Time scale	BROWNIAN colloid	MOTILE colloid
Brownian motion	$\tau_{diff} \sim \frac{R^2}{D}$	~10^4 s	~10^4 s
Director reorientations (LC-particle interface)	$\tau_{reor} \sim \frac{\gamma R^2}{K}$	~10^{-1}-10^1 s	~10^{-1}-10^1 s
Particle motion (advection)	$\tau_a \sim \frac{\rho d^2}{\eta}$ or $\tau_{adv} \sim \frac{R}{V_0}$	~ 10^{-6} s	~10^1-10^3 s
Estimated Ericksen number	$E_r = \frac{\tau_{reor}}{\tau_{adv}}$	-	~ 1 – 10^{-4} s

Table 2. Summary of the different time scales involved in nematic colloidal transport mechanisms. Data for the case of Brownian colloids has been extracted from Ref. ([69]). In the case of driven or motile colloids dispersed in CCN-37, γ is in the range 4 – 8 Pa · s, K is in the range 6 – 10 pN (see Chapter 2, Section 4.1), and our experiments feature speeds in the range 0.02 – 2 µm · s^{-1}.

For driven colloids, random displacements and orientational fluctuations are advected by hydrodynamic flows at a characteristic time scale $\tau_{adv} \sim \frac{R}{V_0}$, with V_0 denoting the colloid speed. Assuming again that τ_{diff} is the largest time scale, the effect of hydrodynamics,

arising from particle motion, on the LC director can be assessed by using the Ericksen number, $E_r = \frac{\tau_{reor}}{\tau_{adv}} \approx \frac{\gamma R V_o}{K}$, which compares viscous and elastic stresses. Large values of the Ericksen number indicate that the director field can be distorted by backflow effects due to particle displacements, while low values assess the importance of orientational distortions on hydrodynamic time scales. Using characteristic values of the whole range of our experimental conditions (see **Table 2**), we obtain $\tau_{reor} \sim 0.1$ s and $\tau_{adv} \sim 10$ s. This result in $E_r \sim 10^{-2}$, indicative that director reorientations are much faster than the other processes at play, namely, τ_{adv}.

When comparing our experiments to those performed on anomalous diffusion in Brownian nematic colloids, we find that the latter are in the complementary regime, with director relaxation being the slowest process and suggesting that the physics of that system should be different from the motile colloids shown here.

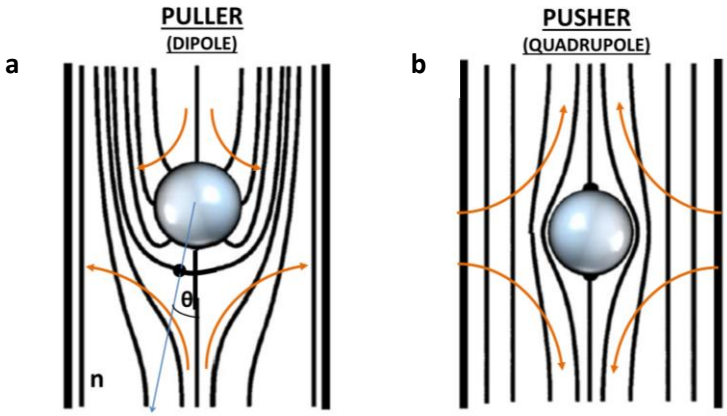

Fig. 57. Backflow patterns advected around coated and bare silica particles. a) Puller-like flows are associated to dipolar LC configurations (homeotropic anchoring), while **b)** pusher-like flows are associated to quadrupolar distortions of the NLC around the inclusion (planar anchoring). The instantaneous particle velocity misalignment with respect to the local director is denoted by the blue arrow and is given by the angle, θ. The flows have been assumed to be the same as that observed for the LCEEK mechanism ([139]).

Based on the discussion above, we conclude that particles in our system move along an essentially frozen nematic orientational field, **n**, within which a colloid may instantaneously misalign its direction of motion in a random manner. Such framework fits within the assumptions of both Lintuvuori et al. ([156]) and Daddi-Moussa-Ider. et al. ([157]). These authors argue that the misaligned director configuration is affected by a torque $f \propto V_o R^2 \sin 2\theta$ ([156]), where θ is the angle between the local director and the instantaneous particle velocity. The sign of f depends on the flow pattern advected around the particles, namely positive for puller-like and negative for pusher-like flows (**Fig. 57**). Although such backflow patterns have not yet been established in the case of sedimenting colloids, they have been measured for LCEEK-driven colloids ([139]), showing that for homeotropic anchoring displaying dipolar configuration the flow is puller-like (**Fig. 57a**) while it is pusher-like for quadrupolar configurations featuring tangential anchoring (double-boojums) (**Fig. 57b**). As a result, we can conclude that the nematic torque would tend to keep the particles aligned with the far-field direction for quadrupolar distortions, while, contrarily, it enhances misalignment for dipolar distortions, and thus, it might promote superdiffusive behaviour in the latter case, consistently with the experimental observations.

The role on the superdiffusive behaviour of the torque exerted on the misaligned director can be further demonstrated with the arguments raised by Bruno et al., and Despósito et al. ([158], [159]). In this case, for transport in active complex media, the instantaneous particle motion perpendicular to **n** is considered to obey a Langevin-like differential equation,

$$\gamma \frac{dr^{\perp}(t)}{dt} = f(t) + \xi(t),$$

which expresses the balance between the friction drag, with γ being the rotational viscosity, and two stochastic forces that operate on the particles. On the one hand, $\xi(t)$ represents the internal noise effects of thermal origin, for which a zero-mean white noise statistics is assumed. On the other hand, $f(t)$ introduces a source of stochasticity associated to the specific inherent dynamics of the nematic colloid. The latter can be associated to the random kicks arising from the transient misalignment of the instantaneous particle velocity with respect to the far-field nematic director. According to our arguments above, $f(t)$ will be proportional to the exerted torque, and thus to $\sin 2\theta\,(t)$. The temporal fluctuations of this torque are accessible in our experiments by monitoring the position of the point defect-hedgehog distortion. Actually, the latter can only be reliably assessed for the 10μm particles, for which we have measured the defect distance to the particle surface, d (which is a function of T and R) and its orientation $\theta(t)$ (**Fig. 58**).

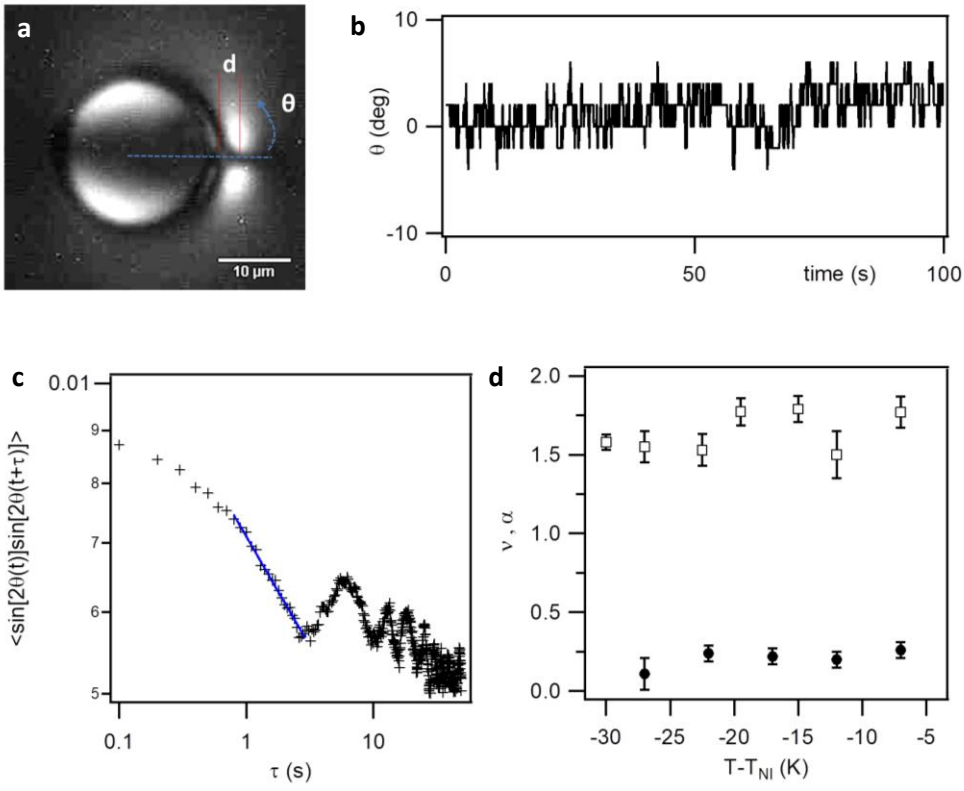

Fig. 58. Analysis of the orientational fluctuations for the dipolar configuration. a) Position, *d*, and relative orientation, θ, of the point defect-hedgehog for a particle of diameter 20 μm, observed between crossed polarizers in a cell of thickness 25 μm. The scale bar is 10 μm. **b)** Defect orientation with respect to the horizontal LC far-field as a function of time for a particle of diameter 10 μm under electrokinetic drive at $T-T_{NI}= -15^{o}C$. **c)** Autocorrelation of the driving torque, $f \propto \sin 2\theta\,(t)$, for the data in **b)**. The solid line is a power law fit to $< f(t)f(t+\tau) > \sim\tau^{-\alpha}$, with α = 0.22. **d)** Exponent of the mean square displacement, ν (□), and force autocorrelation, α(○), as a function of temperature, for 10 μm particles under electrokinetic drive.

From these data, the statistical properties of $f(t)$ are obtained, in particular its time autocorrelation, $\langle f(t)f(t+\tau)\rangle = \Lambda(|\tau|) \propto \langle \sin(2\theta(t))\sin(2\theta(t+\tau))\rangle$. Experimentally, we find that our data are compatible with a scaling of the type $\Lambda(\tau) \propto \Lambda_o(\tau/\tau_0)^{-\alpha}$. Here, Λ_o measures the intensity of the intrinsic orientational fluctuations, and the positive exponent α, according to our measurements, stays bounded and lower than unity, *i.e.*, 0 < α < 1 (**Fig. 58c,d**). The same authors, Despósito *et al.*, argue that under these circumstances, the mean square displacement associated to the generalized Langevin equation reads ([158], [159]),

$$MSD\ (\tau) = \langle [\Delta r^{\perp}(\tau)]^2 \rangle = \frac{2K_BT}{\gamma}\left[\left(\frac{\tau}{\tau_o}\right) + \epsilon\kappa_{1,\alpha}\left(\frac{\tau}{\tau_o}\right)^{2-\alpha}\right],$$

where $\kappa_{1,\alpha}$ is a positive numerical factor, and ϵ, denotes a dimensionless ratio between the two acting random forces. For α smaller than unity, the first purely diffusive contribution is subdominant in front of the superdiffusive term with exponent $2-\alpha$, so one should expect $\langle [\Delta r^{\perp}(\tau)]^2 \rangle \sim \tau^{2-\alpha}$ in the presence of superdiffusion in the transversal particle motion. When comparing ν, the transversal superdiffusion exponent, (see **Fig. 54**) with α, our results are consistent, within error bars, with the prediction $\alpha + \nu = 2$, specially in the high temperature range (**Fig. 58d**).

The analysis above proves that the observed superdiffusive behaviour is the result of the persistence in the misalignment of the dipolar director field surrounding the particles. However, it does not explain the observed increase in the superdiffusive exponent with particle size and with temperature. Thus, we finally interpret, in a qualitative way, the observed trends of the anomalous exponents (superdiffusion) when changing both colloid radius and temperature. We propose a way to estimate the strength of this effect by looking at the intensity of in-plane director fluctuations $< (\delta\hat{n})^2 >$ with respect to a Boltzmann factor (K_BT). By inverse Fourier transforming the director correlation function under the one-constant approximation, this ratio is expressed as ([2]),

$$\frac{< (\delta\hat{n})^2 >}{(K_BT)} \propto \frac{1}{K\ h}\int \frac{d\boldsymbol{q}}{q^2} \backsimeq \frac{1}{K\ h}\int_{\delta^{-1}}^{l^{-1}} \frac{dq}{q} = \frac{1}{K\ h} ln\frac{\delta}{l},$$

where h stands for the cell thickness, $\delta\ (R)$ is taken as the length over which orientational fluctuations spread around a colloid of radius R, in other words, the distortion caused by the inclusion, and l is a cut-off setting the minimum length-scale that justifies the continuum description of the nematic elasticity. This calculation yields to $\nu \sim \ln(\delta)/K$, which depends implicitly on temperature through both, δ and K. We assume δ to be proportional to the extension of the point defect-hedgehog located at one of the particles sides, d (**Fig. 58a** and **Fig. 59a**), which we observe to increase with temperature (**Fig. 59c**). Using the temperature dependence of K shown in Chapter 2, Section 4.1, we find that the trend experimentally observed for ν is consistent with the above theoretical prediction (see **Fig. 59d,e**). Within this same framework, the observation that ν is consistently larger for larger particles (**Fig. 55**) can be justified by the well-known fact that the range of LC distortions around the colloid is proportional to the inclusion size ([39]).

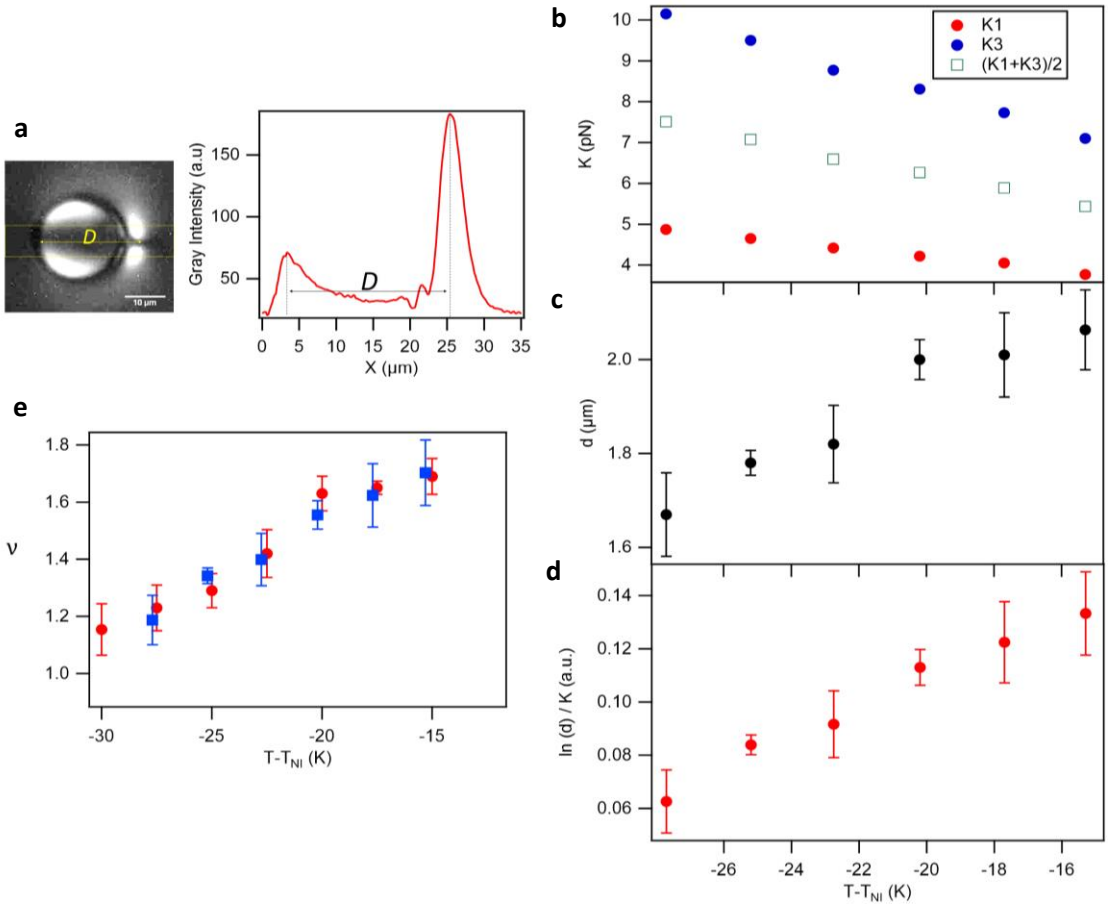

Fig. 59. Scaling arguments for the temperature dependent superdiffusive behaviour. (a) The distance from the defect to the particle surface is determined from the grayscale profile in a thick band along the diameter of the particle. Under these imaging conditions, the position of the defect core results in a maximum average intensity, while the locations across the particle diameter exhibits another local maximum intensity. **(b)** Temperature dependence of the splay (K1) and bend (K3) elastic constants of CCN-37 ([147]). For the single constant approximation we use the arithmetic mean of K1 and K3. **(c)** Change with temperature of the distance between the particle surface, d, and the defect for a dipolar distortion of a 20 μm silica particle dispersed in a cell with thickness gap ~25 μm. **(d)** Computed temperature evolution of the scaling prediction for the anomalous diffusive exponent, $\upsilon \sim \ln(\delta)/K$. **(e)** Temperature variation of the superdiffusive exponent for a phoretic 5 μm particle with dipolar LC configuration (◯) and estimation of our scaling prediction (□). The model is fitted to the data by means of a linear transformation.

5. Open questions and future perspectives

From experiments performed and related to this Chapter 3, new phenomena in nematic colloids physics emerged, such as the oscillation of perfect quadrupolar Saturn-Ring defects or the propulsion of the same distorted configuration under the LCEEK mechanism, even transition between defects have also been observed.

5.1. Experimental system

The NLC cell setup is the same as shown in Section2. In this case, 10 µm silica spherical particles featuring homeotropic anchoring promoted the quadrupolar Saturn-Rings distortions around the inclusions. The SR disclination line appears in a plane perpendicular to the far-field alignment direction of the LC. POM has been used to monitor the dynamics of the defect, but also particle translation.

The applied electric field has been in the range of 0.3 - 0.8 $V \cdot \mu m^{-1}$ with a fixed frequency, f = 50 Hz (except in experiments where the experimental AC conditions are detailed).

All the experiments have been performed above $T-T_{NI} = -10^{o}C$, thus, not far from the nematic/isotropic temperature transition.

5.2. Oscillating Saturn Rings

The experiments shown here feature a constant input of electric energy which promotes the system out of equilibrium. Apart from driving motion, the AC allows for the appearance of distorted configurations of the quadrupolar Saturn Ring, which, at a certain point, starts to oscillate around the inclusion (**Fig. 60**).

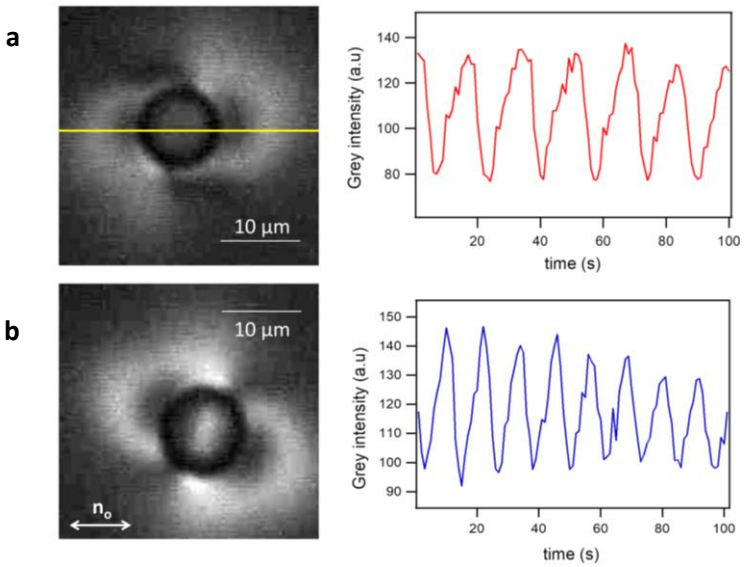

Fig. 60. Periodically oscillating Saturn-Rings. (**a** and **b**) Two micrographs obtained between crossed polarizers showing different oscillating modes of the dynamic defects while an AC field of 0.5 $V \cdot \mu m^{-1}$ with a fixed frequency of **a)** 50 Hz **b)** 60 Hz is being applied. The plot shows the average grey scale intensity versus time evidencing the oscillation periodicity (see also **Videos6a,b**). In this experiment $T-T_{NI} = -5^{o}C$. The far-field director is depicted in the micrographs. The yellow line denotes the dynamical defect tracking in terms of grey intensity.

When the system's temperature is increased, material properties are affected, mostly elasticity and anchoring conditions, which can lead to dynamical defects under energetic supply (**Fig. 60**). The observed SR oscillations are very stable and regular as the energy is constantly controlled by the AC electric field. Different modes of oscillation have been observed for different driving frequencies, 50 and 60Hz (**Fig. 60a,b**). For defect characterization, a line tracing the particles equator allow to monitor the mean grey intensities although an accurate quantitative analysis requires a more detailed monitoring of the defects dynamics (The images captured per second does not allow to characterize the frequency and period of the SRs oscillations) (**Fig. 60**).

The structure of the deformation modes is supposed to be controlled by the balance between anchoring strength and material properties. This case is reminiscent to the active nematic emulsions one displaying the same SR deformation ([160]), where the dynamic behaviour is determined, somehow, by the activity, and where the geometrical rearrangements of the topological defects also plays a role.

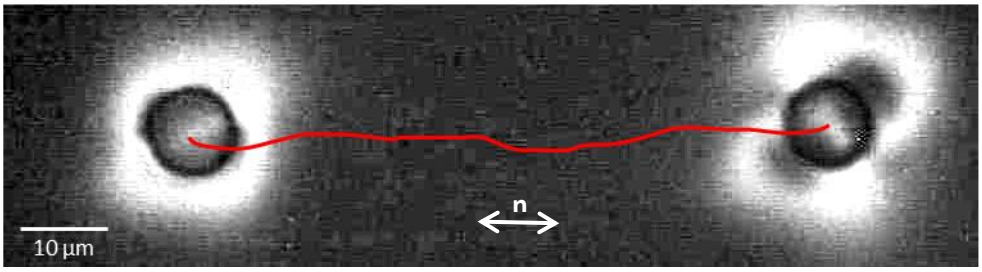

Fig. 61. Motion of an oscillating SR. Image showing a micrograph sequence with an elapsed time of 135 seconds obtained between crossed polarizers of a translating SR structure. The quadrupolar configuration is transported about 80 µm at a velocity, v = 0.6 ± 0.1 µm · s^{-1}. Experiment performed at $T-T_{NI} = -5^{o}C$. In this experiment the AC field frequency is 40 Hz. See **Video7**.

The transport of the particle with the oscillating SR structure along the far-field nematic director has also been observed (**Fig. 61**). In the latter, the flow patterns related to the distorted structure allow for particle transport. In this experiment the inclusion has been transported a distance of about 80 µm under an AC electric field of amplitude 0.5 V · μm^{-1} with a fixed frequency 40 Hz (**Fig. 61-Video7**).

5.3. Transport of particles with distorted Saturn Rings

Flow patterns advected at particles surface appear from the application of an AC electric field. Perfectly symmetric Saturn-ring configurations lead to quadrupolar distortions where the flow patterns are symmetric, and thus, the pumping fluid around the particles. This leads to no net propulsion as the fore-aft symmetry at both extremes of the particle is not broken. The material properties are affected by temperature, which can lead to the distortion of the quadrupolar structure at temperatures close to the T_{NI}. Thus, unbalancing flow paterns at particle surface can allow for net propulsion.

When temperature is increased in the NLC cell, and under the application of an AC electric field, the SR configuration does not present a perfect quadrupolar symmetry, and thus the flow patterns advected to the particle can result on a net pumping of the fluid (see **Fig. 62**).

The latter induces particle motion along the far-field nematic director. The ballistic velocities achieved by the particles are on the order v = 0.25 ± 0.1 μm · s^{-1}, which are comparable to the case of dipolar configurations in specific conditions (see Section 3).

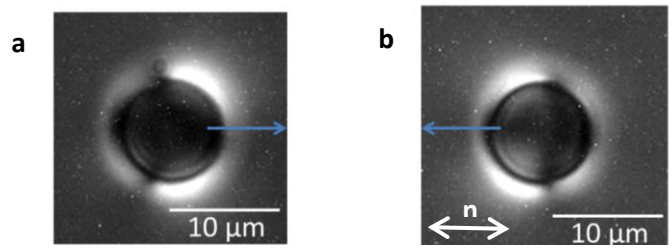

Fig. 62. Transport of inclusions featuring distorted quadrupolar SR configurations. Micrographs of 10 μm silica coated-spherical particles observed between crossed polarizers featuring distorted SR configurations. The distortions in **a)** in **b)** are of contrarily sense (indicated by blue arrows), and thus, the pumped fluid, which drives the particles. See **Videos8a,b**. The amplitude of the AC field is of 0.5 V · μm^{-1} with a fixed frequency f=15Hz for this experiment.

5.4. Transition between topological distortions

At relatively high temperatures, $T–T_{NI}$ = –5°C, and under the application of an external electric field, electro-hydrodynamic instabilities can appear in a NLC cell ([3]). The nucleation points where the instabilities will develop are nematic discontinuities, such as the presence of inclusions. In the latter, the presence of surface inhomogeneities or particle asperity coupled to the out-of-equilibrium nature of the system promotes transitions between topological defects.

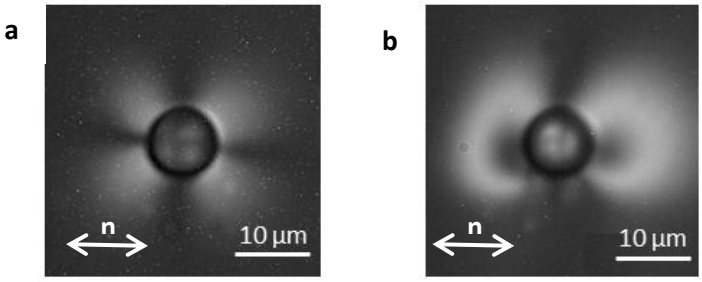

Fig. 63. SR transits to butterfly-like structure. a) Saturn-ring quadrupolar structure observed between crossed polarizers and obtained under an AC electric field of 0.3 V · μm^{-1} and f = 100 Hz. **b)** Butterfly-like structure observed between crossed polarizers and obtained under an AC electric field of 0.8 V · μm^{-1} and f = 100 Hz. See also **Video9**.

In the first set of experiments, increasing the AC amplitude from 0.3 V · μm^{-1} to 0.8 V · μm^{-1} (with a fixed frequency, f=100Hz) leads to the distortion of the initial quadrupolar SR structure to a butterfly-like structure (**Fig. 63**). The latter presents motion perpendicular to the far-field director (See **Fig. 63** and **Video9**). In this configuration, the local nematic director surrounding the particle features a dipolar configuration perpendicular with respect to **n**. Thus, particle propulsion is in that direction, with speeds on the order of v = 80 ± 30 μm · s^{-1}. The achievable speeds are extremely larger when compared to the motion of single point defect-hedgehog or distorted SRs configurations.

The second set of results correspond to the transition between topological defects at a fixed electric field amplitude and frequency, 0.8 V · μm^{-1} and f = 100 Hz. In this case, surface

inhomogeneities and particle asperities coupled to the onset of electrohydrodynamic instabilities can lead to the distortion of the elastic matrix around the inclusion featuring transitions between point defect-hedgehog to Saturn-rings going through the non-common butterfly-like structures.

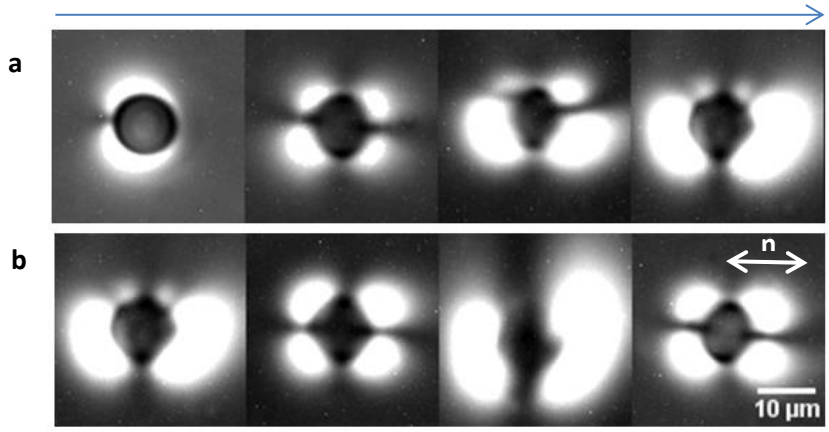

Fig. 64. Transitions between topological distortions of a 10 µm silica-coated particle. a) Transition from a point defect-hedgehog topological distortion to a butterfly-like structure going through the well-known Saturn-Ring. In **b)** the butterfly-like structure transform into the most stable Saturn-Ring configuration. All the micrographs are observed between crossed polarizers. In this experiment the AC electric field is of 0.8 V · μm^{-1} and the frequency f=100Hz. The transition between defects is driven by surface homogeneities or particle asperities. The blue arrow denotes the pass of time.

The motion of the colloid is parallel to **n** for point defect-hedgehog and SRs, which is in contrast to butterfly-like configurations, whose motion is perpendicular to **n**. The achievable speeds range from 20-40 µm · s^{-1} for the typical and well-known configurations (point defect-hedgehog and SRs) and is extremely large for butterfly-like structures, about 100 µm · s^{-1}, where the elastic matrix seems to be more distorted (**Fig. 64**). The transition between structures can be attributed to electrohydrodynamic instabilities in the dispersed colloids.

6. **Conclusions**

In this chapter, we have analysed the anomalous diffusive transport of isolated motile colloids in liquid crystals. To be more specific, we have reported the relationship between the diffusive particle transport and the LC configuration around the driven nematic colloid, but also the origin and temperature dependence of the superdiffusive behaviour for particles featuring dipolar configurations.

- Motion along the far-field director is essentially ballistic in all cases.

- The nematic configuration around the inclusion determines the transversal transport modes with respect to the far-field nematic director, the former being diffusive for quadrupolar distortions and superdiffusive for dipolar distortions.

- All the results obtained seem not to depend significantly on both driving mechanism and colloidal speed.

- The superdiffusive behaviour arises from the persistence of the dipolar configuration misalignment with respect to the nematic director. This observation has been evidenced by measuring the autocorrelation of the point defect-hedgehog orientation in time.

On the other hand, new physical aspects related to out-of-equilibrium colloids dispersed in liquid crystals emerge.

- Increasing temperature in the NLC cells allows the elastic deformation into non common structures, distorted Saturn-Rings.

- These configurations can lead, under the application of an AC electric field, to dynamical defect oscillations, but also to the transport of these inclusions by means of uncompensated ionic flows around the colloid.

- Under the application of an AC electric field the distorted structures can develop transitions between topological distortions, where the butterfly-like structure leads to ballistic transport perpendicular to the far-field director.

Differently from its fundamental interest, the presented scenarios in this chapter points towards the exploration of new phenomena emerging from particles translating in a NLC. The latter allow exploring new modes of dynamic self-assembly. Going further with this idea, the realization of prototypes based on soft matter systems capable to feature micro-motility can also be a good option.

Chapter 4

Colloidal Assemblies

1. Introduction

Colloidal suspensions, either active or artificially-activated, are a flourishing research field in soft condensed matter physics as they allow investigating the non-equilibrium physics of interacting unities across different length scales ([90]-[92]). The interacting entities tend to form coherent structures, and thus, new collective dynamic effects can arise. In such cases, collective effects are difficult to predict based only on the knowledge of the behaviour of the individual particles. In this respect, new physical concepts like giant density fluctuations ([161]) or active crystals ([98]) arises from collective behaviour.

The formation of self-assembled clusters from artificial particles driven by an external field has been recently reported by different research groups who use electric ([50]), magnetic ([115]) or optic fields ([98]). In such cases, the driven particles are dispersed in an isotropic medium, and typically, are propelled through patterned structures or assembled along confinement.

Moreover, an alternative approach that is gaining interest is the use of an anisotropic material, such as a nematic liquid crystal. In the latter, the dispersed particles can be driven by an electric field along predefined tracks ([138], [141], [142], [162]). The use of an anisotropic medium provides different advantages in artificially-activated particle systems. For example, controlling the main molecular orientation of the dispersing medium, either by the action of an external field or imposed by the anchoring conditions at the surface, but also the ability to switch between the different liquid crystalline phases by varying the system temperature, to control the energy supply or to avoid confinements which may alter particle motion due to steric constraints.

In this Chapter we show experiments based on the dynamics of an ensemble of anisometric colloidal particles. The particles are driven under the LCEEK (see Chapter 1, Section 4.2.2) mechanism and are self-assembled into two different configurations, namely aster and rotating-mill. The particle clusters organize around a single localized topological defect, which is generated by means of a photosensitive surface. The latter allows modifying the local director field, and thus, steering the colloidal trajectories. Furthermore, in order to better understand the dynamics of the system, a simple simulation scheme is presented which describes well the observed phenomena.

The work shown in this chapter has been performed in collaboration with Dr. Pietro Tierno and Dr. Arthur Straube, who performed the simulations shown in this chapter.

2. Experimental setup, materials and methods

- EXPERIMENTAL CELL

The experimental NLC cells consist of a colloidal dispersion which is inserted between parallel glass plates coated with a thin ITO transparent electrode. The presence of electrodes allows the application of external electric fields perpendicular to the plates. The plates are glued together with the ITO facing inwards featuring a cell gap thickness of about 20 µm (see Chapter2, Sections 1 and 2). One of the plates is functionalized with a mixture of both photo- and non-photosensitive azosilane compounds, in the form of a self-assembled monolayer, so that azosilane isomerization can be promoted by light irradiation (see Chapter2, Section 3.2 and 6.2). In contrast, the counter-plate is treated with a spin-coated polyimide compound to achieve strong and permanent homeotropic anchoring of the mesogens (see Chapter 1, Section 3.3).

As colloidal inclusions, peanut-shaped microparticles (d_x = 4 µm and d_y = 3 µm) have been chosen. In this case, the anchoring promoted at the particle surface is planar (see Chapter 2, Section 4.2). In the experiments shown in this chapter, particle shape endowed the breaking of the flow symmetry patterns around the particles, which is a requirement for LCEEK mechanism to be effective. The choice of commercial anisometric particles ensures that most of the particles belonging to an ensemble are similarly propelled.

Peanut-shaped particles are dispersed in the NLC MLC-7029 (see Chapter 2, Section 4.1) which features negative dielectric anisotropy. Initially, the homeotropic anchoring conditions at the substrate sets the NLC molecules to be perpendicular to it. After application of an AC electric field between plates, the NLC aligns perpendicular to the applied field, and thus, parallel to the glass plates. This leads to degenerate planar alignment conditions, since all-in plane molecular orientations are energetically equivalent. This feature enables to address locally the nematic director, thanks to the photosensitive surface, where attractor points can be generated in order to accumulate particles.

- IRRADIATON PROTOCOL

In absence of illumination or under white light, the AZO molecules adopt their most stable, elongated *trans* isomeric form, which leads to homeotropic anchoring of the LC molecules on the functionalized surface. Irradiation of the sample with UV-light (360 nm) promotes the transition of the AZO molecules into the bent *cis* form within seconds, which triggers local planar anchoring of the LC. This process can be easily reverted under blue light (465 nm) which recovers the initial *trans* state (see Chapter 2, Section 3.2 and 6.2). Moreover, the irradiation is performed under the microscope objective where the Gaussian intensity profile of the UV beam forces the isomerization of the AZO compound, and thus, LC molecules develop an in-plane radial pattern starting from the centre of the light spot. In this material configuration, the NLC molecules feature a pure splay (radially-spread) texture, which organize around a central defect point (**Fig. 65a**).

The photosensitive surface allows to transform the initial NLC splay (radial) texture into a bend-splay (spiral) texture. This process is achieved by erasing the central region of an

imprinted UV area with a smaller spot of blue light, which enforces the *cis* to *trans* isomerization leading to homeotropic NLC alignment (**Fig. 65b**).

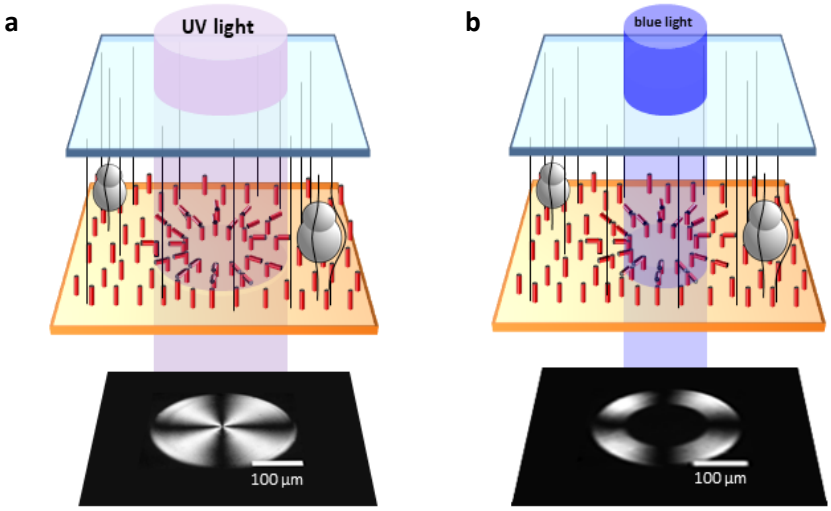

Fig. 65. Scheme illustrating the experimental irradiation protocol. a) Irradiating the sample with UV-light triggers the *trans* (homeotropic) to *cis* (planar) transition of the AZO compound (NLC). The splay texture observed between crossed polarizers is evidenced with a cross-like LC pattern. **b)** Erasing the central region of a UV area previously imprinted, with blue light, enforces the relaxation of the initial configuration to the bend-splay texture. This configuration is revealed by a micrograph between crossed polarizers of a corona.

After inducing the topological defects, which will serve as attractor points for particles to be assembled, the application of an external AC electric field forces the bulk of the NLC to adopt the previously defined splay or bend-splay textures. These configurations extend for few millimeters along the sample, well beyond the size of the irradiated spot.

The capability to switch between underlying patterns allows defining different steering trajectories for the colloids to self-assemble. In our case, pure splay textures define radial patterns emanating from the centre of the topological defect while bend-splay textures follow spiral ones. Thus, particles will self-assemble into an aster or a rotating mill-like cluster.

- SINGLE PARTICLE CHARACTERIZATION

To better understand the mechanism of motion we start by describing the transport properties of an individual anisometric particle. For this purpose, one has to consider the experimental geometry (**Fig. 66a**). In the absence of the AC electric field, the homeotropic anchoring conditions at both plates forces the nematic director to point along the z-axis. Since the NLC features negative dielectric anisotropy, under the applied field, the nematic director orients perpendicular to the external field, say along the xy plane. As the anisometric inclusions align their symmetry axis with the local LC director due to the planar anchoring condition on its surface and LC elasticity, the dispersed particles also align along the nematic director, say along the x-axis.

As commented in Chapter 1, Section 2.1, colloidal particles distort the elastic matrix inducing topological defects around its surface. The polystyrene peanut-shaped particles used in these experiments feature planar anchoring of the LC molecules around them, and display

two point surface defects located at both apexes of the particles, in the form of a "double-boojum" (**Fig. 66b**) (see Chapter1 Section 2.1 and Chapter 2 Section 7.1). In the frequency range 5-40 Hz particles are propelled along the local nematic director due to electroosmotic flows permanently generated around the particles, which are induced by the external AC electric field, with the large lobule of the particles commonly pointing ahead during propulsion.

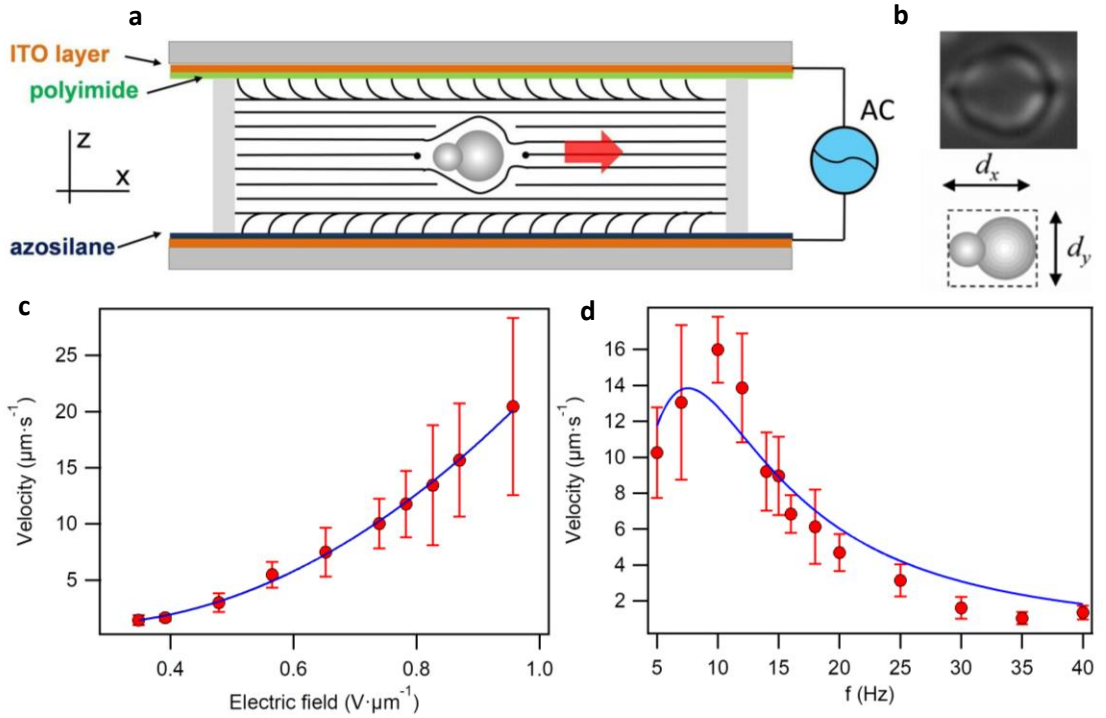

Fig. 66. Single particle transport characterization. a) Schematic of the experimental cell showing one anisometric particle enclosed between two ITO-functionalized plates and dispersed in a NLC of negative dielectric anisotropy. An AC voltage is applied between both plates. **b)** Micrograph between crossed polarizers of an anisometric colloid featuring lateral dimensions d_x = 10.2 μm and d_y = 8.2 μm. **c)** Speed, v_0, versus amplitude, *E*, of the applied electric field for an individual anisometric particle featuring a constant field frequency f = 10Hz. **d)** Speed, v_0, versus frequency, f, of the applied electric field for an individual particle while the amplitude of the sinusoidal AC field is kept at $0.76\,V\cdot\mu m^{-1}$. Scattered points are experimental data, and the continuous red line is a quadratic fit or a non-monotonic function for the amplitude and the frequency of the applied electric field, respectively. Error bars indicate the standard deviation over 10 particles.

In brief, the oscillating AC field generates convection rolls due to ion migration around the inclusions. From these induced vortexes, the flow structure is determined by the LC director configuration around the particles and by the anisotropic ionic mobility. In the absence of perfect quadrupolar symmetry, such as in the presence of anisometric inclusions, this process results in net propulsion, since the fore-aft symmetry of the LC director around the particle is broken (see also Chapter 1, Section 4.2.2). In this case the particles acquire a constant speed v_0. Given the confined geometry, the motion is quasi two-dimensional due to the high viscosity of the NLC medium, although material elasticity may also be important. Furthermore, it is important to notice that effects resulting from the attraction towards the two electrodes are negligible since the AC field is applied perpendicular to the plane of motion.

The particle phoretic speed, v_0, can be controlled by varying the amplitude *E* of the applied AC field, as can be seen in **Fig. 66c**. Here, the dependence of v_0 on *E* is quadratic as one power of E induces the charge separation and the second one drives the resulting ICEO flow (see Chapter 1, Section 4.2.2). In our experiments, the propulsion velocity is independent of the polarity of the applied field, thus enabling the use of AC fields. Moreover, from the fit to the experimental data, we determine the threshold field for motion, $E_0 = 0.16 \pm 0.06\ \mathrm{V} \cdot \mu\mathrm{m}^{-1}$ for a field frequency = 10 Hz (**Fig. 66c**). Or in other words, here, E_0 is the minimum field required to generate enough electroosmotic flow to provide particle propulsion. Furthermore, the velocity dependence on frequency, $v(f)$, is even more complex due to the nature of the ionic motion within the LC (**Fig. 66d**), and is expressed by the formula given in Chapter 1, Section 4.2.2.

$$v(f) = v_o \frac{f^2 {\tau_e}^2}{(1 + f^2 {\tau_c}^2)(1 + f^2 {\tau_e}^2)}$$

Here, f is the frequency of the external AC electric field and τ_c and τ_e are the characteristic charging times of the particles and the electrodes, respectively. From the experimental data of the obtained speed for individual particles at a fixed field amplitude of $0.76\ \mathrm{V} \cdot \mu\mathrm{m}^{-1}$, we can fit the intrinsic time scales that characterizes the LCEEK process, and thus, the time scales involved in the physics of the propulsion, yielding $\tau_c \approx 0.016\ s$ and $\tau_e \approx 0.032\ s$. These two time scales will also be important in the pairwise long-range particle repulsion, as further explained.

- COLLOIDAL TRANSPORT ELASTICALLY – MEDIATED BY BACKFLOW

The experimental NLC cell geometry allows nematic bulk reorientation, and thus, backflow can mediate particle propulsion. Backflow arises near the confining walls where the net flow is nonzero due to molecular reorientation. Note that the configuration shown in this chapter 4 is the complementary to that explained in Chapter 1 Section 4.2.1, where the LC has a positive dielectric anisotropy.

Initially, in the absence of the AC electric field, the homeotropic anchoring conditions at both plates forces the nematic director to point along the z-axis. Since the NLC features negative dielectric anisotropy, under the applied field, the nematic director orients perpendicular to the external field, say along the xy plane. As a consequence, and for the range of frequencies studied, nematic bulk reorientation occurs under the application of an AC electric field. Thus, the director field is able to bend inducing a net flow to the overall fluid. To account for this effect, LCEEK and backflow-mediated transport can be decoupled by means of a high frequency carrier wave (1 KHz). In this case, ions remain immobile, and phoretic effects are negligible, while nematic bulk reorientation is let to occur at a lower frequency. Tests have been performed at constant field amplitude of $0.76\ \mathrm{V} \cdot \mu\mathrm{m}^{-1}$ with different modulating frequencies, 10, 20 and 100 Hz, displaying no appreciable differences.

In our experiments we have checked the particle speed for both transport mechanisms, nematic bulk reorientation ($v_0 = 0.1\ \pm 0.05\ \mu\mathrm{m} \cdot \mathrm{s}^{-1}$) and LCEEK ($v_0 = 10\ \pm 10\ \mu\mathrm{m} \cdot \mathrm{s}^{-1}$). The latter feature speeds more than two orders of magnitude larger, thus, the backflow-

mediated colloidal transport due to bulk reorientation of the material is insignificant in our experimental system. For a better comparison with the LCEEK mechanism see **Video10**.

3. Results and discussion

To better encompass the discussion based on colloidal assemblies, the explanations and data presented in this Section 3 is split as follows. Initially, we will present experiments, data treatment and discussion based on two different colloidal assemblies: aster and rotating mill. Afterwards, we will present the theoretical model related to the above mentioned experiments, which allows understanding the different phases observed during the assembly process by combining different physical ingredients such as phoretic motion, dipolar forces and hydrodynamics. Finally, simulations reveal qualitative but also quantitative good agreement with the experiments.

3.1. ASTER assemblies

Particles constituting the colloidal assemblies are propelled under the LCEEK mechanism, and acquire a constant speed when moving within the viscous fluid. Particle motion is parallel to the confining substrates and perpendicular to the applied AC electric field. Moreover, a balance between viscous friction and phoretic drive is established, so particles move as if propelled by a force $F = \gamma\, v_0$, where γ is the friction coefficient of the particles. In our experiments, we have restricted to frequencies above 10 Hz to ensure a monotonic dependence of the particle speed (**Fig. 66d**), and we have kept the amplitude of the sinusoidal AC field at $0.76\, V \cdot \mu m^{-1}$. The latter value is below the threshold for the onset of bulk electrohydrodynamic instabilities of the LC, which we want to avoid. Moreover, the field amplitude acts as a scaling parameter both in the phoretic drive and in the inter-particle interactions. In contrast, as shown below, the AC frequency has a more subtle influence in the relevant physical processes leading to the present colloidal clusters.

- DENSITY PROFILE OF THE PARTICLE ASSEMBLIES

Once the LC director is in a radial configuration (**Fig. 67a**), the AC field drives the particles within an area of interest of few square millimetres towards the centre of the topological defect created at the centre of the original light spot (**Fig. 67b**). The far-field trajectories of individual particles are radial and centripetal; they basically follow the underlying LC director (**Fig. 67c –** see **Video11**). As more particles arrive, the nematic colloids assemble into circular clusters with a steady-state inter-particle distance comparable to the size of the inclusions. Near the cluster, particles trajectories depart from radial as they tend to accommodate into the arrested assembly. The average inter-particle distance changes as the cluster grows, becoming smaller close to the centre than near the cluster's periphery (**Fig. 67c**). This behaviour suggests the existence of a net repulsive pairwise interaction. This interaction balances the steady phoretic drive acting on individual particles and prevents the irreversible aggregation of the particles due to LC elasticity. The repulsive interaction among inner particles has to balance the phoretic drive of an increasing number of arriving outer particles, which explains the inhomogeneous density distribution of the assemblies.

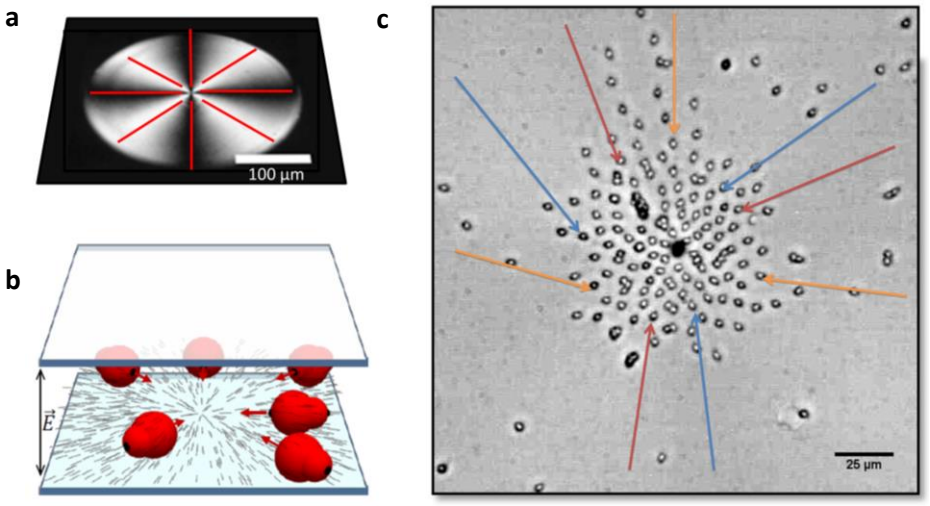

Fig. 67. Self-assembling nematic colloidal clusters. a) Image under crossed polarizers of the NLC texture after UV-light irradiation, which leads to a Maltese cross "attractive" pattern. Red lines denote the nematic director disposition. **b)** Anisometric colloidal particles dispersed in the NLC MLC-7029 are propelled under the application of an AC field perpendicular to the sample plane. The photosensitive coating above one of the surfaces allows defining topological defects which will serve as "attractor points" in the NLC cell to assemble the particles. **c)** Micrograph of a quasi-two-dimensional cluster of particles showing the superimposed trajectories of particles joining the cluster. The amplitude of the field is $0.76\ V \cdot \mu m^{-1}$ and f = 20 Hz while assembling. See **Video11**.

The cluster organizes in three well-defined regions characterized by different states of aggregation after hundreds of particles have accumulated (**Fig. 68a**). The central region, namely the innermost core (I), is an arrested, jammed state where particles remain mostly immobile with only minor rearrangements as the assembly grows. The density profile of a growing cluster at different stages is shown in **Fig. 68b**. The arrested core starts to be visible when the cluster achieves a minimum radius of approximately 80µm under the conditions of the AC applied field, f = 20 Hz and $E = 0.76\ V \cdot \mu m^{-1}$ (**Fig. 68b**). Within the core, the radial-averaged particle density is roughly homogenous, although far from close-packing ([163]). One can also observe the short-range heterogeneity in the form of particle chaining (**Fig. 68a**) presumably due to the LC-mediated anisotropic interactions. This is a consequence of the quadrupolar configurations of **n** due to the planar anchoring of the LC to the polystyrene particle surface, but also to the anisometric nature of the particles. Although the size of the core grows with the arrival of new particles, its packing density remains mostly constant (**Fig. 68b**).

The intermediate region (II) features a liquid-like state, where particles are separated by an inter-particle distance, and can be clearly observed under bright-field microscopy, but also retain their mobility. The radial-averaged particle area fraction, $\phi(r)$, decreases roughly linearly with the distance to the boundary with region (I) (**Fig. 68b**). As the cluster grows, both the slope and the radial corona corresponding to this region remain mostly unchanged. In other words, clusters of different sizes feature the same radial width and structure of the liquid-like corona, and they only differ on the growing size of the inner arrested core.

Finally, at area fractions below 0.1 (region III in **Fig. 68a** and **Fig. 68b**), $\phi(r)$ follows, as a good approximation, an exponential decay to zero, in analogy to an ideal gas under barometric conditions, and similarly to the reported behaviour of sedimenting active colloidal particles in very diluted regimes ([102]) (see section 3.6).

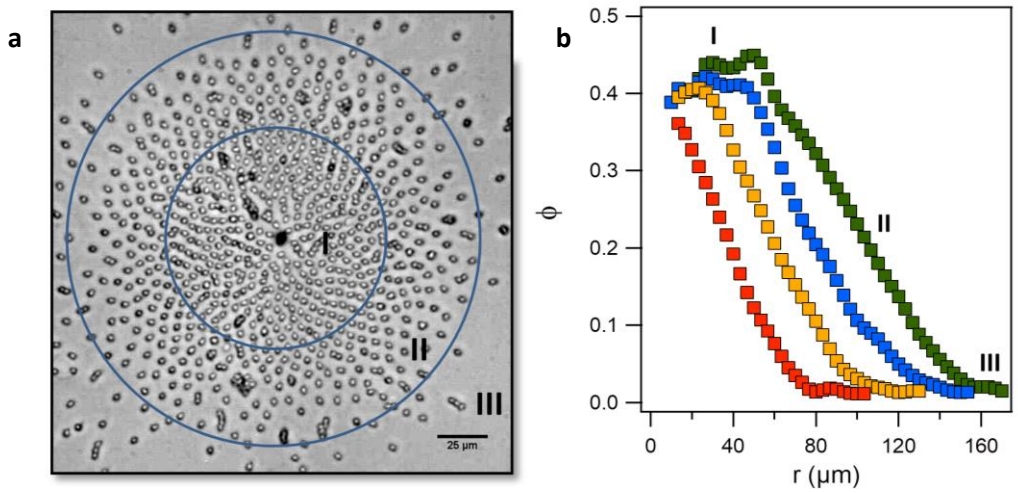

Fig. 68. Growing colloidal assembly. a) Micrograph of a cluster assembling while a f = 20 Hz AC field is being applied. Numbers indicate the three regions discussed in the text. **b)** Area fraction occupied by the particles vs. distance from the cluster centre for the same experiment. Elapsed times since the beginning of assembly are 150s (■), 250s (■), 350s (■) and 500s (■).

- BOND-ORIENTATIONAL ORDER

To quantify the structural distortion present in our assemblies with respect to a hexagonal phase, we use the bond-orientational order parameter. This parameter is indicative of how close to a hexagonal arrangement the neighbourhood of each particle pertaining to the cluster is. In fact, this allows characterizing the particle ordering in this quasi-two-dimensional cluster by using a radially-resolved expression of the order parameter, which is computed for each particle as,

$$\psi_{6,k} = \left| \frac{1}{N_k} \sum_{j=1}^{N_k} \exp(-i6\theta_{k,j}) \right|^2 .$$

Here, the sum extends over the N_k nearest neighbours of particle k in the assembly, and $\theta_{k,j}$ is the bond-orientational angle between the particle and its jth neighbour. Even though particles are anisometric, as an approximation, we set the nodes of the lattice at the centre of mass of each particle, whose position has been tracked before. Nearest neighbours have been determined by the Delaunay-Voronoi triangulation of the particles position in the assembly using Mathematica (**Fig. 69**). In **Fig. 69** the average radial profile $\psi_{6,k}$ is shown at different stages during the formation of the particle assembly. The radially-resolved order parameter $\psi_6\ (r)$ is further obtained by circularly averaging $\psi_{6,k}$ (**Fig. 69c**). Actually, for a perfectly hexagonal rearrangement, this definition would result in $\psi_{6,k} = 1$.

The value of ψ_6 in region (I) is lower than expected for a solid-like system where particles present close-packing. The disorder present in our system is due to the use of non-spherical particles, particle polydispersity, or surface asperities that may change particle orientation with respect to the local director field, and thus, promote non-symmetric aggregation ([164]). Another important contribution to disorder is the short-range elastic interactions mediated by the LC matrix, that promotes the off-centered chaining of the particles and prevents optimal packing.

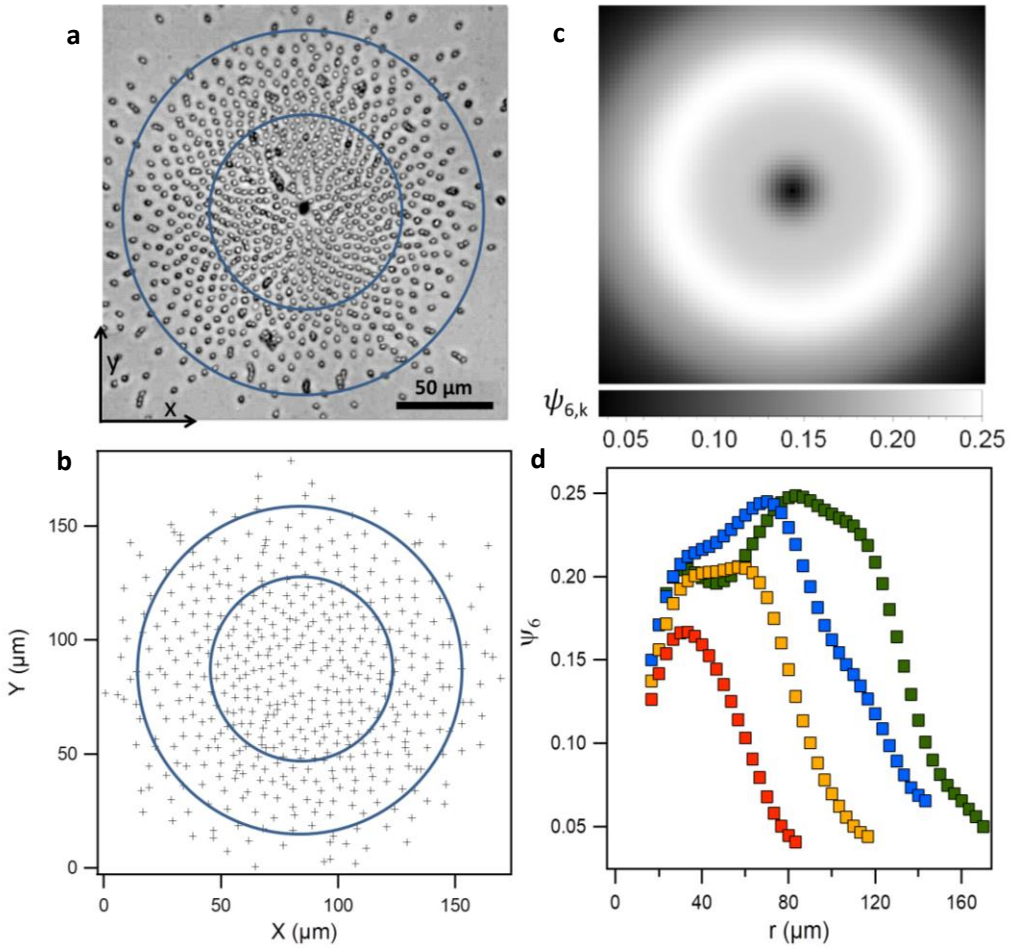

Fig. 69. Determination of the bond-orientational order parameter. a)) Bright field micrograph of a cluster assembling while a f=20 Hz AC field is being applied. The quasi-two-dimensional cluster is formed in the x/y plane. Elapsed time since the beginning of the assembly is 350s **b)** Tracked particles positions after an elapsed time of 250s for the same experiment shown in the above micrograph. **c)** Distribution of the circularly-averaged bond-orientational order parameter, $\psi_6\,(r)$ for the same experiment shown in **a)**. **d)** Profile of the bond-orientational order parameter as a function of the distance from the cluster centre. Elapsed times since the beginning of the assembly are 150s (■), 250s (■), 350s (■) and 500s (■).

Interestingly, as can be seen in **Fig. 69d**, the average value of ψ_6 changes in a non-monotonic way with the distance from the cluster centre. ψ_6 achieves a maximum value in region (II), where the density profile decays linearly, and further dropping to zero in region (III). The position of this maximum shifts to higher radii as more particles arrive, consistently with the growth process described above (see Density Profile of the Particle Assemblies), where the width of the liquid-like region remains mostly constant (region II) as the cluster grows, but the size of region (I) increases. The observed non-monotonic behaviour is in contrast to experiments with sedimenting spherical colloidal particles, where the hexagonal order is a monotonic function of the packing density ([163]).

In conclusion, the most ordered part of our assemblies corresponds to the liquid-like stage, region II, which corresponds to the lower-density regime, where the short-range elastic interactions do not play a role. This unusual behaviour can be attributed to an inter-particle repulsion that enhances hexagonal ordering and is evidenced in the density profile of the clusters (**Fig. 68b** and **Fig. 69c**,**d**).

3.2. Rotating Mill assemblies

As commented before, controlling the orientation of the nematic director allows steering the colloidal particles trajectories which are propelled under the application of an AC electric field perpendicular to the sample. Thus, taking advantage of the photosensitive surface allows inducing spiral patterns around a central topological defect (**Fig. 70**) (see Section 2, Irradiation protocol). The spiral patterns are characterized by a radial corona texture observed under POM, which is shown in **Fig. 70a**. After application of the AC electric field, the planar alignment in this corona (the non-black region in **Fig. 70a**) extend inwards and outwards forming the above mentioned spiral pattern (**Fig. 70b**) for particles to follow, as depicted in **Fig. 70c**.

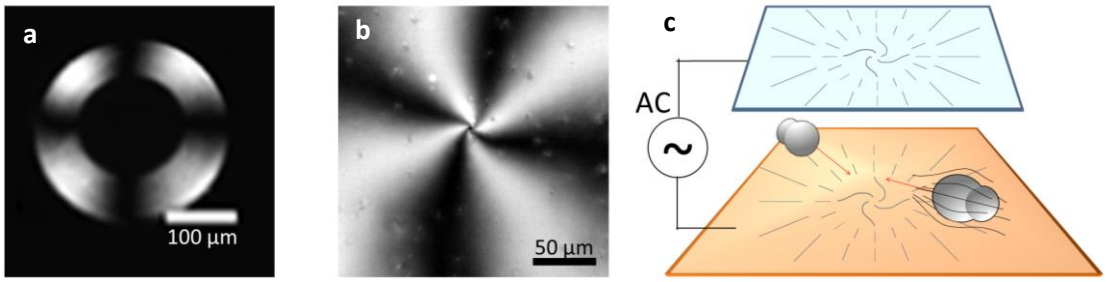

Fig. 70. Steering colloidal trajectories in a spiral pattern. a) Micrograph between crossed polarizers showing the photo-aligned corona before the application of the AC field. **b)** Image between crossed polarizers shows the spiral pattern induced by UV-light on the NLC after application of an AC electric field. **c)** Schematically depicted propulsion mechanism in a spiral pattern. Upon application of an AC electric field, the planar regions expand, and the particles are electrophoretically driven along the local director which performs a spiral pattern.

- DENSITY PROFILE OF THE PARTICLE ASSEMBLIES

Once the LC director is in a bend-splay configuration (**Fig. 70b**), the AC field drives the particles within an area of interest of few square millimetres towards the centre of the topological defect, which appears as a black spot at the centre of the image (**Fig. 71a –** see **Video12**). The far-field trajectories of individual particles feature a radial component but also a tangential one (**Fig. 71a**). As in the ASTERS experiments, when more particles arrive, the nematic colloids assemble into circular clusters with a steady-state inter-particle distance comparable to the size of the inclusions and its radially-averaged density increases with time. Colloidal particles are permanently rotating around the topological defect due to the constant input of energy, and the cluster rotates similarly to a rigid body. The cluster's rotational motion follows the chirality of the underlying pattern, which actually, can be easily disassembled by switching off the AC field or reducing it below E_0 (see Section 2).

Differently to the case of ASTER-like assemblies, the average inter-particle distance does not significantly change as the cluster grows (see **Fig. 68b** and **Fig. 71b**). Thus, different aggregation states are not clearly evidenced. This behaviour, apart from confirming the existence of a net repulsive pairwise interaction between particles, also evidences the differences between underlying patterns, where the arrested, jammed state only starts to develop when thousands of particles have reached the cluster for the configuration in **Fig. 71**.

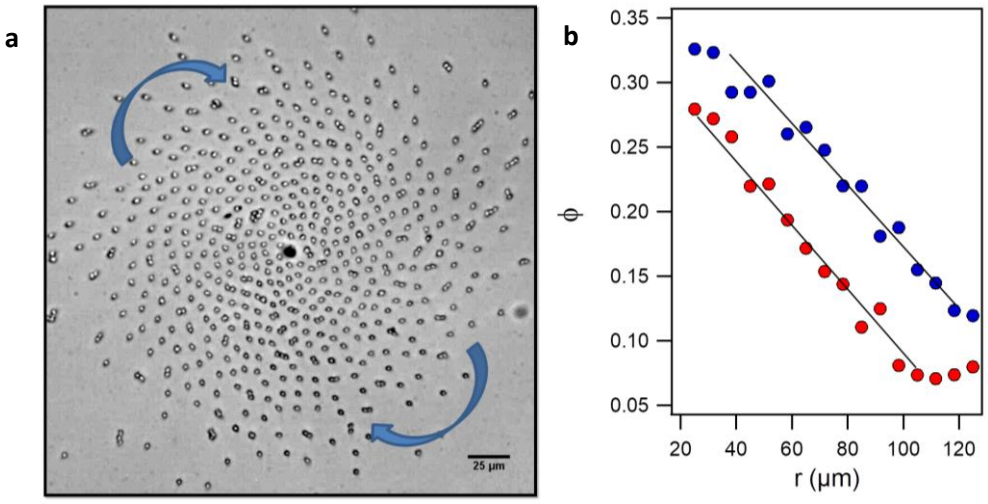

Fig. 71. Formation of nematic colloidal rotating mills. a) Formation of a rotating mill while a f = 20 Hz AC electric field is being applied. The arrows indicate the sense of rotation of the whole cluster. **b)** Area fraction occupied by the particles vs. distance from the cluster centre for the same experiment. Elapsed times since the beginning of assembly are 200 s (●) and 300 s (●). See **Video12**.

The rotating mill cluster only features two well-defined regions which are characterized by a liquid-like state followed by a gas-dispersed phase after hundreds of particles have accumulated (**Fig. 71b**). The tangential component of the velocity prevents to develop the jammed core for the studied clusters (less than *N*=1000 particles), and the inner particles of the cluster remain mostly constant spinning around the topological defect (**Fig. 71a**). In this case, the radially-averaged density profile follows a linear decay with the distance to the centre of the cluster in analogy to the liquid-like region of the asters assemblies, and as cluster grows, for reasonable times (t ~ 200 s), no other aggregation states can be found. The density profile of a growing cluster at different stages is shown in **Fig. 71b**.

- CLUSTER'S ROTATIONAL MOTION

In order to analyse the dynamic state of the rotating mills assemblies particle image velocimetry (PIV) has been performed (**Fig. 72**), which allows determining the velocity for each particle. Indeed, for the micrograph shown in **Fig. 72a**, we find that the cluster organizes in a rotating mill, with an almost constant linear velocity everywhere in the cluster, although particles within the inner zone feature lower velocities (**Fig. 72b**).

The particle detection has been achieved as explained in Chapter 2, Section 7.2. The obtained data allow performing particle image velocimetry (PIV) analysis, extracting the positions (x_i, y_i) of each particle i, and finally, analyse the radial (v_ρ) and azimuthal (v_θ) components of the particles velocities averaged over the ensemble. The two velocities have been averaged using the expression $\mathcal{v}_{\rho,\theta} = \sum_i \mathcal{v}_{\rho,\theta}{}^{(i)} / \sum_i |\mathcal{v}_i|$, and are also expressed in polar coordinates from the central defect point (**Fig. 72c**). Both series of data present complementary trends for v_ρ and v_θ while the rotating-mill is forming. The radial velocity vanishes when the rotating mill is formed, while the azimuthal one approaches to – 1. In the graphs shown in **Fig. 72**, both quantities are negative since the particles are moving towards the centre, and thus, against the radial direction, outwards by definition ($v_\rho < 0$), and in a clockwise sense ($v_\theta < 0$).

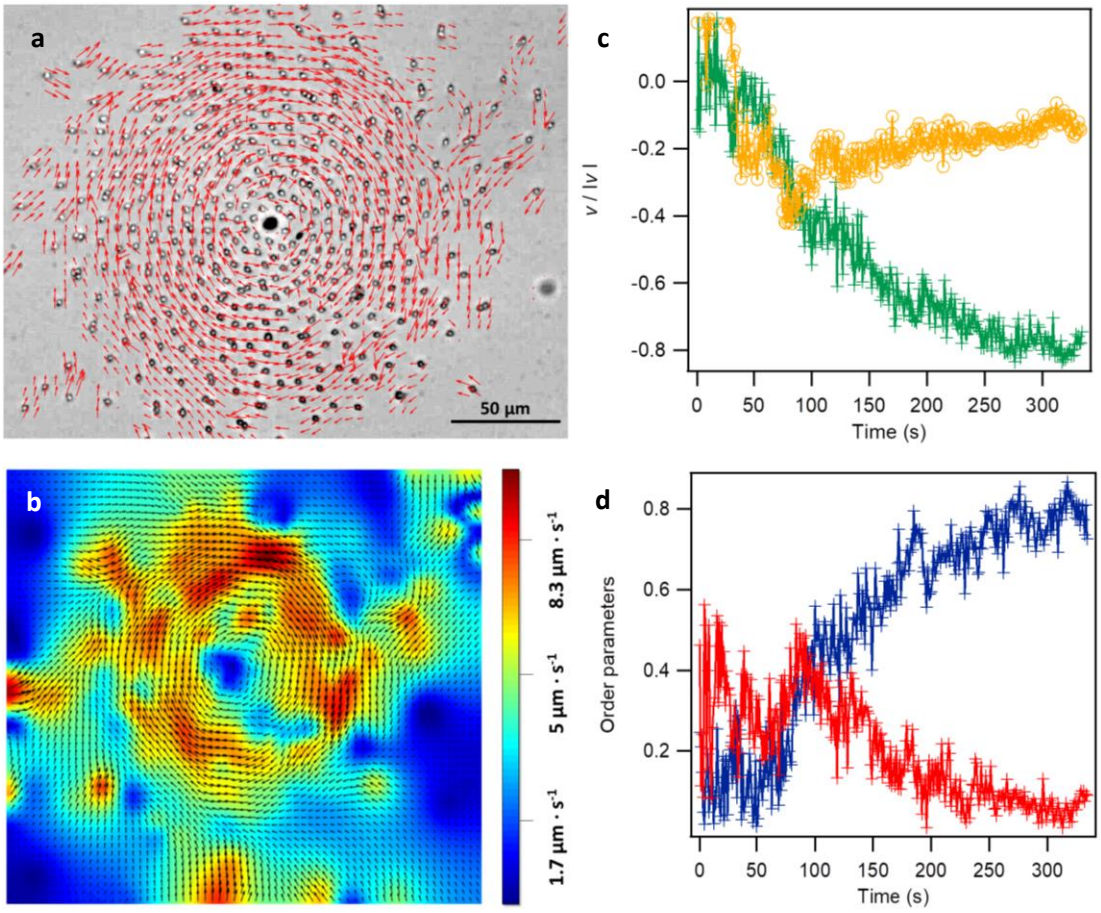

Fig. 72. Dynamics of a rotating mill cluster. a) Bright-field micrograph of the assembled rotating mill while a f = 20Hz AC field is applied (same experiment shown in **Fig. 71** and **Video12**). The velocity field of each particle is superimposed to the image. **b)** Particle Image Velocimetry showing the velocity magnitude for the particles constituting the assembly. **c)** Time evolution of the two velocity components when particles self-assemble into a rotating-mill configuration. The instantaneous azimuthal (v_θ, green) and radial (v_ρ, yellow) velocities are averaged over the number of particles of the ensemble. **d)** The two order parameters which allow describing the colloidal assembly, the polarity (*P,* red) and the angular momentum (*M,* blue) versus time.

Apart from the instantaneous velocity, the dynamics of the rotating mills can also be characterized in terms of two order parameters that describe, respectively, the degree of particle alignment and the collective rotation. The first one is the normalized polarity *P* of the ensemble, defined as

$$P = \left| \frac{\sum_i v_i}{\sum_i |v_i|} \right|,$$

with v_i being the velocity of the particle i at a position r_i from the center of mass of the ensemble, and the summation is performed over all the particles present in the ensemble. The second parameter is the normalized angular momentum, defined as

$$M = \left| \frac{\sum_i r_i \times v_i}{\sum_i |r_i||v_i|} \right|.$$

As described in Ref. ([165]), both order parameters are necessary to quantitatively determine whether the collection of propelling particles is in a coherent flock state (high value of *P*, low *M*) or in a single-mill state (low *P*, high *M*). For our experiments, colloidal

assemblies show a negligible polarity P, while the angular momentum M increases in time towards unity (**Fig. 72d**).

To conclude, the polarity of the particles, and thus the linear momentum, is lost when particles self-assemble in a spiral pattern. This is in contrast to the azimuthal velocity which reaches a maximum when all the particles are spinning around the central defect core, and thus, when the global angular momentum is maximum (**Fig. 72**).

3.3. Colloidal assemblies - Frequency dependence

Assemblies formed at different driving frequencies are different in the liquid-like region, where the inter-particle repulsion is effective, for both aster and rotating-mill configurations (**Fig. 73**). Notice here that the presented rotating mills are too small to collapse into a jammed core state, as mentioned above.

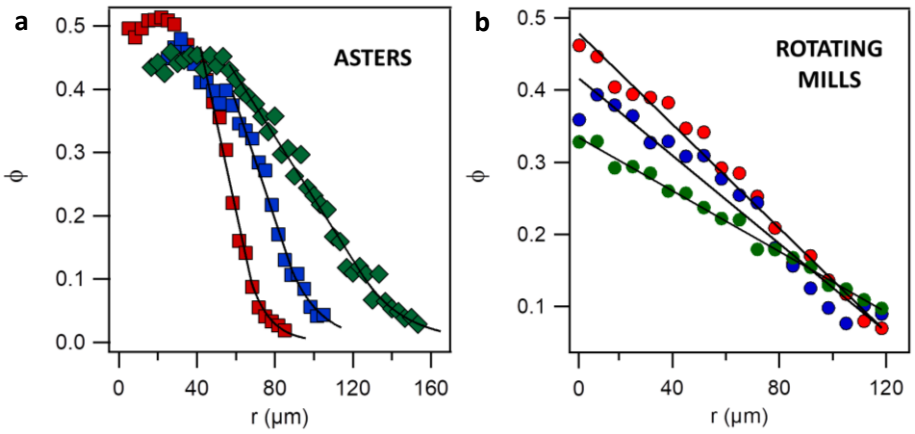

Fig. 73. Radially-averaged density profile of the experimental colloidal assemblies. a) Area fraction occupied by the particles versus distance from the centre of the cluster for aster-like experiments performed at f = 10 (■), 15 (■) and 20 (■) Hz. The line through the data is a linear fit to the area fraction profile in region (II), and an exponential fit in the dilute region (III) (see **Fig.68**). **b)** The particle area fraction is plotted for rotating mill experiments performed at different driving frequencies, f = 10 (●), 15 (●) and 20 (●) Hz. The line through the data is a linear fit to the area fraction profile displaying a liquid-like region.

In the following, and to facilitate the analysis and interpretation of the data, we have only focused on the pure splay textures of the LC, and thus, on particles exhibiting radial trajectories inducing aster-like assemblies.

When comparing aster assemblies formed at different frequencies of the AC field, clusters feature a similar packing density in the arrested cores (region I in **Fig. 68a**) but are clearly differentiated in the width and density distribution of region (II) (**Fig. 73a**). In this case, one can compare the average slope in the range with linear density profiles, region (II), for experiments performed at different driving frequencies. This reveals a nonlinear trend with the driving frequency (**Fig. 74a**). In fact, by dividing the average slope by the velocity of each experiment, our data suggests that the slope is proportional to the corresponding phoretic speed of driven isolated particles (**Fig. 74b**). As discussed in the next section, this result suggests that the net inter-particle repulsion is frequency-independent (**Fig. 74c**).

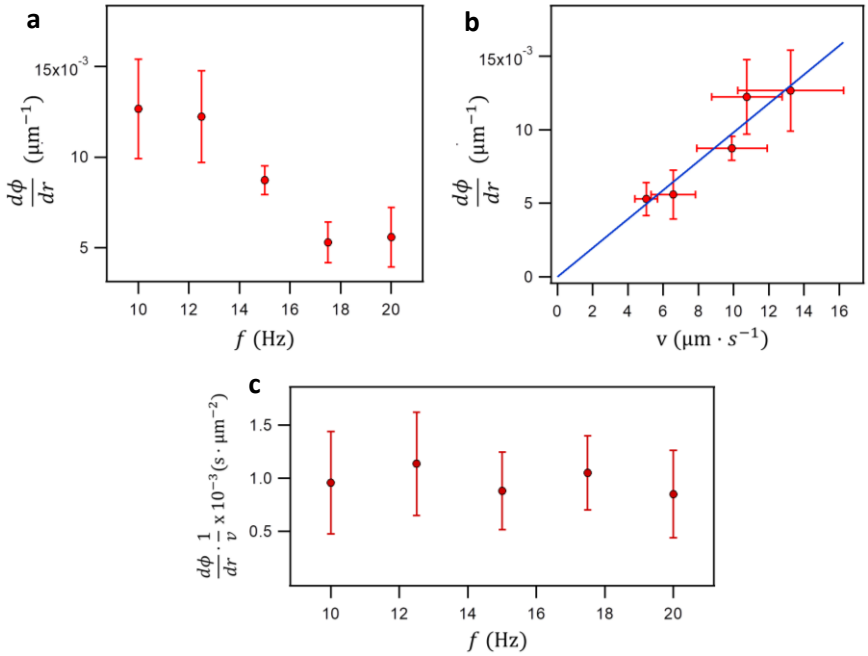

Fig. 74. Analysis of the experimental colloidal clusters featuring asters configuration. a) Average slope of the density profile of region (II), versus frequency. **b)** The same data is plotted as a function of v_0. **c)** Average slope of the density profile of region (II) divided by particle velocity at a given frequency versus frequency. This scaling shows the frequency-independent inter-particle repulsion for our colloidal system. The error bars are the standard deviation for different experimental realizations.

- SCALING ARGUMENTS – TOY MODEL

The linear spatial variation and the scaling with the particle speed v_0 of the density profile in region (II) (**Fig. 74**) can be understood as the result of the interplay between the centripetal phoretic force, γv_0, which clusters particles together, and a long-range inter-particle repulsion. This effect can be qualitatively described with the help of a simple toy model based on particles linked by springs (**Fig. 75**).

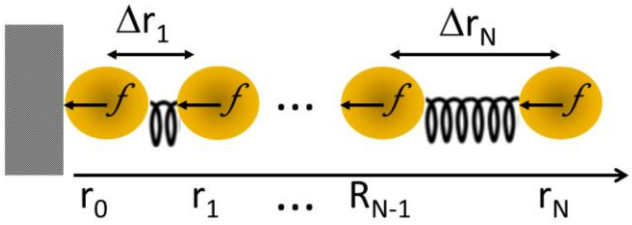

Fig. 75. Spring-based toy model. Model system for a 1-D equilibrium assembly of particles propelled under a force *F* that is balanced by a nearest-neighbor repulsion potential. The latter is represented by a spring, as shown between the two inner- and the two outermost particles.

Let us consider a one-dimensional stack of N particles featuring mechanical equilibrium, with a constant force (phoretic), F, pulling each particle towards an immobilized particle to the left (see **Fig. 75**), which can represent the inner region (I) of the colloidal asters. Contrarily to this centripetal force, a pairwise repulsion potential between neighbouring particles, which can be modelled as a spring with constant K and length q, balances the phoretic drive.

Taking into account that the left-most particle is pinned to the represented wall, force balance leads to an equilibrium particle position for the n^{th} particle

$$r_n = nq - n\left[N - \frac{n-1}{2}\right] l,$$

where $l = F/K$.

One can estimate the one-dimensional particle number density as $n(r_n) = {}^{1}/_{\Delta r_n}$. Using the above equation, and taking into account large particle systems (in the limit $N \gg 1$), we find,

$$n(r) \approx \frac{n_*}{\sqrt{1 + 2{n_*}^2 lr}}.$$

Here, $n_* = (q - Nl)^{-1}$ is the maximum number density, where inter-particle distance is shortest. The above expression can be expanded for small distortions of the spring,

$$n(r) \approx n_* - \frac{{n_*}^2 F}{K}\, r,$$

This results in a linear decay for the number density with a negative slope proportional to F/K, which is proportional to the strength of propulsion and inversely proportional to the elastic constant strength, or in our case, to the repulsion between particles. This scaling is consistent with the experimental observations (**Fig. 73** and **Fig. 74**). Moreover, assuming that the force acting on each particle is the same that propels particles, $F = \gamma v_0$, we recover the linear scaling with v_0 of the density decay (**Fig. 74b**).

Afterwards, we can finally write the expression which relates the slopes of the particle number density and the pairwise interaction potential as,

$$\frac{dn}{dr} \propto -\frac{F}{K} \propto -\frac{\gamma v_0}{U''(q)}.$$

This equation allows relating the experimental observed trends with the predictions of a theoretical model where the repulsion between particles is taken as a potential ($U(q)$) which accounts for the different ingredients present in the physical system, as discussed in the forthcoming Section, Theoretical Model. The most important conclusion extracted from experiments is that this potential should not introduce any dependence on frequency considering the observed scaling with the phoretic speed.

3.4. Theoretical model

To better understand the physical behaviour of the colloidal clusters, and thus, the transition between the different colloidal phases and the observed density profiles, we developed a theoretical model in the group and performed numerical simulations which qualitatively agree with the experimental observed trends.

The simulation system consists of a two-dimensional ensemble of N particles moving in the xy plane. The colloidal inclusions are approximated to be hard spheres that propel along the director field, although experiments are performed with peanut-shaped particles. In other words, we disregard the orientation dynamics of the particles. In accordance with the experimental conditions, the analysis of the data obtained from the theoretical model has been restricted to a given amplitude, E_0, of the AC electric field, while the frequency has been tuned. In order to reproduce particle propulsion, we have assumed overdamped dynamics, which basically means that the velocity of the particles is proportional to the force acting on them, as had been previously evidenced in experiments. Thermal fluctuations have been neglected due to the large medium viscosity, although may generally play a role in the motion of a free driven particle in a LC (see Chapter 3) ([153]).

In the model developed taking into account the above assumptions, each particle with position $r_i = (x_i, y_i)$ $(i = 1, \dots, N)$ is governed by the equation of motion,

$$\frac{d\boldsymbol{r_i}}{dt} = v_i(f)\hat{\boldsymbol{n}}(r_i) - \frac{1}{\gamma}\sum_{j\neq i}\frac{\delta U}{\delta \boldsymbol{r}_{ij}}.$$

Here, the first term on the right hand of the equality describes the propulsion of each individual particle driven along the LC nematic vector $\hat{\boldsymbol{n}}(r)$. The hard spheres are put into motion and experience a friction force with an effective drag coefficient, γ. The second term accounts for the pairwise repulsive interactions between the particles separated by a distance $r_{ij} = |\boldsymbol{r}_i - \boldsymbol{r}_j|$ with a repulsive interaction potential that combines different ingredients

$$U = U_{hd}(r_{ij}) + U_{ad}(r_{ij}) + U_{hc}(r_{ij}) + U_{qq}(r_{ij}, \hat{\boldsymbol{n}}).$$

This potential takes into account the long-range hydrodynamics (U_{hd}) induced by the electroosmotic flows, the induced dipolar (U_{ad}) interaction between neighboring particles due to particle polarization under the application of an AC electric field, the short-range hard-core repulsion (U_{hc}) and finally, the elastic quadrupolar interactions (U_{qq}) mediated by the NLC matrix.

The different contributions for the interaction potential are specified below.

- SELF-PROPULSION IN A PATTERNED ENVIRONMENT

Particles are propelled in a NLC following an imprinted pattern. The mechanism acting on particles for propulsion is LC-enabled electrokineticss (LCEEK) (see Chapter 1, Section 4.2.2), which actually, determines the particles velocity, and thus, the individual motion.

Two different assembly configurations are possible. The first one corresponds to the pure splay texture, and thus, to the plane radial pattern, which can be expressed analytically by minimizing the elastic free energy density functional of a nematic liquid crystal in polar coordinates for the given distortion. The obtained pattern, centered at the origin and having the inward direction, presents the solution $\hat{\boldsymbol{n}} = \left(\hat{n}_\rho, \hat{n}_\varphi\right) = (-1,0)$ for the director field. Transforming to the Cartesian coordinates yields

$$\hat{n}(r) = \left(\hat{n}_x(r), \hat{n}_y(r)\right) = (-\cos\varphi(r), -\sin\varphi(r)),$$

where $\varphi(r) = \varphi(x, y)$.

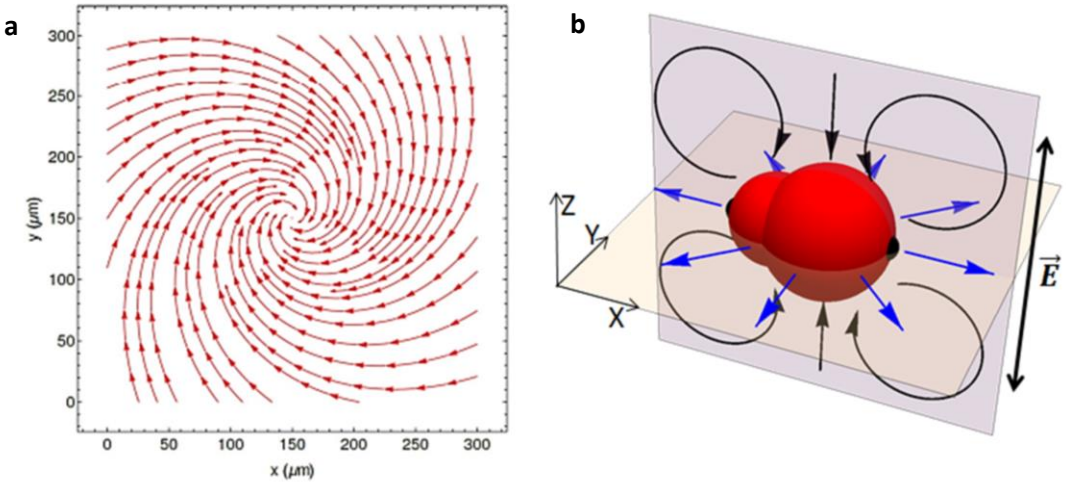

Fig. 76. Particle self-propulsion in a patterned environment. a) Vector field of the spiral pattern calculated following the model in the text over an area of 300 x 300 μm^2. **b)** Sketch of the hydrodynamic repulsion arising from the phoretic ionic flows, which are pushed away from the particles in the plane of the assembly xy. In this case, the local director field is along the x axis.

On the other hand, the director field for a spiral pattern is modelled in polar coordinates as

$$\hat{\boldsymbol{n}}(r, t) = \boldsymbol{n}(\psi(r - q)),$$

and is defined by the function ψ which is obtained, as before, by minimizing the energy functional of the NLC. In polar coordinates. In this case, the director field spirals out of the origin according to $\hat{\boldsymbol{n}} = \left(\hat{n}_\rho, \hat{n}_\varphi\right) = (\cos\psi, \sin\psi)$. For our experiments, we are interested in patterns that spiral in (particles self-assemble in a single point defect), thus we flip the sign of the radial component of the director, $\hat{n}_\rho \to -\hat{n}_\rho$, and then pass to Cartesian coordinates (x,y) (**Fig. 76**). As a result, the components of the director field $\hat{\boldsymbol{n}}(r) = \left(\hat{n}_x, \hat{n}_y\right)$ can be represented as,

$$\hat{\boldsymbol{n}}(r) = \left(\hat{n}_x, \hat{n}_y\right) = (-\cos(\varphi(r) - \psi(r)), (-\sin(\varphi(r) - \psi(r)).$$

In our system, particle propulsion is due to the appearance of electroosmotic flows around the particles, which develops under the application of an AC electric field, as a result of charge separation in the vicinity of the particle (**Fig. 76b**). This physical aspect can be interpreted in the model as an effective slip velocity at particle's surface, meaning that, fluid is moving with respect to the particle surface. For a spherical particle with tangential

anchoring, the induced flows are of quadrupolar symmetry, allowing no net propulsion. Thus, in experiments, the asymmetric peanut-like shape of the particles breaks the quadrupolar symmetry of the flows, leading to a constant strength of propulsion over the particles, whose intensity is dependent on the applied electric field by means of both, amplitude and frequency of the AC. The dependence of the mean particle velocity on the AC frequency, which agrees with the reported experimental data (see Chapter 4, Section 2), can be represented by the following expression,

$$v(f) = v_0\alpha(f), \qquad \alpha(f) = \frac{f^2{\tau_e}^2}{(1+f^2{\tau_c}^2)(1+f^2{\tau_e}^2)}.$$

Here, as in the experiments, τ_c and τ_e are the characteristic charging timescales for a spherical particle and the electrodes, respectively. We also use the angular frequency $\omega = 2\pi f$. The frequency dependence of particle velocity is determined by the dimensionless function $\alpha(f)$, which starts to grow at small frequencies until reaching a maximum at $f_* = (\tau_e\tau_c)^{-1/2}$ and decaying until zero at high frequencies. To obtain comparable results to that experimental ones, τ_e and τ_c have been chosen in analogy with the experimental data (see Chapter 4, Section 2).

The speed of individual particles obtained experimentally features a dispersion of up to 20%. Thus, it can be modelled as

$$v_i(f) = v_0(f)(1 + 0.2\xi),$$

where ξ is a Gaussian random variable representing experimental noise.

- INDUCED HYDRODRYNAMIC REPULSION

The descriptions of inter-particle interactions are described in the following sub-sections. As commented before, electroosmotic flows, whose near-field determines particle self-propulsion, are induced around each particle. These generally complicated hydrodynamic forces can be cast into an effective repulsive interaction potential.

Earlier experiments ([139]) show that particles propelled in a NLC displaying planar anchoring at the particle surface push ionic flows away from them. In our experiments, the electric field is perpendicular to the plane of particles propulsion, and thus, we conclude that induced flows can move radially outwards from each particle in the plane of the assembly (see **Fig. 76b**). Our particles are not perfectly spherical, even so we have assumed that in-plane isotropic flows are valid in the far-field. The osmotic flows leading to the inter-particle repulsion are the same that provide particle propulsion, thus, their dependence on the AC frequency is the same as that determined for particle speed, $\alpha(f)$. Finally, one has to consider the far-field of hydrodynamic velocities for quadrupolar-like configurations, which is known to decay as r^{-3}, for both isotropic and LC medium ([137], [139]). As two particles approach, the radial flows surrounding the particles overlap, resulting in a net repulsive force. Taking into account the above considerations, the repulsive potential can be expressed as

$$U_{hd}(r,f) = C_{hd}\frac{\alpha(f)}{r^2}, \qquad \alpha(\omega) = \frac{f^2{\tau_e}^2}{(1+f^2{\tau_c}^2)(1+f^2{\tau_e}^2)},$$

with a constant prefactor C_{hd}.

- INDUCED ELECTROSTATIC DIPOLAR REPULSION

In the model, the potential U_{hd} provides particle propulsion but also induces ionic flows extending outwards from the particle and preventing particle aggregation. Although the repulsive potential is enough to balance the phoretic drive and to reproduce the linear density profile of the aster assemblies (see **Fig. 68b**), both these ingredients are caused by the same physical origin and flows scale similarly with the frequency, $\propto \alpha(f)$. As a result, the force balance between propulsion and hydrodynamic repulsion remains identical, and thus, the density profiles of the clusters are unaffected by a frequency change. This observation is in contradiction with the obtained experimental results, where the density profile of the assembled clusters depends on the driving frequency (see **Fig. 73**).

This implies that there must be another physical ingredient playing a role in particle repulsion which allow for cluster rarefication.

In our experimental setup, one of the reasons for confining the colloidal dispersion in a narrow cell is to prevent chaining in the *z* direction (out-of-plane). This effect has just been observed for particles translating or pinned in different planes (see **Fig. 77**).

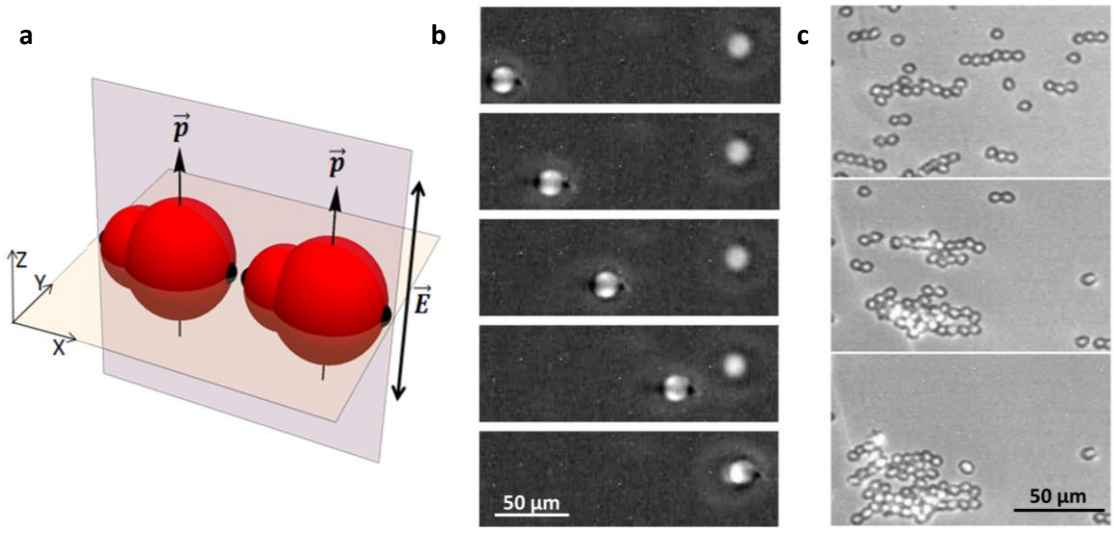

Fig. 77. Induced electrostatic repulsion. a) Sketch of the induced electric dipoles, which are parallel, co-planar and perpendicular to the plane of the assembly (xy), resulting in a net repulsion. **b)** Attraction and pinning of two silica spherical particles (10 µm diameter) dispersed in the NLC MLC-7029 featuring a point defect-hedgehog driven by an AC field (15 Hz and 0.6 V·µm^{-1}) perpendicular to the LC cell. The NLC cell is about 50 µm in this experiment. **c)** Peanut-shaped particles (d_x = 10.2 µm and d_y = 8.3 µm) driven by an in-plane AC field of 15 Hz and 0.1 V·µm^{-1} in a NLC of positive dielectric anisotropy (5CB). The AC field is horizontal to the snapshots (complementary geometry to that one shown in **a)**. The cell thickness is about 20 µm.

When an AC field is applied through the NLC cell, particles experience a charge separation leading to the formation of electric double layers surrounding each particle, and thus, electric dipoles are induced. Particles interact electrically due to their polarization along the

applied electric field. The induced electric dipoles are parallel to the *z*-axis and perpendicular to the plane of propulsion *x/y*, where the dipolar repulsion force also acts. Taking into account that the dipolar interaction is isotropic and repulsive in the particles' plane, the dipole-induced potential can be written as,

$$U_{dd}(r,f) = C_{dd}\frac{\beta(f)}{r^3}, \qquad \beta(\omega) = \frac{(1/4 + {\tau_c}^2 f^2){\tau_e}^2 f^2}{(1+f^2{\tau_c}^2)(1+f^2{\tau_e}^2)},$$

With a constant prefactor C_{dd}.

Evaluating $\beta(f)$ one could observe that this repulsion potential persists at large frequencies, which allows reproducing the experimentally observed gradual expansion of the particle cluster with the frequency.

- ELASTICALLY-MEDIATED LIQUID CRYSTAL INTERACTIONS

The elasticity of the LC mediates particle arrangement in the inner region of the assembled cluster (**Fig. 78**). In our experiments, particles feature planar anchoring, and thus, a distorted quadrupolar configuration in the form of two surface defects. To account for the interactions responsible for the optimal particle rearrangement we can consider the simplest quadrupolar potential,

$$U_{qq}(r,\hat{n}) = \frac{C_{qq}}{r^5}\,(3 - 30\cos^2\vartheta + 35\cos^4\vartheta),$$

Where $\vartheta = \vartheta(r,\hat{n})$ is the angle between the vector connecting the centres of interacting particles, and the far-field orientation of the nematic director $\hat{\boldsymbol{n}}$, and $\boldsymbol{r} = |\vec{r}|$ is the distance between particles.

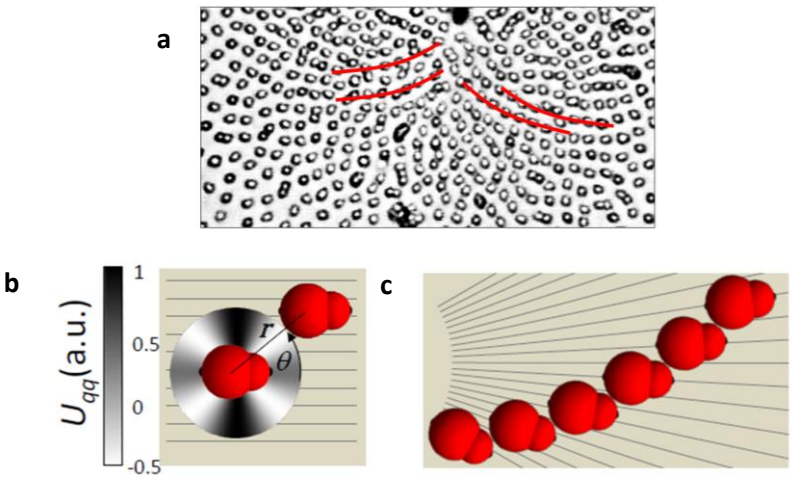

Fig. 78. Elastic liquid crystal interactions. a) Experimental micrograph showing the inhomogeneous particle chaining in the inner region of the cluster (region I). **b)** LC-mediated elastic quadrupolar interactions, U_{qq}, are anisotropic and become attractive when the long axes of particles are shifted about 45° with respect to the local LC director. **c)** Particle chaining due to the radial LC director disposition. Elasticity promotes the formation of arched particle chains.

This potential only accounts for particle re-arrangement as this interaction is frequency independent and has a shorter spatial range than the other long-range repulsive

interactions. When particles become closer in the inner region of the cluster, the quadrupolar LC interaction promotes the off-centered chaining observed in **Fig. 78**. This fact, coupled with the underlying radial director field, are the responsible for the formation of arch-like chains.

- SHORT-RANGE HARD-CORE REPULSION

In order to account for the finite size of the particles, we can introduce a short-range repulsive potential of the form,

$$U_{hc}(r) = 4\epsilon\left[\left(\frac{\sigma}{r}\right)^{48} - \left(\frac{\sigma}{r}\right)^{24} + \left(\frac{1}{4}\right)\right],$$

which is significant for small distances, $r < 2^{1/24} \cdot \sigma$ and is otherwise zero.

Here, the effective diameter of the particles is set to σ = 4.2 μm in order to account for the experimentally observed fact that particles, when assembled, do not come into contact.

3.5. Simulations results

An important aspect of the model is the choice of electrokinetic parameters. It is crucial not only to agree with experiments but also for understanding the interplay of the different physical ingredients.

There are basically three different frequency dependent mechanisms involved in the clusters self-assembly, namely, particle propulsion and both mechanisms of long-range repulsion. All of them are dependent on two time scales, the particle, τ_c , and the electrode, τ_e, charging times, which are determined simultaneously by fitting the propulsion speed of individual particles (see section 2).

As explained before, aster experiments reveal that in the studied range of driving frequencies, inter-particle repulsion seems not to depend on the frequency. Actually, the relative strengths of these potentials, U_{hd} and U_{dd}, can be chosen such that the sum of their relative strength is nearly frequency independent (**Fig. 79c**). Moreover, tuning the potentials' amplitude while keeping their strength fixed allows to adjust the slopes of the density profiles.

The described model has been applied to simulate 700 particles with specific parameters that fulfil all the above conditions. As shown in **Fig. 79** our model captures all the details of the experimentally observed assembly, including the existence of three states of aggregation and the reported scaling of the liquid-like region (see **Video13**). Further, we note that for this number of assembled particles in the simulations, the formation of the central solid core is found only for the highest centripetal force obtained at *f* = 10Hz.

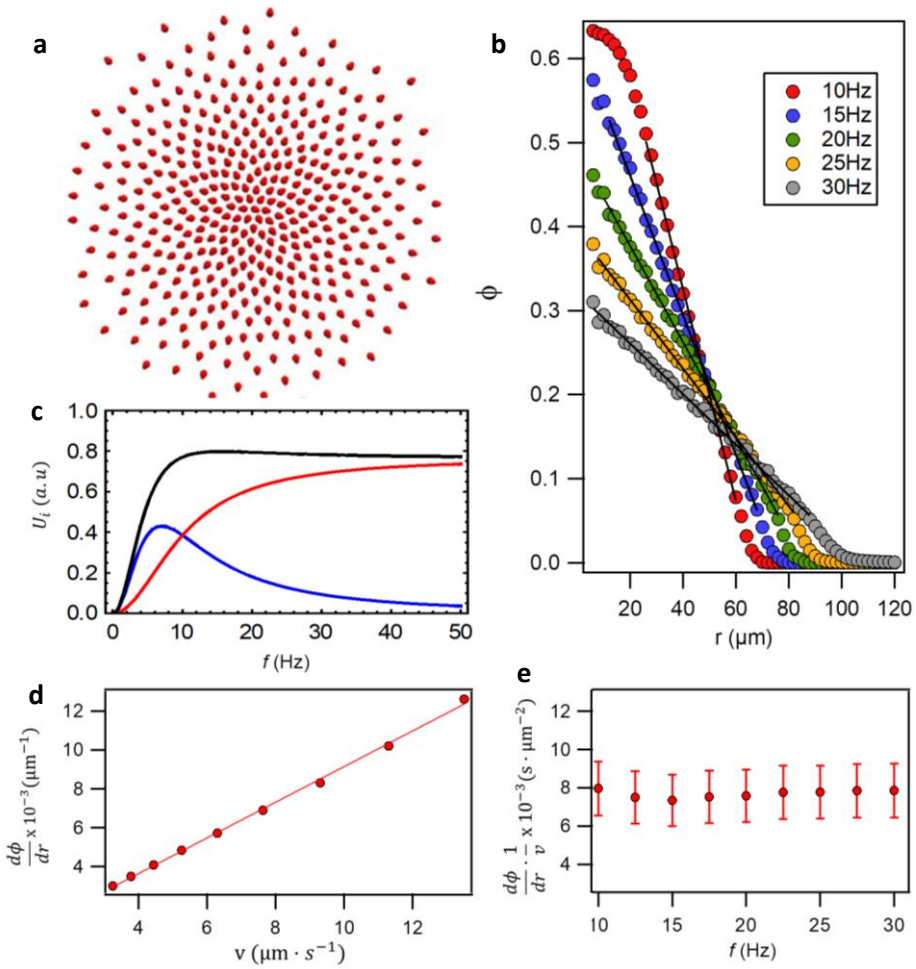

Fig. 79. Simulation results. a) Simulated cluster assembly with the model described in the text and obtained at a frequency of 10 Hz while keeping constant the amplitude of the electric field 0.76 V · μm^{-1}. In the picture, solid spheres are replaced by peanut like-shaped particles. **b)** Area fraction occupied by particles as a function of distance from the centre of the cluster for simulations performed at different driving frequencies. The data corresponds to clusters assembled with 700 particles. **c)** Normalized repulsive inter-particle potentials interactions, U_{hd} (blue), U_{dd} (red) and the sum of both, $U_{hd} + U_{dd}$ (black). Potentials are calculated for a center-to-center distance of 15 μm, and as a function of the driving frequency. **d)** Slope of the linear-region of the density profiles in **b)** versus the speed of individual phoretic particles. **e)** Average slope of the density profiles shown in **b)** divided by particle speed at a given frequency versus frequency. This scaling evidences the frequency-independent inter-particle repulsion for our colloidal system, and thus, the model agreement with the experiments. The error bars are the standard deviation for different simulations. See **Video13**.

By tuning the amplitude and strength of the model parameters and defining a spiral-like underlying pattern, the model also allows performing simulations based on the rotating mill assemblies, showing analogous results to that experimentally obtained (**Fig. 80** – **Video14**) (For the experimental results see Section 3.2). The comparison between experimental and numerical data has been performed by measuring the same observables for both experiments and simulations. We have, thus, analysed the radial (v_ρ) and azimuthal (v_θ) components of the particles velocities averaged over the all ensemble. The two velocities have been measured by the expression $v_{\rho,\theta} = \sum_i v_{\rho,\theta}{}^{(i)} / \sum_i |v_i|$. Apart from the instantaneous velocity, the dynamics of the rotating mills has also been characterized in terms of the polarity *P* and the angular momentum, *M*, which define the degree of particle alignment and collective rotation, respectively, as commented in section 3.2.

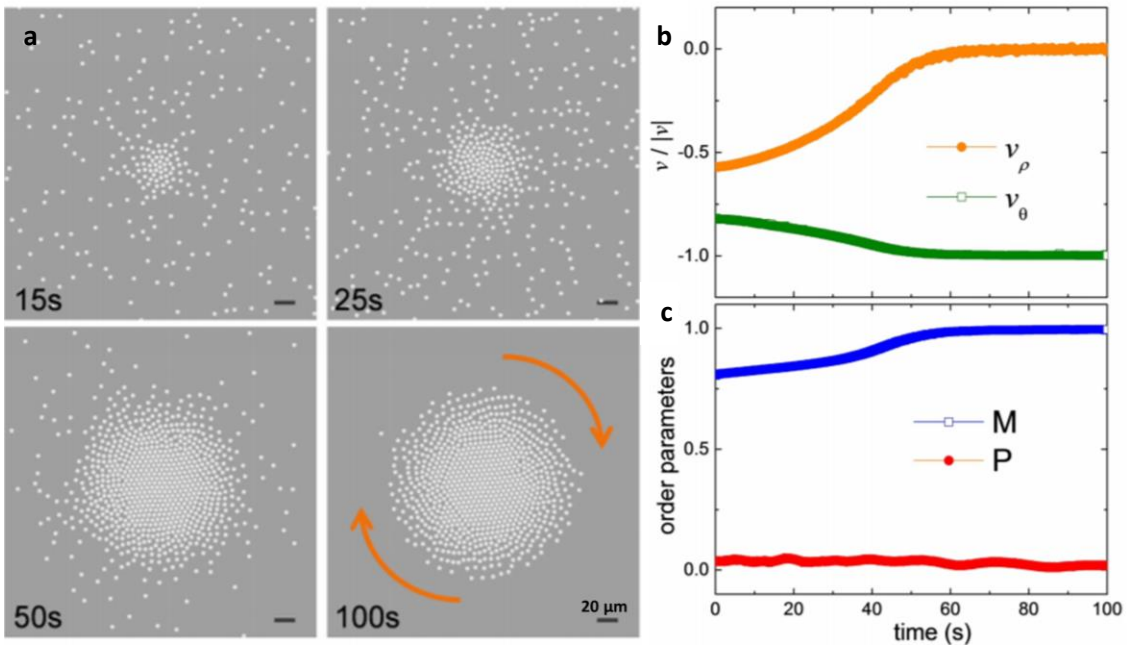

Fig. 80. Rotating mill simulations results. a) Sequence of numerical simulations for a rotating mill-like assembly with the model described in the text. The results correspond to a cluster of 700 particles assembled at a frequency of 10 Hz while keeping constant the amplitude of the electric field 0.76 $\mathrm{V}\cdot\mu\mathrm{m}^{-1}$ for different elapsed times. **b)** Time evolution of the two velocity components when particles self-assemble. The instantaneous azimuthal (v_θ) and radial (v_ρ) velocities are averaged over the number of particles of the ensemble. As particles self-assemble, the radial component of the velocity is lost while the azimuthal maximizes. **c)** The two order parameters which allow describing the colloidal assembly, the polarity (*P*) and the angular momentum (*M*) versus time. Since particles are spinning around the topological defect, the particles velocity vector do not display collective alignment, and thus, $P \sim 0$. See **Video14**.

3.6. Equation of state

The constant input of energy provided by the AC electric field takes the system out-of-equilibrium. In absence of a topological defect, particles would move without assembling. In contrast, inducing a topological defect allows particles to cluster in a radial configuration, developing in three well-defined different regions which present stationary phases, as evidenced in previous sections (see Section 3.1). The propelling particles constantly exert a radial pressure towards the single point topological defect. Moreover, switching off the electric field or reducing it under the threshold field for particle motion, melts the cluster, and the anisometric particles slowly diffuse in the NLC cell. Thus, we can define a non-equilibrium equation of state for our nematic colloidal system. As mentioned before, the phoretic driving force is counterbalanced by an inter-particle repulsive interaction, thus, the packing-density profile of the liquid-like region can be related to the mechanical pressure exerted by the outer particles. For this purpose, we determine the phoretic force, F, from the speed of an individual particle and the friction coefficient (see both below and Chapter 4, section 2). Afterwards, the mechanical pressure p in our system can be defined such that it is zero outside of the cluster, and its value at a distance *r* from the centre of the cluster is given by,

$$p(r) = \frac{F}{wr}\int_r^\infty \frac{\phi(r')}{a_0} r' dr'.$$

Here, $a_0 \sim 10\ \mu m^2$ and is the area covered by the anisometric particles, w is the thickness of the particle layer, which we take as the diameter of the largest particle lobule, $w = 3\ \mu m$.

In order to estimate the force exerted by the particles, F, we consider the friction coefficient to be that of an spherical particle, $\gamma = 6\pi\eta_{\parallel}a$, where $a = 1.5\ \mu m$ is the particle hydrodynamic radius. The NLC is characterized by the viscosities parallel, $\eta_{\parallel}$, and perpendicular, $\eta_{\perp}$, to the far-field nematic director, but here only the parallel one will be important as particle motion takes place along the director field. We measured the viscosity parallel to the far-field orientation in a separate experiment by comparting the velocities of paramagnetic colloids under the action of a magnetic field gradient for both water and the NLC MLC-7029 (see Chapter 2, section 8.2). Thus, only the viscosity parallel with respect to **n** $\eta_{\parallel} = 1.4 \cdot 10^3 \mathrm{Pa} \cdot \mathrm{s}$ will be relevant for particle motion in our system.

The results of the data analysis are presented as pressure versus area fraction of particles for both experiments and simulations (**Fig. 81**). The $p - \phi$ isotherms are continuous through all the different aggregation states, which is consistent with the existence of an inter-particle repulsion and it is also evidenced by the hexatic order parameter, which is fully never lost (see Section 3.1). As shown in **Fig. 81**, the pressure-density for different driving frequencies, and thus different driving forces, collapse onto a single master curve, thus leading to an equation of state for this out-of-equilibrium system. This result could be expected after the knowledge based on the effective frequency-independent particle interactions.

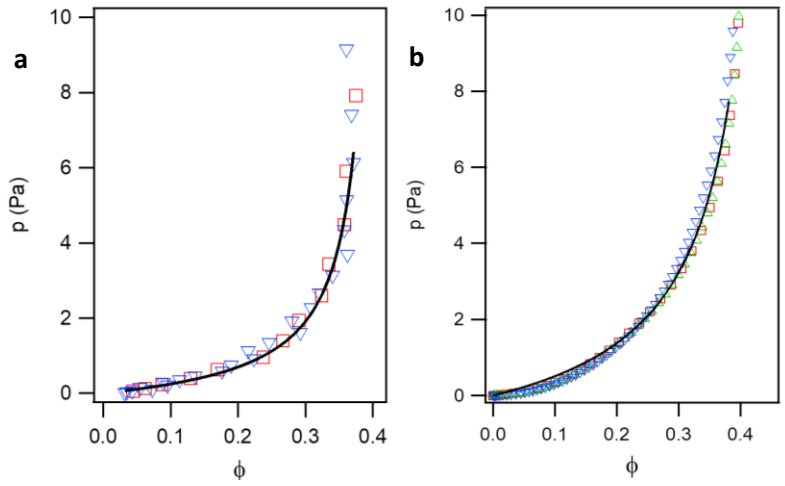

Fig. 81. Colloidal assemblies' pressure. Estimation of the mechanical pressure as a function of the particle area fraction for clusters assembled at different driving forces for both **a)** experiments and **b)** simulations. The data shown are taken at 10 (□), 15 (△) and 20 (▽) Hz. Continuous lines are fits to a hard-disk equation of state in the liquid-like region or compressible phase.

The obtained results for the pressure-density isotherm data in region II for the colloidal assemblies shown here can be well described by an equation of state similar to the hard-disk case ([166]),

$$p \propto \frac{\phi}{1 - 2\phi + (\phi_0^2 - 1)\left(\frac{\phi}{\phi_0}\right)^2},$$

Where ϕ_0 is the extrapolated close-packing area fraction. The similar behaviour of our system with respect to that of a hard-disk can be explained by considering that the net inter-particle repulsion prevents the LC elastically-mediated attraction and enhances an ordered diluted region.

- GAS – LIKE PHASE ANALYSIS

Following with the analysis of the density profile for the radial assemblies configurations, at area fractions below 0.1 (region III in **Fig. 68a** and **Fig. 68b**), $\phi(r)$ follows, as a good approximation, an exponential decay to zero. This result is in analogy to an ideal gas under barometric conditions, and similar in general trends to the reported behaviour of sedimenting active colloidal particles in very diluted regimes ([102]).

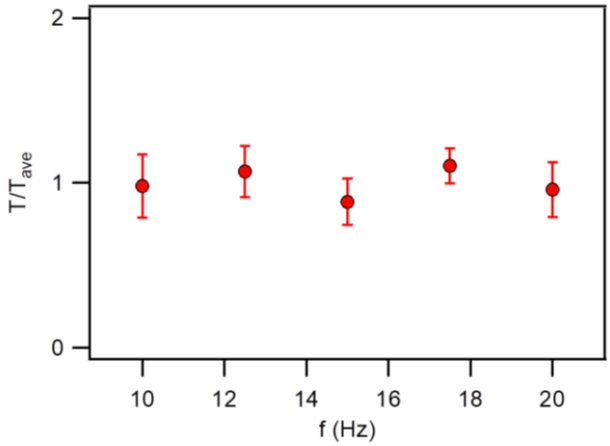

Fig. 82. Effective temperature. Experimental obtained effective temperatures relative to its average value for experiments performed at different driving frequencies. The data has been obtained from the exponential fit of the density profile in the gas-like phase, region III in **Fig. 68a** and **Fig. 68b**. The error bars are the standard deviations over different realizations.

Given the relatively large viscosity of the dispersing medium, thermal fluctuations seem not to play a role, and thus, to be negligible, as evidenced in **Fig. 81**. Comparing experiments performed at different driving frequencies allow determining the effective temperature with the expression,

$$\phi(r) \propto \exp\left(-\gamma v_0 / K_B T_{eff}\right) \cdot r.$$

As shown in **Fig. 82**, the effective temperature T_{eff} of the system is frequency-independent, consistently with the purely driven nature of our system, which is different to those systems based on sedimenting active particles ([102], [104]).

4. Open questions and future perspectives

Until now, the colloidal assemblies shown in this thesis feature a circular shape with a central point defect as attractive unit. In this radial configuration, particle ordering results on a distorted lattice which can be regarded as a distorted "conformal crystal" (see **Fig. 83**) ([167]).

Conformal crystals can be understood as different mathematical transformations which allow triangular mapping on the plane (see **Fig. 83**). The most common definition of a conformal crystal involves a soft, deformed but topologically perfect crystal. As a consequence of the perfect lattice re-arrangement, angle preservation in conformal mapping results everywhere in a six-folded coordination. This is in contrast to the obtained clusters in this thesis. Here, particles can present different coordination modes, which can be directly related to the generation of density variations in the cluster ([168]).

Moreover, changing the geometry, and by replacing the circular topological defect with a radial NLC alignment by a continuous straight wall where the NLC director is aligned perpendicular to it, allows to obtain distorted conformal crystals where the particles spread along the wall and curvature should not play a role.

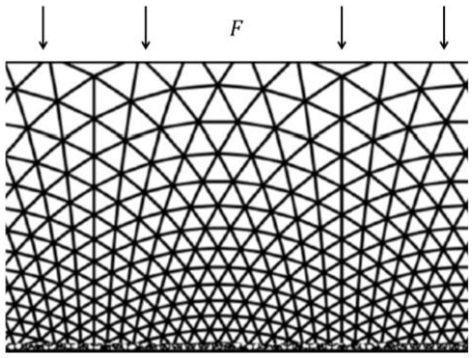

Fig. 83. Perfectly conformal lattice. This conformal lattice is the one used to model the behaviour of repulsive particles in a gravitational field.

The earliest experiments reported in the literature based on conformal crystals have been performed in an isotropic fluid using ferromagnetic spheres of about 1mm in diameter ([167]). Briefly, by applying a perpendicular AC magnetic field to the particles plane, the induced magnetic moment is along the applied field, and thus, particles exhibit a repulsive interaction in the self-assembly plane. By tilting the sample a certain angle, a gravitational force is introduced in the system allowing to obtain conformal crystals. A few years later, researchers showed that under confinement, and by using poly-methylmethacrylate (PMMA) particles of about 1 µm under the application of an AC electric field gradient, circular clusters are induced where the triangular lattice structure is mostly never lost ([169]). Actually, the latter looks like the nematic colloidal assemblies shown in this Chapter.

In this section, we present experiments based on colloidal self-assembly in a NLC mediated by a plane wall. In this case, colloidal peanut-shaped particles are propelled along the nematic director which is aligned perpendicular to the confining wall, thus mediating

colloidal self-assembly in one dimension. The obtained structures are similar to that of distorted “conformal crystals”.

4.1. Experimental system

The experimental NLC cells consist of a cell gap thickness of about 25 µm (see Chapter2, Sections 1 and 2). In this case, the cell gap is made by a NOA81 photosensitive resin (See also Chapter 5, Section 2). This feature enables to address particle self-assembly towards a localized wall where particles will aggregate and form the clusters. The experimental system is depicted in **Fig. 84**.

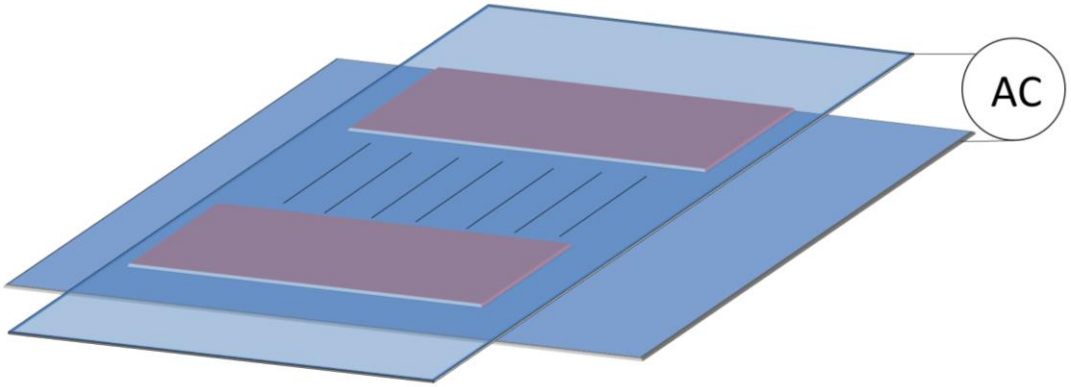

Fig. 84. Schematically depicted NLC cell. ITO plates are glued facing inwards within a defined cell gap thickness of about 25 µm achieved by a NOA81 wall, which is depicted in red colour in the scheme. Black lines denote the nematic far-field after application of an AC electric field, and thus, particle trajectories.

4.2. Distorted conformal crystals

In our experiments, the confinement is induced by a solid wall where particles self-assemble (**Fig. 85a** – see **Video15**). Thus, the confinement is only 1D, with absence of lateral confining walls.

The analysis of the cluster has been performed with the Delaunay-Voronoi triangulation, which reveals different particle rearrangement, with particles featuring five, six or seven nearest neighbours, although other coordination numbers can be found (**Fig. 85b** and **Fig. 85c**). This observation agrees with other experimental systems displaying conformal ordering ([169]).

As observed in **Fig. 85a** and **Fig. 85d**, the cluster organizes in two well-defined regions characterized by different states of aggregation after few hundreds of particles have accumulated. The inward region is an arrested, jammed state where particles remain mostly immobile with only minor rearrangements as the assembly grows. This region is followed by a linear decay which gives evidence of the inter-particle repulsive interaction (**Fig. 85d**). This is in agreement with the experiments shown in this Chapter featuring a radial geometry. The third phase, gas-like, corresponds to the outer region of the cluster where almost no particles are present (more experiments should be perfomed to characterize this region). Going further, one can observe that the normalized nearest neighbour distance increases with the distance to the wall, thus, we can conclude that the pressure exerted by the outer

particles is counter-balanced by the well-evidenced inter-particle repulsion and this can lead to distorted conformal crystals featuring both an inhomogeneous density profile and frustration in particle arrangement (**Fig. 85e**). The presence of non-spherical particles coupled to surface inhomogeneities and with the presence of short-range elastic LC interactions induces a distorted colloidal crystal where disorder is enhanced with respect to that shown in refs. ([167]) and ([168]).

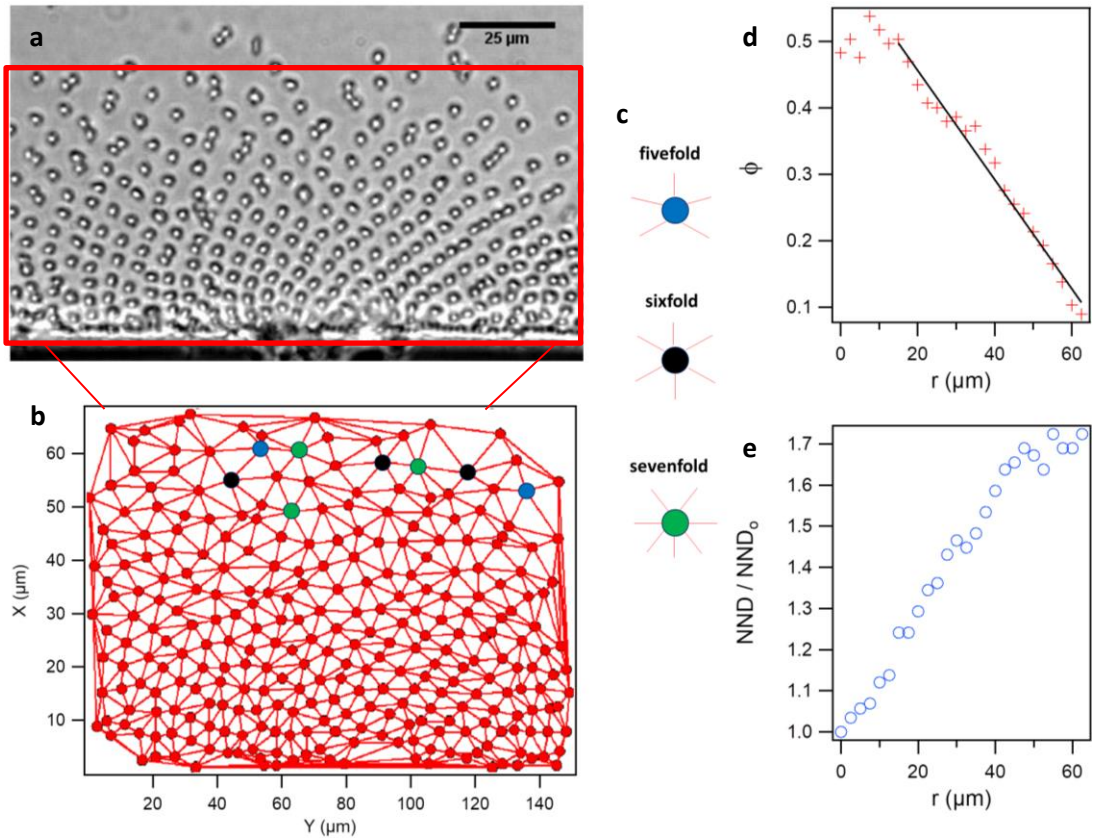

Fig. 85. Distorted "Conformal crystal" in a planar geometry. a) Bright-field micrograph of a cluster of peanut-shaped particles assembled into a plane interface while an AC electric field of f = 15 Hz and amplitude 0.76 V · μm^{-1} is being applied. The red square denotes the area of analysis. **b)** Delaunay triangulation for the particles in the assembly shown in **a)**. The different coordination modes are represented by different coloured dots, which are described in **c)**. **c)** Coordination modes for the particles in the assembly, where particles display until 8 different neighbours, although only five (●), six (●) and seven (●) coordination modes are represented. **d)** Area fraction occupied by the particles as a function of the distance to the solid wall. **e)** Nearest neighbour distance (NND) versus the distance to the wall in the cluster. Here, NND_0 denotes the minimum inter-particle distance. See **Video15**.

5. Conclusions

In this chapter, we have investigated the out-of-equilibrium two dimensional assemblies of anisometric colloidal particles driven towards a single point topological defect in a nematic liquid crystal. The anisotropy of the dispersing medium combined with the experimental geometry result in the onset of different electrokinetic phenomena generated by the AC electric field.

- The presence of a photosensitive surface allows for the *in situ* elastic modification of the underlying nematic liquid crystal pattern, obtaining two different configurations: aster and rotating-mills. Moreover, elasticity also plays a role in forcing the driven particles to orient along the nematic director, thus allowing for steering colloidal trajectories.

ASTER – Like configuration

- The external electric field provides a constant propulsion force to each particle that promotes particle aggregation towards the topological defect, but also generates a pairwise repulsion force that leads to a cluster steady-state characterized by different phases and packing densities, namely an inner-jammed core, followed by a liquid-like phase and ending in a diluted, gas-like phase.

- The radial configuration allows to monitor the continuous pressure-driven gas to solid-like phase transition where some degree of hexatic order is present. Surprisingly, we find a re-entrant behaviour in the colloidal ordering as the bond-orientational order reaches a maximum in the liquid-like phase, where colloidal arrangement is enhanced by inter-particle repulsion.

- Our experimental results suggests that the frequency-independent pairwise inter-particle repulsion is a combination of multiple effects, including hydrodynamic coupling of the electrokinetic flows induced around the particles and dipolar repulsion arising from the choice of the material and the experimental nematic cell geometry.

- Numerical simulations agrees with the experiments, and reveal that the geometry of the observed assemblies is the result of a balance between different electrokinetic phenomena arising from hydrodynamics, dipolar interaction and phoretic forces evolving at different length scales.

- Qualitative and quantitative agreement between the experiments and numerical simulations has been achieved by tuning the simulation potential parameters leading to a nearly frequency-independent repulsion interaction in the range of frequencies studied. This allows us to conclude that all the physical ingredients present in the system can be cast into a long-range effective repulsive potential.

- Importantly, and differently to typical nematic colloidal objects, the elasticity of the liquid crystal plays only a secondary role in the observation of phase coexistence.

- The colloidal assemblies have been analysed in terms of a mechanical force between centripetal driving acting on individual particles and pairwise inter-particle repulsion which oppose to particle aggregation. The $p - \phi$ isotherms, corresponding to the liquid-like region, obtained at different driving frequencies collapse onto a single master curve. Additionally, are also continuous throughout all the cluster states where the particle ordering is fully never lost.

- Experiments performed at different driving frequencies do not show differences on the gas-like region, where differences arising from the driving propulsion or "the particle's activity" do not play a role. Thus, we cannot assume our colloids as active. On the other hand, colloidal particles trajectories are coupled to the nematic director. Thus, we can conclude that our system is purely driven.

- Although we have imposed the formation of radial clusters by means of a topological defect, we do not expect our results to depend on the designing geometry, and similar effects could be expected in a free-defect assembly or in a confined 1D system.

ROTATING MILL – Like configuration

- The tangential component of the velocity prevents to develop the jammed core for the studied assemblies, although it is visible when thousands of particles reach the cluster. As a consequence, the radially-averaged density profile follows a linear decay with the distance to the centre of the cluster in analogy to the liquid-like region of the asters assemblies.

- When particles are self-assembled around the topological defect, they are spinning around the central defect core with a characteristic azimuthal velocity, which reaches a maximum when all particles present in the ensemble are rotating as if a solid body. This is in contrast to the radial velocity, which decreases as the cluster grows.

- Dynamic clustering can also be characterized by the normalized angular momentum, which determines if the ensemble of propelling particles is in a single-mill state. In our experiments the angular momentum M increases in time towards unity giving evidence of the full ensemble rotation around a single point.

- The theoretical model and further simulations allow to reproduce both qualitatively and quantitatively the experiments performed where the underlying pattern features a spiral-like texture and all the electrokinetical physical ingredients are at play.

Another aspect of these colloidal clusters is particle organization. In our experiments the balance between the phoretic driving and the pairwise repulsion interaction leads to a lattice-like structure resembling a conformal crystal where the triangular lattice is distorted due to experimental issues. Thus, new physical colloidal ordering in out-of-equilibrium can emerge due to both anisotropies on the dispersing and on the dispersed media.

On the whole, our experiments demonstrate control capabilities for micro-scale colloidal self-assembly by using anisotropic materials. Here, the degree of control in the driving strength and the versatility to switch between steering directions, among others, are some the advantages of this method.

These non-equilibrium colloidal systems can be relevant to study dynamic aspects of driven rather than active systems but can also be useful as featuring similar collective behaviour such as swarming or flocking, which will be evaluated on the forthcoming Chapter 5.

Chapter 5

Collective colloidal transport

1. Introduction

One of the most important capabilities of soft active matter is its ability to spontaneously organize from a random initial state into complex self-organized structures on different length scales, such as swarms ([170]) or flocks ([75]). Typically, this requires communication between individuals in the same group and is performed through complex internal pathways.

In contrast to living systems or active matter, where the organisms response to an external stimuli is determined by internal signalling between entities, the motion of propelled particles can be externally adjusted, e. g. by optical ([171]), electrical ([118]) or thermal ([172]) fields. Experiments based on the mentioned systems show a large sort of dynamical states ranging from living crystals ([98]) to swarming processes ([118]). Moreover, imposing both geometrical and boundary conditions allow conditioning particles' collective behaviour.

Constricted pathways affects the transport properties of systems featuring collective behaviour ([120]). At the macroscopic scale, the presence of disorder in the form of walls, barriers or obstacles is able to modify or alter the flow of, for instance, granular media ([173]). Ensembles of particles forced to pass through small constrictions display complex dynamics, which can include flow intermittency due to the formation of particle bridges or arches ([174]). The latter is known as "clogging" phenomena and is the responsible for the flow arrest in typical systems such as microfluidic devices. Moreover, clogging effects are also directly related to "jamming", which occurs when an ensemble of particles reaches a solid-like phase. In contrast to jamming, clogging effects are more difficult to be controlled and characterized due to the system heterogeneity.

Typical experimental examples for clogging realizations are addressed at the level of a single bottleneck ([174]), although experiments on ordered ([175]) or disordered ([176]) landscapes lead also to a rich variety of transport phenomena. Using colloidal particles as model systems for clogging allows both to induce driving forces for particle transport and to tune the inter-particle interactions leading to a high level of clogging flexibility.

Another interesting feature that is attracting interest is the use of both microfluidic devices and anisotropic materials, such as nematic liquid crystals. The study of nematic liquid crystals in the field of microfluidics is still at an early stage, although a systematic study of the influence of the channel dimensions and geometry, the anchoring conditions at the bounding substrates or the magnitude of the flow rate have been investigated ([177]). Furthermore, the dispersed colloidal particles in the nematic liquid crystal constricted by the microfluidic device can be specifically guided or transported by using the flow-induced structures like disclination lines ([178]).

In this Chapter we show experiments based on understanding the dynamics of an ensemble of flocking particles and the implementation of obstacles for the flock to pass through, but also the collective behavior of an array of self-assembled clusters. In these experiments, the anisometric particles are driven under the LCEEK (see Section 4.2.2) mechanism and are propelled through pre-defined paths, both photo-induced and by means of microfluidic

boundaries. For experiments featuring a photosensitive surface, particles ensembles can be transported anywhere within the NLC cell allowing for flocking states. Furthermore, we have started to explore the effect of bounding the colloidal dispersion in a microfluidic device under the application of an AC field. In this case, the material anisotropic viscosity can adopt different values within the cell, which will affect particle transport. The latter, coupled with the typical features of NLC, such as anchoring conditions or elasticity leads to new physical observations of nematic colloids propelled under confinement.

2. Experimental setup, materials and methods

Two different experimental setups have been used in this chapter. The first one has been described in the previous Chapter 4, which consists on a photosensitive azosilane layer capable to switch between the *trans* (homeotropic) to the *cis* (planar) isomer (NLC anchoring condition). Moreover, the colloidal dispersion can be confined in a specific geometry with the preparation of microfluidic channels.

- SYSTEM 1 – EXPERIMENTAL PHOTOSENSITIVE CELL

The experimental NLC cells are equivalent to those shown in Chapter 4, Section 2. Briefly, the cells consist on two ITO coated glass plates facing inwards featuring a cell gap thickness of about 20 µm. One of the plates features a photosensitive surface while the other is treated to achieve a strong homeotropic anchoring of the mesogens.

The same peanut-shaped microparticles have been used as in Chapter 4 whose asymmetry allow breaking the flow patterns around the particles induced under the LCEEK mechanism. The NLC is MLC-7029, which features negative dielectric anisotropy.

- **Irradiation protocol**

As explained in Chapter 4, section 2, irradiation of the photosensitive surface is achieved through the microscope objective, typically x20. Briefly, irradiation of the sample with UV-light (360 nm) promotes the transition of the AZO molecules into the bent *cis* form within seconds, which triggers local planar anchoring of the NLC.

For the experiments described in this chapter there are 2 different irradiation protocols:

1. Swarm translocation

The first set of experiments presented in this Chapter corresponds to the translocation of swarms of particles, which can be transported everywhere within the cell.

Initially, UV irradiation forces the isomerization of the AZO compound, and thus, LC molecules develop an in-plane pattern starting from the centre of the light spot. Two different configurations can be achieved due to NLC elasticity, aster or rotating mill (see Chapter 4). Afterwards, the topological defect can be pulled from the initial position (center of the topological defect) for a certain distance. This translocation is performed through a disclination line that forms as the UV light spot is dragged between the initial and the final destination on the photosensitive surface.

2. Pattern array

The second set of experiments present in this Chapter corresponds to the formation of an array of patterns.

In this case, the irradiation protocol is different to the one shown before although sharing the same physical principle and the focusing through the microscope objective.

This protocol is based on placing a physical mask between the LED UV source and the microscope objective (**Fig. 86a**). The mask consists on an acetate slide that selectively blocks light (**Fig. 86b**). In some cases, the masks display a Gaussian profile of grey intensities emanating from the centre of the object to project which induces a light gradient similar to that obtained in experiments performed in Chapter 4. These allow to induce from single point defects to arrays of topological defects, but also patterning different shapes or even to "write" above the photosensitive surface as shown in **Fig. 86c**.

To project it in our samples, the mask is placed at the field diaphragm of an epi-illumination module in the microscope, and focused on the sample by means of the microscope objective (see also Chapter 2, section 6.1). Different motifs have been printed and tested, as can be observed in **Fig. 86c** and forthcoming sections (see Section 3.2).

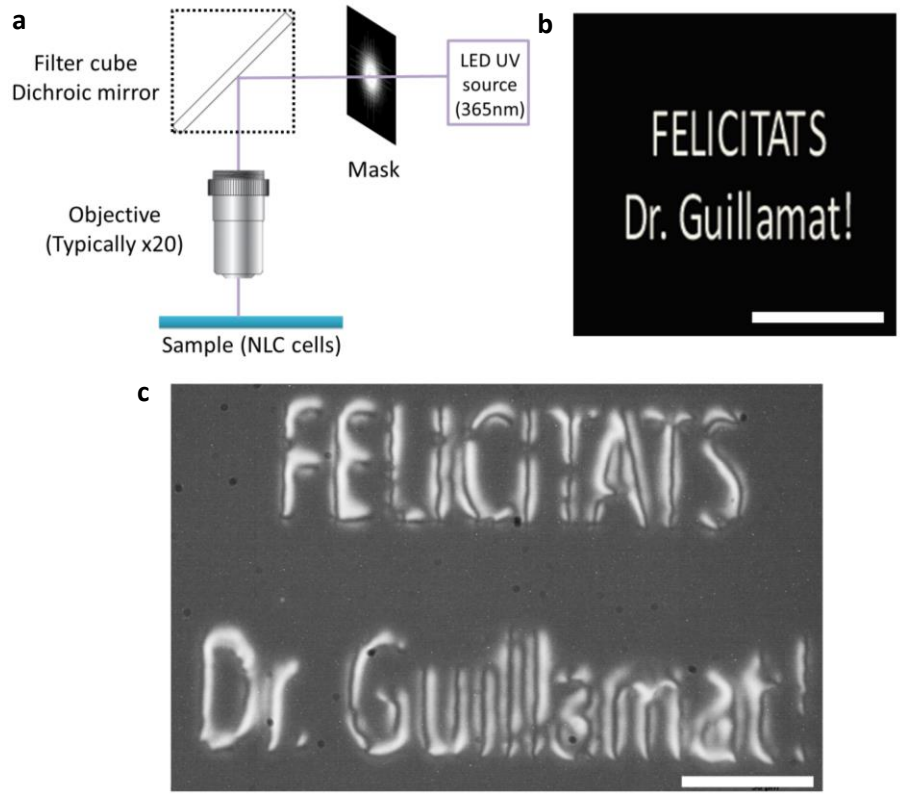

Fig. 86. Irradiation protocol using masks as blocking light agents. a) Schematic part of the experimental setup of the custom-built LED epi-illumination setup mounted on the optical polarization microscope used in this Chapter. **b)** Acetate slide, which selectively blocks light, allows to "write" or define patterns above the photosensitive surface. The scale bar is 3 mm. **c)** Experimentally obtained imprinted pattern after UV irradiation using the procedure shown in **a)** and the mask in **b)**. The scale bar is 100 µm.

- SYSTEM 2 – EXPERIMENTAL MICROFLUIDIC-CONFINED CELL

The experimental NLC cells constructed are similar to those shown earlier, although constructed using soft lithography. The PDMS (polydimethylsiloxane) acts as a mould for the UV-resin NOA81 to fill in. The latter allows to confine the colloidal dispersion in a preferred geometry but also defines the cell gap distance.

More precisely, the geometry of the NLC cell consists of two ITO coated glass plates featuring strong and permanent homeotropic anchoring of the mesogens, which are rubbed

to impose a preferred far-field nematic direction that is set along the microfluidic device. The two plates are stuck together facing inwards by using a photo-polimerizable resin, NOA81 UV, which replicates the shape of the soft PDMS master stamp ([179]), as detailed below. The replicated UV-resin pattern allows both to confine the colloidal dispersion and to act as the cell gap distance, which is about 25 µm.

In these experiments, we use the same peanut-shaped microparticles dispersed in the NLC MLC-7029.

- **Fabrication of the PDMS stickers**

The stamps are made using a soft lithography technique. Initially, a master is made with the photoresin SU-8 using photolithographic techniques and is placed and stuck in a Petri dish (**Fig. 87**). Afterwards, a typical amount of 20 mL of PDMS is used to fill the Petri dish to form a layer of about 3 mm in thickness (**Fig. 87b**). The Petri dish is left in the oven at 60^{o}C for about 4 hours. The last step consists on peeling the PDMS master layer, which contains the desired mould, from the Petri dish (**Fig. 87c**).

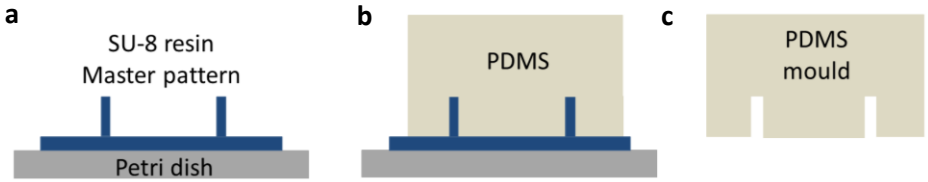

Fig. 87. Sketch of the fabrication process of a PDMS mould. a) The SU-8 resin master pattern is attached to the Petri dish. **b)** The Petri dish is filled with PDMS which replicates the master pattern shape. **c)** The polymerized PDMS layer is carefully peeled from the Petri dish obtaining the PDMS mould.

- **Assembly of the microfluidic devices**

Once the mould is prepared, it has to be attached to the ITO surface. In our case, and for our purpose, the sealing is reversible and the mould can be reused (**Fig. 88a**). The voids left on the mould are filled with the photo-polimerizable resin NOA81 by means of capillary forces. This process is performed at about 50^{o}C to decrease the resin's viscosity, thus ensuring the total spreading of the compound along the mould. Afterwards, the photo-polymerizable resin is cured using a UV gun (360 nm) for 5 seconds (**Fig. 88b**). Since oxygen inhibits the free-radical polymerization required to build the polymer network, the PDMS permeability to gases ensures that a thin superficial layer of the photo-polymerizable resin remains uncured. Thus, the UV-cured pattern is attached to the ITO substrate, but the superficial area of the cured pattern is still active, which allows for NLC cell self-assembly. For this purpose, an ITO substrate facing inwards is pressed towards the not yet UV-cured pattern and a UV-gun is used to seal the cell (**Fig. 88c**).

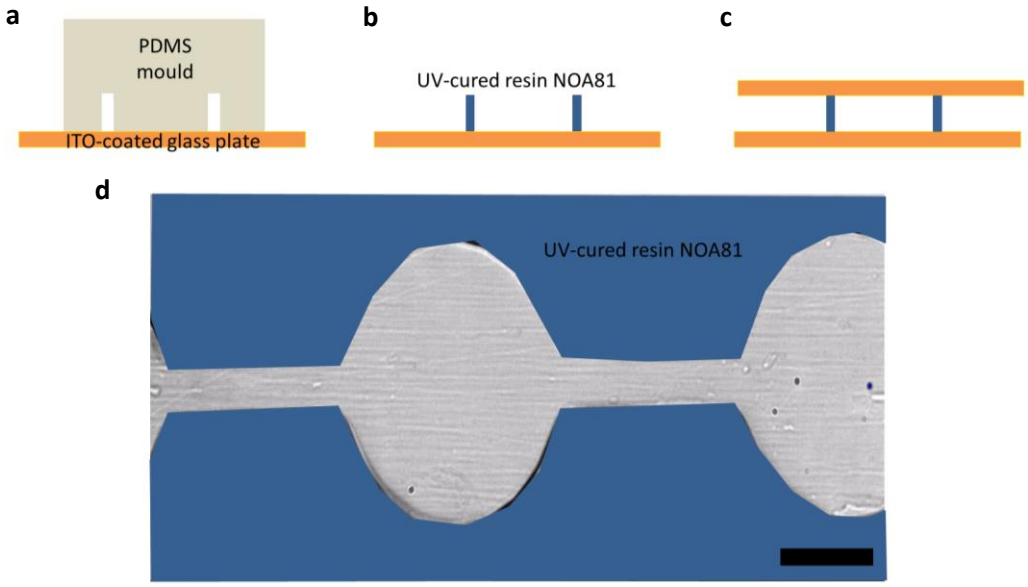

Fig. 88. Sketch for the assembly of a microfluidic device. a) The PDMS mould is gently pressed onto the ITO surface and the voids left are filled with the photo-polymerizable resin NOA81. **b)** Sketch of the experimental setup after UV-polymerization of the resin. **c)** Self-assembly of the microfluidic NLC cell allowed by the uncured thin film of the photo-polymerizable resin. **d)** Bright-field micrograph of a microfluidic NLC cell displaying a channel with different shapes. The scale bar is 100 µm. The part corresponding to the UV-cured resin NOA81 is coloured in blue.

3. Results and discussion

To better encompass the discussion of the experiments shown in this Chapter, the explanations and data presented is split as follows. Initially, we present experiments and their data treatment based on the transport of colloidal swarms, which can also be described by using the Theoretical Model present in Chapter 4, section 3.4. Here, Dr. Arthur Straube also has performed some simulations to study the dynamical transport of colloidal clusters. Afterwards, we will present the colloidal collective dynamics and the topological constraints when an array of topological defects is patterned onto the photosensitive NLC cell. Later, we will show some experiments related to clogging effects which have been performed by using microfluidic channels. Finally, some new colloidal collective aspects when passing through microfluidic constrains are presented.

3.1. Swarm translocation

The transport of swarms has been studied using both experiments and simulations.

- EXPERIMENTS

In the previous Chapter 4, we have described the formation of a single cluster, either an aster or a rotating-mill like configuration. In this sense, the photosensitive surface also allows to transport this dynamic state everywhere within the cell.

For a given assembled cluster, particle speed due to electroosmotic flows generated around the particles, or in other words by the LCEEK mechanism, drops to zero at electric field frequencies above 40 Hz (see Chapter 4, Section 2). In our case, and to ensure a great stability of the NLC, we chose to work at a frequency of 1 KHz as the frequency to "freeze" the assembly at place, while taking advantage of the photosensitive surface to pull the topological defect from an initial position (center of the assembled cluster) for a certain distance. This translocation is performed through a disclination line that forms as the UV light spot is dragged between the initial and the final destinations on the photosensitive surface. This process is demonstrated in the sequences of images in **Fig. 89**, where a mill pattern is translocated a distance of about 175 µm (see also **Video16**). During translocation, the colloidal swarm moves as a polarized pattern developing a leading edge which is followed by all the other particles. These dynamic features allow studying flocking aspects by evaluating the two corresponding order parameters *M* and *P* (**Fig. 89**) (see also Chapter 4, Section 3.2 and 3.5).

To better understand the process and the dynamics involved we will briefly describe the whole protocol related to the analysis of the corresponding order parameters.

Initially, a colloidal mill is assembled under f = 10Hz, thus the angular momentum, *M*, is enhanced with respect to the polar order parameter, *P*. The colloidal rotating mill is subsequently held or frozen in place by switching the frequency to f = 1KHz, where the LCEEK mechanism is deactivated but the cluster do not disassemble. While the cluster is immobile (f = 1 KHz), a UV-light spot is dragged from the center of the mill to a destination spot (**Fig. 89a**). When the frequency is switched back to f = 10Hz, LCEEP becomes active

again, dismantling the assembly as particles are driven towards the destination spot. Both order parameters rapidly exchange values, as seen in **Fig. 89b**, raising the value of *P* and reducing the angular momentum, *M*, as the cluster disassembles. During the swarm translocation, particles move at a constant speed towards the translocated topological defect, raising the value of *P* to unity, while *M* tends to vanish. After 150 s, enough particles have clustered around the destination spot for the mill pattern to form again, thus increasing the corresponding value of *M* and decreasing the degree of alignment of the propelled particles, thus lowering *P*.

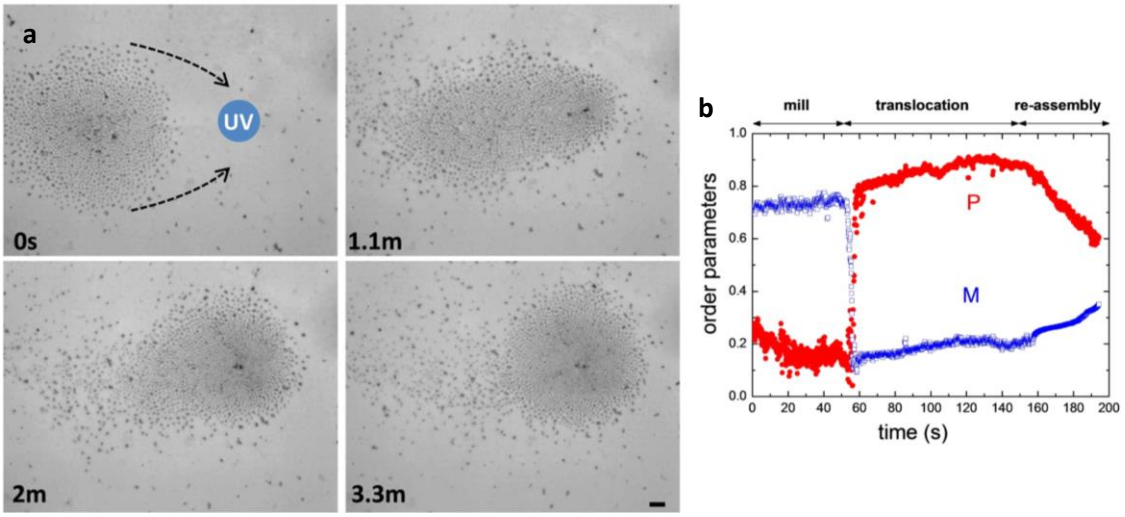

Fig. 89. Colloidal swarm translocation. a) Images showing a cluster that is transported to a different place of the experimental cell due to *in situ* reconfiguration of the NLC field with UV light (360 nm). The blue disk in the first image indicates the location of the translocated topological defect. The experiment shown here has been performed with an AC field amplitude of $0.76\ V \cdot \mu m^{-1}$ and frequency f = 10Hz. The scale bar is 20 µm. **b)** Order parameters *P* and *M* measured from the particles trajectories in **a)**. See also **Video16**.

- SIMULATIONS

In order to numerically reproduce the experimental situation obtained in **Fig. 89**, Dr. Arthur Straube has performed a procedure similar to the experimental one. In particular, the operation of transferring one defect from one initial position to a new one at a certain distance has been achieved by switching from one spiral pattern to another one with a shifted position after a given time, t (**Fig. 90**). The two different patterns have been simulated using the equation shown in Chapter 4, section 3.4 featuring the two of them different chirality, as shown in Fig.91a.

After, Dr. Arthur Straube has simulated the translocation process by using the theoretical model described in Chapter 4, section 3.4. The system consists on N=1000 particles dispersed in a rectangular box with dimensions, L_x=500 µm and L_y= 650 µm.

The results of the numerical simulations are shown in **Fig. 90** (see also **Video17**) with the corresponding calculated order parameters *M* and *P,* which are shown in **Fig. 90c.** At time t = 0 s, the particles are uniformly distributed within a circle of radius 200 µm. The colloids start to move performing spiral orbits towards the centre of attraction forming a rotating mill. During this process, both parameters, *M* and *P*, are non-vanishing and their evolution has opposite tendencies in agreement with the experimental observed trends.

The switch from pattern1 to pattern2 (**Fig. 90a**) occurs at t = 50 s, when the behavior of *P* and *M* displays an abrupt jump caused by the instantaneous shift of the "centre of attraction", and thus, particle propulsion to the translocated position. In contrast to this instantaneous switch, reconstruction of the destination mill is gradual, in analogy with the experimental observed trends, as can be seen from the smooth decrease in *P* and increase in *M*. Eventually, the centre of mass of the particles ensembles nearly reaches the translocated position of the spiral pattern, and we observe another rotating mill. This state approximately corresponds to $P \approx 0$ and $M \approx 1$.

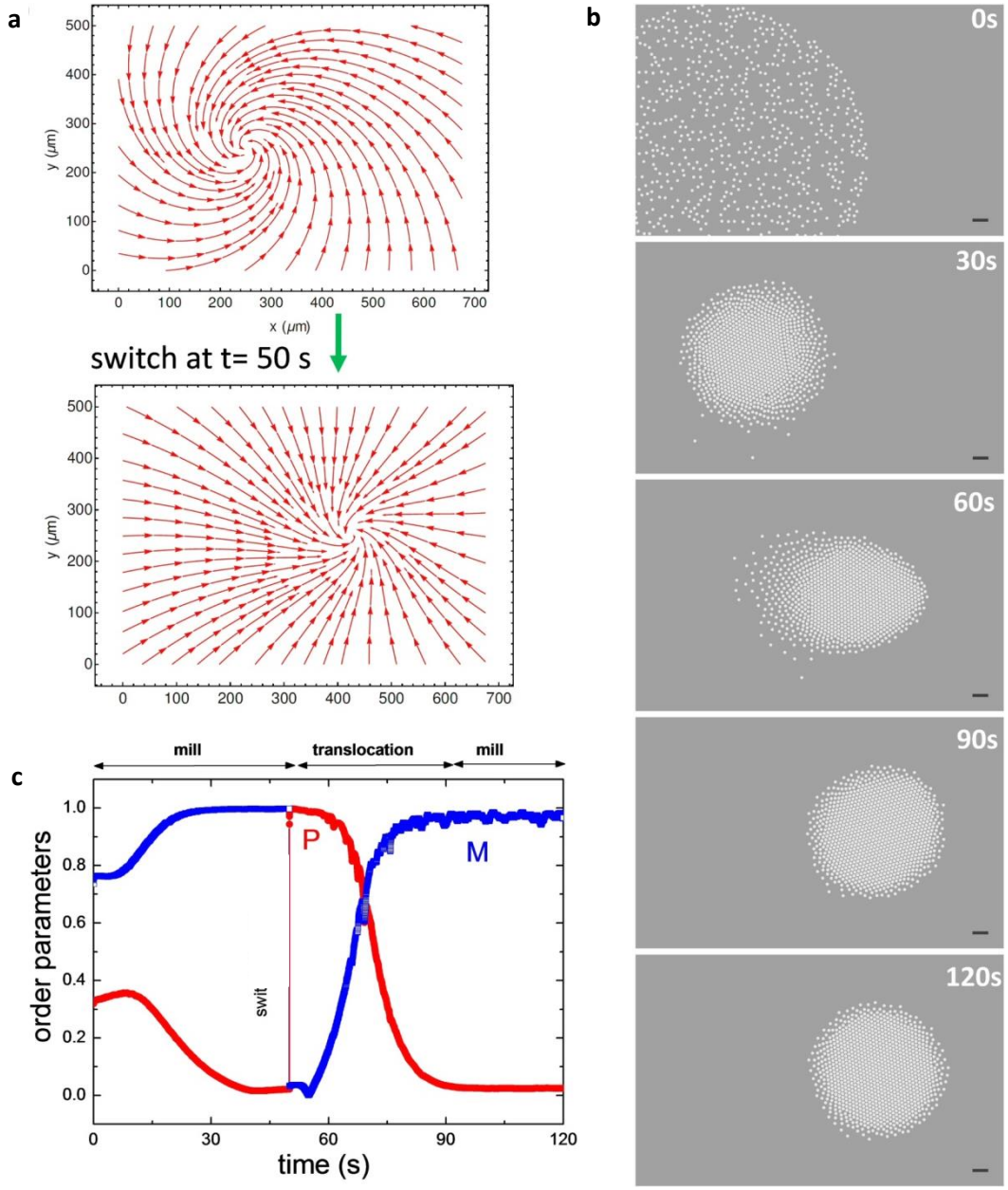

Fig. 90. Simulations of the colloidal swarm translocation. a) Image shows the vector field spiral pattern obtained. Both vector fields cover the same area (500 x 675 μm^2) and are exchanged in the simulation after t = 50 s. **b)** Sequence of images from numerical simulations showing the translocation process for N = 1000 particles. Before the switching time, t, a colloidal mill is assembled above the pattern shown in top of **a)**, and later is transported by switching the underlying pattern, bottom of **a)**. Scale bars for all the images are 20 μm. **c)** Corresponding normalized order parameters *M* and *P* versus time. Note the different initial state in simulations and in experiments (see above). In simulations, the colloidal mill does not need to be frozen before translocation.

3.2. Patterning the photosensitive substrate

Taking advantage of the photosensitive surface allows to print any desired shape and size where the photo-induced pattern is modulated through the physical mask. The latter allows inducing chains of rotating mills or even 2D colloidal objects constituted by of out-of-equilibrium colloidal assemblies.

Two adjacent UV light-induced topological defects are shown in **Fig. 91** displaying strength +1 (blue dots in **Fig. 91**). The NLC imprinted pattern has been realized by using a mask which contains two adjacent entities shown **Fig. 91b** (inset). The latter feature a linear grey level density decay emanating from the centre to the outer region, allowing for a radial configuration of **n** after irradiation.

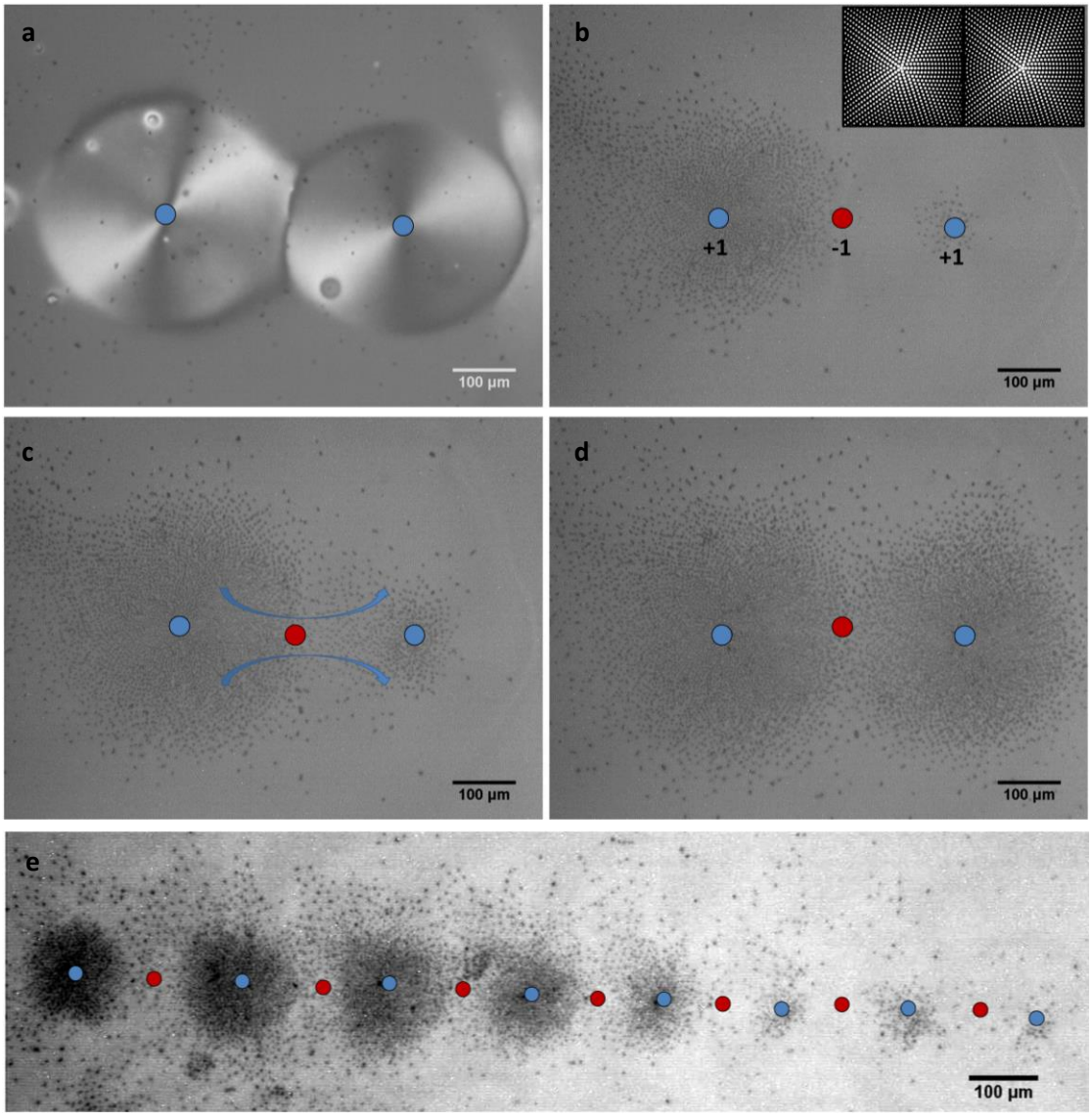

Fig. 91. Chains of colloidal rotating mills mediate particle transport. a) Two adjacent UV-light-induced topological defects displaying *s=+1* (●). t = 0 s. **b)** Particles self-assemble around the topological defect located at the left of the image while an AC electric field of amplitude $0.76\ V \cdot \mu m^{-1}$ and frequency f = 10Hz is being applied. t = 50 s. Red (blue) dots denotes s=+1 (s=-1) topological defects. **c)** Once the rotating mill on the left has accumulated enough particles, the *s=-1* (●) defect mediate particle transport between the two clusters. t = 120 s. See also **video18**. **d)** Both clusters are constituted. t = 220 s. **e)** MIcrograph of another colloidal particle transport experiment displaying a chain constituted by eight rotating mills entities. The particles flow is from left to right.

The induced s=+1 topological defects act as attractor points for particles to self-assemble (**Fig. 91b**). Initially, under the application of the AC field, all particles tend to self-assemble to the topological defect on the left hand side of **Fig. 91b**. After a few minutes, and when particles have occupied all the area determined by the UV-light spot corresponding to a single cluster, a topological defect featuring s=-1 (red dots in **Fig. 91**) and located in between the two attractive ones, mediates particle transport between the latter (**Fig. 91c** – see also **Video18**). This topological defect s=-1 appears from the condition that the elastic matrix, in the continuum, must have a zero net topological charge, since defects are created in a homogeneous director field. In order to compensate the two s=+1 topological constraints, one s=-1 is created between the two induced topological defects and the other elsewhere within the cell.

Going further, one can induce a 1D chain of rotating mills (s=+1). In this system, particle transport between entities is mediated by the s=-1 topological defects (**Fig. 91e**). This fact opens, basically, two new perspectives for our work based on colloids dispersed in NLCs. On the one hand the elastic frustration of the NLC material due to topological constraints and, on the other hand, the out-of-equilibrium colloidal assembly and transport for the designing and use of micro-machines.

The experiments shown in this thesis are based on driven particles in anisotropic fluids, where particle propulsion is coupled to the material far-field director. Thus, controlling the underlying pattern allows modifying particle trajectories, and thus, the type of colloidal assemblies. Taking advantage of the photo-mask technique, we have been able to induce 2D arrays of out-of-equilibrium colloidal clusters (**Fig. 92** – see also **Video19**).

In **Fig. 92** we show a 2D array of topological defects distributed in the form of 3 columns x 3 raw. Actually, the UV-light induced mask contained a larger grid, which exceed the field of view for the x10 objective but still allow studying regular patterns. Under the application of an AC field, the elastic matrix adopts the texture shown in **Fig. 92** where the nine photo-induced topological defects s=+1 (blue dots in **Fig. 92**) appear connected through s=-1 entities (red dots in **Fig. 92**). As comented, to satisfy the topological constraints, an s=-1 topological defect is created in between each pair of s=+1 defects, leading to an unbalanced elastic matrix containing thirteen s=-1 topological defects and the nine photo-induced s=+1 topological defects. Interestingly, the elastic matrix itself induce four s=+1 topological defects (green circles in **Fig. 92**), specifically located, in order to compensate the total topological charge reaching an s=+1 for the whole grid. Finally, that will be countervailed by inducing an s=-1 topological defect everywhere within the cell.

Furthermore, we show the colloidal self-assembly in 2D-induced topological arrays. When particles tend to reach the attractive point, the photo-induced topological defects (red dots) feature a rotating mill configuration, while the attractive points induced by the elastic matrix itself (green circles) feature aster-like assemblies. Here, in our driven system, particles follow the trajectories defined by the underlying pattern. Thus, different self-assembled configurations have been found for the photo-induced topological defects and the ones induced itself by the elastic matrix.

Even though this is just a proof of concept for collective colloidal transport, these systems allow studying reversible elastic frustration in NLCs, meaning that the pattern, and thus, the colloidal assemblies can be easily induced or erased by using light sources. This can allow to study interesting topological aspects.

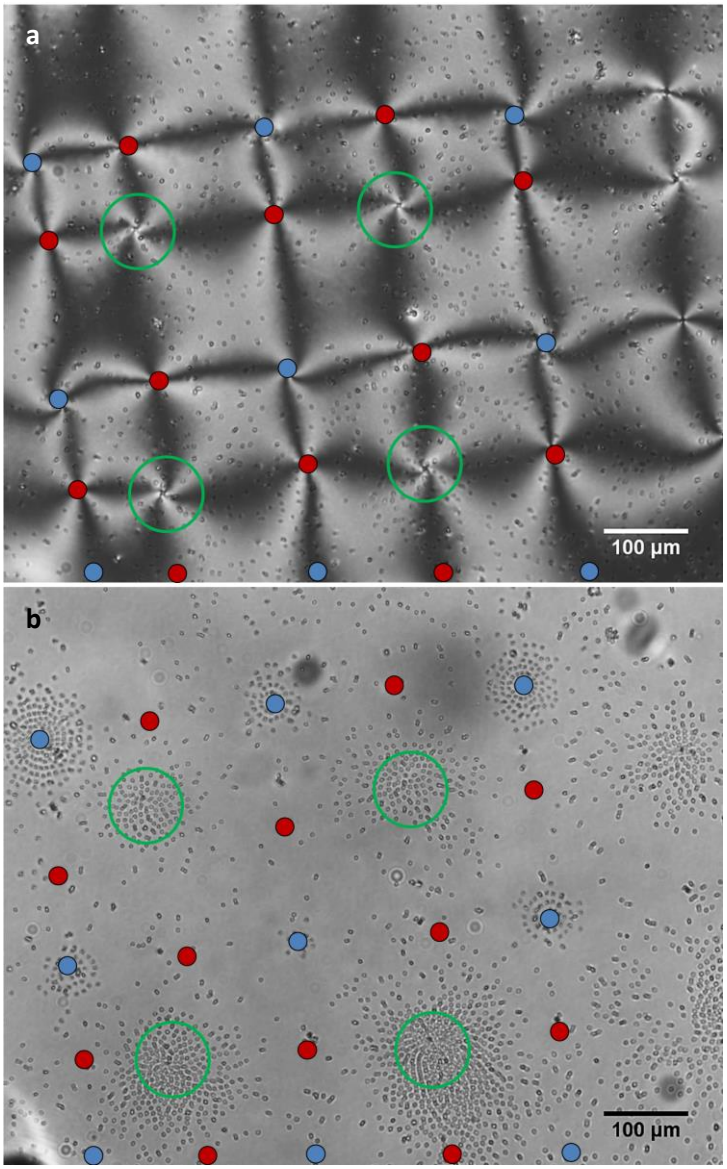

Fig. 92. Two-dimensional array of photo-induced objects. a) Image obtained under crossed polarizers of an imprinted pattern of 3x3 photo-induced topological defects while an AC electric field of amplitude $0.76\ V \cdot \mu m^{-1}$ and frequency f = 10 Hz is being applied. Red dots (green circles) denotes photo-induced (self-induced) topological defects with s=+1. Contrarily, blue dots denotes topological defects with s=-1. The s=+1 defects denoted by green cercles are induced in order to compensate the total topological charge of the whole elastic matrix. **b)** Bright-field micrograph of the colloidal clusters assembled above s=+1 topological defects while the s=-1 topological defects mediate particle transport between attractive points. Notice that the points below the image denoting topological defects do not correspond to the precise location of them. See also **Video19**.

3.3. Microfluidic devices

In earlier sections, ensembles of colloidal particles were transported along arbitrary paths above the photosensitive layer by pulling the initial topological defect position to another one mediated by the UV-light spot or by inducing one- or two-dimensional arrays of colloidal

clusters. Thus, one can think that this technique can be combined with the flow in microfluidic devices. In our case, and to simplify the experimental realization, we have implemented microfluidic channels in the NLC cells featuring no photosensitive substrate, although the main molecular orientation will be fixed along the microfluidic device (see section 2). In such systems are present different effects due to flow constriction, such as clogging.

Typically, clogging effects have been observed in systems of micron-sized particles dispersed in isotropic fluids due to fluid pumping along narrow paths ([180]), similarly to that observed in granular media ([181]). In contrast, we have not been able to find bibliographic data of micron-sized colloidal particles dispersed in a NLC which are driven along a microfluidic device featuring narrow paths under the application of an external AC field. It must be taken into account that particles dispersed in a NLC had been driven before in a microfluidic device by using disclination lines ([178]).

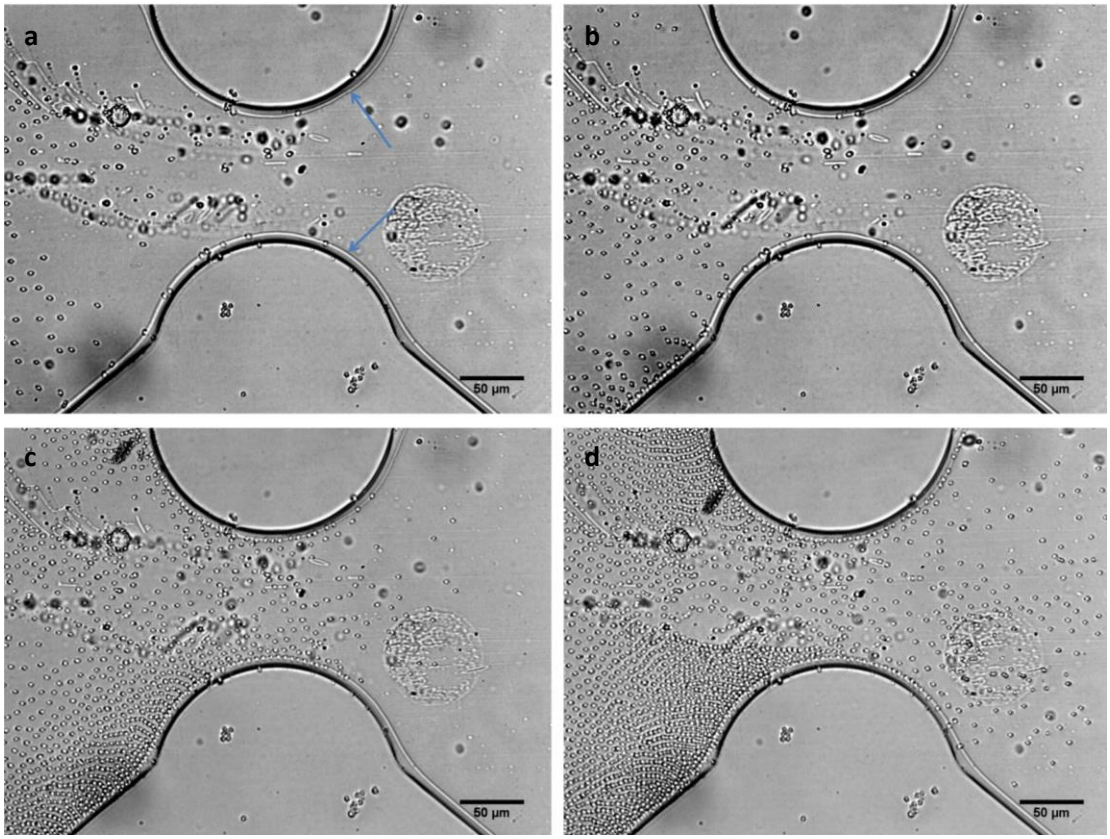

Fig. 93. Clogging effect of particles dispersed in a NLC and driven through a narrow constriction. a) Initially, particles are driven towards the narrow (75 µm spaced) path while an AC electric field of amplitude $0.76\,V\cdot\mu m^{-1}$ and frequency f = 10 Hz is being applied. Blue arrows denote singularities in form of disclination lines. **b)** Particles reach the field of view and start to self-assemble into the walls of the microfluidic channels after 25 s. **c)** The microfluidic channel wall gets saturated of particles and some of them pass through the constriction (80 s). **d)** Finally, particles stick to the wall and build a grid preventing particle transport through the narrow path (160 s). See **video20**.

Particles propelled in confined microfluidic environments behave as colloidal flocks travelling in a defined plane at a constant speed (**Fig. 93a,b**). The flock of particles occupies the full width of the device (**Fig. 93c**), until reaching both the confining wall and the narrow path (**Fig. 93c,d** – see also **Video20**). When particles get close to the wall, they get attached to it

similarly to the conformal crystal experiments shown in Chapter 4. Under the application of the AC field, singularities in form of disclinations lines (denoted by blue arrows in **Fig. 93a**) appear tracing the confining walls. Thus, the latter can act as attractive entities for the particles to form clusters building large structures which allow for particle stacking and prevent particle flow. The "clogged" steady-state achieved in our system is shown in **Fig. 94a**. Interestingly, the clogged state obtained in our experiments seems to be the opposite to that typical observed for isotropic fluids (red arches in **Fig. 94b**). Although in our system particle aggregation is avoided due to the repulsive interaction between particles (assessed in Chapter 4), here, clogging effects do not come from the flow constriction over a narrow path but from the interaction between particles and the components constituting the NLC cell.

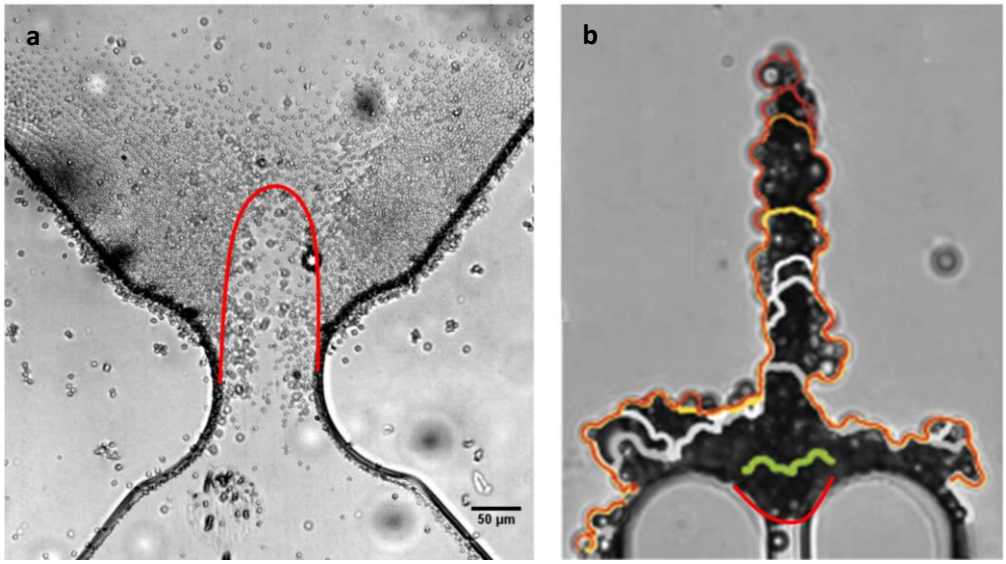

Fig. 94. Comparison between colloidal clogging effects in isotropic and anisotropic fluids. a) Steady-state of particles stacked on the wall forming an arch-like chaining in the opposite direction to that typically observed for isotropic fluids. The experiment has been performed while an AC electric field of amplitude $0.76\ V \cdot \mu m^{-1}$ and frequency f = 10 Hz is being applied and the photogram corresponds to 200 s of the sequence shown in **Fig. 93**. The image has been rotated 90° to better show the clogging effect. **b)** Typical image displaying the aggregates shape obtained in a single pore isotropic system. Particle diameter is of 4 µm. Adapted from ref. ([180]).

4. Open questions and future perspectives

Most of the work shown in this Chapter 5 is still an open question. In this section, we will show some future potential use of the techniques shown during the development of this Chapter 5, which can address the study of frustrated lattices of colloidal self-assembled clusters or the study of the colloidal dynamics performing well-defined and complex trajectories, as further explained.

4.1. Patterning the photosensitive substrate

Controlling the molecular orientation of the NLC allows to define the colloidal trajectories that particles may follow. As shown in Sections 3.1 and 3.2, photo-patterning the substrate, and thus, the NLC allows inducing from single topological defects to arrays of self-assembled clusters. In experiments shown in Chapter 4 and 5, the sense of rotation, i.e., the chirality, of the rotating mills is randomly selected, since the irradiation paterns are invariant under rotation.

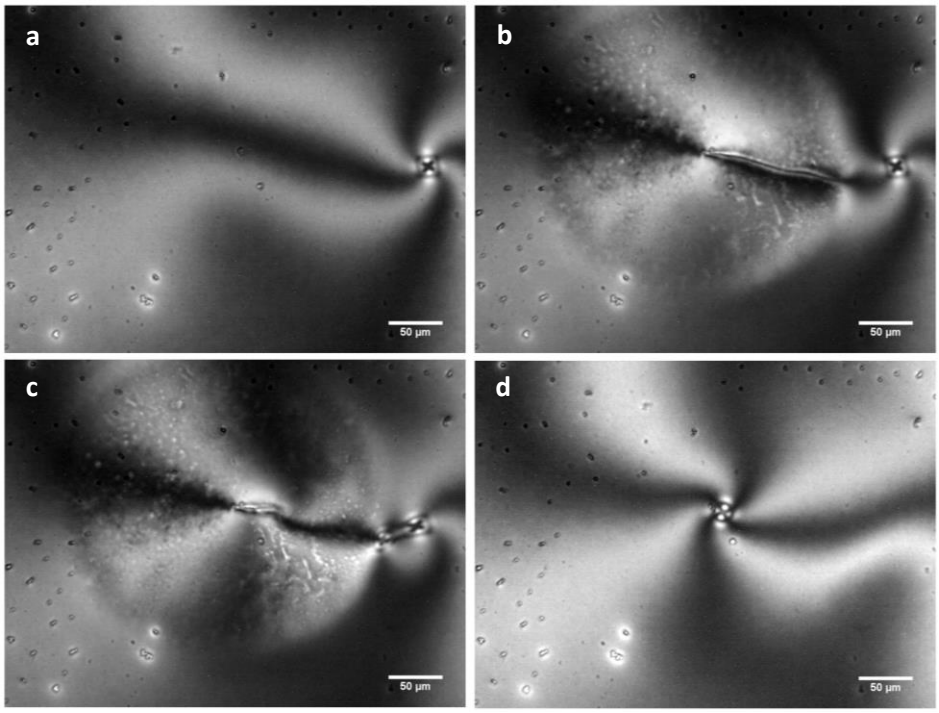

Fig. 95. Switching the chirality of a rotating mill by means of UV-light. a) The initially-induced handedness of the rotating mill is randomly selected. The rotating mill display an anti-clockwise configuration while an AC electric field of amplitude $0.1\ V \cdot \mu m^{-1}$ and frequency f = 1 KHz is being applied. **b)** A second UV-light spot creates a topological defect close to the previously induced. **c)** The initially-induced topological defect annihilates with an s=-1 defect induced in between the two existing ones. **d)** The final configuration of the rotating mill displaying opposite chirality (clockwise) with respect to the initial one. See also **Video21**.

We have found that the chirality of the underlying pattern can be switched between two states, R- (clockwise) or L- (anti-clockwise) (**Fig. 95**). This effect can be achieved with the use of a photosensitive surface and under specific conditions of the applied AC electric field, basically, for amplitudes below the Fredericksz transition. Here, in the limit where the molecular reorientation will occur, a UV-light spot allows to create a topological defect close

to the initial one, which will feature the opposite chirality (**Fig. 95a,d** – see also **Video21**). This process is achieved in the threshold limit range of the bulk material reorientation.

Moreover, using the photo-mask technique, which may allow defining a preferred chirality *a priori,* can be a good option to induce lattices of different chiral objects which allows for the study of frustration in anisotropic fluids (**Fig. 96a,b**).

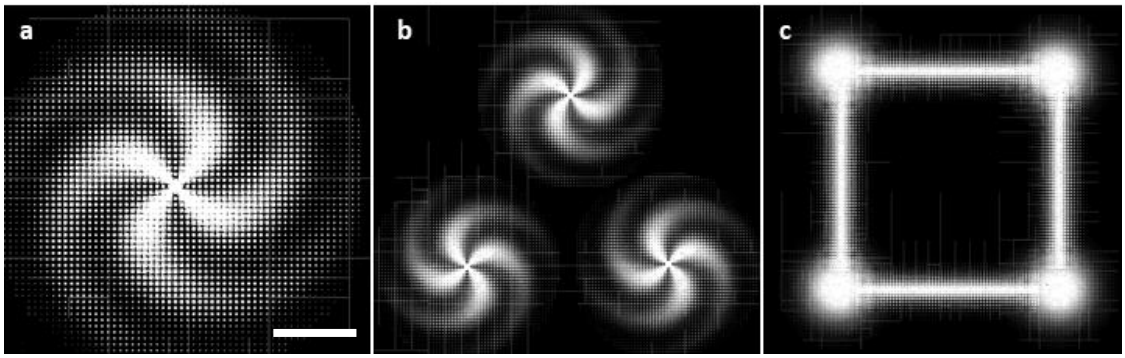

Fig. 96. Different masks designs for photo-patterning the NLC cell. a) An acetate mask displaying a clockwise (R-) rotating mill for patterning the photosensitive substrate. **b)** Array of three rotating mill forming a triangular lattice allowing for frustration. **c)** More complex patterns combining single point topological defects which are connected through narrow paths. All the masks display a gradient of intensities being maximum at the centre of the desired shape and minimum at the outer region, the one close to the black background.The scale bar is 200 µm.

Going further, and inducing a Gaussian grey intensity profile to the masks, one can print any designed shape, e.g. a circle or a square, or going further, a mixed pattern combining both topological defects and tracks (**Fig. 96c**).

All these possibilities together make this technique, coupled with the use of a photosensitive substrate, a powerful reversible tool to guide and control colloidal collective dynamics dispersed in a NLC.

4.2. Microfluidic devices

Colloidal transport through narrow paths allow studying clogging effects, as explained in Section 3.3, but also to explore the transport properties of the particles dispersed in a NLC in a confined environment.

Guiding the nematic director allows defining the trajectories for the particles to follow. Typically, NLC cells used during this thesis (Chapters 3 and 4) are only confined in the third dimension, namely the height of the cell. Moreover, constrictions in the plane of particles motion have been introduced in the form of walls by using a microfluidic device (**Fig. 97a**). The latter confine the anisotropic material, which adopts the device shape, giving rise to an interaction between the NLC and the confining walls. In this geometry, colloidal transport mediated by backflow effects (see Chapter 1, section 4.2.2 and Chapter 4, section 2), under the application of an AC electric field and due to molecular bulk reorientation at the boundaries, can become relevant due to the material confinement and the anchoring conditions at the confining walls.

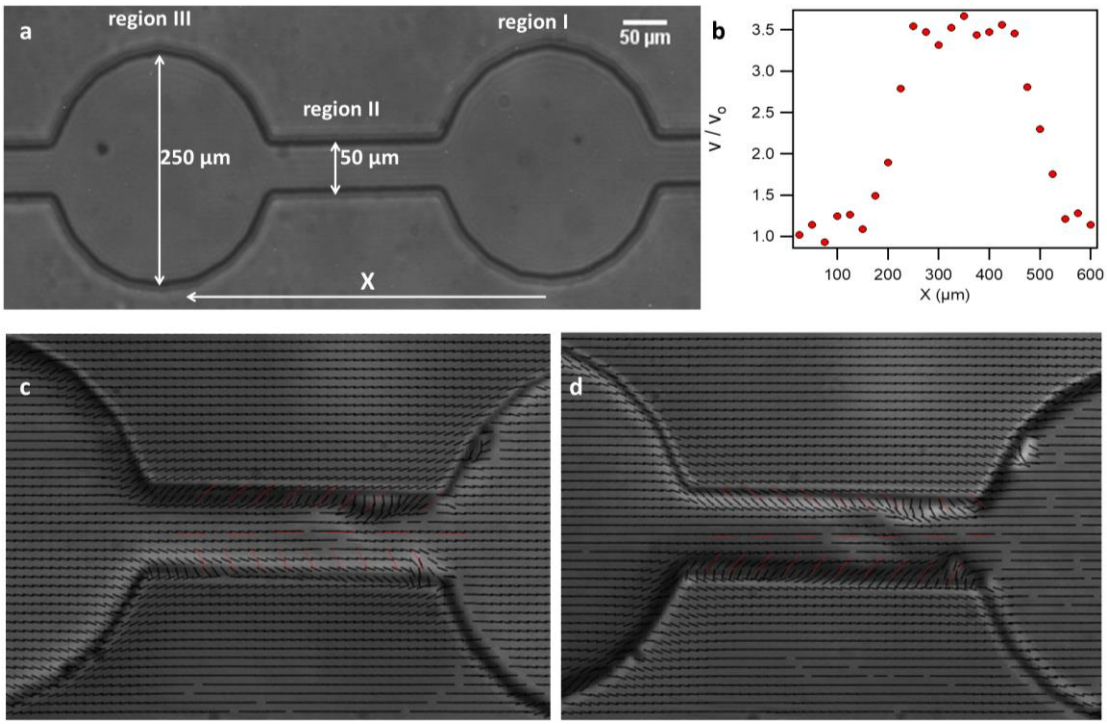

Fig. 97. Colloidal transport through narrow paths. a) Bright-field micrograph of the microfluidic device. The different regions described in the text are depicted here. The x direction denotes particle propulsion. **b)** Normalized velocity of a particle moving along the x direction inside the microfluidic device. **c) – d)** Director field orientation of the confined NLC while an AC electric field of amplitude $0.8\,V\cdot\mu m^{-1}$ and frequency f = 1 Hz is being applied. The red lines denote the nematic director. The nematic director is of opposite direction in **c)** and **d)** with respect to the horizontal. The AC electric field conditions allow monitoring the nematic reorientation at the boundaries with the confining walls.

Interestingly, we have found that when a particle travels through a narrow constriction its speed gets increased (**Fig. 97b**). Initially, particles travel at a certain velocity within region I in **Fig. 97a**. After a few seconds, particles reach the narrower constriction (region II) and their velocity gets increased until leaving the narrow channel (region III). This effect has been observed both for different conditions of the applied AC electric field and different channels sizes. Different phenomena can give rise to this particle acceleration such as viscosity anisotropy, backflow-mediated colloidal transport... For our system, we suspect that all these effects are coupled together. In **Fig. 97c,d** we show the nematic director field of the confined NLC cell under the application of the AC field acquired at two different times. Actually, it must be mentioned, that a custom-built microscope designed in the group by Prof. Jordi Ignés and Berta Martínez allows determining the nematic director of the NLC. These measurements reveal the reorientation of the nematic director at the confining walls, thus enhancing the backflow-mediated colloidal transport. Finally, the director field viscous anisotropy will vary along the confining cell, and thus, the main property of NLCs, anisotropy. The latter affect all the parameters existing in a NLC namely, the dielectric or conductivity properties but also the viscosity of the material.

5. Conclusions

In this chapter we have investigated the out-of-equilibrium transport of colloidal particle ensembles driven along both a photosensitive surface and a microfluidic device. The different experimental setups and geometries allow to study flocking, clogging and confining effects of particles dispersed in a NLC but also topological aspects of the LCs.

Patterning the photosensitive substrate

- The transport of colloidal swarms along a photosensitive surface has been achieved through a disclination line that forms as the UV-light spot is dragged between the initial and the final destination on the photosensitive surface, allowing for flocking effects. While our colloidal swarm has been transported along a single track, more complex patterns may be easily designed to steer the colloidal motion.

- Taking advantage of the photo-mask technique, we have been able to induce one- and two-dimensional arrays of out-of-equilibrium colloidal clusters. These systems allow studying dynamics performed by the particles in pre-defined arrays, which actually reveal interesting topological aspects from the elastic matrix they reside in.

The advantages of using a photosensitive layer over other strategies to propel microscale matter in a NLC are the possibility to control the molecular orientation of the dispersing medium using an external field, and the independent control of the surface topology through optical means. They can be modified independently and can be easily changed during the experiments, a feature that gives further functionality to the transport in colloidal systems. Moreover, the implementation of the photo-mask technique allows to print any designed shapes and sizes combining single point topological defects with single tracks.

Microfluidic devices

- Particles propelled in confined microfluidic environments behave as colloidal flocks travelling in a defined plane at a constant speed. This fact is a consequence of the inter-particle repulsive interaction exerted between particles under an AC field. Thus, no clogging effects should be observed. Interestingly, we have found that the particle flow over a narrow constriction can be clogged due to the interaction between particles and the components constituting the NLC cell. In this case, the clogged state is configured differently from that observed in isotropic fluids.

- Transport of particles show an increase of the speed when travelling through narrow constrictions. This phenomenon can be attributed to the variation on the NLC anisotropy due to the constriction along narrow paths.

The use of liquid crystals in microfluidic environments is currently an emerging field of research, which will allow for further manipulation, assembly, store or transport of microscopic inclusions.

Chapter 6

Concluding remarks

1. Conclusions

The out-of-equilibrium dynamics exhibited by the driven particles inside a nematic liquid crystal are complex and difficult to predict. In this thesis, we have managed to define and steer or guide the trajectories of the colloidal particles by taking advantage of the material elasticity. Typically, we have used surface chemistry to modulate the nematic far-field director at the boundaries, in particular, by means of a photosensitive substrate. These protocols allow from the study of single colloids dispersed in liquid crystals to collective dynamics performed by hundreds or even thousands of particles.

Most of the initial objectives and goals of this thesis have been achieved, especially in the chapter 3 and chapter 4, although most of the work shown in chapter 5 is still work in progress.

First, we have analysed the anomalous diffusion transport of single particles driven along an aligned nematic liquid crystal. Motion is essentially ballistic along the driving direction for all the experiments while it can be superdiffusive in the transversal direction. The type of distortions of the elastic LC matrix around the moving colloids determines the transversal transport modes, the latter being diffusive for quadrupolar distortions and superdiffusive for dipolar distortions. The results obtained do not depend significantly on both driving speed and propulsion mode, while increasing temperature or particle size clearly enhances the anomalous diffusion. Based on existing models that analyse the dynamics of active particles in complex media, our experiments show a clear connection between superdiffusive motion and the persistence of fluctuating dipolar liquid crystal distortions.

Second, we have investigated the out-of-equilibrium two-dimensional assembly of colloidal particles driven towards a topological defect in a nematic liquid crystal. The elastic matrix can be modified by locally varying the anchoring conditions at the bounding plates under light irradiation which can lead to two different configurations, namely aster and rotating mill-like. The anisotropy of the dispersing medium combined with the geometry of the experiments result in the onset of different electrokinetic phenomena generated by an alternating current. The field provides a constant propulsion force local to each particle that promotes particle assembly and generates a pair-wise repulsion that leads to a steady-state characterized by different particle organization, and thus, different phases and packing densities kept by the pressure exerted by the driven particles. Switching off the electric field melts the cluster. Thus, our driven system allows to define a non-equilibrium equation of state and directly determine the effective pressure and temperature provided by the system. Our experimental configuration allows to monitor phase transitions without degrading the hexatic order by the effect of confining walls. Remarkably, we find a new behavior in the colloidal ordering, as the bond-orientational order parameter reaches a local maximum within the liquid-like region, where particle ordering is enhanced by inter-particle repulsion. Numerical simulations reveal that the geometry of the observed assemblies is the result of a balance between a disparity of electrokinetic phenomena and different length scales involving hydrodynamics, phoretic forces, and dipolar interactions arising at the interface between the colloidal particles and the nematic liquid crystal. Qualitative and quantitative agreement between experiment and numerical model allow us to conclude that

all particular ingredients of the system can be cast into a more general framework of individual propulsion and long-range inter-particle repulsive interaction. Importantly, the elasticity of the liquid crystal plays only a secondary role in particle assemblies for driven nematic colloids. This is in contrast to the typical interactions observed for colloids dispersed in a NLC, under equilibrium conditions.

Third, we have investigated the out-of-equilibrium transport of colloidal particle ensembles driven along both a photosensitive surface and a microfluidic device. The transport of colloidal swarms along a photosensitive surface allow to study for flocking effects, while taking advantage of the photo-mask techinque allows to induce one- or two-dimensional arrays of out-of-equilbrium colloidal clusters. Finally, particles propelled in confined microfluidic environments behave as colloidal flocks travelling in a defined plane until reaching the narrow constriction where particles get stuck due to the interaction between them and the components constituting the NLC cell.

2. **Open questions and future perspectives**

During the realization of this thesis we have had the opportunity to learn about nematic colloids and begin to understand the basic processes taking place when motion is involved. Although we have managed to contribute to the understanding of colloidal systems out-of-equilibrium, numerous questions have arised, as evidenced during the entire dissertation in the open questions and future perspectives section of each chapter.

First, experiments based on single particle transport should prompt theoretical studies to substantiate our interpretations and conjectures, together with variants of the experiments here reported that may deepen our understanding of colloidal transport in anisotropic media both for active and driven scenarios. For instance, we have supposed the NLC flow around the particles to be equal for both sedimentation and LCEEK mechanism, although particle flows for sedimentation-diffusion experiments has not been established yet.

On the other hand, our motile colloids display analogous mechanisms to that of active particles in particular scenarios, although particle trajectory is fixed by the far-field director. Is possible that nematic colloids feature a mixed behavior between active and driven scenarios when motile?

Second, our out-of-equilibrium colloidal assemblies demonstrate enhanced control capabilities endowed by their dispersion in anisotropic fluids. Our experimental realizations can be relevant as test-bed to study dynamic aspects of swarming and flocking in active colloids, and active behavior in organized fluids. Compared to existing realizations of active colloidal assembly, our system provides additional features that may prompt original research directions.

Resum

1. Introducció

La primera secció del resum en català consta d'una introducció als cristalls líquids i a les partícules dispersades en aquests. Són conceptes bàsics i fonamentals que ajuden a la comprensió de les posteriors seccions que s'han estudiat durant la realització d'aquesta tesis.

1.1. Cristalls líquids

Els cristalls líquids (CLs) són fluids anisotròpics que presenten estats de la matèria intermitjos entre líquids isòtrops, com l'aigua, i els sòlids cristal·lins (**Fig.1**) ([1]–[4]). Tot i que els CLs són típicament fluids viscosos, a l'escala molecular presenten un cert grau d'alineament u ordre intern (**Fig.1b**). Aquests tipus de materials estan formats per unitats anisomètriques que interactuen entre elles donant unes propietats particulars als CLs. De fet, aquesta interacció entre unitats augmenta l'ordre orientacional dels constituents del material. Això vol dir què, de mitjana, els constituents dels CLs estan disposats en una mateixa direcció.

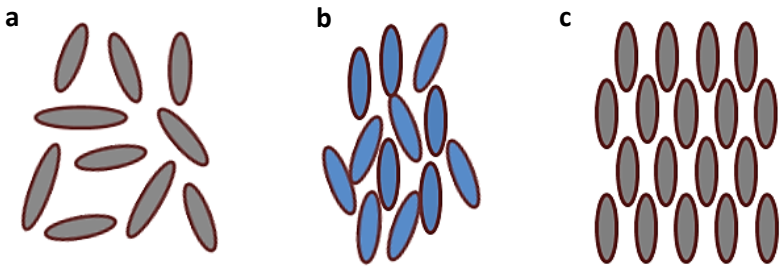

Figura. 98. Fase d'un cristall líquid. Representació esquemàtica d'un **(a)** fluid isòtrop, el qual no presenta ordre orientacional ni posicional, **(b)** un cristall líquid que presenta ordre orientacional i, **(c)** un cristall, el qual exhibeix tant ordre orientacional com posicional.

Degut a l'odre intern d'aquests materials, els CLs exhibeixen anisotropia en la majoria de les seves propietats físiques, així, els valors d'una certa magnitud no són iguals quan es mesuren al llarg de l'eix principal o perpendicular a aquest. Les principals manifestacions de l'anisotropia es detallen en les seccions següents.

Tot i que hi ha un gran nombre de cristalls líquids depenent de la seva naturalesa i composició, en el nostre cas considerarem generalment CLs nemàtics ja que presenten la fase més simple a l'hora d'introduir les característiques dels CLs. A més a més, els cristalls líquids nemàtics (CLNs) han estat el medi de dispersió usat durant la realització d'aquesta tesis.

La fase nemàtica és la menys ordenada de les fases dels CLs. Els seus components unitaris presenten ordre orientacional, el qual resulta de la interacció entre aquests per alinear-se entre ells en una direcció preferida (**Fig.1b**). En la fase nemàtica, la mitjana en la orientació molecular de llarg abast es descrita per un vector unitari, $\vec{n}$ (també indicat com **n**), que s'anomena el camp director. Tot i que les molècules que constitueixen el material són polars, hi ha una re-disposició centrosimètrica en el material, així, $\vec{n}$ i $-\vec{n}$ són equivalents.

1.2. Anisotropia en els cristalls líquids

Els CLs presenten ordre intern, on la direcció de l'orientació preferida de les molècules del CL està donada pel camp director. Així, aquests materials exhibeixen diferents valors per una donada magnitud quan es mesuren en direccions diferents, en concret, per les direccions paral·leles i perpendiculars respecte la principal orientació molecular. Aquest qualitat s'anomena anisotropia i és la principal característica d'aquests materials.

Algunes de les manifestacions més rellevants d'aquesta propietat dels CLs, com la birefringència i l'anisotropia dielèctrica, es detallen a continuació.

- **Anisotropia òptica – Birefringència**

Els materials que presenten una orientació molecular preferida, interactuen amb la llum de forma diferent als cristalls isòtrops. Així, la llum viatja a diferents velocitats depenent de la direcció cristal·logràfica per la qual es propagui. Aquest es un fenomen típic que mostren els sòlids cristal·lins anisotròpics, però també els CLs.

En els CLs la llum viatja a diferents velocitats depenent d'on es trobi polaritzada, paral·lela o perpendicularment respecte a **n**. Conseqüentment, els CLs presenten dos índexs de refracció diferents corresponent als rajos de la llum polaritzats al llarg del camp director i perpendicular a aquest ($n_{\parallel}$ i $n_{\perp}$, respectivament). La diferència entre els dos índexs de refracció s'anomena birefringència. Els materials birefringents es poden caracteritzar amb la tècnica de la microscòpia òptica de polarització (POM).

- **Anisotropia dielèctrica**

La permitivitat elèctrica (ε) descriu l'habilitat del material per polaritzar-se com a resposta a l'aplicació d'un camp elèctric (E), però també com el camp elèctric afecta i es afectat pel medi. En els CLs, aquesta quantitat es diferent quan es mesura paral·lel ($\varepsilon_{\parallel}$) i perpendicular ($\varepsilon_{\perp}$) al camp director. La diferència entre les dos constants defineix l'anisotropia dielèctrica del material ($\varepsilon_a = \varepsilon_{\parallel} - \varepsilon_{\perp}$).

En els CLs que presenten valors positius d'anisotropia dielèctrica ($\varepsilon_a > 0,\ \varepsilon_{\parallel} > \varepsilon_{\perp}$), les molècules tendeixen alinear-se paral·leles al camp extern aplicat. Per contra, un material que presenti valors negatius de l'anisotropia dielèctrica s'alinearà perpendicular al camp extern aplicat ($\varepsilon_a < 0,\ \varepsilon_{\parallel} < \varepsilon_{\perp}$) ([2]).

1.3. Distorsions en els cristalls líquids nemàtics

Els CLNs, en absència de restriccions externes, tendeix a tenir una alineació homogènia en una direcció del camp director, **n**. No obstant això, la presència de fluctuacions tèrmiques, parets delimitants o camps externs poden induir inhomogeneïtats o deformacions sobre el material fent variar **n** al llarg de la mostra. En aquest cas, l' escala de longitud de la deformació és molt més gran que la mida dels constituents i pot ésser descrit i modelat amb el funcional de Frank-Oseen basat en l'energia lliure elàstica, que es pot escriure ([16], [17]),

$$f = \frac{1}{2}K_1(\text{div }\mathbf{n})^2 + \frac{1}{2}K_2(\mathbf{n}\cdot\text{curl }\mathbf{n})^2 + \frac{1}{2}K_3(\mathbf{n}\text{ x curl }\mathbf{n})^2,$$

on K_1 , K_2 i K_3 són les constants relacionades amb les diferents distorsions *splay, twist* i *bend* que pot patir un CLN. Típics valors per les constants elàstiques són de l'ordre de 10^{-12} N ([18]).

A l'hora d'utilitzar els CLNs, normalment es confinen entre superfícies, que després d'un tractament químic, definiran la disposició del CLN degut a la interacció superfície-CLN. Aquesta interacció es coneguda com "ancoratge del CL" ([19]–[21]).

El camp director pot estar bàsicament orientat de tres maneres diferents respecte el pla de les superfícies. Aquesta interacció es troba definida per l'angle polar θ. Quan les molècules del CLN estan disposades paral·leles a la superfície, l'ancoratge és *planar* i $\theta \sim 0^o$. Per contra, quan **n** es perpendicular a la superfície, i per tant, $\theta \sim 90^o$, l'ancoratge s'anomena *homeotropic*. L'ancoratge *tilted* correspon a tots els estats intermitjos entre les configuracions abans esmentades.

Fins ara, la descripció de les deformacions del camp director del CLN han ocorregut a l'escala de **n**. Tot i això, disposicions inhomogènies de **n** també es poden trobar localment en forma d'un defecte puntual (defectes topològics) (**Fig.2**) o de singularitats (línies de disclinació).

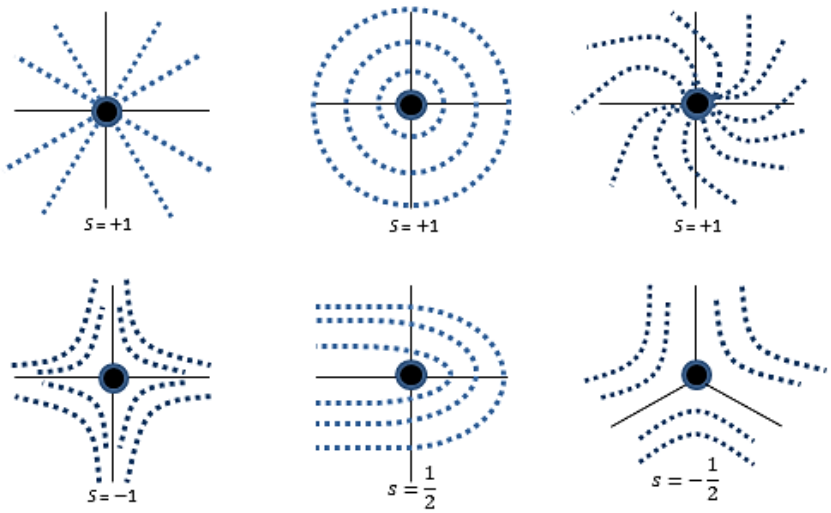

Figura. 2. Defectes topològics en un cristall líquid nemàtic bi-dimensional. Esquemes de les configuracions del camp director al voltant del nucli del defecte.

1.4. Col·loïds dispersats en cristalls líquids nemàtics

Quan una micro-partícula es dispersa en un medi de CLN, la distorsió del camp director causada per la partícula condueix a la formació de defectes als voltants de la inclusió, que dependran principalment de les condicions d'ancoratge a la superfície de la partícula, l'elasticitat del cristall líquid i el radi de la partícula ([36]),([37]). Bàsicament i de forma breu, l'orientació del CLN a prop d'una superfície pot ser *homeotropica* o *planar*. En el primer cas, les molècules s'orienten perpendicularment a la superfície, mentre que en l'altre cas

s'orienten en paral·lel a la mateixa. Exemples dels defectes que es formen quan aquestes partícules es dispersen en un CLN es poden veure a la **Fig.3**.

A la pràctica i per inclusions esfèriques, que generalment són un mètode robust per estudiar dispersions col·loïdals en cristalls líquids, podem trobar diferents configuracions de **n** al voltant de la partícula. Breument, quan l'ancoratge és homeotropic (**Figs.3b,c,f,g**) podem trobar configuracions de **n** tant dipolars ("point defect-hedgehog") (**Figs.3b,f**) com quadrupolars ("Disclination loop Saturn-Ring") (**Figs.3c,g**). En canvi, quan l'ancoratge és planar només configuracions quadrupolars són possibles en forma de "Double-boojums" (**Figs.3d,e,h**).

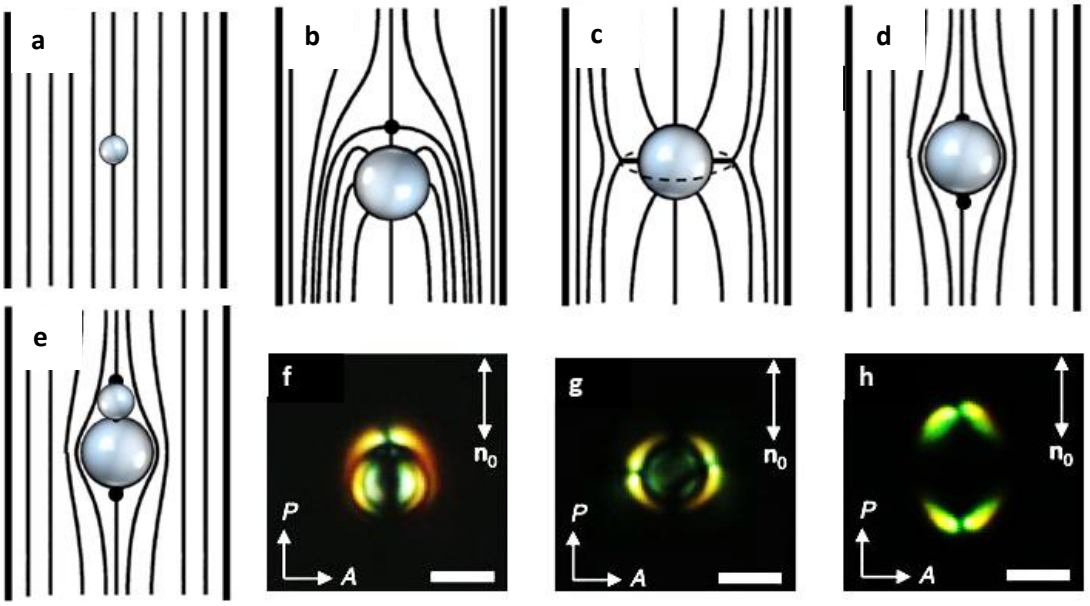

Figura. 3. Descripció esquemàtica de les distorsions obtingudes experimentalment al voltant de partícules de diferent forma i condicions d'ancoratge dispersades en CLNs. a) Les micro-partícules petites no distorsionen **n**. **b**)-**h**) Partícules que distorsionen **n** per poder satisfer les condicions de contron elàstiques. Les partícules amb ancoratge homeotropic poden exhibir un **b**) "point defect-hedgehog" o un **c**) "Saturn-Ring". Partícules esfèriques **d**), o en forma de **e**) cacauet que presenten un ancoratge planar (tangencial) amb dos defectes superficials als extrems anomenats "Boojums". **f**)-**h**) Micrografies experimentals obtingudes entre polaritzadors creuats de partícules disperses en CLNs mostrant un **f**) "point defect-hedgehog", **g**) "Saturn-ring" i **h**) "double-boojum". En les micrografies experimentals, **n** és perpendicular al analitzador. La barra d'escala correspon a 4 µm de llargària. Adaptat de la ref. ([42]).

L'auto-assemblatge de col·loïds en CLNs està mediat per la elasticitat del material. Bàsicament, les micro-partícules que mostren configuracions dipolars del camp director interactuen via dipol formant estructures en forma de cadenes amb tots els dipols alineats en un sentit. Per altra banda, les configuracions quadrupolars també formen cadenes, però en aquest cas les micro-partícules es disposen a un cert angle (uns 30^0) respecte el camp director per satisfer les constriccions elàstiques.

1.5. Propulsió de partícules – Electroforesi no lineal

El mecanisme pel qual micro-partícules dispersades en un cristall líquid es poden propulsar s'anomena "Liquid Crystal-Enabled electrokinetics" (LCEEK). Aquest mecanisme involucra electroforesi (LCEEP) i electroosmosi (LCEEO) ([38], [43], [133], [137]–[140]). Típicament, la electroforesi fa referència al moviment de la partícula en un fluid sota l'acció d'un camp

elèctric extern, i la electroosmosi al moviment del fluid respecte una superfície sòlida, en aquest cas, la partícula. Per la propulsió, es generen moviments iònics (vòrtexs) al voltant de les partícules mediant la seva propulsió a una velocitat constant.

Sota l'acció d'un camp elèctric altern, la separació de cargues induïda és sensible a la configuració del camp director al voltant de la partícula. Així, la configuració nemàtica definirà el patró de fluxos: configuracions quadrupolars (dipolars) del camp director indueixen fluxos quadrupolars (dipolars). Els fluxos induïts sota el mecanisme "LCEEO" es defineixen com "puller" per ancoratges homeotropics (**Figs.4a-b,e-f**) i "pusher" per ancoratge planar (**Figs.4c-d**). En les partícules que exhibeixen comportaments de "pullers" el fluid es mou contra la partícula mentre que els "pushers" expulsen el fluid cap al "bulk". Per obtenir un bombeig net dels fluxos electroosmòtics al voltant de la partícula cal que aquests no siguin simètrics, essent el cas per les configuracions dipolars. Com a conseqüència, només les configuracions dipolars permeten la propulsió de la partícula, com es pot observar a la **Figs.4e-f**.

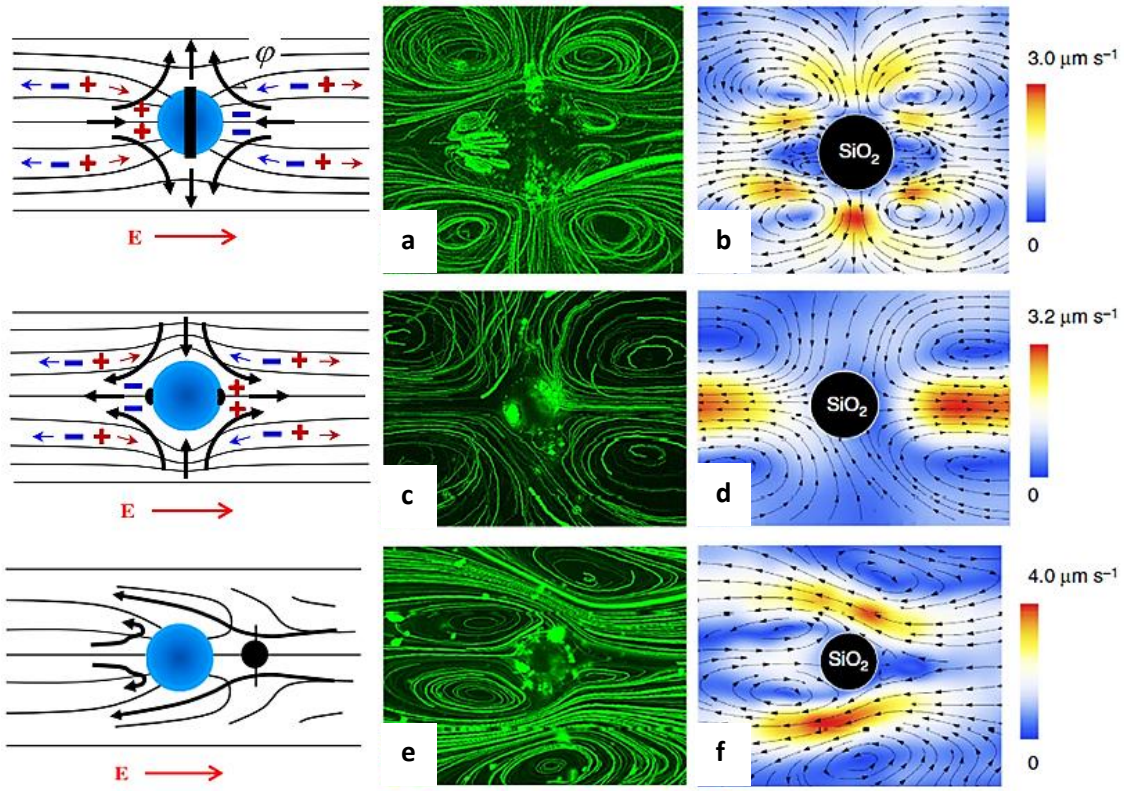

Fig. 4. Trajectòries dels fluxos LCEEO obtinguts experimentalment de partícules amb diferents condicions d'ancoratge. a,c,e) Micrografies dels fluxos de fluid obtinguts experimentalment amb microscòpia FCPM utilitzant partícules fluorescents com a traçadors. **b, d, f**) Simulacions d'ordinador dels fluxos obtinguts per diferents condicions d'ancoratge. **a, b**) Una partícula amb ancoratge perpendicular, amb configuració de Saturn-Ring, mostra un patró de fluxos quadrupolars I simètrics. **c, d)** Partícula esfèrica amb ancoratge planar ("double-boojums") que mostra fluxos quadrupolars. Les velocitats en **b)** i **d)** són de polaritat oposada, induint fluxos de tipus "puller" (**b**) i "pusher" (**d**). **e, f**) Partícules amb ancoratge homeotropic ("point defect-hedgehog") induint patrons de flux dipolars. En aquesta configuració les partícules poden ser propulsades. Adaptat de les refs. ([43], [139]).

2. Protocols i muntatges experimentals

Les cel·les experimentals utilitzades durant el transcurs d'aquesta tesis es componen bàsicament de dues plaques de vidre-(ITO) (vidre recobert amb una fina capa conductora transparent que actua com elèctrode) que s'enganxen amb totes dues cares mirant una a l'altra. Les plaques de vidre es poden funcionalitzar amb diferents molècules o materials per obtenir una configuració definida de **n**. Per dur a terme els estudis presentats en aquesta tesis, els espaiats entre plaques fets servir típicament van des de 15 µm fins a 25 µm, i corresponen al gruix dels espaiadors de Mylar (nom comercial per al polietilè tereftalat als USA).

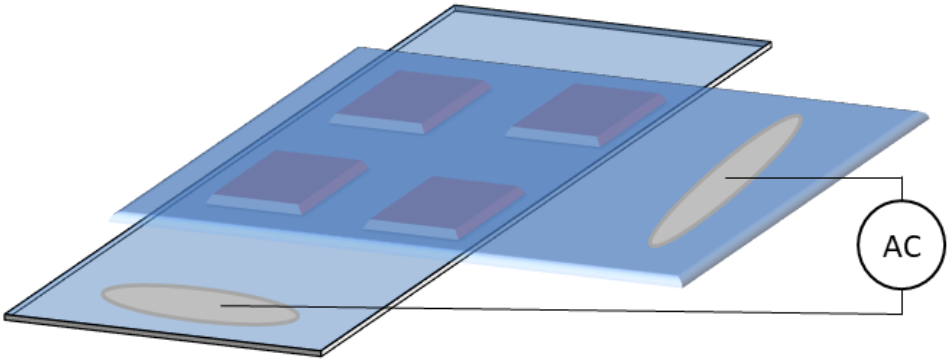

Fig. 5. Descripció esquemàtica d'una cel·la de CLN on s'aplica un camp elèctric extern. Les superfícies d'ITO estan enganxades entre elles amb les dues cares mirant cap dins. La cel·la té un espaiat entre superfícies típic de 15 µm and 25 µm. El contacte elèctric s'obté mitjançant una dispersió col·loïdal de plata situada entre els cables elèctrics i la superfície d'ITO.

2.1. Dispersions col·loïdals

Els CLNs usats durant el transcurs d'aquesta tesis són el CCN-37 (Nematel) i el MLC-7029 (Merck). Com a inclusions col·loïdals hem utilitzat partícules micro-mètriques de diferents materials (silicat i poliestirè) i forma (esfèrica o en forma-cacauet).

Pels experiments del Capítol 3 el CLN utilitzat ha set el CCN-37, mentre que en els Capítols 4 i 5, el CLN és el MLC-7029. Tots dos CLNs presenten anisotropia dielèctrica negativa (ε_a < 0). Així, sota l'aplicació d'un camp elèctric perpendicular a la superfície dels elèctrodes el CLN es reorientarà paral·lel al pla d'aquests.

Les partícules esfèriques de silicat utilitzades en el Capítol 3 poden ser prèviament funcionalitzades o utilitzades directament. Els diàmetres típics de partícula utilitzats durant el transcurs d'aquesta tesi són ϕ = 5 µm i ϕ = 10 µm. Per altra banda, partícules en forma de cacauet, anisomètriques, s'han fet servir en els Capítols 4 i 5. El material és poliestirè i les dimensions típiques són d_x = 4µm and d_y = 3µm.

3. Transport d'una partícula individual

En aquesta secció, hem estudiat el transport d'una partícula individual dispersada en un CLN. Les partícules presenten diferents configuracions del director al seu voltant, podent ésser dipolars o quadrupolars (veure secció 1.4). D'aquestes observacions hem estudiat el caràcter difusiu quan les partícules són mòbils. El moviment es balístic en la direcció de la propulsió, coincidint amb la direcció de llarg abast del camp director. Pel que fa a les fluctuacions transversals, esdevenen superdifusives quan els defectes topològics al voltant de la partícula són de caràcter dipolar. A diferència, els resultats difícilment varien de la difusió típica per partícules que mostren configuracions quadrupolars del camp director. A més a més, hem observat que el fenomen pot ser reproduït amb diferents mètodes i velocitats de propulsió. Tot i això, sembla que el fenomen es força dependent de la mida de la partícula i la temperatura del sistema.

En aquest punt, hem proposat un mecanisme basat en la geometria del flux-induït al voltant de la partícula per justificar la persistència de les fluctuacions tèrmiques que afecten a la orientació del "point defect-hedgehog" (configuració dipolar). Anant més enllà també hem explicat la dependència del comportament superdifusiu amb la temperatura i la mida de la partícula basant-nos en paràmetres geomètrics i del material.

3.1. Protocols i muntatges experimentals

Les cel·les experimentals de CLN són força similars, tot i que en els experiments de sedimentació la mostra ha d'estar inclinada uns cert graus, en el nostre cas, $\alpha = 8.5^{o}$.

Pels experiments de sedimentació la cel·la consisteix de dos vidres funcionalizats, mentre que en el cas de la propulsió forètica aquests vidres també presenten un recobriment d'ITO actuant com a elèctrode. Per tots els experiments l'espaiat de la cel·la és de 15±2 µm i es troba funcionalitzada amb un compost basat en poliimides que permet adoptar un ancoratge planar del CLN al substrat, i després de rascar-lo, un alineat homogeni del camp director (veure secció 2 i 2.1).

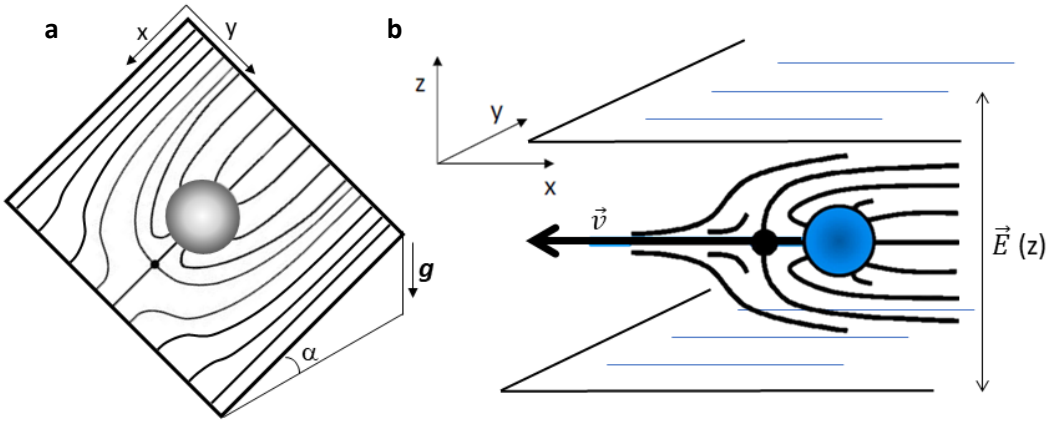

Fig. 6. Descripció esquemàtica dels sistemes experimentals usats en el transport d'una partícula individual. a) Escenari de sedimentació per una partícula amb configuració dipolar. **b)** Partícula propulsada forèticament per l'aplicació d'un camp elèctric perpendicular al moviment d'aquesta. En totes dues geometries el camp director està alineat en l'eix x, coincidint amb la direcció de propulsió.

3.2. Resultats i discussió

El primer set de resultats correspon a la sedimentació d'una partícula de 5 µm amb una configuració dipolar (**Fig.7**). Les trajectòries analitzades són mínimament de 100 µm de llargada (**Fig.7a**). L'anàlisi de les trajectòries ha estat resolt entre el temps que necessita una partícula per viatjar una distancia igual a la seva mida i el temps que necessita per sobrepassar la distància entre l'espaiat de cel·la. El moviment paral·lel al camp director es balístic amb velocitats de l'ordre de 0.1 µm·s^{-1} (**Fig.7b**). Per altra banda, l'anàlisi mostrat en la **Fig.7c** mostra un comportament superdifusiu per les fluctuacions transversals amb un exponent $\nu \approx 1.4$.

Un comportament superdifusiu similar també s'ha trobat per una altra set d'experiments de sedimentació realitzats amb partícules de 10 µm que presentaven configuracions dipolars de **n**. Per altra banda, ja que les partícules més grans sedimenten més ràpidament, es podria pensar que aquest paràmetre juga algun paper, tot i que hem observat que el comportament difusiu no depèn de la velocitat.

Pel que fa a les partícules propulsades forèticament presenten un comportament molt similar al observat amb partícules propulsades sota l'acció de la gravetat, per sedimentació.

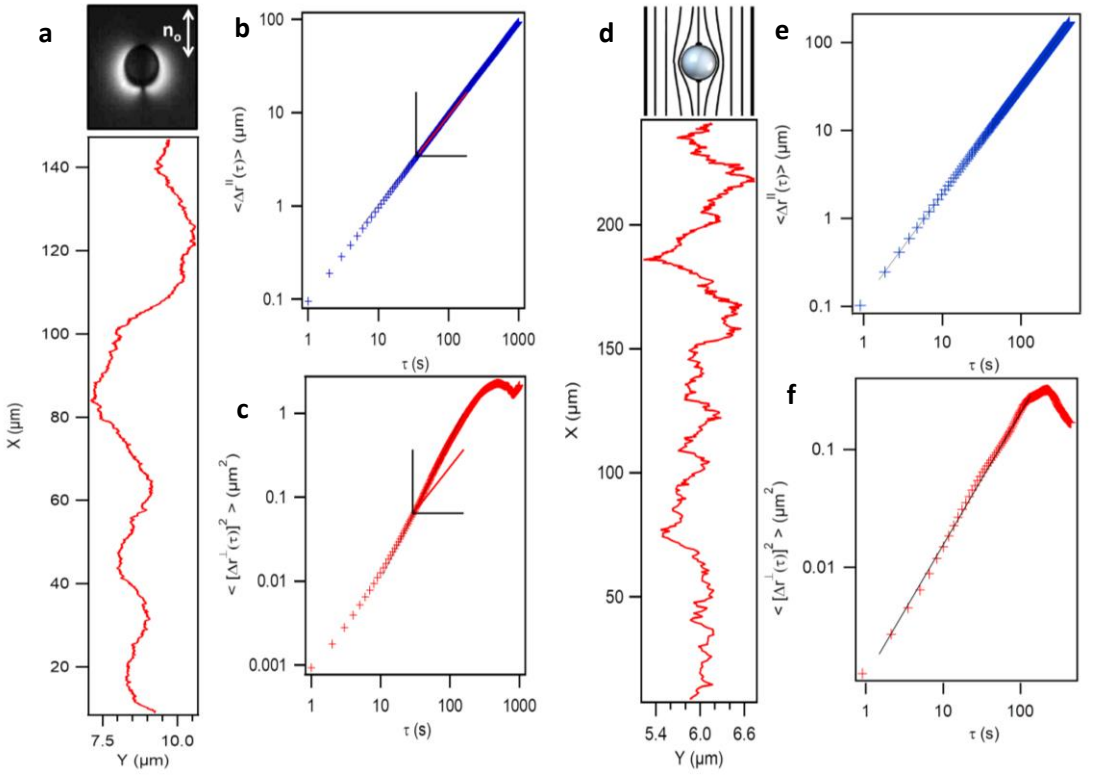

Fig. 7. Sedimentació d'una partícula de 5 µm amb configuració dipolar i una amb configuració quadrupolar. a) Trajectòria d'una partícula en el pla xy a $T - T_{NI} = -27.5^{o}C$ L'inset mostra la configuració dipolar al voltant de la partícula. **b)** Desplaçament mitjà (MD) paral·lel al camp director vs. temps. El comportament en aquesta direcció es balístic. **c)** Desplaçament quadràtic mitja (MSD) perpendicular al camp director vs. temps. La línia sòlida és un ajust a una llei de potències resultant de un exponent $\nu = 1.41 \pm 0.04$. **d)** Trajectòria d'una partícula amb configuració quadrupolar en el pla xy a $T-T_{NI}= -17.5^{o}C$. L'inset mostra un esquema de la configuració del CLN al voltant de la inclusió. **e)** Desplaçament mitjà (MD) paral·lel al camp director vs. temps. El comportament en aquesta direcció es balístic. **f)** Desplaçament quadràtic mitja (MSD) perpendicular al camp director vs. temps. La línia sòlida és un ajust a una llei de potències resultant de un exponent $\nu = 1.0 \pm 0.1$.

Un altre set d'experiments de sedimentació, però ara variant la condició d'ancoratge del CLN a la partícula s'han dut a terme. En aquest cas, les partícules no es troben funcionalitzades i la configuració del camp director al voltant de la inclusió és de tipus quadrupolar. Per aquest tipus d'experiments s'ha realitzat el mateix anàlisis. Cal evidenciar que en aquest cas, la propulsió forètica no és una opció degut a la simetria dels fluxos induïts. Els resultats obtinguts es mostren en la **Fig.7**. Tal i com s'esperava, el moviment al llarg del camp director segueix una tendència balística, com també s'ha observat per les configuracions dipolars (**Fig.7e**). En canvi, comparant el cas amb les configuracions dipolars, els exponents són ara més baixos i difícilment difereixen de la difusió normal pels modes de transport transversals al camp director (**Fig.7f**).

A l'hora de la discussió dels resultats, cal tenir en compte els diferents mecanismes de transport involucrats en el moviment de la partícula. Les fluctuacions tèrmiques indueixen tant el típic moviment Brownià, amb una escala de temps, $\tau_{diff} \sim \frac{R^2}{D}$, com la fluctuació en la orientació del camp director al voltant de la partícula amb una escala de temps $\tau_{reor} \sim \frac{\gamma R^2}{K}$. Típicament, el moviment Brownià domina a temps llargs. Així, a escales de temps més curtes, les fluctuacions en l'orientació del director poden donar lloc a comportaments difusius anòmals ([69]). Una altra escala de temps important, en els col·loides propulsats, és el temps d'advecció. En el nostre cas, tant el moviment Brownià com les fluctuacions en l'orientació del CLN es troben afectades per l'advecció de la partícula en moviment amb una escala de temps, $\tau_{adv} \sim \frac{R}{V_0}$. Assumint que el procés a temps més llarg és el τ_{diff}, l'efecte de la hidrodinàmica pot ser evaluat utilitzant el nombre d'Ericksen, $E_r = \frac{\tau_{reor}}{\tau_{adv}} \approx \frac{\gamma R V_o}{K}$. Valors grans del nombre d'Ericksen indiquen que el camp director pot ser distorsionat degut a efectes del flux-induït, mentre que valors baixos avaluen la importància de les fluctuacions en l'orientació en escales de temps on la hidrodinàmica juga un paper. Utilitzant valors característics de tot l'estudi experimental, obtenim $\tau_{reor} \sim 0.1$ s i $\tau_{adv} \sim 10$ s. Això resulta en un $E_r \sim 10^{-2}$, indicatiu que les re-orientacions del director són molt més ràpides que els altres processos hidrodinàmics.

Basat en l'anterior discussió, podem concloure que les partícules, en el nostre sistema, es mouen essencialment en un camp director, **n**, estàtic, congelat. Així, una partícula pot instantàniament desalinear la seva direcció d'una forma aleatòria. Aquesta hipòtesis s'ajusta a les conjectures del Lintuvuori et al. ([156]) i Menzel et al. ([157]. Aquesta autors discuteixen que el desalineament en la configuració del director es troba afectat per un par de forces $f \propto V_o\, R^2 \sin 2\theta$ ([156]), on θ és l'angle entre el camp director local i la velocitat instantània de la partícula. El signe de f depèn del patró de fluxos adherits al voltant de les partícules, concretament positiu per fluxos de "puller-like" i negatiu per "pusher-like". Com a resultat, es pot concluir que el par de forces tendirà a mantenir alineades les configuracions quadrupolars, mentre que, contràriament, afavorirà el desalineament respecte el camp director per configuracions dipolars. Això pot promoure el comportament superdifusiu, com s'ha observat experimentalment anteriorment.

3.3. Conclusions

En aquesta secció hem analitzat el comportament difusiu d'una partícula dispersada i transportada en un cristall líquid nematic. Més específicament, hem estudiat la relació entre el transport difusiu i la configuració del camp director al voltant de la partícula, però també l'origen del comportament superdifusiu per partícules que presenten una configuració dipolar.

- El moviment paral·lel al camp director és essencialment de tipus balístic.

- La configuració del cristall líquid al voltant de la inclusió determina els modes transversals de transport perpendicular al camp director. Essent el comportament difusiu per configuracions quadrupolars i superdifusiu per configuracions dipolars.

- Tots els resultats obtinguts no depenen significativament ni del mètode de propulsió ni de la velocitat de la partícula.

- El comportament superdifusiu es conseqüència de la persistència de la configuració dipolar per desalinear-se respecte el camp director. Aquesta observació s'ha pogut corroborar experimentalment a través de l'observació de les fluctuacions en l'orientació del defecte situat al voltant de la partícula.

4. Assemblatges de partícules

Aquesta quarta secció està basada en l'assemblatge de partícules col·loïdals combinant experiments, teoria i simulacions. Aquests ens serveixen per investigar les dinàmiques col·lectives d'eixams de partícules anisomètriques auto-assemblades sobre un defecte topològic puntual, que actua com a punt atractor, en un CLN. El caràcter elàstic del material permet definir dos patrons diferents, "splay" i "bend-splay" (veure secció1.3). Això s'obté manipulant les condicions d'ancoratge del material a la superfície mitjançant una placa fotosensible. Les partícules segueixen les trajectòries definides per la matriu elàstica, així, textures del CLN purament radials (splay) donaran lloc a assemblatges de tipus aster, i textures mixtes (bend-splay) a assemblatges del tipus rotating mill. Per les configuracions d'aster, hem observat la formació de clústers estacionaris que mostren un gradient radial de la densitat amb tres estats diferents d'agregació. La part més interna del clúster correspon a un nucli sòlid, que es troba seguit per una corona en fase semblant a líquid, i finalment trobem una fase diluïda, semblant a un gas. Més enllà, hem descrit el nostre sistema amb una equació d'estat de no-equilibri i hem determinat la pressió i temperatura efectives del sistema. Pel que fa als assemblatges tipus rotating mill hem obtingut un patró del CLN en forma d'espiral que indueix aquest tipus d'auto-assemblatge dinàmic. Per entendre els diferents tipus d'assemblatges i les diferents fases obtingudes hem desenvolupat un model teòric que combina la propulsió forètica, forces dipolars i hidrodinàmiques, permetent capturar la física bàsica present en el nostre sistema. Més tard, el Dr. Arthur Straube ha dut a terme simulacions basades en el model descrit en la tesis que reprodueixen tant qualitativa com quantitativament els resultats obtinguts experimentalment.

4.1. Protocols i muntatges experimentals

En aquest apartat, les cel·les de CLN experimentals consisteixen en dos substrats prèviament funcionalitzats amb una capa transparent d'ITO, que actuarà com elèctrode. Els dos substrats s'enganxen miran un a l'altre amb un espaiat aproximat de 20 µm. Un dels substrats està funcionalizat amb una mescla de silans (foto- (AZO) i no-fotosensibles) donant lloc a una placa fotosensible (**Fig.8**), mentre que l'altre promou un ancoratge homeotropic del CLN a la superfície.

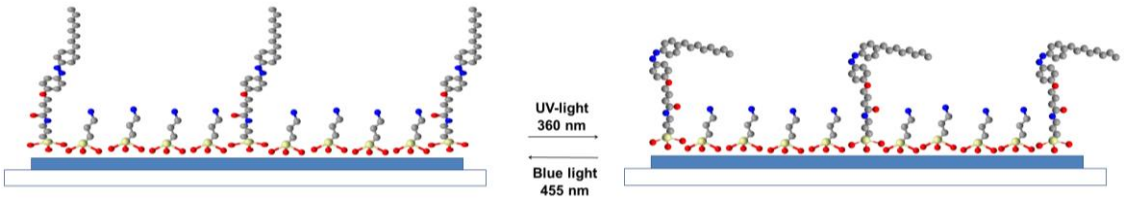

Fig. 9. Esquema il·lustrant la superfície fotosensible. Superfície fotosensible resultant de la reacció entre dos silans, un foto- i un no-fotosensible. L'aplicació de llum UV promou la isomerització de la forma *trans* a la *cis*. La modulació inversa s'obté amb llum blava.

Les micro-partícules utilitzades en aquesta secció són en forma de cacauet (d_x = 4 µm and d_y = 3 µm). Aquest tipus de partícules permeten trencar la simetria dels fluxos induïts al voltant d'aquestes permetent així la propulsió. Les partícules es dispersen en el CLN MLC-7029 que presenta anisotropia dielèctrica negativa (veure secció 1.2).

- **Protocol d'irradiació**

En absència de llum o sota llum blanca, les molècules d'AZO, corresponent al compost fotosensible, adopten la seva forma més estable, *trans*. Aquesta disposició elongada de les molècules AZO dona lloc a un ancoratge homeotropic de les molècules del CLN a la superfície. Quan s'irradia la mostra amb llum UV (360 nm), es promou la transició de les molècules d'AZO de la forma *trans* a la *cis*, i com a conseqüència, el CLN adopta una disposició planar sobre la superfície. La modulació inversa s'obté amb llum blava (465 nm). Degut a que les mostres són irradiades a través de l'objectiu del microscopi, els patrons induïts mostren un patró radial en el pla que comença al centre del feix de llum irradiat. Amb aquest material, les configuracions obtingudes són purament de splay (radial) (**Fig.9a**) o de bend-splay (espiral) (**Fig.9b**). El canvi de configuracions s'obté prenent avantatge de les propietats elàstiques del material.

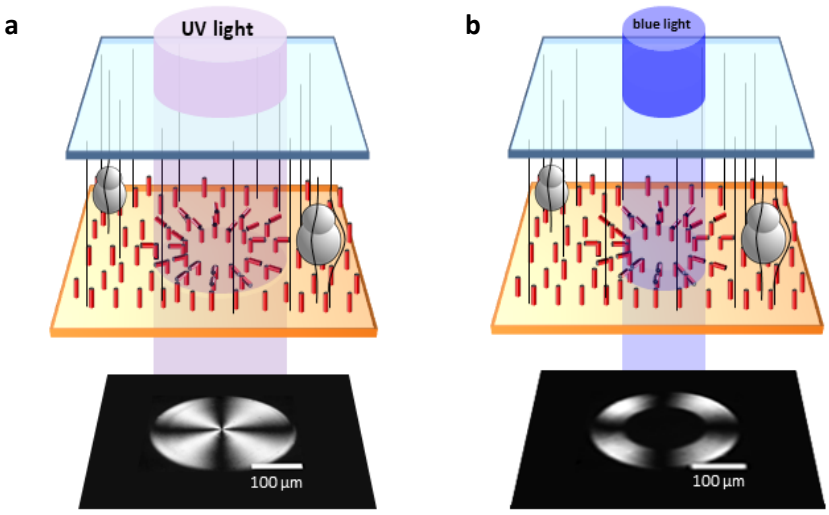

Fig. 9. Esquema il·lustrant el protocol experimental d'irradiació. a) Irradiar la mostra amb llum UV promou la transició de la forma tr*a*ns (homeotropic) a la *cis* (planar) del compost AZO (CLN). La textura splay es veu evidenciada sota polaritzadors creuats com una creu de Malta. **b)** Borrant una regió central del patró inicialment imprès amb llum blava força la relaxació inicial d'splay a una de bend-splay. Això es veu evidenciat com una corona sota polaritzadors creuats.

- **Caracterització d'una partícula individual**

Per entendre millor el mecanisme de propulsió, cal considerar la geometria experimental (**Fig.10a**). En absència del camp elèctric, les condicions de contorn forcen el CLN a adoptar una disposició homeotropica, així el CLN està disposat sobre l'eix z. Com que el CLN té anisotropia dielèctrica negativa, sota l'aplicació d'un camp extern, el CLN s'alinearà perpendicular a aquest, i com a conseqüència paral·lel als substrats, en el pla xy.

Com s'ha comentat en la secció 1.4, les partícules col·loïdals dispersades en un CLN distorsionen la matriu elàstica induint defectes topològics prop a la seva superfície. Les partícules en forma de cacauet de poliestirè mostren un ancoratge planar del CLN a la seva superfície, i mostren dos defectes puntuals en forma de "boojums" (**Fig.10b**).

La propulsió de les partícules es degut a fluxos induïts al voltant de la partícula. L'anisometria de la partícula fa que els fluxos es trobin desequilibrats a banda i banda

d'aquesta, i per tant, això pot resultar amb una propulsió neta. Degut a la geometria confinada i a l'elevada viscositat del medi, el moviment esdevé en dos dimensions.

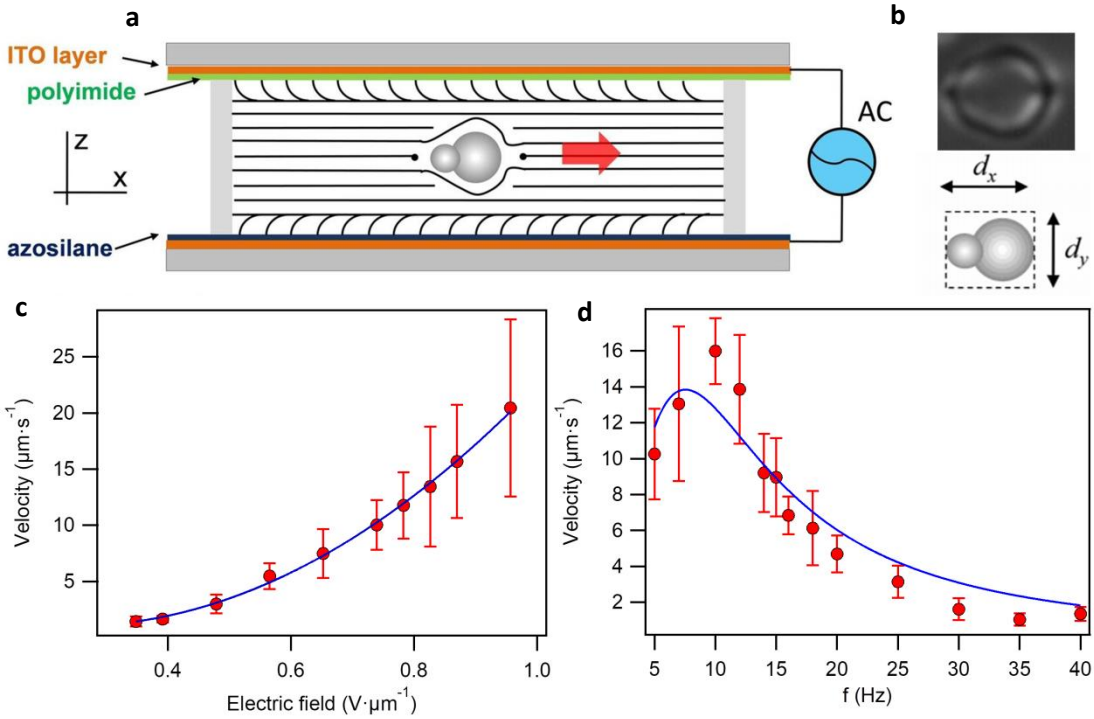

Fig. 1099. Caracterització del transport d'una partícula individual. a) Esquema de la cel·la experimental mostrant una partícula anisomètrica. El camp elèctric s'aplica entre els dos substrats d'ITO. **b)** Micrografia entre polaritzadors creuats d'una partícula anisomètrica que presenta dimensions laterals d_x = 10.2 μm i d_y = 8.2 μm. **c)** Velocitat, v_0, versus amplitud, *E*, del camp elèctric aplicat per una partícula individual sota una freqüència = 10Hz. **d)** Velocitat, v_0, versus freqüència, *f*, del camp aplicat per una partícula individual mentre l'amplitud del camp sinusoïdal es manté, $0.76\ V \cdot \mu m^{-1}$. Els punts aïllats corresponen a les dades experimentals, mentre que la línia roja es un ajust quadràtic o una funció no monotònica per l'amplitud i la freqüència del camp elèctric aplicat, respectivament. Les barres d'error són la desviació estàndard sobre 10 partícules.

La velocitat foretica de la partícula, v_0, pot ser controlada a través de l'amplitud del camp elèctric aplicat (veure **Fig.10c**). En els nostres experiments, la dependència de v_0 amb *E* és quadràtica ja que una potència de E indueix la separació de càrregues i l'altra indueix el seu moviment resultant en un flux electroosmòtic.

Un altre paràmetre de control es la freqüència del camp aplicat, on la dependència de la velocitat amb la freqüència pot ser expressada per la següent formula (veure **Fig.10d**),

$$v(f) = v_o \frac{f^2 {\tau_e}^2}{(1 + f^2 {\tau_c}^2)(1 + f^2 {\tau_e}^2)}.$$

Aquí, la freqüència del camp elèctric altern aplicat depèn bàsicament de dos temps característics, τ_c i τ_e, que corresponen als temps de càrrega característics de les partícules i dels elèctrodes respectivament. De les dades experimentals obtingudes a una amplitud del camp fix, $0.76\ \mathrm{V} \cdot \mu\mathrm{m}^{-1}$, podem ajustar les escales de temps intrinsiques del procés, donant lloc a $\tau_c \approx 0.016\ s$ i $\tau_e \approx 0.032\ s$. Aquestes does escales de temps són les important en la repulsió de llarg-abast observada, tal i com s'explica a continuació.

4.2. Resultats i discussió

Les partícules que formen els assemblatges col·loïdals són propulsades sota l'acció del mecanisme LCEEK (veure secció 1.5). Les partícules adopten una velocitat constant quan es transporten a través del fluid viscós. Així, s'estableix un balanç entre les forces viscoses de fricció i les forces forètiques de propulsió. En els nostres experiments, ens hem restringit a estudiar freqüències superiors a 10 Hz per assegurar una dependència monotònica de la velocitat de les partícules (**Fig.10d**), i hem mantingut l'amplitud del camp elèctric sinusoïdal a $0.76\ V \cdot \mu m^{-1}$.

- **ASTERS**

Un cop el camp director local del CLN es troba en una configuració radial (**Fig.9a**), el camp elèctric propulsa les partícules, que mostren trajectòries de tipus radial, seguint el patró prèviament imprimit. A mesura que arriben més partícules, les partícules es re-organitzen formant clústers circulars que mostren una distància entre-partícules comparable a la mida d'aquestes (**Fig.11a**). La distància mitja entre-partícules varia a mesura que el clúster creix, essent més petita al centre que a la perifèria del clúster. Aquest comportament suggereix la presencia d'una repulsió neta entre-particules, que, balanceja la propulsió forètica i evita l'agregació irreversible de les partícules. La interacció repulsiva permet explicar la inhomogènia distribució de la densitat per aquest tipus d'assemblatges.

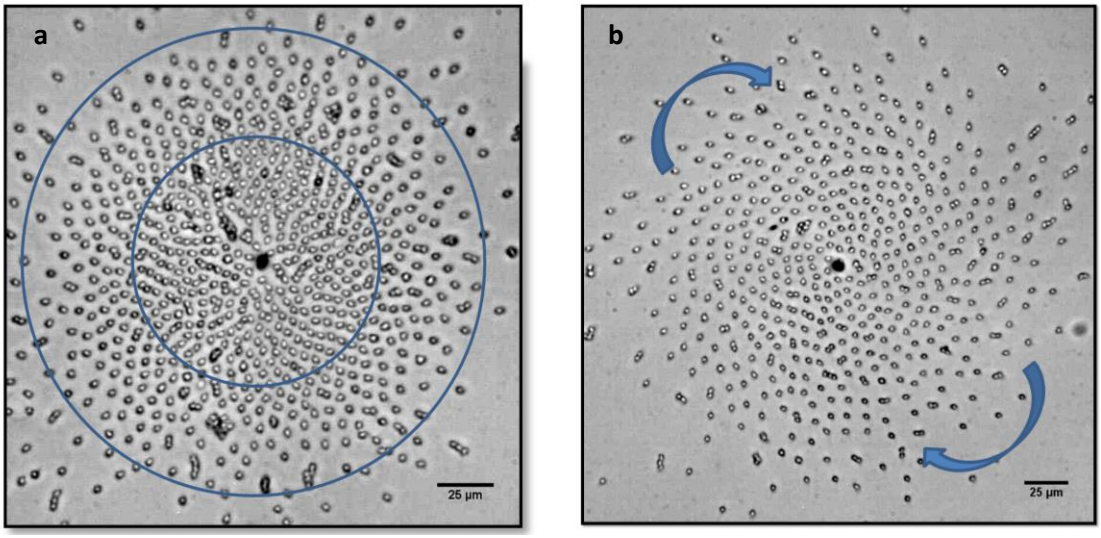

Fig. 11100. Formació de clústers col·loidals en cristalls líquids nematics. a) Fotografia de microscòpia òptica mostrant la formació d'un aster mentre un camp elèctric perpendicular als elèctrodes es aplicat. Els cercles blaus delimiten les tres regions descrites en el text. **b)** Micrografia mostrant la formació d'un rotating mill on les partícules s'auto-ensamblen en forma d'espiral. Les fletxes mostren el sentit de rotació del clúster.

El clúster s'organitza en tres regions ben definides (**Fig.11a**). La regió central (I) o nucli central correspon a un estat "jammed", on les partícules es troben bàsicament immòbils i on gairebé no s'observen re-organitzacions. Aquesta fase es troba seguida d'una regió intermèdia (II) que es disposa similar a un líquid, on les partícules es troben separades per una distància específica i on la fracció d'àrea de partícules o densitat decreix linealment. Finalment, aquesta fase líquida es troba seguida per un decaïment exponencial cap a zero, ressemblant un gas ideal en condicions baromètriques.

Per altra banda, també hem quantificat la distorsió estructural present en els nostre assemblatges col·loïdals respecte a una fase hexagonal. Per això, hem fet servir el paràmetre d'odre de l'orientació dels enllaços (ψ_6). Aquest paràmetre indica com de pròxima és la nostra distribució de partícules a un empaquetament hexagonal. Així, ens permet caracteritzar el ordre present en els assemblatges bi-dimensionals. De forma interessant, hem observat que ψ_6 no varia d'una forma monotònica. ψ_6 adopta un màxim en la regió (II) on el perfil de densitats decau linealment. Així, la part més ordenada dels nostres assemblatges col·loïdals correspon a un règim de "baixa" densitat, on les interaccions elàstiques del CLN de curt abast no juguen cap paper. Així, aquest comportament inusual pot ser atribuït a la repulsió entre-partícules.

- **ROTATING MILLS**

Un cop el camp director del CLN es troba en una configuració de bend-splay (**Fig.9b**), les partícules són propulsades sota l'acció del camp elèctric aplicat perpendicularment als elèctrodes. Les partícules segueixen una trajectòria radial però també tangencial, donant lloc a un assemblatge en forma d'espiral (**Fig.11b**). A mesura que arriben més partícules es mantenen rodant al voltant del defecte topològic com si es tractés d'un cos rígid. El moviment rotacional del clúster segueix la quiralitat del patró inicialment imprès. Diferent que en el cas dels asters, a mesura que creix l'assemblatge no s'observa un canvi en la distància entre-partícules. Així, no queda evidenciat els tres estats d'agregació observats en el cas dels asters. Això evidencia les diferències entre les diferents configuracions aster i rotating mill, on en l'últim, la regió central només s'observa quan milers de partícules s'han auto-ensamblat.

Per tal d'analitzar els estats dinàmics que mostren els assemblatges en forma de rotating mill, vam utilitzar la tècnica "particle imatge velocimetry (PIV)". Així, es pot determinar la component de la velocitat radial (v_ρ) i azimutal (v_θ) de cada partícula, i posteriorment fer la mitjana sobre tot l'assemblatge. Hem observat que la velocitat radial tendeix a 0 quan es forma el rotating mill mentre que la tangencial augmenta cap a la unitat. A part de la velocitat instantània, també es pot caracteritzar les dinàmiques dels rotating mills en termes de dos paràmetres d'ordre diferents. Aquests són, la polaritat de les partícules, i així el moment linear, que bàsicament es perd quan les partícules formen el patró en forma d'espiral, i el moment angular global, què és màxim quan les partícules es troben rodant al voltant del defecte.

- **DEPENDÈNCIA AMB LA FREQÜÈNCIA DELS ASSAMBLATGES**

Els clústers formats a diferents freqüències són diferents en la regió líquida, on la repulsió entre-partícules és efectiva, per totes dues configuracions, aster i rotating mills (**Fig.12**). Tot i això, per facilitar l'anàlisi e interpretació de les dades ens hem restringit només a configuracions d'aster, on les trajectòries de les partícules són purament radials.

Quan es comparen clústers formats a diferents freqüències del camp elèctric, la densitat del nucli intern no varia significantment, però sí que es veuen diferències en la corona de la regió (II). Comparant experiments realitzats a diferents freqüències observem una tendència no monotònica de la pendent mitjana de la regió (II) quan es varia la freqüència. Més enllà,

dividint la pendent mitjana entre la velocitat de cada experiment, les nostres dades suggereixen que el pendent es proporcional a la força forètica de partícules propulsades individualment. Així, tal i com es discuteix en la tesis, aquest resultat suggereix que la repulsió entre-partícules és independent de la freqüència.

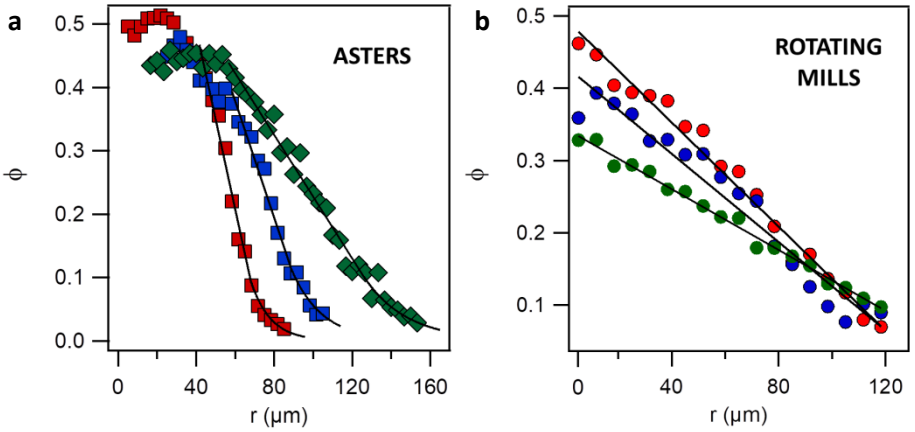

Fig. 12. Perfil de densitat radial dels clústers col·loïdals obtinguts experimentalment. **a)** Fracció d'area ocupat per partícules versus la distància al centre del clúster per configuracions d'aster realitzades a f = 10 (■), 15 (■) i 20 (■) Hz. La línia recta es un ajust lineal al perfil de la fracció d'àrea ocupada per partícules en la regió (II), i un ajust exponencial a la regió diluïda (III). **b)** La fracció d'àrea ocupada per partícules en front del radi del clúster per experiments amb configuració de rotating mill per experiments realitzats a f = 10 (●), 15 (●) i 20 (●) Hz. La línia recta és un ajust lineal al perfil de la fracció d'àrea ocupada per partícules, que mostra una regió líquida.

La variació espacial lineal i l'escalat amb la velocitat de la partícula del perfil de densitat de la regió (II) es pot entendre com un balanç entre la força centrípeta, $F = \gamma v_0$, que agrega les partícules i una repulsió de llarg-abast entre-partícules. Aquest efecte es pot descriure qualitativament amb l'ajuda d'un simple model basat en motlles. Aquest model permet relacionar els diferents pendents obtinguts amb la interacció repulsiva entre partícules a través d'un potencial.

- **MODEL TEÒRIC I RESULTAT DE LES SIMULACIONS**

Per poder entendre millor el comportament físic dels clústers col·loïdals obtinguts, i també, la transició entre les diferents fases i els perfils de densitat obtinguts, en el grup, hem desenvolupat un model teòric, i també s'han realitzat simulacions (Dr. Arthur Straube) que estan en concordança amb les tendències experimentals observades.

El sistema de simulació consisteix en un eixam bi-dimensional de N partícules que són propulsades en el pla xy. Les inclusions col·loïdals són esferes dures que es propulsen al llarg del camp director. Per similitud amb les condicions experimentals els anàlisis s'han dut a terme a una amplitud del camp elèctric fixada i a una freqüència variable. Per reproduir la propulsió de la partícula s'han assumit dinàmiques "overdamped" que vol dir que la velocitat de les partícules es proporcional a la força exercida sobre elles, tal i com s'ha demostrat en els experiments. Les fluctuacions tèrmiques es negligeixen, tot i que poden jugar un paper (veure secció 3.2).

En el model desenvolupat tenint en compte les suposicions mencionades, cada partícula amb posició $r_i = (x_i, y_i)$ $(i = 1, \dots, N)$ es troba governada per l'equació de moviment,

$$\frac{d\boldsymbol{r_i}}{dt} = v_i(f)\hat{\boldsymbol{n}}(r_i) - \frac{1}{\gamma}\sum_{j\neq i}\frac{\delta U}{\delta \boldsymbol{r}_{ij}}.$$

Aquí, el primer terme descriu la propulsió de cada partícula individual que es propulsada sobre el camp director del CLN, $\hat{n}(r)$. Les esferes es posen en moviment i experimenten una força de fricció amb un coeficient, γ. El segon terme té en compte la interacció repulsiva entre-partícules separades per una distància $\boldsymbol{r}_{ij} = |r_i - r_j|$, amb un potencial d'interacció repulsiva que combina diferents ingredients.

$$U = U_{hd}(r_{ij}) + U_{dd}(r_{ij}) + U_{hc}(r_{ij}) + U_{qq}(r_{ij}, \hat{n}).$$

Aquest potencial té en compte les hidrodinàmiques (U_{hd}) de llarg abast induïdes pels fluxos electroosmòtics, les interaccions dipolars (U_{dd}) induïdes entre partícules veïnes degut a la polarització sota l'acció d'un camp elèctric extern, les interaccions "hard-core" (U_{dd}) de curt abast i la interacció quadrupolar (U_{qq}) degut a la interacció entre la partícula i la matriu elàstica del material (CLN).

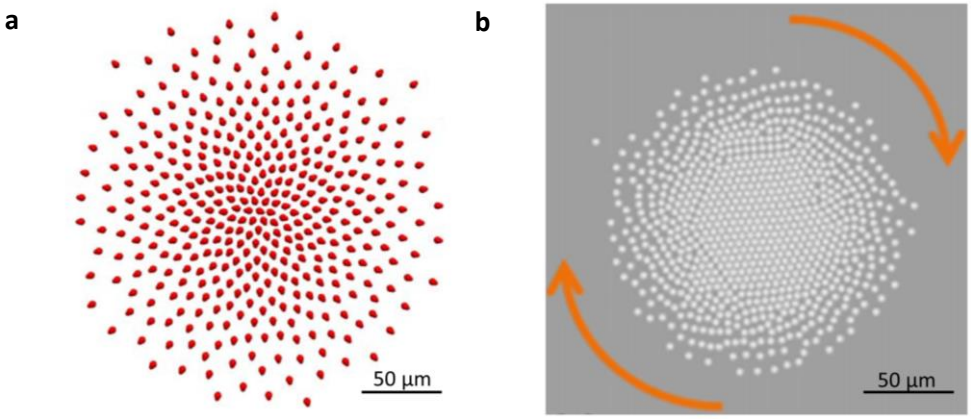

Fig. 13. Simulacions dels clústers de partícules obtinguts amb el model descrit en el text. a) Simulació d'un clúster auto-ensamblat de partícules presentant una configuració d'aster. En la imatge, s'han reemplaçat les partícules esfèriques per unes en forma de cacauet. b) Simulació d'un clúster de partícules presentant una configuració de rotating mil.

Un aspecte important del model és la selecció dels paràmetres electrocinètics. És crucial triar-los bé no només per obtenir concordança amb els resultats experimentals però per entendre el balanç dels diferents processos físics que tenen lloc. Bàsicament hi ha tres paràmetres que depenen de la freqüència involucrats en la formació dels clústers, específicament, la propulsió de les partícules i els dos mecanismes de repulsió de llarg abast, les hidrodinàmiques i les interaccions dipolars. Totes tres depenen de dos escales de temps, el temps de càrrega de la partícula, τ_c , i de l'elèctrode, τ_e, que són obtinguts simultàniament de l'ajust sobre la propulsió de les partícules individuals (veure secció 4.1). De fet, hem modificat l'amplitud relativa dels potencials , U_{hd} i U_{dd}, per tal de que la suma dels potencial esdevingués independent de la freqüència. Així, hem pogut ajustar les pendents dels perfils de densitat.

El model descrit s'ha aplicat per simular un eixam de 700 partícules amb uns paràmetres específics que compleixen les condicions abans esmentades. Tal i com es mostra en la **Fig.13**

el model captura tots els detalls dels clústers obtinguts experimentalment, incloent l'existència de tres estats d'agregació.

- **EQUACIÓ D'ESTAT**

L'aportació constant d'energia gràcies al camp elèctric extern promou el sistema fora de l'equilibri. En absència d'un defecte topològic, les partícules es propulsarien però sense formar clústers. En el cas d'induir el defecte topològic permet format aquest tipus de clústers radials. Les partícules propulsades exerceixen una pressió constant cap al centre del defecte topològic. Apagant el camp elèctric o disminuint-lo per sota el llindar per la reorientació del CLN, les partícules difonen lentament per la cel·la experimental. Així, es pot definir una equació de no-equilibri pel nostre sistema col·loïdal ja que podem definir la força que exerceix cada partícula. Això permet calcular la pressió mecànica del sistema.

Avaluant experiments realitzats a diferents freqüències, i per tant, a diferents velocitats i diferent força actuant a cada experiment veiem que les corbes de pressió – densitat, $p - \phi$, col·lapsen sobre una mateixa curva màster.

4.3. Conclusions

En aquesta secció hem estudiat clústers bi-dimensional de partícules en forma de cacauet assemblades en un defecte topològic puntual en una cel·la de cristall líquid. L'anisotropia del medi dispersant combinada amb la geometria experimental resulta de l'origen de diferents fenòmens electrocinètics generats pel mateix camp elèctric extern.

- La presència d'una superfície fotosensible permet la modificació *in situ* de la configuració elàstica del cristall líquid nematic, obtenint dos configuracions diferents: asters i rotating-mills. Així l'elasticitat juga un paper important a l'hora de dirigir les trajectòries col·loïdals.

ASTERS

- El camp elèctric proporciona una força de propulsió constant a cada partícula que promou l'agregació sobre un defecte topològic puntual, però també genera una força repulsiva entre-partícules que porta a diferents estats d'agregació del clúster, específicament, una regió interna, seguida d'una fase líquida i acabant en una fase dispersa, similar a un gas.

- Els nostres experiments suggereixen que la repulsió entre-partícules és independent de la freqüència. Aquesta és conseqüència d'una combinació de múltiples efectes, incloent acoblaments hidrodinàmics dels fluxos electrocinètics generats al voltant de les partícules i les forces dipolars degudes a la geometria experimental i a les propietats material en qüestió.

- Les simulacions numèriques concorden amb els resultats experimentals, revelant que els assemblatges col·loïdals son el resultat d'un balanç delicat enter diferents forces actuant al mateix temps.

- Important i diferent dels típics clústers col·loïdals obtinguts en el camp dels "nematic colloids" és que la elasticitat juga un paper minoritari en la coexistència de fases.

- Els assemblatges col·loïdals es poden caracteritzar amb una equació d'estat de no equilibri quan s'analitza la pressió mecànica exercida per les partícules pertanyents al assemblatge.

ROTATING MILLs

- La component tangencial de la velocitat evita que el nucli "jammed" es desenvolupi pels assemblatges estudiats, tot i que es visible quan milers de partícules formen el clúster. Com a conseqüència el perfil de densitat radial segueix un decaïment lineal des de el centre del defecte topològic, contràriament al cas dels asters.

- Les partícules s'auto-assemblen al voltant del defecte topològic i estan rodant amb una velocitat azimutal característica, que adopta un màxim quan totes les partícules roden com si fos un cos rígid. Al contrari, la velocitat radial decreix a mesura que el clúster creix. Aquest fet es veu evidenciat pels paràmetres d'ordre del moment lineal de les partícules, o la polaritat, que bàsicament es nul i el moment angular global, què és màxim quan les partícules roden al voltant del defecte.

Com a conclusió final, els nostres experiments demostren capacitat de control per l'assemblatge de micro-partícules en fluids complexos, com ara cristalls líquids. El grau de control sobre la propulsió de les partícules i la capacitat de definir trajectòries per les partícules per auto-assemblar-se són alguns dels grans avantatges d'aquest mètode.

5. Transport col·loïdal col·lectiu

Aquesta última secció experimental de la tesis està basada en dirigir i guiar el moviment col·lectiu de partícules a través de superfícies fotosensibles i de dispositius de confinament. Els primers experiments consisteixen en un eixam de partícules transportat al llarg d'una trajectòria pre-definida. Això es pot realitzar gràcies a la superfície fotosensible abans esmentada (veure secció 3.1). Prenent avantatge d'aquesta última també hem pogut imprimir un patró amb una xarxa de defectes topològics. Finalment, mostrem la implementació de dispositius de micro-fluídica per tal de fer-hi passar els eixams de partícules a través.

5.1. Protocols i muntatges experimentals

En aquesta secció s'han utilitzat dos sistemes experimentals diferents. El primer, és idèntic al descrit en la secció 4.1 i consisteix en una superfície fotosensible. Més enllà, les dispersions col·loïdals també han estat confinades mitjançant dispositius de micro-fluídica.

- SISTEMA 1 – EXPERIMENTAL PHOTOSENSITIVE CELL

El primer sistema experimental és idèntic al descrit en la secció 4.1. Tot i això, hem utilitzat dos protocols diferents d'irradiació.

- **Protocol d'irradiació – Transport d'eixams de partícules**

Pels experiments basats en el transport d'un eixam de partícules, inicialment s'indueix un defecte topològic (veure secció 4.1). Posteriorment, aquest defecte topologic es arrastrat de la seva posició inicial una certa distància. Aquest procés es du a terme a través d'una línia de disclinació que es forma quan el feix de llum UV es arrossegat de la posició inicial a la final en la superfície fotosensible.

- **Protocol d'irradiació – Xarxa de defectes topològics**

En aquest cas, el protocol d'irradiació es du a terme posant una màscara física entre la font de llum UV i l'objectiu del micoscopi. La màscara és una fulla d'acetat que bloqueja la llum selectivament. Aquesta màscara, en alguns casos, mostra un perfil Gaussià d'intensitats de grisos començant des del centre de l'objecte a projectar i expandint-se cap a l'exterior.

- SISTEMA 2 – DISPOSITIUS DE MICRO-FLUÍDICA

En aquest cas, les cel·les experimentals són similars a les realitzades en procediments anteriors tot i que estan construïdes utilitzant litografia tova. Més precisament, dos superfícies d'ITO són funcionalitzades de forma que l'ancoratge sigui de tipus homeotropic. Aquestes superfícies es rasquen per tenir una alineació preferencial del camp director al llarg del dispositiu de micro-fluídica. Les dos superfícies d'ITO s'enganxen miran una a l'altra a través d'una resina polimeritzable amb llum UV (NOA81), que replica la forma del motlle tou de PDMS. El motlle replicat amb la resina UV permet tant el confinament amb la forma desitjada com actuar d'espaiador en la cel·la experimental, obtenint una distància d'uns 25 µm.

5.2. Resultats i discussió

Incialment, el transport col·lectiu d'eixams de partícules sobre una superfície fotosensible s'ha estudiat tant de forma experimental com en forma de simulacions. Tot i això, en aquest resum només es mostraran els resultats experimentals. Més enllà, hem utiliitzat aquesta superfície fotosensible per projectar patrons pre-definits que ens permetran induir objectes col·loïdals en les cel·les de CLN. Finalment, hem confinat les dispersions col·loidals per mitjà de dispositius de micro-fluídica per tal de veure com afectava al flux de partícules el pas per petites obertures.

- **Transport d'un eixam de partícules**

Per qualsevol dels clústers assemblats, la velocitat de la partícula tendeix a zero per freqüències per sobre de 40Hz del camp elèctric aplicat (veure secció 4.1). En el nostre cas hem triat una frequencia de 1 KHz per congelar, deixar immòbil, l'assemblatge sobre el defecte topològic puntual. Posteriorment, hem desplaçat el defect topològic gràcies a la superfície fotosensible. Aquest procés s'ha dut a terme a través d'una disclinació que es forma quan el feix de llum UV es desplaçat dins la cel·la. Aquest procés es pot observar en la **Fig. 14**, on un assemblatge amb configuració de rotating mill es transportat una distància aproximada de 175 µm. Durant la translocació de l'eixam de partícules, aquestes es mouen com un patró polaritzat l'extrem frontal amb forma de fletxa. Aquests estats dinàmics permeten estudiar estats de "flocking". Per això, cal evaluar els dos paràmetres d'odre *M* i *P* (veure secció 4.2). Breument, el paràmetre d'odre global angular, *M*, augmenta respecte el paràmetre d'ordre linear polar, *P*, quan el rotating mill s'ensambla. Posteriorment, el defecte topològic es translocat, i les partícules desmonten l'assamblatge per seguir la nova trajectòria fixada, intercanviant-se els valors de *M* i *P*. Finalment, les partícules es tornaran a agregar formant altre cop un clúster de tipus rotating mill, on *M* tornarà a augmentar.

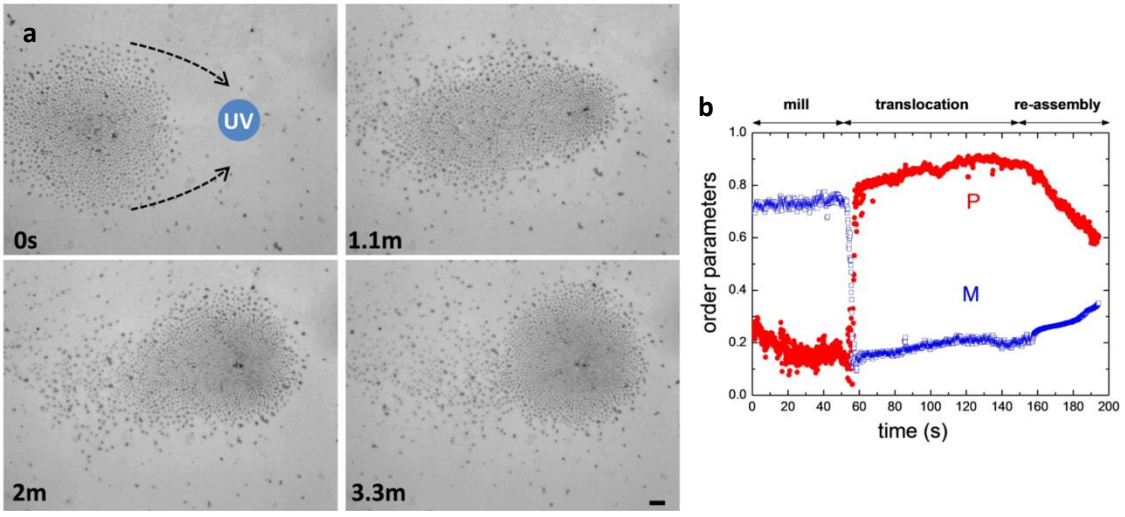

Fig. 14101. Translocació d'un eixam de partícules. a) Imatges mostrant el transport del clúster a una zona diferent de la cel·la experimental. El punt blau indica la destinació del feix de partícules. L'escala correspon a 20 µm. **b)** Paràmetres d'ordre, *P* i *M,* mesurats de les trajectòries de les partícules mostrades en **a)**.

- **Projecció de patrons sobre la superfície fotosensible**

Prenent avantatge de la superfície fotosensible permet projectar qualsevol tipus d'objecte de mida i forma. El patró és induït a través d'una màscara física que permet des de la projecció de cadenes de rotating mills fins a la projecció d'objectes bi-dimensionals (veure **Fig.15**).

En la **Fig.15** es mostra una xarxa de defectes topològics bi-dimensional induïts amb un feix de llum UV i distribuïts en la forma de 3 columnes x 3 files. Sota l'aplicació d'un camp elèctric altern extern, la matriu elàstica adopta la forma de la **Fig.15a**, on els nou defectes topologics foto-induïts s=+1 (punts blaus **Fig.15**) apareixen connectats mitjançant defectes de càrrega s=-1 (punts vermells **Fig.15**). Per complir la condició elàstica de contorn, un defecte amb càrrega s=-1 es creat entre mig de cada parell de defectes induïts s=+1. En aquest punt, el valor de la càrrega topològica total de tota la xarxa és de s=-3. De forma interessant, la matriu elàstica indueix ella mateixa quatre defectes topològics s=+1 (cercles verds **Fig.15**) localitzats de forma específica per tal de compensar la càrrega topològica total, obtenint finalment un valor s=+1 pel global de la xarxa. Finalment, aquest defecte global s=+1 es balancejat degut a la creació d'un altre defecte s=-1 en qualsevol lloc dela cel·la.

Quan les partícules són propulsades, els defectes foto-induïts (punts vermells) mostren un assemblatge de tipus rotating mill, mentre que els punts induïts per la pròpia matriu elàstica (cercles verds) mostren assemblatges de tipus aster. En el nostre sistema les partícules són "sensors" de la configuració del cristall líquid.

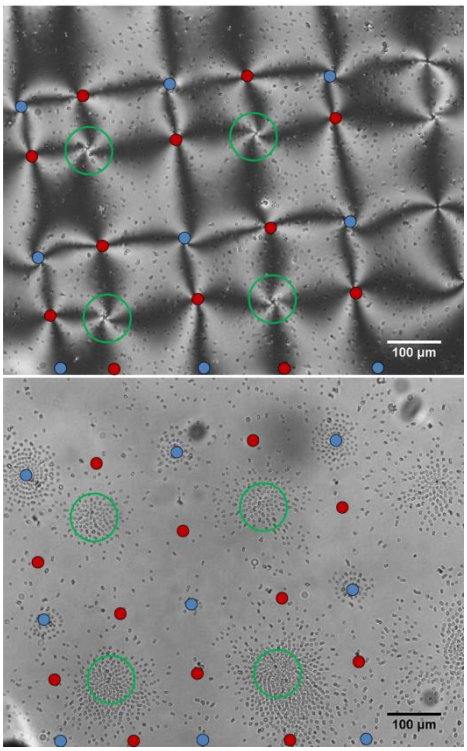

Fig. 15. Xarxa bi-dimensional d'objectes foto-induits. a) Imatge sota polaritzadors creuats d'una xarxa projectada de defectes topològics 3x3. Els punts vermells (cercles verds) mostren els defectes photo-induits (induïts per la pròpia matriu elàstica). Contràriament, els defectes s=-1 corresponen als punts blaus.. **b)** Imatge de microscòpia de camp clar mostrant els clústers col·loïdals assemblats sobre els defectes topològics s=+1, mentre que els defectes s=-1 promouen el transport col·loidal entre defectes topològics.

- **Dispositius de micro-fluídica**

Típicament, els efectes de "clogging" han estat observat en sistemes de partícules micro-mètriques dispersades en fluids isotròpics degut al seu pas al llarg de constriccions estretes ([180]). De forma contrària, no hem observat en la literatura de la dispersió i el transport de partícules micro-mètriques en fluids anisotropics degut a l'aplicació d'un camp elèctric extern.

En la propulsió d'eixams de partícules en dispositius confinats els eixams es comporten com "flocks" o núvols col·loïdals que es transporten en un pla definit a una velocitat constant (**Figs.16a,b**). El núvol de partícules ocupa tota l'amplada del confinament del dispositiu, fins que arriba fins al pas estret (**Figs.16c,d**). Quan les partícules s'apropen a la paret lateral. Sota l'aplicació d'un camp elèctric extern, singularitats en forma de línies de disclinació (es mostren com fletxes blaves en la **Fig.16**) apareixen al voltant de les parets del confinament. Així, les partícules s'hi poden enganxar i prevenir el flux de partícules a través del pas estret (**Fig.16d**). De forma interessant, la configuració de l'estat "clogged" final dels nostres experiments sembla contrari a aquells obtinguts en fluids isotròpics ([180]).

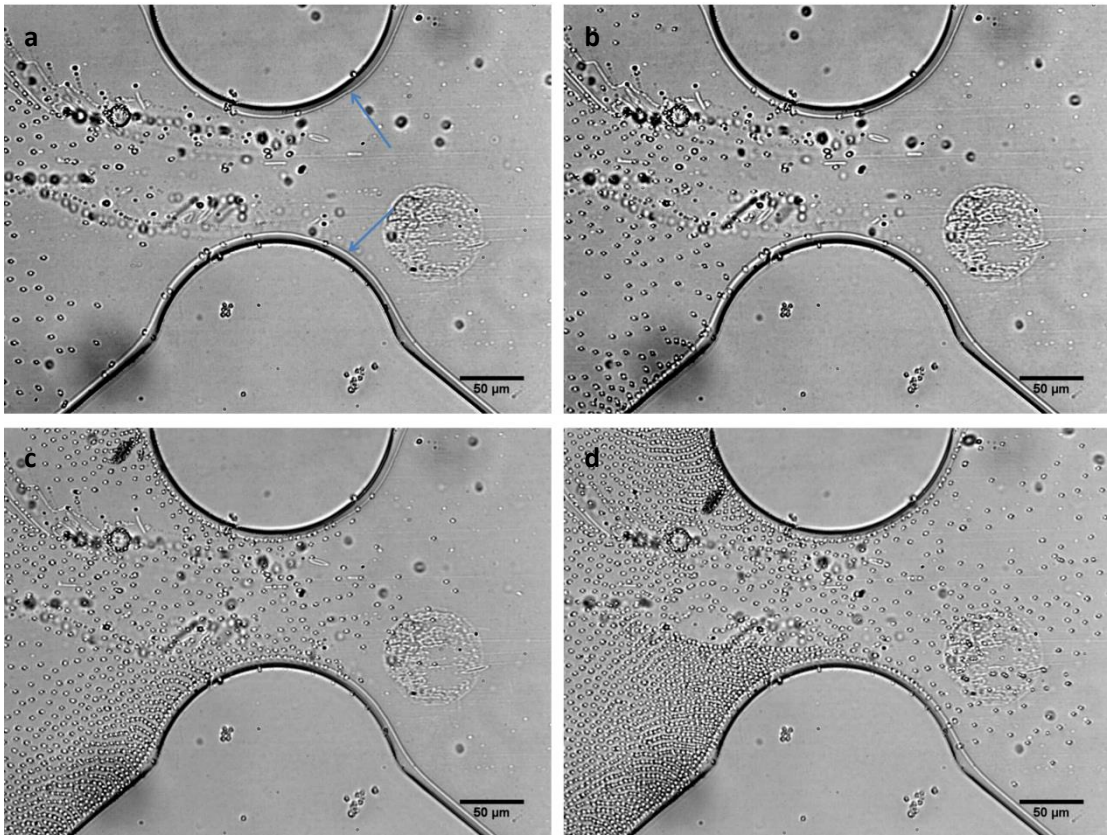

Fig. 16102. Efectes de "clogging" en partícules dispersades i transportades en un cristall líquid nematic a través d'una constricció.. a) Inicialment, les partícules són dirigides cap al pas estret (75 µm d'amplada). **b)** Les partícules apareixen en el camp de visió i es comencen a assemblar a les parets del dispositiu de confinament després de 25 s. **c)** La constricció queda saturada de partícules tot i que algunes d'elles encara passen a través de la constricció (80 s). **d)** Finalment, les partícules queden enxganxades a les parets del confinament i formen una paret prevenint el transport de partícules a través de la constricció (160 s).

5.3. Conclusions

En aquesta secció hem mostrat el transport col·loïdal d'eixam de partícules que es troben fora de l'equilibri degut a l'aplicació d'un camp elèctric extern. Els eixams de partícules són transportats gràcies a la implementació d'una superfície fotosensible i dispositius de confinament, permetent estudiar estats de "flocking" i "clogging".

Projectant sobre la superfície fotosensible

- Gràcies a la superfície fotosensible podem definir qualsevol tipus de trajectòria. En aquest cas a través d'una línia de discilnació que es forma quan el feix de llum UV es transportat dins la cel·la. Això permet definir trajectòries a les partícules per estudiar efectes de "flocking".

- Prenent avantatge de la tècnica basada en la projecció de màscares, hem pogut induir xarxes de clúster col·loïdals bi-dimensionals. Aquests sistemes permeten l'estudi tant de dinàmiques col·loïdals dispersades, com la topologia en fluids de tipus cristall líquid.

Dispositius de micro-fluídica (confinament)

- Les partícules dispersades en un cristall líquid ipropulsades en dispositius de confinament permeten estudiar efectes de "clogging". Tot i la exhistent repulsió entre partícules discutida en anteriors seccions, i per la qual, no s'hauria d'observar efectes de "clogging", aquests són existents en les geometries estudiades. A més a més, l'estat "clogged" final es diferent a aquells típicament observats en fluids isotròpics.

Tot i que l'ús de cristalls líquids en sistemes de confinament, i més específicament, sistemes de micro-fluídica es encara un camp de recerga emergent, aquest podria permetre la manipulació, l'assamblatge o fins i tot l'emmagatzematge col·loïdal.

6. **Conclusions i notes finals**

Els estats dinàmics, fora d'equilibri, observats en partícules dispersades i propulsades en CLNs són complexos i difícils de predir. En aquesta tesis hem pogut guiar o direccionar les trajectòries col·loïdals prenent avantatge de les propietats elàstiques del material. Típicament, hem utilitzat la química de superfícies per definir les propietats d'ancoratge i així, definir una direcció pel camp director. Els protocols mostrats durant la realització de la tesis permeten l'estudi des del transport d'una partícula individual fins a les dinàmiques mostrades pel transport col·lectiu col·loïdal.

Inicialment, hem analitzat la difusió anòmala d'una partícula individual transportada en una matriu de cristall líquid. El moviment és essencialment balístic al llarg del camp director per totes les configuracions estudiades. Per contra, el moviment perpendicular al camp director pot ésser superdifusiu depenent de les condicions d'ancoratge del CLN a la partícula. Més concretament, hem observat que, per configuracions dipolars mostrant un "point defect-hedgehog" el moviment transversal és superdifusiu mentre que per configuracions quadrupolars mostrant "double-boojums" el comportament és difusiu. També hem observat que aquest comportament no depèn significativament del mode de propulsió ni velocitat de la partícula.

Posteriorment, hem investigat l'assamblatge col·loïdal de clústers bi-dimensionals dirigits cap a un defect topològic induït en la matriu elàstica del cristall líquid nematic. Modificant l'ancoratge a través d'un feix de llum UV i gràcies a una superfície fotosensible, hem pogut induir dos tipus de configuracions diferents: asters i rotating mills. Sota l'aplicació d'un camp elèctric altern perpenciular a la mostra les partícules poden ser propulsades. L'anisotropia del material cominada amb la geometria dels experiments és l'origen de diferents fenòmens electrocinètics generats pel mateix camp elèctric. El camp elèctric proporciona una propulsió constant donant una força igual a cada partícula que promou l'assamlatge de les partícules sobre el defecte topològic, tot i això hi ha una repulsió efectiva entre-partícules que evita la agregació irreversible de les partícules. Així, els clústers amb configuració de aster són caracteritzats per diferents fases i diferents densitats d'empaquetament. Més enllà, hem pogut definir una equació d'estat pel nostre sistema fora d'equilibri. Les simulacions numèriques revelen que la geometria dels clústers col·loïdals observats és el resultat d'un balanç delicat entre diferents fenòmens electrocinètics que involucren fluxos hidrodinàmics, forces forètiques i interaccions dipolars generades a la interfase partícula-cristall líquid. Els resultats de les simulacions numèriques mostren acord amb els experiments, tant qualitativa com quantitativament.

Finalment, hem estudiat el transport col·loïdal d'eixams de partícules propulsades tant, sobre una superfície fotosensible, com dins de dispositius de confinament. Les diferents geometries experimentals permeten estudiar efectes de "flocking" i "clogging", però també apsecte de topologia en cristalls líquids.

Perspectives futures podrien ser l'estudi teòric dels experiments relacions amb el transport d'una partícula individual o l'implementació de noves tècniques experimentals que permetin la direcció i guiatge de partícules de formes complexes.

List of references

[1] O. Lehmann, On Flowing Crystals, *Zeitschrift für Phys. Chemie*, **4**, 461–472 (1889).

[2] P. G. de Gennes, J. Prost, *The Physics of Liquid Crystals* (Clarendon Press, 1995), *International Series of Monographs on Physics*.

[3] P. Oswald, P. Pieranski, *Nematic and Cholesteric Liquid Crystals: Concepts and Physical Properties Illustrated by Experiments* (CRC Press, 2005), *Liquid Crystal Book Series*.

[4] P. Oswald, P. Pieranski, *Smectic and Columnar Liquid Crystals: Concepts and Physical Properties Ilustrated by Experiments* (Taylor & Francis, Boca Raton, FL, 2006), *Liquid Crystal Book Series*.

[5] V. Luzzati, T. Gulik-Krzywicki, A. Tardieu, Polymorphism of Lecithins. *Nature*. **218**, 1031-1034 (1968).

[6] L. J. Yu, A. Saupe, Observation of a biaxial nematic phase in potassium laurate-1-decanol-water mixtures. *Phys. Rev. Lett.* **45**, 1000-1003, (1980).

[7] S.-W. Tam-Chang, L. Huang, Chromonic liquid crystals: properties and applications as functional materials. *Chem. Commun.* **17**, 1957-1967, (2008).

[8] H. Hasegawa, T. Hashimoto, Morphology of block polymers near a free surface. *Macromolecules*. **18**, 589-590, (1985).

[9] Z. Dogic, S. Fraden, Smectic phase in a colloidal suspension of semiflexible virus particles. *Phys.Rew.Lett.* **78**, 2417-2420, (1997).

[10] Q. Liu, M. G. Campbell, J. S. Evans, I. I. Smalyukh, Orientationally ordered colloidal co-dispersions of gold nanorods and Cellulose Nanocrystals. *Adv. Mater.* **26**, 7178-7184, (2014).

[11] G. Friedel, Les états mésomorphes de la matière. *Annales de Physique.* **18**, 273-474, (1922).

[12] H. Sackmann, D. Demus, The Polymorphism of Liquid Crystals. *Mol. Cryst.* **2**, 81-102, (1966).

[13] B. Senyuk, Liquid Crystals: a Simple View on Complex Matter (2005). (available online at www.personal.kent.edu/~bisenyuk/liquidcrystals).

[14] M. Philip, C. Robinson, M. Abramowitz, W. Davidson, MicroscopyU: The source for microscopy education (2012), (available online at www.olympusmicro.com).

[15] M. J. Stephen, J. P. Straley, Physics of liquid crystals*. Rev. Mod. Phys.* **46**, (1974).

[16] C. W. Oseen, The theory of liquid crystals. *Trans. Faraday Soc.* **29**, 883-899, (1933).

[17] F. C. Frank, Liquid crystals. On the theory of liquid crystals. *Discuss. Faraday Soc.* **25**, 19-28, (1958).

[18] B. S. Scheuble, G. Weber, R. Eidenschink, Liquid crystalline ciclohexylcarbonitriles: Properties of single compounds and mixtures. *Proc. Eurodisplay*. (1984).

[19] B. Jérôme, Surface effects and anchoring in liquid crystals. *Rep. Prog. Phys.* **54**, 391-451, (1991).

[20] D.-K. Yang and S.-T. Wu, *Fundamentals of Liquid Crystal Devices* (Wiley, 2014). *Series in Displays tecnhnology*.

[21] D. Berreman, Solid surface shape and the alignment of an adjacent nematic liquid crystal. *Phys. Rev. Lett.* **28**, 1683-1686, (1972).

[22] A. D. Price, D. K. Schwartz, Anchoring of a nematic liquid crystal on a wettability gradient. *Langmuir*. **22**, 9753-9759, (2006).

[23] V. Fréedericksz, V. Zolina, Forces causing the orientation of an anisotropic liquid. *Trans. Faraday Soc.* **29**, 919-930, (1933).

[24] G. E. Volovik, Topological singularities on the surface of an ordered system, *JETP Letters*. **28**, 59-61, (1978).

[25] G. H. Brown, *Advances in Liquid Crystals* (Elsevier Science, 2013).

[26] O. D. Lavrentovich, V. M. Pergamenshchik, Patterns in thin liquid crystal films and the divergence ('Surfacelike') elasticity. *Int. J. Mod. Phys. B.* **9**, 2389-2437, (1995).

[27] D. R. Link, M. Nakata, Y. Takanishi, K. Ishikawa, H. Takezoe, Patterns in hybrid nematic liquid-crystal films: Topography and topology. *Phys. Rev. Lett.* **87**, 1-4, (2001).

[28] O. V. Manyuhina, A. M. Cazabat, M. Ben Amar, Instability patterns in ultrathin nematic films: Comparison between theory and experiment. *Euro. Phys. Lett.* **92**, (2010).

[29] S. Hernàndez-Navarro, P. Tierno, J. Ignés-Mullol, F. Sagués, Nematic colloidal swarms assembled and transported on photosensitive surfaces. *IEEE Trans. Nanobioscience.* **14**, 267–271, (2015).

[30] M. J. Park, O. O. Park, Alignment of liquid crystals on a topographically nano-patterned polymer surface prepared by a soft-imprint technique. *Microelectron. Eng.* **85**, 2261-2265, (2008).

[31] J. Nehring, A. Saupe, On the schlieren texture in nematic and smectic liquid crystals. *J. Chem. Soc.* **68**, 1–15, (1972).

[32] I. I. Smalyukh, Y. Lansac, N. A. Clark, R. P. Trivedi, Three-dimensional structure and multistable optical switching of triple-twisted particle-like excitations in anisotropic fluids, *Nat. Mater.* **9**, (2009).

[33] M. A. Gharbi, M. Nobili, C. Blanc, Use of topological defects as templates to direct assembly of colloidal particles at nematic interfaces, *J. Colloid Interface Sci.* **417**. 250-255, (2014).

[34] I. Muševič, *Liquid Crystal Colloids* (Springer International Publishing, 2017).

[35] I. Muševič, Nematic Liquid-Crystal Colloids. *Materials.* **11**, 24, (2018).

[36] M. V. Kurik, O. D. Lavrentovich, Defects in liquid crystals: homotopy theory and experimental studies. *J. Exp. Theor. Phys.* **31**, 196–224, (1988).

[37] H. Stark, Physics of colloidal dispersions in nematic liquid crystals. *Phys. Rep.* **351**, 387-474, (2001).

[38] O. D. Lavrentovich, Transport of particles in liquid crystals. *Soft Matter*. **10**, 1264-1283, (2014).

[39] P. Poulin, Novel colloidal interactions in anisotropic fluids, *Science.* **275**, 1770-1773, (1997).

[40] Y. Gu, N. L. Abbott,"Observation of Saturn-ring defects around solid microspheres in nematic liquid crystals. *Phys. Rev. Lett.* **85**, 4719-4722, (2000).

[41] O. V. Kuksenok, R. W. Ruhwandl, S. V. Shiyanovskii, E. M. Terentjev, Director structure around a colloid particle suspended in a nematic liquid crystal. *Phys. Rev. E.* **54**, 5198-5203, (1996).

[42] B. Senyuk, O. Puls, O. M. Tovkach, S. B. Chernyshuk, I. I. Smalyukh, Hexadecapolar colloids. *Nat. Commun.* **7**, 1-7, 2016.

[43] O. D. Lavrentovich, Active colloids in liquid crystals. *Current opinion in Colloid & Interface Sci.* 21, 97-109, (2015).

[44] B. Senyuk, Q. Liu, S. He, R. D. Kamien, R. B. Kusner, T. C. Lubensky, I. I. Smalyukh, Topological colloids. *Nature.* **493**, 200-205, (2013).

[45] S. M. Hashemi, U. Jagodič, M. R. Mozaffari, M. R. Ejtehadi, I. Muševič, M. Ravnik, Fractal nematic colloids. *Nat. Commun.* **8**, 1–9, (2017).

[46] P. Poulin, D. A. Weitz, Inverted and multiple nematic emulsions. *Phys. Rev. E.* 57, 626-637, (1998).

[47] O. P. Pishnyak, S. Tang, J. R. Kelly, S. V. Shiyanovskii, O. D. Lavrentovich, Levitation, lift, and bidirectional motion of colloidal particles in an electrically driven nematic liquid crystal. *Phys. Rev. Lett.* **99**, 1–4, (2007).

[48] R. C. Hayward, D. A. Saville, I. A. Aksay, Electrophoretic assembly of colloidal crystals with optically tunable micropatterns. *Nature*. **404**, 56–58, (2000).

[49] S. Hernández-Navarro, J. Ignés-Mullol, F. Sagués, P. Tierno, Role of anisotropy in electrodynamically induced colloidal aggregates. *Langmuir*. **28**, 5981-5986, (2012).

[50] J. Yan, M. Han, J. Zhang, C. Xu, E. Luijten, S. Granick, Reconfiguring active particles by electrostatic imbalance. *Nat. Mater.* **15**, 1-6, (2016).

[51] P. Poulin, J.-C. Loudet, P. Barois, Colloidal ordering from phase separation in a liquid-crystalline continuous phase. *Nature*. **407**, 611-613, (2000).

[52] V. G. Nazarenko, A. B. Nych, B. I. Lev, Crystal structure in nematic emulsion. *Phys. Rev. Lett.* **87**, (2001).

[53] I. Muševič, M. Skarabot, D, Babic, N. Osterman, I. Poberaj, V. Nazarenko, A. Nych, Laser trapping of small colloidal particles in a nematic liquid crystal: Clouds and ghosts. *Phys. Rev. Lett.* **93**, 1–4, (2004).

[54] I. I. Smalyukh, A. N. Kuzmin, A. V. Kachynski, P. N. Prasad, O. D. Lavrentovich, Optical trapping of colloidal particles and measurement of the defect line tension and

colloidal forces in a thermotropic nematic liquid crystal. *Appl. Phys. Lett.* **86**, 5-8, (2005).

[55] B. Lev, A. Nych, U. Ognysta, S.B. Chernysuk, V. Nazarenko, M. Skarabot, I. Poberaj, D. Babic, N. Ostermann, I. Musevic, Anisotropic laser trapping in nematic colloidal dispersion. *Eur. Phys. J.* **20**, 215-219, (2006).

[56] M. Škarabot, M. Ravnik, D. Babic, N. Ostermann, I. Poberaj, S. Zumer, I. Musevic, A. Nych, U. Ognysta, V. Nazarenko, Laser trapping of low refractive index colloids in a nematic liquid crystal. *Phys. Rev. E.* **73**, 1-10, (2006).

[57] I. Musevic, M. Skarabot, U. Tkalec, M. Ravnik, S. Zumer, Two-Dimensional nematic colloidal crystals sef-assembled by topological defects. *Science.* **313**, 954-957, (2006).

[58] M. Skarabot, M. Ravnik, S. Zumer, U. Tkalec, I. Poberaj, D. Babic, N. Ostermann, I. Musevic, Interactions of quadrupolar nematic colloids. *Phys. Rev. E.* **77**, 10100-10106, (2008).

[59] I. I. Smalyukh, O. D. Lavrentovich, A. N. Kuzmin, A. V. Kachynski, P. N. Prasad, Elasticity-mediated self-organization and colloidal interactions of solid spheres with tangential anchoring in a nematic liquid crystal. *Phys. Rev. Lett.* **95**, 1-4, (2005).

[60] U. Ognysta, A. Nych, V. Nazarenko, I. Musevic, M. Skarabot, M. Ravnik, S. Zumer, I. Poberaj, D. Babic, 2D interactions and binary crystals of dipolar and quadrupolar nematic colloids. *Phys. Rev. Lett.* **100**, 7-10, (2008).

[61] I. Muševič, Nematic colloids, topology and photonics. *Philos. Trans. of the Roy. Soc. A*. **371**, (2013).

[62] M. Škarabot, M. Ravnik, S. Zumer, U. Tkalec, I. Poberaj, D. Babic, N. Ostermann, I. Musevic, Two-dimensional dipolar nematic colloidal crystals. *Phys. Rev. E.* **76**, 1-8, (2007).

[63] R. J. Hunter, *Foundation of Colloid Science* (Oxford,2001).

[64] X.-L. Wu , A. Libchaber, Particle diffusion in a quasi-two-dimensional bacterial bath. *Phys. Rev. Lett.* **86**, (2001).

[65] Y. Gambin, G. Massiera, L. Ramos, C. Ligoure, W. Urbach, Bounded step superdiffusion in an oriented hexagonal phase. *Phys. Rev. Lett.* **94**, 16-19, (2005).

[66] I. Y. Wong, M. L. Gardel, D. R. Reichman, E. R. Weeks, M. T. Valentine, A. R. Bausch, D. A. Weitz, Anomalous diffusion probes microstructure dynamics of entangled F-actin networks. *Phys. Rev. Lett.* **92**, 30-33, (2004).

[67] M. M. Alam, R. Mezzenga, Particle tracking microrheology of lyotropic liquid crystals. *Langmuir*. **27**, 6171-6178, (2011).

[68] J. C. Loudet, P. Hanusse, P. Poulin, Stokes drag on a sphere in a nematic liquid crystal. *Science.* **306**, (2004).

[69] T. Turiv, I. Lazo, A. Brodin, B.I. Lev, V. Reiffenrath, V. Nazarenko, O. D. Lavrentovich, Effect of collective molecular reorientations on Brownian motion of colloids in nematic liquid crystal. *Science.* **342**, 1351-1354, (2013).

[70] Y. Luo, D. A. Beller, G. Boniello, F. Serra, K. J. Stebe, Tunable colloid trajectories in

nematic liquid crystals near wavy walls. *Nat. Commun.* **9**, (2018).

[71] W. K. Potts, The chorus-line hypothesis of manoeuvre coordination in avian flocks. *Nature*. **309**, (1984).

[72] C. Becco, N. Vandewalle, J. Delcourt, P. Poncin, Experimental evidences of a structural and dynamical transition in fish school. *Physica A.* **367**, 487-493, (2006).

[73] J. L. Silverberg, M. Bierbaum, J. P. Sethna, I. Cohen, Collective motion of humans in mosh and circle pits at heavy metal concerts. *Phys. Rev. Lett.* **110**, 1-5, (2013).

[74] M. C. Marchetti, J. F. Joanny, S. Ramaswamy, T. B. Liverpool, J. Prost, M. Rao, R. Aditi Simha, Hydrodynamics of soft active matter. *Rev. Mod. Phys.* **85**, 1143-1189, (2013).

[75] T. Vicsek, A. Zafeiris, Collective motion. *Phys. Rep.* **517**, 71-140, (2012).

[76] C. Dombrowski, L. Cisneros, S. Chatkaew, R. E. Goldstein, J. O. Kessler, Self-concentration and large-scale coherence in bacterial dynamics. *Phys. Rev. Lett.* **93**, 2-5, (2004).

[77] M. F. Copeland, D. B. Weibel, Bacterial swarming: A model system for studying dynamic self-assembly. *Soft Matter*. **5**, 1174-1187, (2009).

[78] F. C. Keber, E. Loiseau, T. Sanchez, S. J. deCamp, L. Giomi, M. J. Bowick, M. C. Marchetti, Z. Dogic, A. R. Bausch, Topology and dynamics of active nematic vesicles. *Science*. **345**, 1135-1139, (2014).

[79] H. H. Wensink, J. Dunkel, S. Heidenreich, K. Drescher, R. E. Goldstein, H. Löwen, J. M. Yeomans, Meso-scale turbulence in living fluids. *Proc. Natl. Acad. Sci.* **109**, 14308-14313, (2012).

[80] P. Guillamat, J. Ignés-Mullol, F. Sagués, Taming active turbulence with patterned soft interfaces. *Nat. Commun.* **8**, 1-8, (2017).

[81] C. W. Reynolds, Flocks, herds, and schools. *Comput. Graph.* **21**, 25-34, (1987).

[82] N. G. Chisholm, D. Legendre, E. Lauga, A. S. Khair, A squirmer across Reynolds numbers. *J. Fluid Mech.* **796**, 233-256, (2016).

[83] E. M. Purcell, Life at low Reynolds number. *Amer. Jour. of Phys.* **45**, 3-11, (1977).

[84] H. C. Berg, D. A. Brown, Chemotaxis in Escherichia coli analysed by Three-dimensional tracking. *Nature*. **239**, (1972).

[85] J. Elgeti, G. Gompper, Metachronal waves in arrays of cilia. *Proc. Natl. Acad. Sci.*. **110**, 4470-4475, (2013).

[86] B. J. Nelson, I. K. Kaliakatsos, J. J. Abbott, Microrobots for minimally invasive medicine. *Annu. Rev. Biomed. Eng.* **12**, 55-85, (2010).

[87] R. F. Ismagilov, A. Schwartz, N. Bowden, G. M. Whitesides, Autonomous movement and self-assembly. *Angew. Chemie - Int. Ed.* **41**, 652-654, (2002).

[88] R. Dreyfus, J. Baudry, M. L. Roper, M. Fermigier, H. A. Stone, J. Bibette, Microscopic artificial swimmers. *Nature*. **437**, 862-865, (2005).

[89] M. E. Cates, J. Tailleur, Motility-Induced Phase Separation. *Annu. Rev. Condens. Matter Phys.* **6**, 219-244, (2015).

[90] J. Elgeti, R. G. Winkler, G. Gompper, Physics of microswimmers - Single particle motion and collective behavior: A review. *Reports Prog. Phys.* **78**, (2015).

[91] A. Zöttl, H. Stark, Emergent behavior in active colloids. *J. Phys. Condens. Matter*. **28**, (2016).

[92] C. Bechinger, R. Di Leonardo, H. Löwen, C. Reichhardt, G. Volpe, G. Volpe, Active particles in complex and crowded environments. *Rev. Mod. Phys.* **88**, (2016).

[93] R. Golestanian, T. B. Liverpool, A. Ajdari, Propulsion of a molecular machine by asymmetric distribution of reaction products. *Phys. Rev. Lett.* **94**, 1-4, (2005).

[94] J. R. Howse, R. A. L. Jones, A. J. Ryan, T. Gough, R. Vafabakhsh, R. Golestanian, Self-motile colloidal particles: From firected propulsion to tandom ealk. *Phys. Rev. Lett.* **99**, 8-11, (2007).

[95] P. Illien, R. Golestanian, A. Sen, Fuelled' motion: Phoretic motility and collective behaviour of active colloids. *Chem. Soc. Rev.* **46**, 5508-5518, (2017).

[96] W. F. Paxton, K. C. Kistler, C. C. Olmeda, A. Sen, S. K. St. Angelo, Y. Cao, T. E. Mallouk, P. E. Lammert, V. H. Crespi, Catalytic nanomotors: Autonomous movement of striped nanorods. *J. Am. Chem. Soc.* **126**, 13424-13431, (2004).

[97] A. A. Solovev, Y. Mei, E. B. Ureña, G. Huang, O. G. Schmidt, Catalytic microtubular jet engines self-propelled by accumulated gas bubbles. *Small*. **5**, 1688-1692, (2009).

[98] J. Palacci, S. Sacanna, A. P. Steinberg, D. J. Pine, P. M. Chaikin, Colloidal Surfers. *Science*. **339**, 36-939, (2013).

[99] C. Maggi, F. Saglimbeni, M. Dipalo, F. De Angelis, R. Di Leonardo, Micromotors with asymmetric shape that efficiently convert light into work by thermocapillary effects. *Nat. Commun.* **6**, 1-5, (2015).

[100] C. Maggi, J. Simmchen, F. Saglimbeni, J. Katuri, M. Dipalo, F. De Angelis, S. Sanchez, R. Di Leonardo, Self-Assembly of micromachining systems powered by Janus cicromotors. *Small*. **12**, 446-451, (2016).

[101] G. Vizsnyiczai, G. Frangipane, C. Maggi, F. Saglimbeni, S. Bianchi, R. Di Leonardo, Light controlled 3D micromotors powered by bacteria. *Nat. Commun.* **8**, no. 1-7, (2017).

[102] F. Ginot, I. Theurkauff, D. Levis, C. Ybert, L. Bocquet, L. Berthier, C. Cottin-Bizonne, Nonequilibrium equation of state in suspensions of active colloids. *Phys. Rev. X*. **5**, 1-8, (2015).

[103] A. P. Solon, Y. Fily, A. Baskaran, M. E. Cates, Y. Kafri, M. Kardar, J. Tailleur, Pressure is not a state function for generic active fluids. *Nat. Phys.* **11**, 673-678, (2015).

[104] J. Palacci, C. Cottin-Bizonne, C. Ybert, L. Bocquet, Sedimentation and effective temperature of active colloidal suspensions. *Phys. Rev. Lett.* **105**, 1-4, (2010).

[105] I. Theurkauff, C. Cottin-Bizonne, J. Palacci, C. Ybert, L. Bocquet, Dynamic clustering in active colloidal suspensions with chemical signaling. *Phys. Rev. Lett.* **108**, 1-5, (2012).

[106] A. Ghost, P. Fischer, Controlled propulsion of artificial magnetic nanostructured propellers. *Nano Lett.* **9**,2243-2245, (2009).

[107] P. Tierno, R. Golestanian, I. Pagonabarraga, F. Sagués, Controlled swimming in confined fluids of magnetically actuated colloidal rotors. *Phys. Rev. Lett.* **101**, 1-4, (2008).

[108] P. Tierno, R. Golestanian, I. Pagonabarraga, and F. Sagués, Magnetically actuated colloidal microswimmers. *J. Phys. Chem. B*, **112**, 16525-16528, (2008).

[109] T. M. Squires, M. Z. Bazant, Induced-charge electro-osmosis. *J. Fluid Mech.* **509**, 217-252, (2004).

[110] T. M. Squires, M. Z. Bazant, Breaking symmetries in induced-charge electro-osmosis and electrophoresis. *J. Fluid Mech.* **560**, 65-101, (2006).

[111] S. Gangwal, O. J. Cayre, M. Z. Bazant, O. D. Velev, Induced-charge electrophoresis of metallodielectric particles. *Phys. Rev. Lett.* **100**, 1–4, (2008).

[112] R. A. Robinson, R. Stokes, *Electrolyte solutions (*New York: Academic Press, 1959).

[113] F. Martinez-Pedrero, A. Ortiz-Ambriz, I. Pagonabarraga, P. Tierno, Colloidal microworms propelling via a cooperative hydrodynamic Conveyor belt. *Phys. Rev. Lett.* **115**, 1-5, (2015).

[114] A. Snezhko, M. Belkin, I. S. Aranson, W. K. Kwok, Self-assembled magnetic surface swimmers. *Phys. Rev. Lett.* **102**, 2-5, (2009).

[115] A. Snezhko, I. S. Aranson, Magnetic manipulation of self-assembled colloidal asters. *Nat. Mater.* **10**, 698-703, (2011).

[116] A. Kaiser, A. Snezhko, I. S. Aranson, Flocking ferromagnetic colloids. *Sci. Adv.* **3**, 1-11, (2017).

[117] G. Kokot, A. Snezhko, Manipulation of emergent vortices in swarms of magnetic rollers. *Nat. Commun.* **9**, 1-7, (2018).

[118] A. Bricard, J. B. Caussin, N. Desreumaux, O. Dauchot, D. Bartolo, Emergence of macroscopic directed motion in populations of motile colloids. *Nature*. **503**,95-98, (2013).

[119] A. Bricard, J. B. Caussin, D. Das, C. Savoie, V. Chikkadi, K. Shitara, O. Chepizhko, F. Peruani, D. Saintillan, D. Bartolo, Emergent vortices in populations of colloidal rollers. *Nat. Commun.* **6**, 1-8, (2015).

[120] A. Morin, N. Desreumaux, J. B. Caussin, D. Bartolo, Distortion and destruction of colloidal flocks in disordered environments. *Nat. Phys.* **13**, 63-67, (2017).

[121] S. Zhou, A. Sokolov, O. D. Lavrentovich, I. S. Aranson, Living liquid crystals. *Proc. Natl. Acad. Sci.* **111**, 1265-1270, (2013).

[122] C. Peng, T. Turiv, Y. Guo, Q.-H. Wei, O. D. Lavrentovich, Command of active matter by topological defects and patterns. *Science*. **354**, 882–886, (2016).

[123] M. M. Genkin, A. Sokolov, O. D. Lavrentovich, I. S. Aranson, Topological defects in a living nematic ensnare swimming bacteria. *Phys. Rev. X*. 7, 1-14, (2017).

[124] J. Dunkel, S. Heidenreich, K. Drescher, H. H. Wensink, M. Bär, R. E. Goldstein, Fluid dynamics of bacterial turbulence,. *Phys. Rev. Lett*. **110**, 1-5, (2013).

[125] J. Dervaux, M. Capellazzi-Resta, P. Brunet, Light-controlled flows in active fluids. *Nat. Phys.* **13**, 306-312, (2017).

[126] P. C. Mushenheim, R. R. Trivedi, H. H. Tuson, D. B. Weibel, N. L. Abbott, Dynamic self-assembly of motile bacteria in liquid crystals. *Soft Matter*. **10**, 88-95, (2014).

[127] I. Duchesne, S. Rainville, T. Galstian, Bacterial motility reveals unknown molecular organization. *Biophys. Jour.* **109**, 2137-2147, (2015).

[128] L. Dewenter, C. Alpmann, M. Woerdemann, C. Denz, Video-based analysis of the rotational behaviour of rod-shaped, self-propelled bacteria in holographic optical tweezers. **8427**, (2012).

[129] T. Sanchez, D. T. N. Chen, S. J. Decamp, M. Heymann, Z. Dogic, Spontaneous motion in hierarchically assembled active matter. *Nature*. **491**, 431-434, (2012).

[130] P. Guillamat, J. Ignés-Mullol, F. Sagués, Control of active liquid crystals with a magnetic field. *Proc. Natl. Acad. Sci.* **113**, 5498-5502, (2016).

[131] A. Doostmohammadi, J. Ignés-Mullol, J. M. Yeomans, F. Sagués, Active nematics. *Nat. Commun.* **9**, (2018).

[132] H. Morgan, N. Green, *AC electrokinetics: colloids and nanoparticles* (Microtechnology. Philadelphia, 2003).

[133] I. Lazo, O. D. Lavrentovich, Liquid-crystal-enabled electrophoresis of spheres in a nematic medium with negative dielectric anisotropy," *Philos. Trans. of the Roy. Soc. A.* **371**, (2013).

[134] M. Z. Bazant, T. M. Squires, Induced-Charge Electrokinetic Phenomena: Theory and Microfluidic Applications. *Phys. Rev. Lett.* **92**, 1-4, (2004).

[135] C. Zhao, C. Yang, Advances in electrokinetics and their applications in micro/nano fluidics. *Microfluid. Nanofluidics*. **13**, 179-203, (2012).

[136] N. I. Gamayunov, G. I. Mantrov, V. A. Murtsovkin, Study of flows induced in the vicinity of conducting particles by an external electric field. *Colloid. J.* **54**, (1992).

[137] C. Peng, I. Lazo, S. V. Shiyanovskii, O. D. Lavrentovich, Induced-charge electro-osmosis around metal and Janus spheres in water: Patterns of flow and breaking symmetries. *Phys. Rev. E*. **90**, 1-5, (2014).

[138] O. D. Lavrentovich, I. Lazo, O. P. Pishnyak, Nonlinear electrophoresis of dielectric and metal spheres in a nematic liquid crystal. *Nature.* **467**, 947-950, (2010).

[139] I. Lazo, C. Peng, J. Xiang, S. V Shiyanovskii, O. D. Lavrentovich, Liquid crystal-enabled electro-osmosis through spatial charge separation in distorted regions as a novel mechanism of electrokinetics. *Nat Commun*. **5**, (2014).

[140] S. Paladugu, C. Conklin, J. Viñals, O. D. Lavrentovich, Nonlinear Electrophoresis of colloids controlled by anisotropic conductivity and permittivity of Liquid-Crystalline Electrolyte," *Phys. Rev. Appl.* **7**, 1-8, (2017).

[141] S. Hernàndez-Navarro, P. Tierno, J. Ignés-Mullol, F. Sagués, AC electrophoresis of microdroplets in anisotropic liquids: transport, assembling and reaction. *Soft Matter*. **9**, 7999-8004, (2013).

[142] S. Hernàndez-Navarro, P. Tierno, J. A. Farrera, J. Ignés-Mullol, F. Sagués, Reconfigurable swarms of nematic colloids controlled by photoactivated surface patterns. *Angew. Chemie - Int. Ed.* **53**, 10696–10700, (2014).

[143] A. Ulman, Structure and stability of self-assembled monolayers. *Chem. Rev.* **96**, 1533-1554, (1996).

[144] I. Lelidis, C. Öedman, Influence of substrate nature and growth conditions on the morphology of thin DMOAP films. *Liq. Cryst.* **30**, 643–649, (2003).

[145] P. S. Noonan, A. Shavit, B. R. Acharya, D. K. Schwartz, Mixed alkylsilane functionalized surfaces for simultaneous wetting and homeotropic anchoring of liquid crystals. *ACS Appl. Mater. Interfaces*. **3**, 4374-4380, (2011).

[146] P. Oswald, J. Ignés-Mullol, Modeling a photoinduced planar-to-homeotropic anchoring transition triggered by surface azobenzene units in a nematic liquid crystal. *Phys. Rev. E.* **96**, 1-15, (2017).

[147] P. Oswald, G. Poy, A. Dequidt, Lehmann rotation of twisted bipolar cholesteric droplets: role of Leslie, Akopyan and Zel'dovich thermomechanical coupling terms of nematodynamics. *Liq. Cryst.* **44**, 969-988, (2016).

[148] C. Graf, D. L. J. Vossen, A. Imhof, A. van Blaaderen, A general method to coat colloid particles with silica. *Langmuir*. **19**, 6693-6700, (2003).

[149] J. Sprakel, J. van der Gucht, M. A. Cohen Stuart, N. A. Besseling, Brownian particles in transient polymer networks. *Phys. Rev. E*. **77**, (2008).

[150] R. Angelico, A. Ceglie, U. Olsson, G. Palazzo, L. Ambrosone, Anomalous surfactant diffusion in a living polymer system. *Phys. Rev. E*. **74**, 1-8, (2006).

[151] J. Schwarz-Linek, C. Valeriani, A. Cacciuto, M. E. Catese, D. Marenduzzo, A. N. Morozov, W. C. K. Poon, Phase separation and rotor self-assembly in active particle suspensions. *Proc. Natl. Acad. Sci.* **109**, (2012).

[152] T. Qiu, T.-C. Lee, A. G. Mark, K. I. Morozov, R. Münster, O. Mierka, S. Turek, A. M. Leshansky, P. Fischer, Swimming by reciprocal motion at low Reynolds number. *Nat. Commun.* **5**, 1-8, (2014).

[153] J. Toner, H. Löwen, H. H. Wensink, Following fluctuating signs: Anomalous active superdiffusion of swimmers in anisotropic media. *Phys. Rev. E*. **93**, 1-11, (2016).

[154] C. Ferreiro-Córdova, J. Toner, H. Löwen, H. H. Wensink, Long-time anomalous swimmer diffusion in smectic liquid crystals. *Phys. Rev. E*. **97**, 1-11, (2018).

[155] T. Turiv, A. Brodin, V. G. Nazarenko, Anomalous Brownian motion of colloidal particle in a nematic environment : effect of the director fluctuations. *Cond. Matt. Phys*. **18**, 1-13, (2015).

[156] J. S. Lintuvuori, A. Würger, K. Stratford, Hydrodynamics defines the stable swimming direction of spherical squirmers in a nematic liquid crystal. *Phys. Rev. Lett.* **119**, 1-6,

(2017).

[157] A. Daddi-Moussa-Ider, A. M. Menzel, Dynamics of a simple model microswimmer in an anisotropic fluid: Implications for alignment behavior and active transport in a nematic liquid crystal. *Phys. Rev. Fluids*. **3**, 1–32, (2018).

[158] L. Bruno, V. Levi, M. Brunstein, M. A. Despósito, Transition to superdiffusive behavior in intracellular actin-based transport mediated by molecular motors. *Phys. Rev. E.* **80**. 1-7, (2009).

[159] M. A. Despósito, C. Pallavicini, V. Levi, L. Bruno, Active transport in complex media: Relationship between persistence and superdiffusion. *Physica A*. **390**, 1026-1032, (2011).

[160] P. Guillamat, Ž. Kos, J. Hardoüin, J. Ignés-Mullol, M. Ravnik, F. Sagués, Active nematic emulsions. *Sci. Adv.* **4**, 1-11, (2018).

[161] R. Aditi Simha, S. Ramaswamy, Hydrodynamic fluctuations and instabilities in ordered suspensions of self-propelled particles. *Phys. Rev. Lett.* **89**, (2002).

[162] I. Lazo, O. D. Lavrentovich, Liquid-crystal-enabled electrophoresis of spheres in a nematic medium with negative dielectric anisotropy. *Philos. Trans. of the Roy. Soc.* **371**, (2013).

[163] A. L. Thorneywork, J. L. Abbott, D. G. A. L. Aarts, R. P. A. Dullens, Two-Dimensional melting of colloidal hard spheres. *Phys. Rev. Lett.* **118**, 1-5, (2017).

[164] S. Hernàndez-Navarro, P. Tierno, J. Ignés-Mullol, F. Sagués, Reconfigurable swarms of colloidal particles electrophoretically driven in nematic liquid crystals. *Mol. Cryst. Liq. Cryst.* **610**, 163-172, (2015).

[165] Y. Chuang, M. R. D. Orsogna, D. Marthaler, A. L. Bertozzi, L. S. Chayes, State transitions and the continuum limit for a 2D interacting, self-propelled particle system. *Physica D.* **232**, 33-47, (2007).

[166] A. Santos, M. López de Haro, S. Bravo-Yuste, An accurate and simple equation of state for hard disks. **103**, 4622-4625, (1995).

[167] F. Rothen, P. Pieranski, N. Rivier, A. Joyet, Conformal crystal. *Eur. J. Phys.* **14**, 227-233, (1993).

[168] Z. Yao, M. O. de la Cruz, Topological defects in flat geometry : The role of density inhomogeneity. *Phys. Rev. Lett.* **111**, 1-5, (2013).

[169] V. Soni, L. R. Gómez, W. T. M. Irvine, Emergent geometry of inhomogeneous planar crystals. *Phys. Rev. X*. **8**, (2018).

[170] H. P. Zhang, A. Be'er, E.-L. Florin, H. L. Swinney, Collective motion and density fluctuations in bacterial colonies. *Proc. Natl. Acad. Sci.* **107**, 13626.13630, (2010).

[171] J. R. Gomez-Solano, S. Samin, C. Lozano, P. Ruedas-Batuecas, R. van Roij, C. Bechinger, Tuning the motility and directionality of self-propelled colloids. *Sci. Adv*. **7**, 1-12, (2017).

[172] J. A. Cohen, R. Golestanian, Emergent cometlike swarming of optically driven thermally active colloids. *Phys. Rev. Lett.* **112**, 1-4, (2014).

[173] K. To, P. Lai, H. K. Pak, Jamming of granular glow in a Two-Dimensional hopper. *Phys. Rev. Lett.* **86**, 71-74, (2001).

[174] E. Dressaire, A. Sauret, Clogging of microfluidic systems. *Soft Matter*. **13**, 37-48, (2017).

[175] T. Glanz, R. Wittkowski, H. Löwen, Symmetry breaking in clogging for oppositely driven particles. *Phys. Rev. E*. **94**, 1-7, (2016).

[176] C. Reichhardt, C. J. O. Reichhardt, Active matter transport and jamming on disordered landscapes. *Phys. Rev. E*. **90**. 1–5, (2014).

[177] A. Sengupta, S. Herminghaus, C. Bahr, Nematic liquid crystals and nematic colloids in microfluidic environment. *Mol. Cryst. Liq. Cryst.* **547**, (2011).

[178] A. Sengupta, C. Bahr, S. Herminghaus, Topological microfluidics for flexible micro-cargo concepts. *Liq. Cryst. Rev*. **9**, 73–110, (2014).

[179] D. Bartolo, G. Degre, P. Nghe, V. Studer, Microfluidic stickers. *Lab on a chip*. **8**, 274-279, (2007).

[180] M. R. De Saint, M. Abkarian, H. Tabuteau, Dynamics of colloid accumulation under flow over porous obstacles. *Soft Matter*. **12**, 1041–1050, (2016).

[181] I. Zuriguel, A. Garcimartín, D. Maza, L. A. Pugnaloni, J. M. Pastor, Jamming during the discharge of granular matter from a silo. *Phys. Rev. E*. **71**, 1-9, (2005).

List of publications

Below, find a list of chronologically ordered articles, which are already published (P), in press (P_P) or submitted for publication (P_S).

P1. A.V. Straube, J.M. Pagès, A. Ortiz-Ambriz, P. Tierno, J. Ignés-Mullol, F. Sagués, Assembly and transport of nematic colloidal swarms above photo-patterned defects and surfaces. *New. J. Phys*. **20**, (2018).

P2. J.M. Pagès, A.V. Straube, P. Tierno, J. Ignés-Mullol, F. Sagués, Inhomogeneous assembly of driven nematic colloids. *Soft Matter*. **15**, 312-320 (2019).

P_P3. J.M.Pagès, J. Ignés-Mullol, F. Sagués, Anomalous diffusion of motile colloids dispersed in liquid crystals. Accepted in *Phys. Rev. Lett.* (2019)

P_S4. J.M. Pagès, A.V. Straube, P. Tierno, J. Ignés-Mullol, F. Sagués, Collective dynamics and conformal ordering in electrophoretically driven nematic colloids (2019). Submitted to *Phys. Rev. Lett*.